NUMERICAL ASSESSMENT OF EDDY-VISCOSITY TURBULENCE MODELS ON AN AXIAL-FLOW TURBINE AT A LOW REYNOLDS NUMBER

by

Nick Dagoberto Estrada

A Thesis Submitted to the Faculty of

The College of Engineering and Computer Science

in Partial Fulfillment of the Requirements for the Degree of

Master of Science

Florida Atlantic University

Boca Raton, FL

May 2016

NUMERICAL ASSESSMENT OF EDDY-VISCOSITY TURBULENCE MODELS

ON AN AXIAL-FLOW TURBINE AT A LOW REYNOLDS NUMBER

by

Nick Dagoberto Estrada

This thesis was prepared under the direction of the candidate's thesis advisor, Dr. Davood Moslemian, Department of Ocean and Mechanical Engineering, and has been approved by the members of his supervisory committee. It was submitted to the faculty of the College of Engineering and Computer Science and was accepted in partial fulfillment of the requirements for the degree of Master of Science.

SUPERVISORY COMMITTEE:

Davood Moslemian, Ph.D.
Thesis Advisor

Gopal Gaonkar, Ph.D.

Tsung-Chow Su, Ph.D.

Javad Hashemi, Ph.D.
Chair, Department of Ocean and Mechanical Engineering

Mohammad Ilyas, Ph.D.
Dean, College of Engineering and Computer Science

Deborah L. Floyd, Ed.D
Dean, Graduate College

04/15/2016
Date

ACKNOWLEDGEMENTS

This thesis is the result of my own work carried out at Florida Atlantic University, between January 2013 and April 2016 and includes nothing which is the outcome of work done in collaboration, except where stated. No part of the work has been submitted to any other university, institution, or place of learning.

I feel very accomplished, after working extensively on this thesis the last three years. To think, that when I first started my graduate studies, I knew very little about CFD and turbomachinery flows. I have learned firsthand that it takes meticulous research & development to learn and apply the various knowledge and methods.

There are many people to whom I wish to express my sincere gratitude. I would like to acknowledge my thesis advisor, Dr. Davood Moslemian, whom gave me the opportunity to work on this project under his guidance. I thank him for his invaluable suggestions, persistence, patience, encouragement, and continued support while writing my manuscript and throughout this research. I would like to especially thank him for granting me sufficient freedom to pursue my own ideas. I greatly appreciate his constructive advice and suggestions on several occasions, while also being very understanding in multiple situations. I am grateful for the help and support provided by my committee members. I really appreciate the interest they showed in the present research. It is a pleasure and privilege to work with them.

My gratitude goes to the IT support of our virtual machines and high performance computing software and hardware. I greatly appreciate the help from Scott Ridenour, James

Mauser, Mahesh Neelakanta, and Eric Bornstein. They were very helpful and patient in fulfilling my requests and computer problems. I am pleased to acknowledge my colleague, Daniel Rodriguez, for his helpful advice, discussions, and help in proof-reading some of the chapters. I would like to thank all my classmates for all their support and help. I would like to thank Dr. Takayuki Matsunuma from AIST for the experimental data he shared, which was essential in validation of the numerical solutions. Last, but certainly not least, I would like to thank my family, particularly my parents, for their never-ending encouragement and support.

ABSTRACT

Author: Nick Dagoberto Estrada

Title: Numerical Assessment of Eddy-Viscosity Turbulence Models of an Axial-Flow Turbine at a Low Reynolds Number

Institution: Florida Atlantic University

Thesis Advisor: Dr. Davood Moslemian

Degree: Master of Science

Year: 2016

The flow field behavior of axial flow turbines is of great importance, especially in modern designs that may operate at a low Reynolds number. At these low Reynolds numbers, the efficiency loss is significantly augmented compared to higher Reynolds number flows. A detailed incompressible numerical study of a single stage axial-flow turbine at a low Reynolds number is investigated with the use of multiple eddy-viscosity turbulence models. The study includes epistemic uncertainty quantification as a form of numerical error estimation. The numerical results show good qualitative and quantitative agreement with experimental data. It was found that the shear stress transport (SST) $k-\omega$ turbulence model with rotation/curvature correction and inclusion of transition modeling is most capable at predicting the mean velocity distribution, which is further enhanced when the URANS formulation is employed. However, all the cases indicate a large variation in the prediction of the root-mean-squared of the turbulent velocity fluctuations.

NUMERICAL ASSESSMENT OF EDDY-VISCOSITY TURBULENCE MODELS ON AN AXIAL-FLOW TURBINE AT A LOW REYNOLDS NUMBER

TABLES XI

FIGURES XV

NOMENCLATURE XXV

1. INTRODUCTION 1

1.1. Introduction 1

1.2. Thesis Objective 6

1.3. Thesis Outline 7

2. LITERATURE REVIEW 8

2.1. Introduction 8

2.2. Loss Mechanisms in an Axial-Flow Turbine 8

2.2.1. Profile Loss 9

2.2.2. Secondary (or Endwall) Flows 10

2.2.3. Tip Leakage Flow 17

2.3. Unsteady Flow 19

2.4. Pressure Loss Coefficients 19

2.4.1. Effect of Low Reynolds Lapse 21

2.5. Computational Fluid Dynamics Application/Outcomes 22

2.5.1. Existing Numerical Simulations on Experimental Cascade 26
2.5.2. Limitations of CFD 27
2.5.3. Numerical Uncertainty 28
2.6. Experimental Validation Data 32
2.6.1. Experimental Techniques 35
2.6.2. Experimental Uncertainty 36
2.6.3. Post-Processing of Experimental Data 37
2.7. Literature Review Conclusions and Uniqueness of this Investigation 39
3. CONSTRUCTION OF CONCEPTUAL MODEL 41
3.1. Introduction 41
3.2. Physical System and System Surroundings 41
3.3. Operating Environment 42
3.3.1. System Conditions 42
3.3.2. Computer Software 44
3.4. Physical Assumptions that Simplify the System 44
3.5. Phenomena of Interest 45
3.6. System Response Quantities of Interest 45
3.7. Accuracy Requirements for the System Response Quantities of Interest 46
4. FORMULATION OF MATHEMATICAL MODEL 48
4.1. Physical Processes 48
4.2. Physical Models 49
4.2.1. RANS/URANS Approach 50
4.2.2. Eddy-Viscosity Turbulence Models 52

4.2.2.1. k − ε Turbulence Model 54
4.2.2.2. k − ω Turbulence Model 55
4.2.2.3. SST Turbulence Model 56
4.2.3. Production Limiters 57
4.2.4. Curvature Correction for Two-Equation Models 58
4.2.5. Transition Model 59
5. SIMPLE RADIAL EQUILIBRIUM ANALYSIS 65
6. NUMERICAL APPROACH 73
6.1. Geometry Creation 73
6.2. Mesh Generation 78
6.3. CFD Modeling 83
6.3.1. Pre-Processing 85
6.3.2. CFX-Solver 90
6.3.3. CFD-Post 91
7. ANALYSIS OF NUMERICAL RESULTS & DISCUSSION 94
7.1. Spatial Verification & Validation 94
7.1.1. Streamwise Spatial Verification 100
7.1.2. Streamwise Validation 107
7.1.3. Spanwise Verification 112
7.1.4. Spanwise Validation 117
7.1.5. Nozzle Surface Flow 122
7.1.6. Steady State Turbulence Model Discussion 125
7.2. Steady State and Transient Temporal Verification and Validation 128

7.2.1. Steady State Temporal Verification 128
7.2.2. Transient Temporal Verification 135
7.2.3. Transient and Steady State Temporal Validation 145
7.2.4. Steady State and Transient Model Discussion 154
8. FLOW FIELD ANALYSIS AND DISCUSSION 157
9. CONCLUSION 193
APPENDIX 195
REFERENCES 196

TABLES

Table 1: Time-line of measurement technique advancement of low Reynolds number flows at AIST 6

Table 2: Specifications of turbine cascade [24] 34

Table 3: LDV measurement uncertainty [24] 37

Table 4: Design velocity at mid-span 71

Table 5: Design velocity 71

Table 6: Specific work and power delivered by turbine stage 72

Table 7: Mesh element size variation 81

Table 8: Nozzle computational domain $Y+$ parameters 82

Table 9: Rotor computational domain $Y+$ parameters 82

Table 10: Downstream computational domain $Y+$ parameters 82

Table 11: Average solver mesh statistics 83

Table 12: Region information for computational domains 86

Table 13: General settings used for steady state CFD models 89

Table 14: General settings used for transient CFD model 90

Table 15: MeTiS partitioning detail 91

Table 16: Solver detail of mesh partitioning 91

Table 17: Steady state refinement factor for each turbulence model 104

Table 18:Exit plane velocities for the steady state models at mesh size M5 104

Table 19: Streamwise global GCI for specified SRQ and turbulence model (spatial discretization) 105

Table 20: Mean error of the absolute and relative velocities in the streamwise direction for all the models (steady state, M5) 111

Table 21: Mean error of the RMS of the turbulent velocity fluctuations in the streamwise direction for all the models (steady state, M5) 111

Table 22: Spanwise global GCI for specified SRQ and turbulence model at the nozzle exit plane ($ZNZ/Cax, NZ = 1.154$, spatial discretization) 114

Table 23: Spanwise global GCI for specified SRQ and turbulence model at the rotor exit plane ($ZRT/Cax, RT = 1.145$, spatial discretization) 117

Table 24: Mean error in the spanwise direction at the nozzle exit plane for all the models ($ZNZ/Cax, NZ = 1.15$, steady state) 119

Table 25: Mean error in the spanwise direction at the rotor exit plane for all the models ($ZRT/Cax, RT = 1.145$, M5, steady state) 122

Table 26: Steady state physical time scale variation and associated refinement factor 129

Table 27: Exit plane velocities at the specified physical time scale ($SST - Transition - CC$, M5) 131

Table 28: Streamwise global GCI for specified SRQ ($SST - Transition - CC$, M5, steady state temporal discretization) 131

Table 29: Spanwise global GCI for specified SRQ at the nozzle exit plane ($ZNZ/Cax, NZ = 1.154$, $SST - Transition - CC$, M5, steady state temporal discretization) 133

Table 30: Spanwise global GCI for specified SRQ at the rotor exit plane ($ZRT/Cax, RT = 1.145$, $SST - Transition - CC$, M5, steady state temporal discretization) 133

Table 31: Transient time step variation and associated refinement factor..... 135

Table 32: Exit Plane velocities at specified time step ($SST - Transition - CC$, M5) 138

Table 33: Streamwise global GCI for specified SRQ ($SST - Transition - CC$, M5, transient temporal discretization)..... 141

Table 34: Spanwise global GCI for specified SRQ at the nozzle exit plane ($ZNZ/Cax, NZ = 1.154$, $SST - Transition - CC$, M5, transient temporal discretization) 142

Table 35: Spanwise global GCI for specified SRQ and turbulence model at the rotor exit plane ($ZRT/Cax, RT = 1.145$, $SST - Transition - CC$, M5, transient temporal discretization) 143

Table 36: Mean error for the specified SRQ's in the streamwise direction (steady state – $\Delta t/4$ and transient - $15\pi 31\Delta t$) 148

Table 37: Mean error in the spanwise direction at the nozzle exit plane ($ZNZ/Cax, NZ = 1.154$ for steady state – $\Delta t/4$ and transient - $15\pi 31\Delta t$)..... 150

Table 38: Mean error in the spanwise direction at the rotor exit plane ($ZRT/Cax, RT = 1.145$ for steady state – $\Delta t/4$ and transient - $15\pi 31\Delta t$)..... 154

Table 39: Spanwise mean error of the absolute flow angle, axial velocity and tangential velocity at the nozzle exit plane ($ZNZ/Cax, NZ = 1.154$)..... 174

Table 40: Total Pressure Losses at the nozzle exit plane ($ZNZ/Cax, NZ = 1.154$) 175

Table 41: Spanwise mean error of the relative flow angle, axial velocity and tangential velocity at the rotor exit plane ($ZRT/Cax, RT = 1.154$)..... 187

Table 42: Total Pressure Losses at the rotor exit plane ($ZRT/Cax, RT = 1.145$)..... 188

FIGURES

Figure 1: Model of Hawthorne Secondary Flow Model [31] 12

Figure 2: Langston Cascade Secondary Flow Patterns [14] 12

Figure 3: Sharma and Butler Secondary Flow Model [36] 14

Figure 4: Goldstein and Spores Secondary Flow Model [37] 15

Figure 5: Wang et al. Secondary Flow Model [26] 16

Figure 6: Flow over the tip gap for an unshrouded blade [28] 18

Figure 7: Total Pressure (a) net overall loss at nozzle exit [16] and (b) loss at rotor exit mid-span [24] 21

Figure 8: Geometry of Turbine [24] 35

Figure 9: Spanwise distribution of the velocity at the nozzle inlet 38

Figure 10: Absolute velocity at the nozzle exit ($ZNZ/Cax, NZ = 1.154$) 38

Figure 11: Time-resolved absolute velocity at the nozzle exit ($ZNZ/Cax, NZ = 1.154$) 39

Figure 12: Time resolved relative velocity at the rotor exit ($ZRT/Cax, RT = 1.145$) 39

Figure 13: Turbine stage velocity diagram 43

Figure 14: Single stage Axial Turbine (a) Cross-sectional view and (b) Velocity Triangles 67

Figure 15: Variation of coefficients along blade span 69

Figure 16: Variation of flow angles along blade span 69

Figure 17: Macro formatted in Excel sheet 75
Figure 18: Original imported points 75
Figure 19: Nozzle and rotor airfoil span-distribution 76
Figure 20: SolidWorks nozzle and rotor airfoils geometries 77
Figure 21: Complete computational domain 77
Figure 22: Block topology 79
Figure 23: Multiple views of computational mesh 80
Figure 24: CFX-Pre layout 87
Figure 25: Inlet velocity distribution 88
Figure 26: Data extraction planes for comparison with experimental data 92
Figure 27: Velocity components of interest in CFD-Post, (adapted from [92]) 93
Figure 28: RMS residuals for mass continuity and momentum ($SST - Transition - CC$, M5) 95
Figure 29: RMS residuals for the turbulent kinetic energy and specific dissipation ($SST - Transition - CC$, M5) 95
Figure 30: RMS residuals for intermittency and the transition momentum thickness Reynolds number ($SST - Transition - CC$, M5) 96
Figure 31: RMS residual for the wall scale ($SST - Transition - CC$, M5) 96
Figure 32: Mass flow rate surface monitor at stator planes ($SST - Transition - CC$, M5) 97
Figure 33: Mass flow rate surface monitor at rotor and downstream planes ($SST - Transition - CC$, M5) 97

Figure 34: Mass flow rate surface monitor at stator domain exit for all the models 99

Figure 35: Mass flow rate surface monitor at rotor domain exit for all the models 99

Figure 36: CPU requirement vs host memory allocation (steady state, M5) 100

Figure 37: Streamwise mesh dependency study of the absolute velocity ($SST - Transition - CC$) 101

Figure 38: Streamwise mesh dependency study of the relative velocity ($SST - Transition - CC$) 102

Figure 39: Streamwise mesh dependency study of the absolute total pressure loss ($SST - Transition - CC$) 102

Figure 40: Streamwise mesh dependency study of the RMS of the turbulent velocity fluctuations ($SST - Transition - CC$) 103

Figure 41: Local spatial uncertainty for RMS of the turbulent velocity fluctuations ($SST - Transition - CC$, M5) 106

Figure 42: Memory allocation vs mesh element size 107

Figure 43: Streamwise distribution of the absolute velocity for all the models with comparison to experiment (M5, steady state) 108

Figure 44: Streamwise distribution of the relative velocity for all the models with comparison to experiment (M5, steady state) 109

Figure 45: Streamwise distribution of the RMS of the turbulent velocity fluctuations for all the models with comparison to experiment (M5, steady state) 109

Figure 46: Streamwise distribution of the absolute pressure loss for all the models with comparison to experiment (M5, steady state) 110

Figure 47: Spanwise mesh dependence of the absolute velocity at the nozzle exit plane ($ZNZ/Cax, NZ = 1.154, SST - Transition - CC$) 113

Figure 48: Spanwise mesh dependence of the RMS of the turbulent velocity fluctuations at the nozzle exit plane ($ZNZ/Cax, NZ = 1.154, SST - Transition - CC$) 113

Figure 49: Spanwise mesh dependence of the absolute velocity at the rotor exit plane ($ZRT/Cax, RT = 1.145, SST - Transition - CC$) 115

Figure 50: Spanwise mesh dependence of the relative velocity at the rotor exit plane ($ZRT/Cax, RT = 1.145, SST - Transition - CC$) 116

Figure 51: Spanwise mesh dependence of the RMS of the turbulent velocity fluctuations at the rotor exit plane ($ZRT/Cax, RT = 1.145, SST - Transition - CC$) 116

Figure 52: Spanwise distribution of the absolute velocity for all the models with comparison to experiment at the nozzle exit plane ($ZNZ/Cax, NZ = 1.154$, M5, steady state) 118

Figure 53: Spanwise distribution of the RMS of the turbulent velocity fluctuations for all the models with comparison to experiment at the nozzle exit plane ($ZNZ/Cax, NZ = 1.154$, M5, steady state) 119

Figure 54: Spanwise distribution of the absolute velocity for all the models with comparison to experiment at the rotor exit plane ($ZRT/Cax, RT = 1.145$, M5, steady state) 120

Figure 55: Spanwise distribution of the relative velocity for all the models with comparison to experiment at the rotor exit plane ($ZRT/Cax, RT = 1.145$, M5, steady state) 121
Figure 56: Spanwise distribution of the RMS of the turbulent velocity fluctuations for all the models with comparison to experiment at the rotor exit plane ($ZRT/Cax, RT = 1.145$, M5, steady state) 121
Figure 57: Oil-film visualization of nozzle suction surface [24] 123
Figure 58: Nozzle suction surface wall shear streamlines 125
Figure 59: RMS residuals for transition momentum thickness Reynolds number at different time scales ($SST - Transition - CC$, M5) 130
Figure 60: Streamwise steady state temporal dependency study of the RMS of the turbulent velocity fluctuations ($SST - Transition - CC$, M5) 132
Figure 61: Local steady state temporal uncertainty for RMS of the turbulent velocity fluctuations ($SST - Transition - CC$ M5) 132
Figure 62: Spanwise steady state temporal dependency study of the RMS of the turbulent velocity fluctuations at the nozzle exit plane ($ZNZ/Cax, NZ = 1.154$, $SST - Transition - CC$, M5) 134
Figure 63: Spanwise steady state temporal dependency study of the RMS of the turbulent velocity fluctuations at the rotor exit plane ($ZRT/Cax, RT = 1.145$, $SST - Transition - CC$, M5) 134
Figure 64: Inner coefficient loops of RMS Residuals for mass continuity and momentum ($SST - Transition - CC$, M5, transient, $15\pi 31\Delta t$) 136

Figure 65: RMS Residuals for mass continuity and momentum ($SST - Transition - CC$, M5, transient, $15\pi 31\Delta t$) 137

Figure 66: RMS residuals for the turbulent kinetic energy and specific dissipation ($SST - Transition - CC$, M5, transient, $15\pi 31\Delta t$) 137

Figure 67: RMS residuals for intermittency and the transition momentum thickness Reynolds number ($SST - Transition - CC$, M5, transient, $15\pi 31\Delta t$)..... 138

Figure 68: Mass flow rate surface monitor at nozzle exit plane for different time steps ($SST - Transition - CC$, M5) 139

Figure 69: Mass flow rate surface monitor at rotor inlet plane for different time steps ($SST - Transition - CC$, M5) 139

Figure 70: Mass flow rate surface monitor at rotor exit plane for different time steps ($SST - Transition - CC$, M5) 140

Figure 71: Streamwise transient temporal dependency study of the RMS of the turbulent velocity fluctuations (Transient, $SST - Transition - CC$, M5) 141

Figure 72: Spanwise transient temporal dependency study of the absolute velocity at the rotor exit plane ($ZRT/Cax, RT = 1.145$, $SST - Transition - CC$, M5) 143

Figure 73: Spanwise transient temporal dependency study of the relative velocity at the rotor exit plane ($ZRT/Cax, RT = 1.145$, $SST - Transition - CC$, M5) 144

Figure 74: Spanwise transient temporal dependency study of the RMS of the turbulent velocity fluctuations at the rotor exit plane ($ZRT/Cax, RT = 1.145$, $SST - Transition - CC$, M5) 144

Figure 75: Streamwise distribution of the absolute velocity with comparison to experiment (steady state – $\Delta t/4$ and transient - $15\pi 31\Delta t$)..... 145

Figure 76: Streamwise distribution of the relative velocity with comparison to experiment (steady state – $\Delta t/4$ and transient - $15\pi 31\Delta t$)..... 146

Figure 77: Streamwise distribution of the absolute pressure loss with comparison to experiment (steady state – $\Delta t/4$ and transient - $15\pi 31\Delta t$) 146

Figure 78: Streamwise distribution of the RMS of the turbulent velocity fluctuations with comparison to experiment (steady state – $\Delta t/4$ and transient - $15\pi 31\Delta t$) 147

Figure 79: Spanwise distribution of the absolute velocity with comparison to experiment at the nozzle exit plane ($ZNZ/Cax, NZ = 1.154$, steady state – $\Delta t/4$ and transient - $15\pi 31\Delta t$) 149

Figure 80: Spanwise distribution of the RMS of the turbulent velocity fluctuations with comparison to experiment at the nozzle exit plane ($ZNZ/Cax, NZ = 1.154$, steady state – $\Delta t/4$ and transient - $15\pi 31\Delta t$) 150

Figure 81: Spanwise distribution of the absolute velocity with comparison to experiment at the rotor exit plane ($ZRT/Cax, RT = 1.145$, steady state – $\Delta t/4$ and transient - $15\pi 31\Delta t$) 152

Figure 82: Spanwise distribution of the relative velocity with comparison to experiment at the rotor exit plane ($ZRT/Cax, RT = 1.145$, steady state – $\Delta t/4$ and transient - $15\pi 31\Delta t$) 152

Figure 83: Spanwise distribution of the RMS of the turbulent velocity fluctuations with comparison to experiment at the rotor exit plane ($ZRT/Cax, RT = 1.145$, steady state – $\Delta t/4$ and transient - $15\pi 31\Delta t$) 153

Figure 84: CPU requirement vs host memory allocation ($SST - Transition - CC$, M5, steady state time scale dependency)..... 155

Figure 85: CPU requirement vs host memory allocation ($SST - Transition - CC$, M5, transient time step dependency)..... 156

Figure 86: Nozzle tip topology (steady state – $\Delta t/4$)..... 159

Figure 87: Nozzle hub topology (steady state – $\Delta t/4$)..... 160

Figure 88: Nozzle hub endwall flow..... 160

Figure 89: Nozzle blade topology (steady state – $\Delta t/4$) 162

Figure 90: Nozzle mid-span topology (steady state – $\Delta t/4$)..... 163

Figure 91:Distributions of absolute velocity, total pressure, turbulence intensity, and static pressure at the nozzle exit plane ($ZNZ/Cax, NZ = 1.154$,steady state ($\Delta t/4$))..... 164

Figure 92: LDV Experimental data at the nozzle exit plane ($ZNZ/Cax, NZ = 1.154$) 165

Figure 93: Distributions of vorticity and streamwise vorticity at the nozzle exit plane ($ZNZ/Cax, NZ = 1.154$,steady state ($\Delta t/4$))..... 167

Figure 94: Time-averaged distributions of absolute velocity, total pressure, turbulence intensity, and static pressure at the nozzle exit plane ($ZNZ/Cax, NZ = 1.154$,Transient $15\pi31\Delta t$) 168

Figure 95: Time-averaged distributions of vorticity and stream wise vorticity for the transient $15\pi31\Delta t$ numerical solution at the nozzle exit (axial position $ZNZ/Cax, NZ = 1.154$)..... 168

Figure 96: Static Pressure coefficient with secondary flow vectors overlaid (5-hole pressure probe) 171

Figure 97: Spanwise distribution of the absolute flow angle at the nozzle exit plane ($ZNZ/Cax, NZ = 1.154$) 172

Figure 98: Distribution of axial and tangential velocities at the nozzle exit plane ($ZNZ/Cax, NZ = 1.154$) 173

Figure 99: Time-averaged absolute flow angle on nozzle blade surface (transient $15\pi31\Delta t$)..... 176

Figure 100: LDV Experimental data of velocity at the rotor exit plane ($ZRT/Cax, RT = 1.145$)..... 177

Figure 101: LDV Experimental data of turbulence intensity at the rotor exit plane ($ZRT/Cax, RT = 1.145$)..... 178

Figure 102: Distributions of absolute velocity, total pressure, turbulence intensity, and static pressure at the rotor exit plane ($ZRT/Cax, RT = 1.145$, steady state ($\Delta t/4$)..... 179

Figure 103: Time-averaged distributions of relative velocity, total pressure, turbulence intensity, and static pressure at the rotor exit plane ($ZRT/Cax, RT = 1.145$, transient ($15\pi 31\Delta t$) 180

Figure 104: Distributions of absolute velocity at the rotor exit ($ZRT/Cax, RT = 1.145$) 182

Figure 105: Distributions of vorticity and stream wise vorticity at the rotor exit plane ($ZRT/Cax, RT = 1.145$, steady state ($\Delta t/4$) 184

Figure 106: Time-averaged distributions of vorticity and stream wise vorticity at the rotor exit plane ($ZRT/Cax, RT = 1.145$, transient $15\pi 31\Delta t$) 184

Figure 107: Spanwise distribution of the relative flow angle at the rotor exit plane ($ZRT/Cax, RT = 1.145$) 186

Figure 108: Distribution of axial and tangential velocities at the rotor exit plane ($ZRT/Cax, RT = 1.145$) 187

Figure 109: Relative flow angle on rotor blade surface (transient $15\pi 31\Delta t$) 190

Figure 110: Rotor suction surface topology (steady state – $\Delta t/4$) 191

Figure 111: Time-resolved relative velocity at the rotor exit plane ($ZRT/Cax, RT = 1.145$, transient $15\pi 31\Delta t$) 192

Figure 112: Time-resolved relative turbulence intensity at the rotor exit plane ($ZRT/Cax, RT = 1.145$, transient $15\pi 31\Delta t$) 192

NOMENCLATURE

C	:	Chord length
C_{ax}	:	Axial chord length
C_p	:	Specific heat capacity at constant pressure
C_v	:	Specific heat capacity at constant volume
$CD_{k\omega}$	:	Cross-diffusion term in the SST model
CPs	:	Static pressure coefficient
CPt	:	Total pressure loss coefficient
e_a	:	Relative discretization error
F_s	:	Factor of Safety
GCI	:	Grid Convergence Index
H	:	Blade span
k	:	Turbulent kinetic energy
Ma	:	Mach number
N	:	Mesh element size
p	:	Apparent order
P	:	Pressure
P_t	:	Total pressure
P_k	:	Production term
PS	:	Pressure surface side
Ps	:	Static pressure
r	:	Radial distance
rf	:	Refinement factor
R	:	Reattachment line

Re	:	Reynolds number
$Re_{\theta t}$	:	Transition onset momentum thickness Reynolds number
$\breve{\mathrm{R}}\mathrm{e}_{\theta \mathrm{t}}$	:	Local transition onset momentum thickness Reynolds number
R_{T}	:	Viscosity ratio
Re_{v}	:	Vorticity Reynolds number
Rr	:	Reaction ratio
$\boldsymbol{S}$	:	Absolute value of strain rate
S_{ij}	:	Components of the mean strain rate tensor
SS	:	Suction surface
S	:	Separation line
Ss	:	Suction side HSV Separation line
Sp	:	Pressure side HSV Separation line
Tu	:	Turbulence intensity, $100\frac{\sqrt{2k/3}}{U}$
Tu_{Abs}	:	Area-weighted averaged turbulence intensity in absolute frame of reference normalized by V_2
Tu_{Rel}	:	Area-weighted averaged turbulence intensity in relative frame of reference normalized by V_3
$\mathbf{U}$	:	Local velocity
U_∞	:	Free stream velocity
$\mathbf{U}'$	:	RMS of the turbulent velocity fluctuations, $\sqrt{u'^2 + v'^2 + w'^2}$
u', v', w'	:	Local fluctuating velocity
V	:	Area-weighted average velocity, $\sqrt{V_z^2 + V_r^2 + V_\theta^2}$
V_2	:	Area-weighted averaged absolute velocity at nozzle exit plane (axial distance $Z_{NZ}/C_{ax,NZ} = 1.125$)
W_3	:	Area-weighted averaged relative velocity at rotor exit plane (axial distance $Z_{RT}/C_{ax,RT} = 1.145$)
V_{Abs}	:	Area-weighted average absolute velocity in relative frame of reference

		normalized by velocity V_2
V_{Rel}	:	Area-weighted average relative velocity in relative frame of reference normalized by velocity W_3
y	:	Distance to the nearest wall
Z	:	Axial distance
Z_{NZ}	:	Axial distance form nozzle leading edge at mid-span
Z_{RT}	:	Axial distance form rotor leading edge at mid-span
α	:	Absolute flow angle measured from axial direction
β	:	Relative flow angle measured from axial direction
δ	:	Boundary layer thickness
δ_{ij}	:	Kronecker delta
ε	:	Dissipation rate of turbulent kinetic energy
ϵ_{jmn}	:	Tensor of Levi-Civita
ΔP	:	Pressure loss
θ	:	Momentum thickness
ϑ	:	Tangential or circumferential distance
ϑ_r	:	Blade speed
k	:	Turbulent kinetic energy
λ_θ	:	Pressure gradient parameter, $(\rho\theta^2/\mu)(\partial U/\partial s)$
μ	:	Molecular viscosity
μ_t	:	Turbulent viscosity
ρ	:	Density
τ_{ij}	:	Components of wall shear stress
υ	:	Kinematic viscosity
υ_t	:	Kinematic turbulent viscosity
$\boldsymbol{\Omega}$	:	Absolute value of vorticity
Ω_{ij}	:	Components of the vorticity tensor

Ω_m^{rot}	:	Components of the system rotation vector
ϕ	:	Flow coefficient
ψ	:	Loading coefficient
ω	:	Specific turbulence dissipation rate
ω_a	:	Angular velocity
A	:	Saddle Point
Abs	:	Absolute flow or absolute frame of reference
AIAA	:	American Institute of Aeronautics and Astronautics
B.C.	:	Boundary condition
CAD	:	Computer-aided design
CFD	:	Computational Fluid Dynamics
CGT	:	Ceramic gas turbine
CMC	:	Ceramic matrix composite
CV	:	Corner Vortex
D	:	Diameter
DOE	:	Department of Energy
EVM	:	Eddy-viscosity model
hub	:	Blade hub-side
HSV		Horseshoe vortex
in	:	Nozzle or rotor inlet value
LDV	:	Laser Doppler velocimetry
LE	:	Leading Edge
LV	:	Leading Vortex
mid	:	Mid-span
NZ	:	Nozzle value
out	:	Nozzle or rotor outlet value
PDE	:	Partial differential equation

PV	:	Passage Vortex
Rel	:	Relative flow or relative frame of reference
RT	:	Rotor value
R&D	:	Research and Development
RANS	:	Reynolds Averaged Navier-Stokes
URANS	:	Unsteady Reynolds Averaged Navier-Stokes
RE	:	Richardson Extrapolation
RMS	:	Root-Mean-Square
SiC	:	Silicon Carbide
Si_3N_4	:	Silicon Nitride
SRQ	:	System Response Quantity
SST	:	Shear stress transport
SVO	:	Streamwise vorticity
TE	:	Trailing Edge
TIT	:	Turbine inlet temperature
TSLV	:	Trailing Shear Layer Vortex
tip	:	Blade tip-side
V&V	:	Verification and Validation
WIV	:	Wake induced vortex
WICV	:	Wake induced counter vortex

1. INTRODUCTION

1.1. Introduction

In the last 30 years, the applicability of small gas turbines has expanded due to their compactness, lightweight, fuel neutral nature, low emissions, low maintenance cost and increased efficiencies. The small gas turbine market place is dominated by micro-turbines as demonstrated in [1], [2], [3]. These small gas turbines have been used in combined heating and power (CHP) applications, distributed power generation, and hybrid electrical vehicles (HEVs). The global micro-turbine market is dominated by Capstone Turbine Corporation and FlexEnergy in the United States [3]. Capstone Turbine Corporation [4] and FlexEnergy [5] have recuperative micro-turbines with efficiencies just over 30% rated at 200 kW (C200) and 250 kW (GT250S), respectively. These designs sport a single-shaft (single-spool) compromising of the centrifugal-flow compressor impeller, radial-inflow turbine rotor, and generator. Research and development (R&D) between the private sector industry, universities, and federal governments have focused on reducing the installation cost per kW through an increase in efficiency, as this has led to an increase in power output capacity, for further improvement in competitiveness with fuel cells, reciprocating engines, steam turbines, and larger gas turbines.

More recently, Capstone and FlexEnergy have been upgrading their small gas turbines to obtain output powers above 300 kW. FlexEnergy has uprated theirs from 250 kW to 333 kW (GT333S) with the addition of new inlet guide vanes and an improved compressor achieving an efficiency of 32.5% [6]. Meanwhile, Capstone has been working

with the United States Department of Energy (DOE) to develop a two-shaft 370 kW micro-turbine with an efficiency of 42% [3] [7]. The low-pressure section is contingent on the 200 kW models' efficiency improvement increasing the capacity to 250 kW with an advanced aerodynamic compressor, improved generator, and enhanced cooling. The additional power output is then achieved with the addition of a high-temperature and high-pressure turbo-compressor and intercooler.

Prior to these new designs, only Kawasaki [8] (CGT302) and Niigata [9] (RGT3R) had worked on machines with power outputs above 300 kW. These designs reached thermal efficiencies of 42.1% and 31.4% producing 322 kW and 316 kW of output power, respectively. The machine design from Niigata was similar to current micro-turbine turbo-compressor designs boosting a regenerative single-shaft turbine with a centrifugal compressor, and radial turbine. Kawasaki's machine design consisted of a regenerative two-shaft (twin-spool) gas turbine design, where one shaft is for the gas generator section and the other the power conversion section. The gas generator section has an axial flow high-pressure turbine that runs the centrifugal compressor and the power turbine section has an axial flow power turbine. This is essentially a miniaturized gas turbine or mini-turbine. The incorporation of ceramic components and small turbine tip clearances are the two reasons this design achieved a high thermal efficiency [8]. Unfortunately, these models did not attain production status.

Two of the barriers Capstone and the DOE must overcome for the 370 kW project are the development of "new materials, such as ceramics or metal alloys, suitable for higher temperatures" and the development of "different design concepts not currently used by microturbine manufacturers" [10]. The Kawasaki mini-turbine could offer some insight as

it was part of the culminated Japanese 300 kW ceramic gas turbine (CGT) R&D program. First, the axial-flow design for the gas generator turbine and power turbine is significantly different from the radial-inflow turbines used by nearly all micro-turbine manufacturers, accredited to their increased aerodynamic losses at lower power output ranges when compared to radial turbines. Next, the incorporation of ceramic components allows for a reduction of weight, a reduction of size, higher turbine inlet temperatures (TIT's), and elimination of air-cooling that collaboratively have the potential to increase the overall efficiency. Durability test conducted by Takehata et al. [8] "proved the reliability of ceramic components as stationary parts," but not for rotating parts in the Kawasaki mini-turbine. The ceramic component of the turbine nozzle segments was made of Silicon Nitride (Si_3N_4) joined by Silicon Carbide (SiC) fibers. The CGT development review given by Roode [1] clearly shows that the advancement of such monolithic ceramics has decreased, as focus has shifted towards SiC/SiC ceramic matrix composites (CMCs). General Electric (GE) Aviation had prosperous results when testing a low-pressure turbine blade made of a SiC/SiC CMC, making it the-world's-first rotating CMC material [11]. If durability test can further validate the success of ceramic components for stationary and non-stationary applications an electrical efficiency increase of 35% for a recuperative micro-turbine and 40% for a recuperative mini-turbine is plausible as demonstrated in [1].

For the mini-turbine, the estimation of the Reynolds number by Matsunuma et al. [12] showed that these flow conditions lead to a low Reynolds operation, especially in the low-pressure turbine (LPT), where the stator and rotor inlet chord Reynolds number is approximately as low as $5.4x10^4$. The high TIT coupled with the small blade size causes

the low Reynolds number flow. Small general aviation jet engines operating at high altitudes can also operate at a low Reynolds number due to the decreased air density.

It is also important to put special emphasis on investigating the endwall flows in axial turbine blade-to-blade passages. These include flows in the endwall boundary layers, secondary flows, and tip leakage flows. Together they lead to increased losses, which are the main factor in the reduced performance of axial-flow turbines at low Reynolds number. These endwall flows are very difficult to evaluate because they are inherently unsteady and at these low Reynolds numbers the flow is prone to flow separation on the suction surfaces. The rotor-nozzle interaction also causes the flow at the exit of the nozzle blade row to interfere with the rotating potential of the rotor. More knowledge of the endwall flows in an axial turbine at low Reynolds number can help delineate the loss generating mechanisms.

Experimental data is harder to obtain for rotating blades when compared to stationary blades even with the multiple measurement techniques available. For stationary blade measurements, Langston et al. [13], Langston [14], Matsunuma et al. [12] [15], and Matsunuma [16] used a five-hole pressure probe, while Sharma et al. [17] used hotwire probes. For rotating blade measurements, Matsunuma and Tsutsui [18] used a single-element hot wire; Persico et al. [19] used a three dimensional fast-response pressure probe; Restemeier et al. [20] used a combination of 5-hole probes, 3-D hot wires, and pressure transducers; and Schneider et al. [21] used a five-hole pressure probe with a thermocouple. Matsunuma and Tsutsui [22] [23] and Matsunuma [24] [25] used a laser Doppler velocimetry (LDV) measurement system. Apart from experimental data, flow visualizations with the help of ink traces, oil flow and smoke have allowed the flow

structures to be more apparent as in Langston et al. [13], Matsunuma et al. [12] and Wang et al. [26].

The National Institute of Advanced Industrial Science and Technology (AIST) is a Japanese public research organization formed in 2001 conjoining 15 research institutes that were formerly under the Agency of Industrial Science and Technology in the Ministry of International Trade and Industry [27]. AIST participated in the Japanese National R&D projects of 300 kW ceramic turbines and from 1998 to 2008 published many scholarly journals on experimental studies of the unsteady low Reynolds flow in a single-stage axial-flow turbine with free vortex flow as a simple radial equilibrium condition. However, there are minor discrepancies when comparing turbine cascade specifications, as well as different measurement techniques employed in each. *Table 1* summarizes the measurement technique progression at AIST. AIST was able to obtain good quality transverse velocity data at different locations from the nozzle exit to the rotor outlet using an LDV system. The most notable journal article is the "Unsteady Flow Field of an Axial-Flow Turbine Rotor at a Low Reynolds Number" by Matsunuma. Matsunuma has made the blade geometry, measured data, and movies accessible, for "CFD code verification" and "education of gas turbine engineers" [24].

Table 1: Time-line of measurement technique advancement of low Reynolds number flows at AIST

	Measurement Location		
	Stationary		Stationary/Rotating
	Nozzle Inlet	Nozzle Exit	Rotor Flow Field[1]
Timeline	Measurement Techniques Employed		
1998	Single-element hot wire anemometry	5-hole pressure probe[2]	---
1999	3-hole pressure probe	5-hole pressure probe[2] Hot wire anemometry[2]	---
2000	---	---	LDV[3]
2003	---	---	LDV[3]
2004	---	5-hole pressure probe, Single-element hot wire anemometry	Single-element hot wire anemometry[4]
2005	3-hole pressure probe	5-hole pressure probe[2]	---
2006	3-hole pressure probe	5-hole pressure probe	LDV
2007	---	---	LDV
2008	---	---	LDV[5]

1. Downstream of nozzle to downstream of rotor
2. The turbine rotor is omitted
3. Mid-span flow only
4. Measurement location at rotor exit only
5. LDV measurements of the rotor blade suction-surface flow only

1.2. Thesis Objective

The objectives of this thesis is to make a detailed systematic numerical analysis of the unsteady flow field of an axial turbine at a low Reynolds number with use of different parametrically tuned eddy-viscosity turbulence models. These results corroborated with data acquired at AIST will help to understand the unsteady mixing of vortices found in a turbine cascade at low Reynolds number and the reliability of predicting separation, while

optimizing the mathematical formulation implemented. It is important to note that the numerical validation relies on published literature.

1.3. Thesis Outline

A review of pertinent literature concerning the loss mechanisms in axial flow turbines are discussed in chapter 2. This chapter also reviews CFD applications and outcomes of similar flow investigations. Chapter 3 describes the conceptual model used for the study. Chapter 4 presents the formulation of the mathematical model. Chapter 5 presents the results of a simple radial equilibrium analysis. Chapter 6 describes the numerical approach used for the study. Chapter 7 gives a detailed analysis of the numerical results through verification and validation. Chapter 8 describes the flow field in the nozzle and rotor as found in the numerical results with comparisons to the experimental data. Chapter 9 outlines relevant conclusions.

2. LITERATURE REVIEW

2.1. Introduction

A review of the main topics and important notions are necessary in understanding the complex flow field through an axial turbine stage. This chapter presents an examination of present literature relevant to the current investigation, although a comprehensive review of all the contributing research is not possible given the scope. A brief discussion of the loss mechanisms, unsteady flow, pressure loss coefficients, and CFD applications present details of the unsteady flow phenomena in turbomachines. Finally, a discussion of the experimental validation data needed to make comparisons to the numerical results obtained is presented.

2.2. Loss Mechanisms in an Axial-Flow Turbine

The flow fields in axial-flow turbine blade-to-blade passages are very complicated due to the passage geometry and the physical processes present. These flows are three-dimensional, unsteady and viscous. They may be incompressible or compressible with regions of laminar, transitional, and turbulent flows. The flow fields in axial-flow turbines are important as they can cause aerodynamic losses, which in a three-dimensional blade row arise from the loss of kinetic energy in the passage, that translate into efficiency losses. The total aerodynamic loss is a sum of viscous losses, mixing losses, and three-dimensional effects. Estimation of these losses is crucial. Aerodynamic loss mechanisms found in turbomachines are divided into three categories: profile losses, secondary flow losses, and tip leakage losses. According to Denton [28] each of these accounts “for about 1/3 of the

total loss." The individual loss mechanisms are difficult to distinguish due to their interaction with each other, dependence on machine characteristics and flow conditions. These individual loss mechanisms remain an active area of research.

2.2.1. Profile Loss

Profile losses are losses related to the profile or nature of the airfoil cross-sections and the boundary layer growth on the airfoil pressure and suction sides. The blade boundary layer growth, flow separation, trailing edge mixing, and shock loss are the main sources of profile losses. The flow conditions dictate the blade boundary layer growth, where rapid growth of the laminar boundary layer may lead to flow separation. Flow separation is a laminar phenomenon strongly dependent on the transition from laminar to turbulent flow. The rapid deceleration of the flow around the curved suction surface causes an adverse pressure gradient that can lead to separation, where the shear layer detaches. Separation forms a large region of reduced kinetic energy, where losses increase by the turbulent entrainment, forcing the flow back to the surface known as the recirculating zone or separation bubble. Flow separation extends energy dissipation through the formation of eddies and vortices through three important occurrences: changes in the anticipated flow pattern, oscillation of flow and increased boundary drag. Wei [29] notes that the prediction of the boundary layer transition remains a major limitation to accurate prediction of flow separation and its associated losses. The trailing edge mixing losses and shock losses are also included in the profile losses. Where the latter, not encountered in subsonic flow, is not discussed further. The trailing edge mixing loss is due to the interaction of the suction side and pressure side boundary layers, confined to a narrow wake downstream of the trailing edge.

2.2.2. Secondary (or Endwall) Flows

Secondary or endwall flows are complex flow phenomenon defined as any flow that shows departure from the streamwise or primary flow. Review papers by Langston [30] and Sieverding [31] provide general overviews of research on secondary flow in turbine blade passages and outline significant developments. To understand the complex three-dimensional flow through a turbine blade passage secondary flow models based on flow visualizations and experimental field measurements provide visual aids. Figure 1 to Figure 5 show various secondary flow models in order of their introduction. Hawthorne [32] [33] [34] was one of the first to develop and apply classical inviscid secondary flow theories to investigate the formation of streamwise vorticity components when a flow having inlet vorticity is deflected through the cascade. Three main mechanisms contributed to the formation of streamwise vorticity at the exit of the cascade: (a) secondary vortices, (b) trailing shed vortices and (c) trailing filament vortices [33].

The distributed secondary vorticity is caused by the distortion of the inlet boundary layer due to bending of the flow between the passage. This causes a departure from the primary flow as the slower moving particles in the boundary layer want to move towards the center of curvature. The distorted vortex filaments are carried with the flow becoming the passage vortex at the exit of the cascade. This is best visualized by applying the inviscid moment balance equation for cylindrical coordinates in the cross stream direction, Eqn. *2.1*, as in [35].

$$\frac{1}{\rho}\frac{\partial P}{\partial n} = \frac{V^2}{R} \qquad 2.1$$

Where V is the velocity, P is the pressure, ρ is the density, R is the streamline curvature radius, and n is the normal component. This gives the centripital acceleration as a function

of the net cross-stream pressure force per unit mass. Since there is a lower velocity and kinetic energy in the boundary layer there also has to be a reduction of the streamline curvature to balance the normal pressure gradient and centripetal acceleration. This causes more turning of the boundary layer than the main flow.

The trailing vortex sheet is made up of both the trailing filament and trailing shed vortices. Both lie in the stagnation streamline leaving the blade and have the same sense of rotation, but are opposite to that of the passage vortex [33]. The trailing shed vorticity is caused by the spanwise change of circulation around the blade. This spanwise change causes circulation that is shed at the trailing edge. The trailing filament vorticity is caused by the stretching of the inlet vortex filament over the surface of the blade where the vortex filament moves ahead on the convex surface compared to the concave surface due to the differing velocities. Sieverding [31] visually presented the classical secondary flow model as described by Hawthorne [33] [34] shown in Figure 1. The analytical equations given by Hawthorne [33] [34] when compared with experimental results show that the effect of the inlet boundary layer is incorrect. The equations fail to include the formation of the leading edge horseshoe vortex which transforms the incoming normal vorticity to streamwise vorticity independent of flow turning, as shown in [36]. The formation of the horseshoe vortex at the leading edge is the next important aspect of secondary flows.

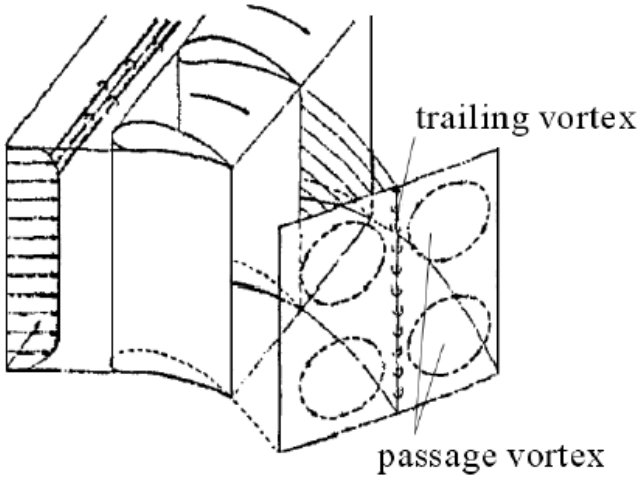

Figure 1: Model of Hawthorne Secondary Flow Model [31]

Langston [14] was the first to introduce a detailed visual analysis of the secondary flow patterns derived from experimental results of Langston and Nice [13], shown in Figure 2. It is visible that as the inlet boundary layer approaches the leading edge of the blade it undergoes deceleration resulting in three-dimensional separation that turns the boundary layer component of vorticity into streamwise vorticity forming a horseshoe vortex. The model also depicts the evolution of the horseshoe vortex legs and the development of the passage vortex.

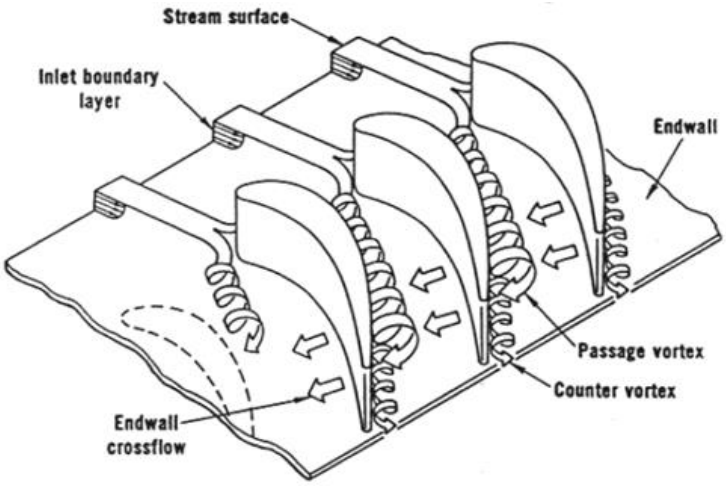

Figure 2: Langston Cascade Secondary Flow Patterns [14]

The pressure side and suction side are the two legs that compose the horseshoe vortex. Both are adjacent to each other with an opposite sense of rotation. The pressure side leg of the horseshoe vortex transports downstream towards the suction side of the adjacent passage because the fluid particles want to move towards the location of less pressure. This transverse pressure gradient drives the low momentum passage boundary layer fluid creating a crossflow as first shown in [14]. As the pressure leg transports downstream it merges with the crossflow from the endwall boundary layer fluid and additional fluid that is swept up from the main stream to form the passage vortex, where it retains the same sense of rotation as the pressure leg of the horseshoe vortex. The suction side leg of the horseshoe vortex convects on the suction surface remaining in the endwall corner. Its rotation is opposite and its size smaller than that of the passage vortex. Sieverding [31] provided a detailed review summarizing the results of experimental secondary flow research up to 1985 giving insight into the topology of the complex three-dimensional flow fields in the endwall regions of a cascade. He determined that the suction side leg wraps around the passage vortex, where the rotational speed of the passage vortex influences its location. The rotational speed is dependent on the inlet flow conditions and cascade geometry.

Sharma and Butler [36] presented their secondary flow model in 1987, shown in Figure 3. Here the inner region of the inlet boundary layer does not become part of the horseshoe vortex instead convecting downstream towards the suction side surface, where it climbs the suction side of the blade exiting on the top of the passage vortex. They hypothesized that the suction side leg of the horseshoe found near the suction side-endwall corner is forced off the endwall due to the interaction with the passage vortex in which the

suction side leg then wraps around the outside of the passage vortex retaining its identity as it spirals around it, from data obtained in [17]. Most notably, Sharma and Butler [17] found that the passage vortex at the shroud region is much weaker than at the hub region due to the radial pressure gradient acting radially inward. This spreads the vertical motion at the hub over a larger area resulting in a reduction of the size of the vortices near the hub.

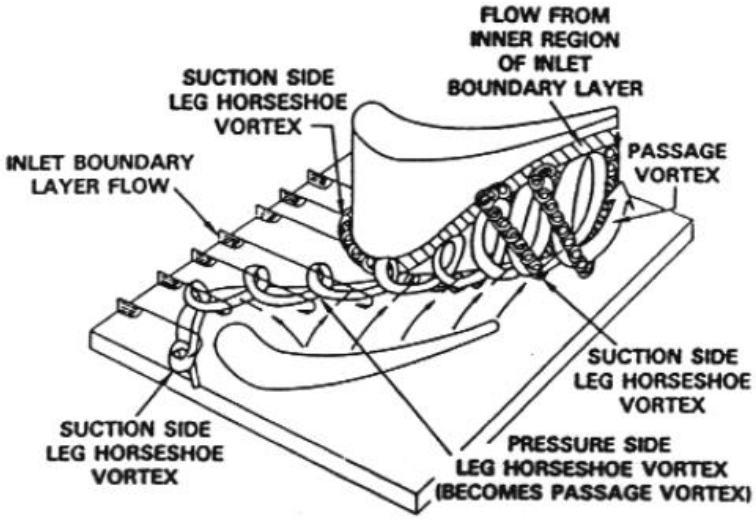

Figure 3: Sharma and Butler Secondary Flow Model [36]

When Goldstein and Spores [37] presented their model in 1988 it included a number of additional vortices nonexistent in the previous models, as shown in Figure 4. The model has similar attributes to the previous models with the exception of two main differences. First, the passage vortex and suction side leg of the horseshoe vortex both lift off the endwall. The passage vortex lifts off at the point of minimum static pressure upon reaching the suction side and the suction leg lifts off as it reaches the separation of the endwall boundary layer then continues along the suction surface above the passage vortex, in direct contrast to Sharma and Butler's orbiting hypothesis. The higher average velocities and lower pressures found away from the suction-surface endwall corner induce the lift off phenomena.

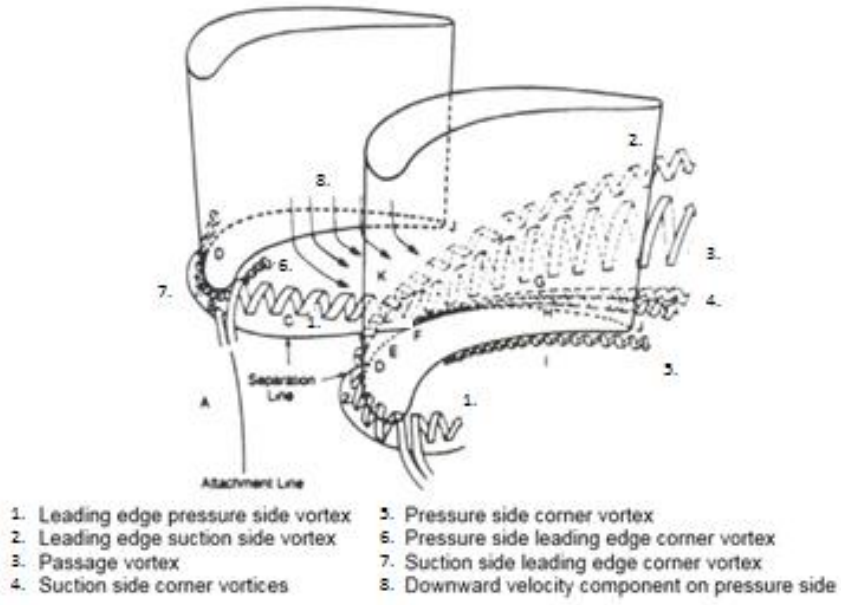

Figure 4: Goldstein and Spores Secondary Flow Model [37]

The second major difference is the inclusion of small but intense corner vortices located at the leading edge, pressure-side endwall junction, and suction-side endwall junction. The formation of the horseshoe vortex directly influences the formation of the leading edge corner vortices that are of opposite rotation to the corresponding horseshoe leg and located underneath the horseshoe vortex. The pressure-surface endwall corner vortex originates due to strong pressure gradients formed from the downwash of fluid onto the endwall region. A similar separation found on the suction side causes two counter-rotating corner vortices to originate just downstream of where the passage vortex lifts off the endwall driven by the interaction of the passage vortex and the airfoil suction surface.

The final secondary flow model of interest was presented by Wang et al. [26] in 1997, shown in Figure 5. This model is similar to Goldstein and Spores in that it introduces additional corner vortices, although they also introduce a wall vortex. First, this model has both legs of the horseshoe vortex formed from a pair of alternately dissipating vortices, instead of a single structure. As the multi-vortex structure progresses downstream, it

becomes one single-vortex pattern. In this model, the suction-side horseshoe vortex moves above the passage vortex, where its strength forces it off the wall orbiting it until it exits below the passage vortex. Wang et al. identified another vortex called the wall vortex also induced by the passage vortex strength, which travels above it towards the passage exit.

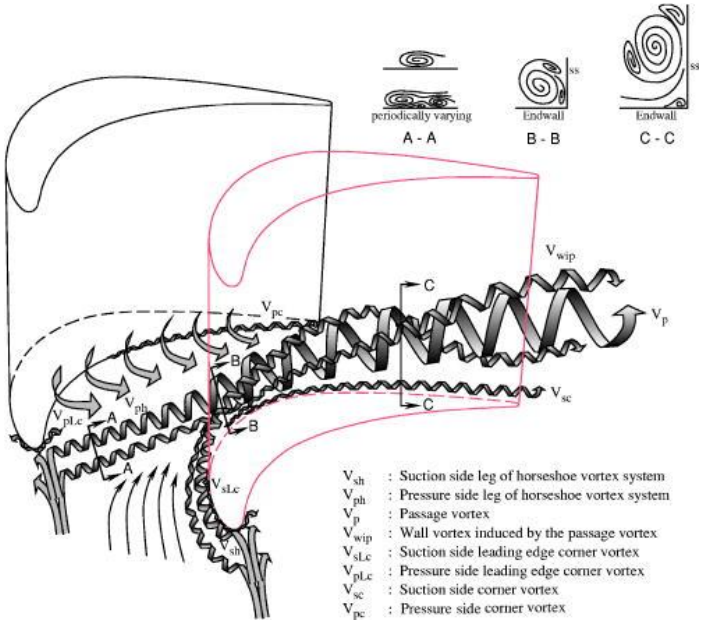

Figure 5: Wang et al. Secondary Flow Model [26]

Although, there are differences between all the secondary flow models there is a general agreement on the basic secondary flow phenomena such as horseshoe vortex, endwall crossflow, and passage vortex between the different models. The horseshoe vortex forms due to the boundary layer approaching the stagnation line on the leading edge directing the flow radially inward into the endwall causing a vortex rollup that splits into two counter-rotating vortex pair feeds. The crossflow creates a pitch-wise pressure gradient that flows from the pressure side to the suction side. This keeps the suction side leg close to the suction side surface and forces the pressure side leg towards the suction side. The passage vortex is a direct result of the amplification of the pressure side leg. Differences between these models are therefore mainly regarding the interaction schemes

of these basic vortices and the supplementary vortices they might induce. It is important to note that all of the illustrated models exaggerate the rate of rotation of the vortices.

The main difference between the different secondary models is the downstream location of the suction leg of the horseshoe vortex. Some of the models place the suction side leg under the passage vortex while others have it above. If the suction leg does wrap around the passage vortex this could be due to its rotational dependence on the inlet flow conditions and geometrical features. This difference could also be attributed to the difficulty of following the vortices path located invariably right in the endwall and suction side corner making it hard to tract as it progresses through the passage.

2.2.3. Tip Leakage Flow

The necessary tip clearance between the tip of a rotor blade and stationary casing gives rise to tip leakage flow. The pressure difference between the pressure surface and suction surface at the tip clearance gap drives the flow movement. As the flow enters from the pressure side corner the flow separates, contracting the incoming flow into a jet. The blade thickness dictates how much the flow mixes out above the blade tip. The tip leakage flow then exits on the suction side where it mixes with the mainstream. The different velocities of the two streams causes a vortex sheet to form at the interface that rolls up into a vortex as the leakage flow moves downstream. The leakage flow reduces the work done by the rotor by increasing the loss through viscous effects and mixing as it passes through the leakage path above the blade tip and mixes with the mainstream at the exit.

Denton [28] gave detailed descriptions of the tip leakage loss of unshrouded blades. Figure 6 displays the two possible configurations of the flow over the tip gap of an unshrouded blade with different blade thicknesses. In both configurations, the flow enters

the tip clearance from the pressure side then separates from the blade tip and contracts to a jet. Depending on the blade thickness, the jet will mix out above the blade tip, as shown in Figure 6 (a); or it is unlikely that it will reattach to the blade tip within the gap, as shown in Figure 6 (b). The former, is usually the case for turbines due to the thickness of the blades being usually more than four times the tip clearance. Control of the blade thickness and tip clearance parameters is optimal in the reduction of tip leakage losses.

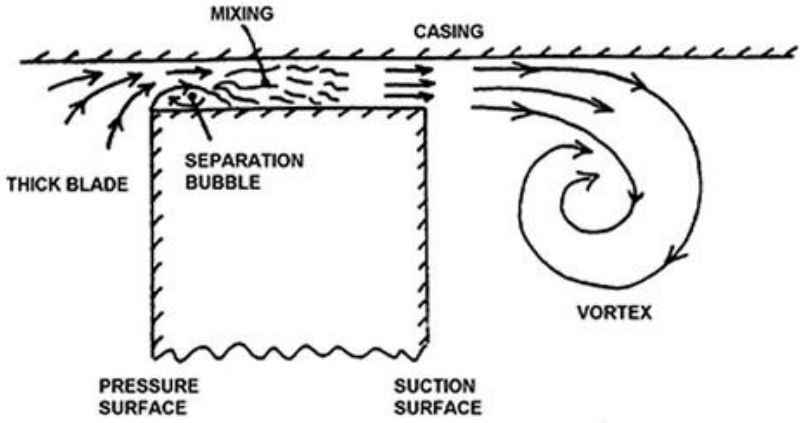

(a)

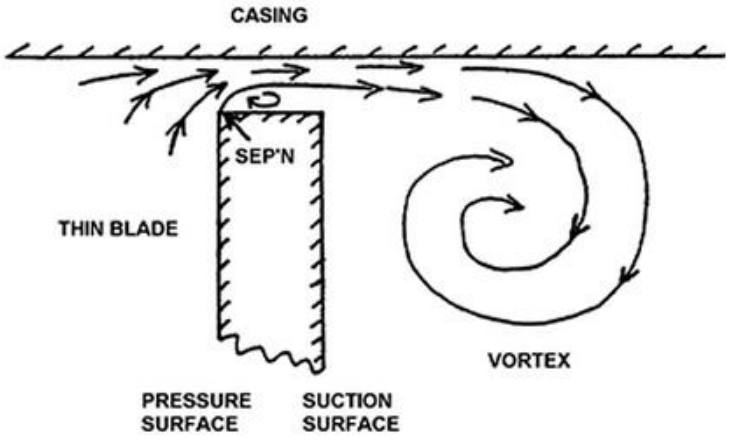

(b)

Figure 6: Flow over the tip gap for an unshrouded blade [28]

2.3. Unsteady Flow

The only blade row that truly may have steady inflow is the first stage stator of the high-pressure turbine; otherwise, the flow in turbine blade rows is inherently unsteady. As Chaluvadi [38] suggests, the unsteady loss generating mechanisms can be classified as "(a) potential interactions of the upstream and downstream blade rows, (b) interactions of the upstream wakes with the downstream blade rows, and (c) leakage and secondary flow vortices interaction with the downstream blades." These unsteady loss mechanisms influence the boundary layer, wake, secondary vortex, and tip leakage vortex growth effecting the loss generation.

The velocity defect of the upstream wakes entering the rotor blade passage appear as negative jets. They travel with the main flow, where they are chopped into segments that travel within the blade passage, continuing to behave as negative jets. Hodson and Dawes [39] examined the negative jet effect using simple analysis, measurements, and CFD. They confirmed that the negative jet effect persists as the wakes progress through the blade row forming two counter rotating vortices. Matsunuma [24] also found that the nozzle secondary vortices and wake at the rotor inlet where chopped periodically and three-dimensionally. The rotating potential of the rotor distorts the nozzle wake and vortices.

2.4. Pressure Loss Coefficients

Pressure loss coefficients are a simple means of expressing the losses in axial-flow turbines. As Denton [28] states, it is the most common as it is "easy to calculate from test data and not because it is the most convenient" for design purposes. In a turbine, there are two parameters of interest: the total (or stagnation) pressure loss and the static pressure.

These coefficients give an overall measure of the loss and blade loading involved with a particular cascade geometry.

The total, or stagnation, pressure loss coefficient is an overall measure of the aerodynamic losses through a blade row. For incompressible flows, the pressure loss coefficient relates the loss of stagnation pressure to the reference dynamic pressure at the outlet. Equation 2.2 is for a stationary blade row, while Eqn. 2.3 is for a rotating blade row.

$$CPt_{NZ} = \frac{Pt_{Abs,in,mid} - Pt_{Abs}}{\frac{1}{2}\rho V_{out}^2} \tag{2.2}$$

$$CPt_{RT} = \frac{Pt_{Rel,in,mid} - Pt_{Rel}}{\frac{1}{2}\rho W_{out}^2} \tag{2.3}$$

The static pressure coefficient is a measure of the static pressure rise. For incompressible flow the stationary and rotating blade row static pressure coefficient are determined using Eqns. 2.4 and 2.5, respectively. The chordwise distribution of the static pressure coefficient gives an idea of the blade loading, where the diffusion can give indication of flow separation as shown in [40]. As Dixon and Hall [41] mention, flow separation "leads to reduced turning and high loss."

$$CPs_{NZ} = \frac{Ps - Pt_{Abs,in,mid}}{\frac{1}{2}\rho V_{out}^2} \tag{2.4}$$

$$CPs_{RT} = \frac{Ps - Pt_{Rel,in,mid}}{\frac{1}{2}\rho W_{out}^2} \tag{2.5}$$

2.4.1. Effect of Low Reynolds Lapse

Low Reynolds number operation bear increased losses inducing a loss of efficiency. Low Mach number designs are typically avoided for this very reason. It is well known that at Reynolds numbers above 10^5 the losses are found to vary according to -0.2 power of the Reynolds number [41], [42]. Figure 7 shows the effect of Reynolds number on the total pressure loss at the exit of a turbine nozzle and rotor. Matsunuma [16] found that at the exit of the turbine nozzle the curve of the -0.35 power of the Reynolds number fits more closely with the data obtained. Matsunuma et al. [24] found that at lower Reynolds number the curve of -0.5 power of the Reynolds number fits more closely with the data at the exit of the rotor. Overall, there was an increase in loss as the Reynolds number decreased, accredited to the blade surface boundary layer transition from a turbulent regime to a laminar regime in the rotor and vice versa in the nozzle.

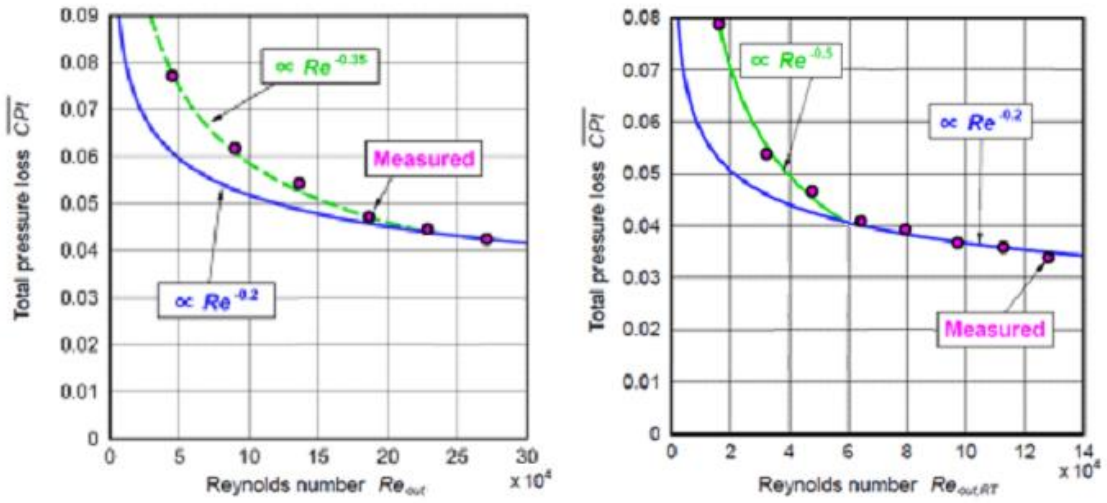

(a) (b)

Figure 7: Total Pressure (a) net overall loss at nozzle exit [16] and (b) loss at rotor exit mid-span [24]

2.5. Computational Fluid Dynamics Application/Outcomes

Computational fluid dynamics (CFD) is the art of modeling mathematical equations that involve complex partial differential equations (PDEs) representing the conservation laws of mass, momentum, and energy. These complex PDEs in discretized algebraic forms are solved using a digital computer to visualize complex gases or fluid flows. CFD provides a quantitative prediction of the problem using mathematical modeling, numerical methods and software tools. Many recent investigations on the formation of secondary flow structures inside a turbine rotor passage focus on the validation of CFD results with experimental results [19], [20], [21], [43], [44], [45], [46], [47]. This it to get a better understanding of the realistic unsteady secondary flow structures found in a turbine cascade, while also helping to optimize the mathematical formulations implemented. In essence, CFD allows application of three-dimensional methods to analyze a particular turbine design. This is essential to predicting the effect of endwall flows on the overall performance.

Most investigations before 1970 focused on experimental observations of the flow features in a cascade to get an understanding of the secondary flow structures. Since the 1970s, many in-house, commercial, and open source CFD codes have been developed and have continued to be created and modified to predict the three-dimensional aerodynamic losses, especially those where strong secondary flows are prevalent. The turbulence models used to close the equations are very useful for prediction of endwall losses. Unfortunately, one that can routinely predict the secondary losses accurately has not been discovered. This could be due to the not yet fully understood secondary flow mechanisms.

With the vast majority of codes available, validation of their effectiveness in capturing the full complex flow field is key.

Many investigators using a wide range of CFD codes have modeled the overall secondary flow features successfully. Straka [48] provides an example of how an in-house numerical code has been developed to predict the three-dimensional, unsteady, and viscous turbulent flow in an axial turbine stage; a similar approach is taken in many commercial and open source codes. Advances in computing now allow some Reynolds-Averaged Navier-Stokes (RANS) simulations to be solved in a matter of hours and Unsteady Reynolds-Averaged Navier-Stokes (URANS) simulations in a few days. Before, steady calculations used to be too time consuming but now have become routine for designs. There are still limitations that arise from only conducting a steady flow analysis, such as how to model the unsteady interaction between the blade rows. For steady flow calculations, the flow leaving a blade row is usually circumferentially averaged at the mixing plane before feeding it into the next row. This assumes that the mixing out of the non-uniform flow occurs instantaneously, instead of mixing out unsteadily. Denton and Dawes [49] show how this technique is effectively applied to multi-stages as a primary design tool for steady calculations, but some modeling of the unsteady interaction of the blade rows is necessary. Horlock and Denton [50] followed this up by showing the improved capabilities of CFD and its effectiveness in turbomachinery designs. With CFD being a primary design tool, the implications of unsteady flow on the loss generation can be continued to be explored to determine the effect of the wakes and vortices mixing out unsteadily.

Kuerner et al. [47] conducted a steady state simulation of a low-pressure turbine at low Reynolds number and compared it with experimental data. They found that the isentropic efficiency decreases as the Reynolds number decreased, indicating an increase in loss. The numerical and experimental results had similar flow features, but the peaks of the displacement thickness associated with the vortices shifted radially. Holmes et al. [51] conducted an analysis of unsteady vs steady flow in a multi-stage turbine using approximately 8,000 processors. The unsteady calculation conducted captured the mixing of vortices between blade rows, while also showing the usefulness of steady calculations in providing meaningful data in a timely fashion. Persico et al. [19] performed an experimental and unsteady numerical simulation of a low aspect ratio turbine stage. The authors found good agreement between the experimental and numerical results in terms of loss core dimensions and loss level. The biggest drawback found in the numerical code was the underestimation of the tip leakage vortex. The general conclusion from the investigation was that the best choice in reproducing the actual blade row interaction without using phase-lagged boundary conditions is to simulate only the rotor blade row, by applying the stator-outlet flow field as the rotating inlet boundary condition.

Restemeier et al. [20] through a numerical and experimental analysis investigated the effect of the blade row axial gap on turbine efficiency. For their specific turbine geometry, it was found that both the experimental data and numerical computations are in reasonable agreement, but it is noted that the unsteady calculations provided better agreement with the experiments. Schobeiri and Abdelfattah [44] conducted RANS and URANS simulations on two different high-pressure turbine designs and compared them with experimental results. The authors found qualitative and quantitative discrepancies

between the experimental and RANS results, while the URANS results provided marginal improvement at the cost of computational time and effort. Tests performed by Schneider [21] on the unsteady formation of secondary flow inside a rotating turbine blade passage found similar results that the unsteady CFD simulation provided better results, although they found them to differ from the steady results. It was determined that the steady RANS CFD is not capable of resolving the dominating flow interactions due to the mixing plane approach. Although, they state that computational effort for URANS is still too great today.

Another alternative to the URANS formulation for analyzing the unsteady nature of the flow is by conducting a Large-Eddy simulation (LES). LES introduces turbulent scale separation in which the small, more universal, turbulent flow scales are spatially filtered from the large unsteady flow motions. LES requires more computing cost as it takes longer to solve, when compared to RANS and URANS, as it can take weeks to get meaningful results. Leonard et al. [46] through RANS, URANS and LES simulations on the mid-span flow of a turbine showed that the RANS formulation provided good estimates of the mean flow quantities but ultimately URANS and LES are the only approaches that can produce the proper unsteady trailing edge flow. Gourdain et al. [45] also compared LES simulations to existing RANS, URANS and experimental data for a compressor. Just as with previous studies, they found that URANS provides an alternative to the RANS formulation, but LES, a fully unsteady numerical code, captured most of the complex flow physics. LES solutions come with a far greater computational effort for routine designs, so in this thesis obtaining RANS and URANS solutions is of greater importance.

Low Reynolds number flows present a problem as the flow is prone to flow separation on the suction surface. This is due to the flow transitioning from laminar to turbulent in the boundary layer, causing flow separation at the suction surface. Additionally, the flow in the rotor has been found to also transition from turbulent to laminar, known as relaminarization. A transition model has to be implemented into the CFD code to properly model the laminar to turbulent transition. One such study was conducted by Muth et al. [43], they tested two similar CFD codes with different transition models at low Reynolds numbers. The calculations were accomplished using the URANS formulation on the turbomachinery-optimized code TRACE and commercial general-purpose code ANSYS CFX. ANSYS CFX with the gamma-theta transition model performed better at lower Reynolds number and Trace at higher Reynolds number with its multi-mode transition model, when compared to experimental results. Although, both codes gave good results, both generate too early transition within the separation bubble leading to early reattachment. Poehler et al. [52] implemented the numerical transition model within TRACE to study the generation of rotor secondary flow with different turbine blade designs, showing an improved design that reduced the rotor secondary flow activity. CFD is an invaluable design tool for predictive modeling, but only through experience and comparison with test data is the accuracy of future and present models established.

2.5.1. Existing Numerical Simulations on Experimental Cascade

To date only Wang [53] has published numerical simulation results of the low Reynolds axial flow turbine cascade at AIST. In 2010, he conducted three-dimensional unsteady and steady simulations with/without compressibility effects. He found that the steady simulations of the incompressible fluid did represent the laminar separation on the

suction surface of the stator [53]. Although, the secondary flow and wake flow behind the stator strength was visible it was vastly under-predicted, as the hub passage vortices are not clearly visible. These results demonstrate the effectiveness of not considering compressibility effects and show the progression current CFD packages have achieved in better predicting the secondary flow strength at the hub.

2.5.2. Limitations of CFD

Assessing the credibility of modeling and simulations in any CFD package is important, as it helps to gauge the accuracy and reliability of the numerical results. Institutions and journals have policies regarding this subject [54] [55]. In CFD modeling there are two major sources that cause the simulation results to differ from their true or exact values: error and uncertainty. Errors are recognizable deficiencies not caused by lack of knowledge, whereas uncertainty is a potential deficiency caused by a lack of knowledge. This is in accordance with the American Institute of Aeronautics and Astronautics (AIAA) Guide [54] which defines error to be "A recognizable deficiency in any phase or activity of modeling and simulation that is not due to a lack of knowledge" and uncertainty to be "a potential deficiency in any phase or activity of the modeling process that is due to the lack of knowledge." Errors can be divided into multiple categories: geometry errors, software errors, modeling errors, user errors, numerical errors, convergence errors, solution errors, spatial and temporal discretization errors, truncation errors, iteration errors, and round-off errors. Uncertainty is associated with the limited accuracy of the sub-models used, and the assumptions and simplifications made, as well as insufficient information on the geometry and uncertainty in experimental data for solution verification.

Verification and Validation (V&V) in CFD is essential to assess and quantify the computational results, therefore giving credibility to the results. Verification addresses the mathematical accuracy of a numerical solution and validation the accuracy of the given model. The AIAA Guide [54] defines verification to be "the process of determining that a model implementation accurately represents the developer's conceptual description of the model and the solution of the model." Then defines validation to be "the process of determining the degree to which a model is an accurate representation of the real world from the perspective of the intended uses of the model." The benchmark for verification is then high accurate solutions to the mathematical model, as the numerical accuracy of the solution accesses the mathematical model. The benchmark for validation are high quality experimental measurements, as the physical accuracy of a mathematical model is determined based on comparison of computational results and experimental data. In this thesis, the experimental data are available, so obtaining highly accurate computational solutions is of more importance.

2.5.3. Numerical Uncertainty

The Richardson extrapolation (RE) method helps in uncertainty quantification of the mathematical model. There are multiple uncertainties that arise from many sources commonly addressed in three steps of the modeling and simulation process: construction of the conceptual model, formulation of the mathematical model, and computation of the simulation results. The uncertainties in these three phases propagate to uncertainties in the simulation results. The primary objective is then identifying, characterizing and quantifying the uncertainties in a simulation.

RE-based discretization errors and uncertainty estimators try to quantify the difference between the exact solution to the discrete equations and the exact solution to the mathematical model known as the discretization error [56]. The discretization error is the main source in numerical errors. For the steady state solution, the computer is accurate enough (double precision), and with a strong enough convergence criteria leaving the remaining numerical error caused by the geometric discretization (mesh) and the numerical discretization (numerical scheme). To quantify each two different parameters defining the error sources are adapted: h, which is representative of the mesh spacing; and p, which stands for the order of accuracy of the numerical scheme. In most finite volume techniques, the numerical scheme is fixed and the mesh is refined known as an h-refinement study. Alternatively, the RE can also be adapted for temporal discretization keeping the mesh spacing and numerical scheme fixed, while the time scale or time step is refined. As a pre-requisite for the steady state solutions, the iterative convergence, and for time dependent solutions, the iterative convergence at every time step must be ensured.

The RE requires five basic assumptions: (1) the discrete solutions are in the asymptotic range, (2) the meshes have a uniform mesh spacing, (3) the meshes have been systematically refined, (4) the solutions are smooth, and (5) other numerical error sources are small as given in [56]. With these considerations, the RE has been adapted as an error estimator that expresses the difference between the numerical solution and the extrapolated solution forming the base for the uncertainty estimator included in this study. The Grid Convergence Index (GCI) defined by Roache [57] is a method for uniform reporting of grid convergence studies providing an estimated 95% uncertainty of the RE error estimate. The GCI accuracy of the discretization error is dependent on the solution or solutions being

in the asymptotic range. That is, the observed order reduces to the formal order of accuracy of the numerical scheme, usually achieved with adequate mesh refinement. Modifications to the GCI have occurred over time as allowing the apparent order of accuracy to increase above the formal order can result in discretization error estimates that underestimate the error, whereas allowing the observed order of accuracy to approach zero allows the discretization error estimates to grow without bounds. The asymptotic range is surprisingly difficult to identify and achieve for all, but the simplest applications [56]. The behavior of the discretization error outside of the asymptotic range is unpredictable, but it is common that it will reach unity with increasing mesh refinement, although singularities and discontinuities may affect the ability to obtain reliable estimates of the discretization error [56].

Celik [58] provides a method in calculating and reporting the discretization error estimates in CFD simulations in which experimental results may or may not be provided. This is the method employed for determining the discretization error in this thesis. The spatial discretization error is explained in depth, but for this study, the temporal discretization error is essentially the same except that the time step Δt is reduced rather than a spatial mesh refinement, thus mesh quality is not a concern. At least three significantly different mesh sizes as determined by the element count, *N*, will have to be selected to run simulations on key variables important to the objective of the simulation study. An important assumption employed is that the volume used in the computation does not change. A grid refinement factor, rf, is used to gauge the level of refinement between two meshes. Having a refinement factor too small, $rf \sim 1$, signifies that the changes will be small, therefore the sensitivity to grid spacing, time scale or time step may be difficult

to identify compared to iterative errors. The spatial mesh refinement factor is calculated using three spatial dimensions in Eqn. 2.6.

$$rf = \left[\frac{N_{Fine}}{N_{Coarse}}\right]^{\frac{1}{3}} \tag{2.6}$$

A systematic refinement of three mesh grids, $N_1 > N_2 > N_3$, gives the refinement factors, $rf_{21} = \left[\frac{N_1}{N_2}\right]^{\frac{1}{3}}$ and $rf_{32} = \left[\frac{N_2}{N_3}\right]^{\frac{1}{3}}$, needed to calculate the apparent order, p. The apparent order is then calculated as follows, assuming that φ_k represents the variable of interest at the k^{th} grid:

$$\epsilon_{21} = \varphi_2 - \varphi_1 \tag{2.7}$$

$$\epsilon_{32} = \varphi_3 - \varphi_2 \tag{2.8}$$

$$S = 1 \cdot sign(\epsilon_{32}/\epsilon_{21}) \tag{2.9}$$

$$q(p) = \ln\left(\frac{rf_{21}^{p} - S}{rf_{32}^{p} - S}\right) \tag{2.10}$$

$$p = \frac{1}{\ln(rf_{21})}\left|\ln(\epsilon_{32}/\epsilon_{21}) + q(p)\right| \tag{2.11}$$

The calculation of the apparent order is best obtained on Richardson nodes, i.e. those that converge in a monotone fashion ($(\varphi_2 - \varphi_1)(\varphi_3 - \varphi_2) > 0$). Oscillatory nodes or non-monotone nodes ($(\varphi_2 - \varphi_1)(\varphi_3 - \varphi_2) < 0$), can give negative apparent orders that are not useful. The GCI, Eqn. 2.12, gives an uncertainty estimate for the fine grid. The

reason the relative discretization error e_a in Eqn. 2.13 is converted into an uncertainty estimate is that it is less reliable.

$$GCI_{fine}^{21} = \frac{F_s e_a^{21}}{r f_{21}^{p} - 1} \qquad 2.12$$

$$e_a^{21} = \left| \frac{\varphi_1 - \varphi_2}{\varphi_1} \right| x100\% \qquad 2.13$$

There are several variants of the GCI for predicting the uncertainty, of which one was developed by Cadafalch et al. [59] that uses an average of the local observed orders of accuracy, and is useful for estimating error and uncertainty locally at nodes because node to node variations in the apparent order of accuracy can cause noisy and unreliable estimates. This global averaging method calculates a globally averaged apparent order for the Richardson nodes using the local GCI's with a factor of safety of $F_s = 1.25$. Oberkampf and Christopher [56] suggest using a factor of safety of $F_s = 3.0$ for the oscillatory nodes along with the globally averaged apparent order. The factor of safety is essential in converting the discretization error into an epistemic uncertainty.

2.6. Experimental Validation Data

Performing experimental research is not only extremely costly, but accessibility of measurement equipment for complex flows is difficult. Extensive experimental investigations on the unsteady flow field of an axial-flow turbine were performed at AIST in Tsukuba, Japan. The present study aims to contribute to this research by conducting a numerical investigation based on a similar setup of the experiments. A detailed description of the facility and experimental technique is given by Matsunuma [24]. The experimental data used in this thesis was from an open circuit annular wind tunnel of the suction type. At the test section, a single-stage subsonic axial-flow turbine with a free vortex design was

installed to ensure radial equilibrium. *Table 2* and Figure 8 show the specifications and geometries of the nozzle and rotor cascades. The maximum velocity attained at the test section is 30 m/s. Like most wind tunnels, this one has a low free-stream turbulence intensity with a value of 0.5%, but it can be varied with the inclusion of turbulence-generating sheets. The cascade has been extensively tested with different experimental techniques. Most notably by Matsunuma et al. [15] using a 5-hole pressure probe; Matsunuma and Tsutsui [18] using a single-element hot wire anemometry; and Matsunuma [24] using a LDV system. A brief review of the experimental techniques and experimental uncertainty is given, followed by how to post-process the experimental data.

Table 2: Specifications of turbine cascade [24]

	Variable	Units	Nozzle			Rotor		
			Tip	Mid	Hub	Tip	Mid	Hub
Number of Blades	N		28			31		
Chord	C	mm	69.2	67.6	66.2	58.6	57.5	58.7
Axial Chord	C_{ax}	mm	45.3	42.8	40.2	33.1	41.0	49.4
Blade Span	H	mm	75.0			74.0		
Blade Pitch	s	mm	56.1	47.7	39.3	50.5	43.1	35.5
Aspect Ratio	H/C		1.08	1.11	1.13	1.26	1.29	1.26
Solidity	C/s		1.23	1.42	1.68	1.16	1.33	1.65
Inlet Flow Angle	α_1	deg(°)	0.0	0.0	0.0	-16.2	22.1	51.6
Exit Flow Angle	α_2	deg(°)	63.9	67.4	71.1	66.9	63.4	58.7
Turning Angle	$\alpha_2 - \alpha_1$	deg(°)	63.9	67.4	71.1	50.7	85.5	110.6
Stagger Angle	ξ	deg(°)	49.3	51.0	52.8	55.9	44.8	33.4
Inside diameter	D_1	mm	350			350		
Outside diameter	D_2	mm	500			500		
Hub-to-tip ratio	D_1/D_2		0.7			0.7		
Tip clearance	K	mm	0.0			1.0		
Upstream axial gap	g	mm	---			31.0	27.7	24.2
Flow Coefficient	ϕ		---			0.43	0.50	0.61
Loading Coefficient	ψ		---			0.88	1.20	1.77
Reaction	Rr		---			0.56	0.40	0.11

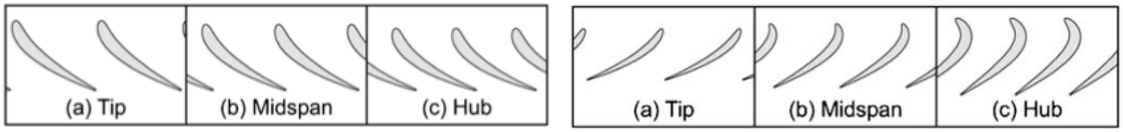

(a) Nozzle (b) Rotor

Figure 8: Geometry of Turbine [24]

2.6.1. Experimental Techniques

The operating point of the single-stage axial flow turbine is defined by the flow condition upstream and the static pressure downstream. The inlet velocity is measured with a 3-hole pressure probe approximately 30-mm upstream of the nozzle mid-span leading edge, at the axial position of $Z_{NZ}/C_{ax.NZ} = -0.706$. Measurements were taken at 73 spanwise locations with a coverage of 1.33% span to 98.7% span, here the potential influence of the nozzle is considered negligible. The inlet velocity is normalized to the test section axial velocity of 4.47 m/s. The reference pressure downstream of the cascade is considered to be zero atm, as the pressure at the outlet is equal to the atmospheric pressure. At the nozzle outlet, the 5-hole pressure probe measures the total pressure, velocity, turbulence intensity, and flow angle. The nozzle outlet is located 6.6-mm from the nozzle trailing edge, at the axial position of $Z_{NZ}/C_{ax.NZ} = 1.154$. Measurements were taken for one nozzle pitch, where 21 (spanwise) x 39 (pitch-wise) points or 819 measurement points characterize the measurement-grid. The spanwise coverage is from 3.3% span to 96.7% span.

The rotor flow field is captured with LDV measurements of the velocity and turbulence intensity from the nozzle exit to downstream of the rotor outlet at 44 axial positions spaced 2-mm apart. The measurement location begins at the same location as the 5-hole pressure probe and has the same spanwise coverage. The LDV system was a

standard two-color, two-dimensional measuring system with a fiber-optic probe based on a four-beam geometry scheme. The LDV system only gives the velocity in the axial and circumferential velocity. To distinguish the absolute and relative coordinate systems the time resolved data for one rotor pitch are indexed by 29 and 32, respectively.

The five-hole pressure probe and LDV data are non-dimensional, normalized by the time-averaged, pitch-wise-averaged, and spanwise-averaged velocity. The absolute velocity of 10.70 m/s and relative velocity of 9.27 m/s normalizes the velocity and turbulence intensity in the absolute and relative frame of reference, respectively. These velocities are tabulated at the axial position of $Z_{NZ}/C_{ax,NZ} = 1.125$ and $Z_{RT}/C_{ax,RT} = 1.145$, respectively. Lastly, an oil-film visualization was used to determine the three-dimensional flow characteristics near the nozzle blade suction surface. The separation and secondary flow lines were traced for quantitative observation of the separation and the secondary flow. Together all the experimental techniques help describe the flow field in the single-stage axial-flow turbine at a low Reynolds number.

2.6.2. Experimental Uncertainty

The experimental data obtained is afflicted with measurement errors. The magnitude of the errors is important to comprehend the results obtained. *Table 3* summarizes the uncertainty (99% coverage) of the LDV measurements, further information can be found in Matsunuma [24]. The 5-hole pressure probe accuracy should be in the range of those determined by Matsunuma et al. [15], which had an associated uncertainty of ± 0.008 for the pressure loss and ± 0.2 degrees for the flow angle.

Table 3: LDV measurement uncertainty [24]

		Time-averaged flow	Time-resolved unsteady flow
Relative velocity	V_{Rel}/V_2	0.0092 (0.92%)	0.0283 (2.83%)
Relative flow angle	θ_{Rel}	0.21 deg	0.69 deg
Turbulence intensity	TU_{Rel}	0.41%	0.66%

2.6.3. Post-Processing of Experimental Data

The experimental data provided is first confirmed before validation of the numerical values can be conducted. Appendix A provides the MATLAB code used to graph the time-averaged measurement results obtained from the LDV system data; a similar code is used for the 5-hole pressure probe and time-resolved data. Figure 9 shows the spanwise distribution of the velocity at the nozzle inlet, here the velocity is normalized by the test section velocity of 4.47 m/s. Figure 10 shows the absolute velocity distribution at the exit of the nozzle measured with a five-hole pressure probe and time-averaged velocity measured by the LDV system at the axial position $\mathrm{Z_{NZ}/C_{ax,NZ}} = 1.154$. Figure 11 shows the time-resolved absolute velocity at four different time indices at the axial position of $\mathrm{Z_{NZ}/C_{ax,NZ}} = 1.154$; it is worth mentioning that the time index of 22 was used instead of 23, as there was an error in that particular data set and based on the literature this axial position pertains to the first axial position of the LDV system. Figure 12 shows the time resolved relative velocity at the rotor exit for four different time indexes at the axial position $\mathrm{Z_{RT}/C_{ax,RT}} = 1.154$; this pertains to the 35^{th} axial position of the LDV system. The five-hole pressure probe and LDV data are in good agreement with those observed and presented by Matsunuma [24].

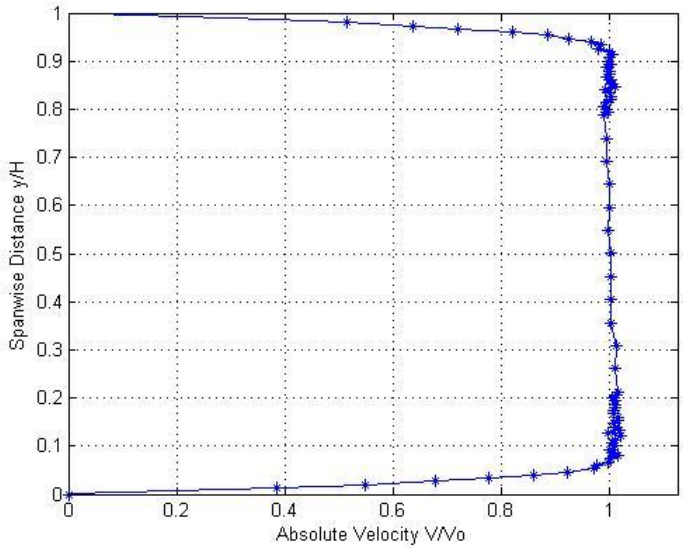

Figure 9: Spanwise distribution of the velocity at the nozzle inlet

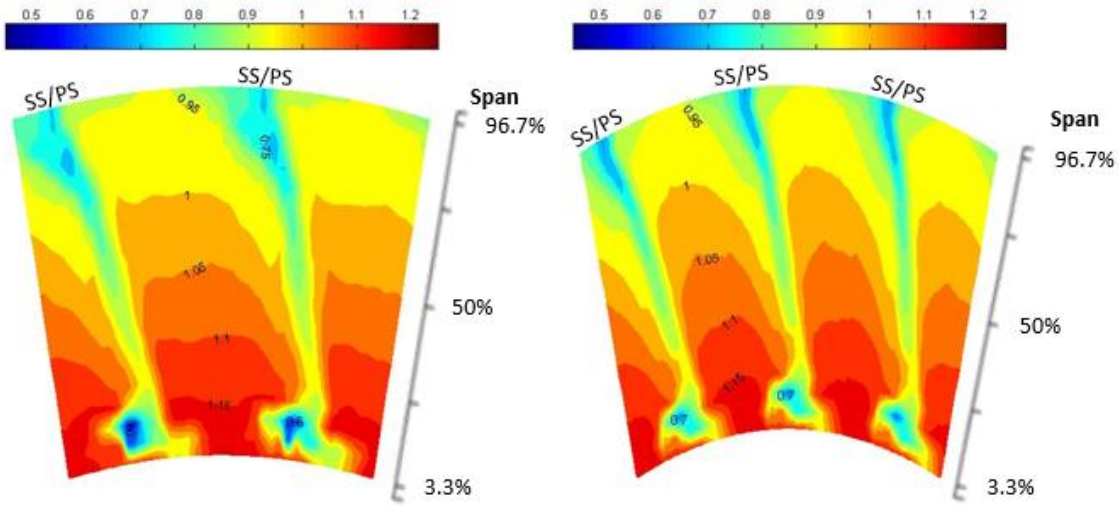

(a) V_{Abs} measured with 5-hole pressure probe (b) V_{Abs} measured with LDV

Figure 10: Absolute velocity at the nozzle exit ($Z_{NZ}/C_{ax,NZ} = 1.154$)

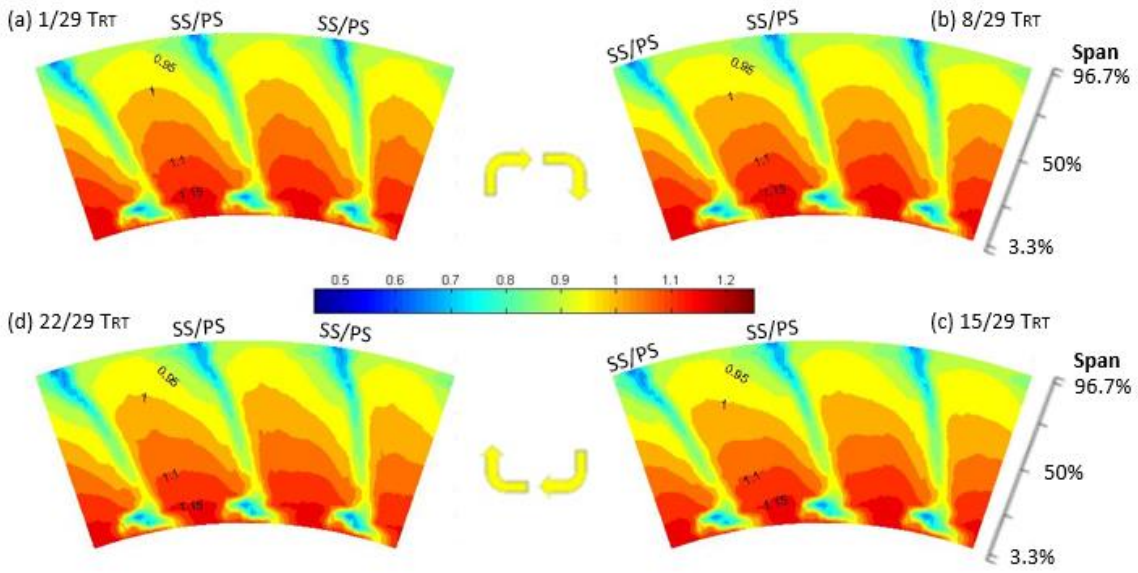

Figure 11: Time-resolved absolute velocity at the nozzle exit ($Z_{NZ}/C_{ax,NZ} = 1.154$)

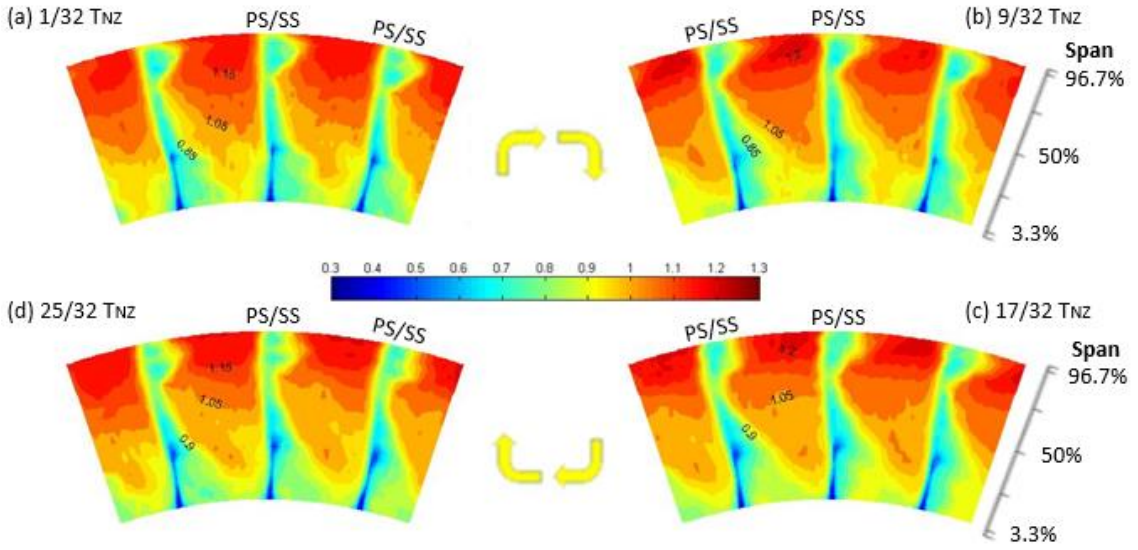

Figure 12: Time resolved relative velocity at the rotor exit ($Z_{RT}/C_{ax,RT} = 1.145$)

2.7. Literature Review Conclusions and Uniqueness of this Investigation

Four important conclusions can be drawn from the literature review. First, the effect of loss mechanisms and unsteadiness, is dependent on the cascade characteristics and flow conditions, effecting the overall performance of the turbine stage. Second, these flows impart losses within the blade passage that get significantly enhanced as the Reynolds

number is decreased, leading to a significant augmentation of the total pressure loss coefficient. Third, the incorporation of unsteady modeling techniques in CFD is important to properly model the actual unsteady blade row interaction. Last, some type of transition model is needed to properly model the separation on the nozzle blade suction surface.

In summary, a unique approach is undertaken to determine the flow field within an axial turbine at a low Reynolds number. This thesis considers the optimization of the mathematical formulation implemented in the CFD program. The potential benefit of this design approach includes a decrease in the necessary amount of time to setup similar models, and increased knowledge of the loss generating mechanisms within the turbine blade passage. It is believed that this approach will determine the mathematical formulation and parametric tuning within the CFD package that best replicates the flow field for this particular design. Such an optimization would allow for more in-depth analysis of the flow field were experimental instrumentation is hard to implement. Unique to this investigation and coupled to the optimization approach is the use of experimental results to quantify the CFD simulation results.

3. CONSTRUCTION OF CONCEPTUAL MODEL

3.1. Introduction

Analyzing the flow field within an axial flow turbine at a low Reynolds number involves integrating knowledge in fluid mechanics [60], thermodynamics [61], aerodynamics [62] and vortex dynamics [63] to evaluate its design and performance efficiencies. Computational fluid dynamics allows the use of numerical methods to analyze such fluid flow problems. This can be a computationally complex goal to achieve within an allotted time and with limited computational resources. These limitations do not impede the analysis; they merely increase the level of uncertainty. In order to analyze the overall system, it must first be broken down into the physical system and system surroundings, operating environment of the system, physical assumptions that simplify the system, phenomena of interest, system response quantities of interest, and accuracy requirements for the system response quantities of interest.

3.2. Physical System and System Surroundings

The physical system is the subsonic three-dimensional, unsteady, and viscous internal flow within an axial-flow turbine at a low Reynolds number. The annular axial-flow turbine is composed of three sections: nozzle, rotor, and downstream section. The fresh atmospheric airflow enters axially into the stationary nozzle accelerating the flow before entering the unshrouded rotor section where the kinetic energy extracted produces shaft work that might drive a compressor, electric generator, output turbine and accessories.

The flow then proceeds to a stationary downstream section following the rotor, where it releases to the atmosphere axially.

The turbine blades ensure radial equilibrium through a free-vortex blading method using uniform inlet conditions [24]. This type of design accounts for the pressure increase from hub to shroud while neglecting the viscous forces, which allows for the work done per unit mass of gas to be equal at all radial positions leading to a uniform stagnation temperature through the stage. This design has a completely axial inlet and outlet velocity for the stage, giving no swirl component entering the nozzle and exiting the rotor. This is typical of a single-stage design, but it also allows the use of the same blade shapes in successive stages in a multi-stage axial turbine.

The only surroundings modeled are the walls of the hub, shroud and airfoil surfaces in the construction of the computational fluid domains. The walls and airfoil surfaces are smooth and adiabatic with a no-slip condition, while the shaft of the rotor is frictionless. For this particular study the alternate surroundings are not of interest, thus they are not modeled.

3.3. Operating Environment

3.3.1. System Conditions

The atmospheric air entering the stage is at 20°C ($\rho = 1.205 \frac{\text{kg}}{\text{m}^3}, \upsilon = 1.51E-5 \frac{\text{m}^2}{\text{s}}, C_p = 1005.0 \frac{\text{J}}{\text{kg-K}}$) with a turbulence intensity of 0.5%. The inlet velocity enters the nozzle (Station – 1) and exits the rotor (Station – 3) with no swirl component ($\alpha_1 = \alpha_3 = 0$). The mean-line inlet velocity of 4.47 m/s exits the nozzle mean-line (Station – 2) with an outlet flow angle of α_2 = 67.4°. The rotor has a tip clearance of 1.0-mm and rotational speed of 402 RPM. This information determines the mean-line flow velocity and angle

distributions, which dictates the radial free-vortex blading needed to ensure radial equilibrium of a uniform inlet velocity profile. *Table 2* gives the cascade specifications; this geometry is representative of a low-pressure turbine. Figure 13 shows velocity triangles superimposed on the mean-line geometry with the nomenclature employed.

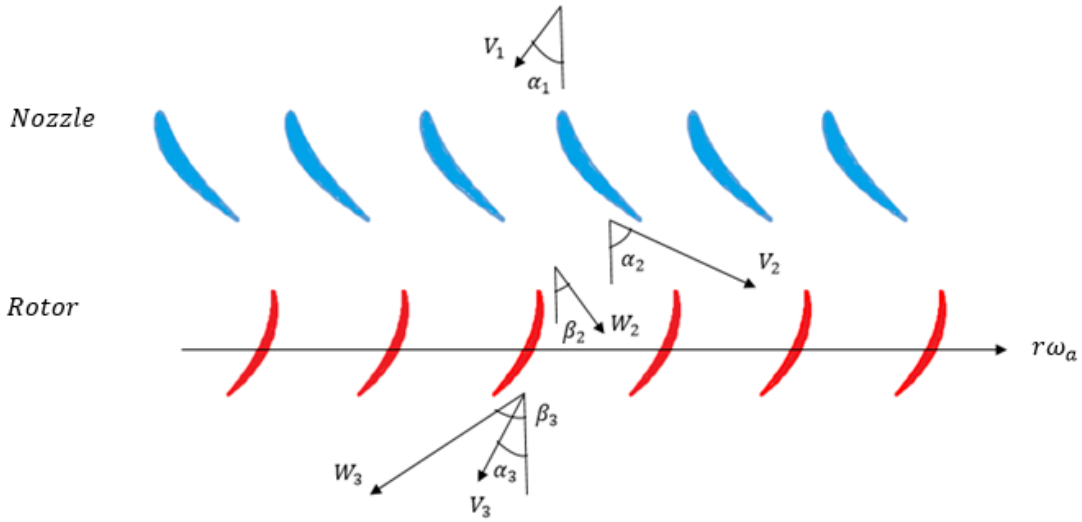

Figure 13: Turbine stage velocity diagram

The operating Reynolds number ranges from $Re_{in,NZ} = \frac{U_\infty C_{ax,NZ}}{\upsilon} = 20{,}000$ at the inlet based on the nozzle chord length and nozzle inlet velocity to $Re_{out,RT} = \frac{U_\infty C_{ax,RT}}{\upsilon} = 35{,}000$ at the rotor outlet based on the rotor chord length and rotor exit velocity. Fielding [42] mentions that "the minimum permissible Reynolds for high efficiency turbines is considered to be 10^5", where the "efficiency increases little at Reynolds numbers above $2x10^5$." The low Reynolds number operation indicates that the inertial effects are small relative to the viscous and pressure forces. Within the single-stage turbine a maximum velocity of 10.7 m/s is observed at the nozzle exit. The Mach numbers range from 0.013 to 0.031 from the nozzle inlet to rotor outlet. This low Mach number ensures that

compressibility effects will be small allowing the use of the simplified incompressible flow equations.

3.3.2. Computer Software

In this thesis, all computations are executed on the High Performance Computing (HPC) cluster at Florida Atlantic University, where one node consists of two Intel Xeon E5-2680v2 Ivy Bridge (2.8 GHz) processors with 10 cores each together with 128 GB of Random Access Memory (RAM) interconnected by Fourteen Data Rate (FDR-10) running under an x86_64 Linux architecture [64]. The data cache size is 25 Mbyte. The code supports parallel execution using standard message passing interface (MPI) techniques and a Multilevel Graph Partitioning Algorithm.

3.4. Physical Assumptions that Simplify the System

The description of the system and operating environment allow for the following assumptions in the analysis:

- The individual nozzle and rotor airfoils are all considered to be machined identically, having no noticeable differences
- The walls and blade surfaces are smooth and adiabatic with a no-slip condition
- The midstream inlet velocity is constant
- The rotational speed of the rotor is constant
- The fluid is a Newtonian fluid
- The flow is Subsonic ($Ma < 1$)
- The flow is considered to be incompressible and adiabatic
- The flow is considered isothermal thus the energy equation is not included
- Constant specific heat C

- Neglect gravity
- Isotropy of turbulence

3.5. Phenomena of Interest

Review of the existing literature about this subject reveals that the flow field in axial turbines at low Reynolds number is very complex due to the three-dimensional nature of the flow, blade passage geometry, existence of non-steady effects, and laminar-turbulent transition. Under these conditions the various phenomena of interest are the horseshoe vortex system, corner vortices, passage vortex, tip leakage flow, wake, flow separation (detaching shear layer), and unsteady mixing of vortices (vortex shedding).

3.6. System Response Quantities of Interest

The numerical system response quantities of interest are the absolute velocity, relative velocity, absolute total pressure drop, and root-mean-square (RMS) of the turbulent velocity fluctuations. The first three are analyzed using non-dimensional values. The normalized absolute velocity and normalized relative velocity are analyzed using Eqns. *3.1* and *3.2*, respectively, allowing for direct comparison to the experimental values given by Matsunuma [24].

$$V_{Abs} = \frac{\sqrt{V_z^2 + V_r^2 + V_{\vartheta,Abs}^2}}{V_2} \tag{3.1}$$

$$V_{Rel} = \frac{\sqrt{V_z^2 + V_r^2 + V_\vartheta^2}}{W_3} \tag{3.2}$$

Where, V_2 and W_3 are the mass flow-averaged absolute and relative velocities obtained at the axial position of $Z_{NZ}/C_{ax,NZ} = 1.125$ and $Z_{RT}/C_{ax,RT} = 1.145$, respectively. The normalized absolute total pressure drop is found using Eqn. *3.3*, calculated in reference to

the inlet total pressure, giving a measure of the total pressure loss along the entire computational domain.

$$\Delta P_{Abs} = \frac{Pt_{Abs,in} - Pt_{Abs}}{Pt_{Abs,in}} = 1 - \frac{Pt_{Abs}}{Pt_{Abs,in}} \qquad 3.3$$

The RMS of the turbulent velocity fluctuations, Eqn. *3.4*, assumes isotropy of turbulence.

$$\mathbf{u}' = v' = u' = w' = \sqrt{\frac{2}{3}k} \qquad 3.4$$

Where, k is the turbulent kinetic energy. RMS of the turbulent velocity divided by the absolute and relative velocity at the exit planes make the absolute and relative turbulence intensity dimensionless.

3.7. Accuracy Requirements for the System Response Quantities of Interest

In order to examine the spatial and temporal convergence for the numerical solution the GCI provides an epistemic uncertainty estimate based on the Richardson Extrapolation. For all the simulations the iterative convergence should first have acceptable residual RMS error values (typically less than $1E-3$), the mass flow rate surface monitors at the inlets and outlets must have reached steady values, and the domain must have imbalances less than 1%. For the transient simulations, the iterative convergence at every time step must also be confirmed. Then convergence of the variables of interest should be confirmed, where the apparent order of accuracy should be in the asymptotic range, but as this is difficult due to the computational resource limitations, it should at least be approaching the formal order of convergence with each mesh grid refinement. This will help to show the stability of the computational processes and accuracy of the results formulated. After the numerical accuracy is established, the normalized absolute and relative velocities, as well

as the RMS of the turbulent velocity fluctuations are used to gauge the accuracy of the numerical results in comparison with the experimental results.

4. FORMULATION OF MATHEMATICAL MODEL

The mathematical model is the representation of physical processes through mathematical concepts that allow for the simulation of a physical system to determine its response to fluid properties, boundary conditions (B.C.'s), and the initial conditions (I.C.'s) of the system. The mathematical relationships given by a set of partial differential equations (PDE's) or integral equations represent the variables and parameters as a function of space and time. The physical processes and the physical models make up the mathematical model.

4.1. Physical Processes

The physical processes follow the fundamental physical laws as dictated by the assumptions set in the conceptual model. The biggest assumption is that of incompressible flow since Mach numbers are below 0.3 [60]. For air at 20℃ standard conditions, the velocity of the fluid should not exceed 100 m/s for the incompressibility assumption to hold. For low Mach number perfect gas flows, this means that the kinetic energy is less when compared to the internal energy, so if brought to rest the total and static temperatures are about equal. Incompressible fluids also have a single reasonable specific heat as in Eqn. *4.1* [61]. In this thesis, the constant-pressure specific heat is used, where it is considered constant due to the isothermal assumption.

$$C \approx C_p \approx C_v \tag{4.1}$$

For the idealized case of an incompressible fluid with constant density and specific heat, the fluid undergoes no temperature change due to addition of kinetic energy, thus

allowing the energy equation to be decoupled from the momentum equation. Therefore, with the above assumptions, the combined mass and momentum conservation equations are known as the incompressible Navier-Stokes equations applicable to laminar and turbulent flows. The incompressible Navier-Stokes equations consist of one continuity equation and three full equations of motion as demonstrated in [65]. The continuity equation, Eqn. *4.2*, expresses mass conservation; here the velocity field is divergence free.

$$\boldsymbol{\nabla} \cdot \boldsymbol{U} = \frac{d\mathrm{U_j}}{dx_j} = 0 \qquad 4.2$$

The conservation of momentum, Eqn. *4.3*, is Newton's second law in terms of momentum.

$$\rho \frac{D\boldsymbol{U}}{Dt} = \rho \frac{d\mathrm{U_i}}{dt} + \rho \frac{d}{dx_j}(\mathrm{U_i U_j}) = -\frac{d\mathrm{P}}{dx_\mathrm{i}} + \frac{d}{dx_j}\tau_{\mathrm{ij}} \qquad 4.3$$

The stress tensor, τ, for an isotropic Newtonian fluid constitutes the relation that the shear stress in the fluid is proportional to the time rate of strain, Eqn. *4.4*.

$$\tau_{ij} = \mu\left(\frac{dU_i}{dx_j} + \frac{dU_j}{dx_i}\right) - \frac{2}{3}\mu\delta_{ij}\frac{d\mathrm{U_j}}{dx_j} = 2\mu S_{ij} - \frac{2}{3}\mu\delta_{ij}\boldsymbol{\nabla} \cdot \boldsymbol{U} \qquad 4.4$$

Where, the strain rate tensor, S_{ij}, is given in Eqn. *4.5*. It is a measure of the rate of deformation in terms of the velocity gradients.

$$S_{ij} = \frac{1}{2}\left(\frac{dU_i}{dx_j} + \frac{dU_j}{dx_i}\right) \qquad 4.5$$

As reference, the Kronecker delta is defined as:

$$\delta_{ij} = \begin{cases} 1 & if \quad i = j \\ 0 & if \quad i \neq j \end{cases} \qquad 4.6$$

4.2. Physical Models

Turbulence is a very fascinating yet difficult topic due to its complexity. The basic features of turbulence shown by the famous Reynolds experiment [60] show that flows can

be laminar, turbulent or transitional in nature. Laminar flow is the regular, smooth and steady motion of fluid elements, where the viscous effects make the small disturbances in the flow die down. The classical definition of turbulence, random and disordered motion in the fluid, does not fully define turbulence accurately. Instead, turbulence is defined with the following important characteristics: the fluid element is random, chaotic, and highly three-dimensional with respect to time and space, thus having no regular ordered motion due to strong mixing [66]. The inertial forces are greater than the viscous forces resulting in a higher Reynolds number and amplification of the perturbations, hence in turbulent flows small perturbations tend to grow ensuring strong mixing, enhancing diffusivity. Turbulent flows also have a wide range of length and time scales that make modeling very hard. Transitional flows prevail between these two limits. If the goal of physically modeling turbulence can be achieved it would mean we have learned something about turbulence such as its structure, concepts and theories. To physically model turbulent flow, the Reynolds-averaged Navier-Stokes approach is taken, where different turbulence models are used to achieve turbulence closure.

4.2.1. RANS/URANS Approach

The Navier-Stokes equations are the basic governing equations for fluid motion that describe both laminar and turbulent flows. If solved with sufficient spatial and time resolution as in a Direct Numerical Simulation (DNS) they would describe the appropriate flow without the need of additional information. This seems like the best option, but turbulent flows generally have a wide range of turbulent length and time scales that require the finest of meshes to resolve the smallest length scales. DNS is still unpractical requiring computing power many orders higher than currently available.

The Reynolds Averaged Navier-Stokes (RANS) equations, first introduced by Reynolds in 1895, are based on a statistical mean solution of the Navier-Stokes equations. The RANS equations seek to average out the turbulent fluctuating terms, so that such high resolution is not necessary. As such, the instantaneous velocity is separated into its average component, $\bar{\boldsymbol{U}}$, and fluctuating component, $\boldsymbol{u}'$, as in Eqn. *4.7*.

$$\boldsymbol{U} = \bar{\boldsymbol{U}} + \boldsymbol{u}' \tag{4.7}$$

Although, the RANS approach is for statistically stationary flows the URANS formulation can potentially model the non-stationary and unsteady aspect of the flow. The ensemble – average of the URANS equations give the averaged equations as well [67].

After the components of the instantaneous velocity are inserted into the incompressible Navier-Stokes equations, remembering that the mean fluctuations are zero and the means of the squared fluctuations differ from zero, the simplified equations become the incompressible RANS equations, Eqns. *4.8* and *4.9*, where the bars are dropped for averaged quantities.

$$\boldsymbol{\nabla} \cdot \boldsymbol{U} = 0 \tag{4.8}$$

$$\rho \frac{d(U_i)}{dt} + \rho \frac{d}{dx_j}(U_i U_j) = -\frac{d\mathrm{P}}{dx_\mathrm{i}} + \frac{d}{dx_j}(\tau_{\mathrm{ij}} - \rho\overline{\mathrm{u_i u_j}}) \tag{4.9}$$

The continuity equation is the same whether the flow is steady or unsteady. These averaged equations are well behaved, but introduce additional unknown terms that act like additional stresses in the fluid, known as turbulent or Reynolds stresses, as in Eqn. *4.10*, which are difficult to determine directly [68].

$$-\rho\overline{u_i u_j} = -\rho \begin{bmatrix} \overline{u_1^2} & \overline{u_1 u_2} & \overline{u_1 u_3} \\ \overline{u_1 u_2} & \overline{u_2^2} & \overline{u_2 u_3} \\ \overline{u_1 u_3} & \overline{u_2 u_3} & \overline{u_3^2} \end{bmatrix} \tag{4.10}$$

Generally, there are ten unknowns: three velocity components, one pressure component, and six Reynolds stress terms. Applying the conservation of mass and continuity equations leaves an indeterminate system with six unknown Reynolds stress terms. The Reynolds stresses are modeled with additional equations to provide a solution to the closure problem of turbulence, where the equations used define the type of turbulence model. Turbulence modeling tries to represent the Reynolds stresses in terms of the time-averaged velocity components that provide all the turbulent effects on the mean flow and mean of the fluctuations. The RANS turbulence models work well in expressing the main features of many turbulent flows by means of one length scale and one timescale. This approach reduces the computer demand substantially, however at the expense of excluding the multitude of length scales involved in turbulence.

4.2.2. Eddy-Viscosity Turbulence Models

The statistical turbulence models of interest belong to the eddy-viscosity models (EVM's) distinguished by the manner in which they prescribe the eddy-viscosity. These models suggest that the turbulence consists of small eddies what are continuously forming and dissipating [67]. EVM's invoke the Boussinesq hypothesis that relates the proportionality of the Reynolds stress tensor, Eqn. *4.11*, to the mean strain rate.

$$-\rho\overline{u_\iota u_j} = 2\mu_t S_{ij} - \frac{2}{3}\rho k\delta_{ij} \qquad 4.11$$

Where the turbulent kinetic energy, k, is defined as

$$k = \frac{1}{2}\overline{u_\iota u_j} \qquad 4.12$$

and μ_t is the eddy (turbulent) viscosity. With this formulation, the turbulent viscosity is a scalar quantity that varies in space making it nonhomogeneous, yet it is the same in all directions as turbulent diffusion is isotropic. Eddy-viscosity is not a fluid property, but

rather a turbulent flow characteristic that models the transfer of momentum by turbulent eddies. Equation *4.13* transforms the turbulent viscosity to a kinematic turbulent viscosity.

$$v_t = \frac{\mu_t}{\rho} \qquad 4.13$$

The question then becomes how to model the eddy or turbulent viscosity. The modeling of the turbulent viscosity gives rise to the different EVM's. There are several subcategories for linear EVM's, dependent on the number of transport equations used to model the eddy-viscosity coefficient. In this thesis the main focus will be on two-equation EVM's, all of which use the turbulent kinetic energy, $k\left[\frac{m^2}{s^2}\right]$, as one of the solved turbulent quantities. The turbulent dissipation, $\varepsilon\left[\frac{m^2}{s^3}\right]$, or the specific dissipation, $\omega\left[\frac{1}{s}\right]$, is the second turbulent quantity used to properly represent the turbulent properties of the flow. ε is rate at which k dissipates, while the relationship between ω and ε is shown in Eqn. *4.14*.

$$\omega = \frac{\varepsilon}{(\beta' k)} \qquad 4.14$$

Where, the specific dissipation, ω, is the reciprocal of the 'turnover time' of turbulence $\tau_\kappa = k/\varepsilon$ [69].

Both the $k-\varepsilon$ and $k-\omega$ EVM's use the RANS equations and two additional equations to achieve closure. The shear stress transport (SST) turbulence model combines both these models and a modification of the eddy-viscosity through blending functions. These EVM's can completely predict a given turbulent flow with no advance information other than boundary conditions, although they impose severe assumptions about the nature of the flow that are based on theoretical concepts.

4.2.2.1. k − ε Turbulence Model

The $k-\varepsilon$ [70]turbulence model uses the transport equations for the turbulent kinetic energy or turbulent mixing energy, k, and the rate of dissipation of turbulent kinetic energy per unit mass, ε. The model equations for the turbulent kinetic energy and turbulent dissipation are presented in Eqn. *4.15* and *4.16*, respectively.

$$\frac{Dk}{Dt} = \frac{d(k)}{dt} + \frac{d}{dx_j}\left(U_j k\right) = \frac{d}{dx_j}\left[\left(v + \frac{v_t}{\sigma_k}\right)\frac{dk}{dx_j}\right] + \widetilde{P_k} - \varepsilon \qquad 4.15$$

$$\frac{D\varepsilon}{Dt} = \frac{d(\varepsilon)}{dt} + \frac{d}{dx_j}\left(U_j \varepsilon\right) = \frac{d}{dx_j}\left[\left(v + \frac{v_t}{\sigma_\varepsilon}\right)\frac{d\varepsilon}{dx_j}\right] + \frac{\varepsilon}{k}\left(C_{\varepsilon 1}\widetilde{P_k} - C_{\varepsilon 2}\varepsilon\right) \qquad 4.16$$

Where, $\widetilde{\mathrm{P_k}}$ is the rate of turbulence energy production, while $C_\mu, C_{\varepsilon 1}, C_{\varepsilon 2}, \sigma_k, and\ \sigma_\varepsilon$ are constants. The closure coefficients for the model as fitted with benchmark experiments of Lauder and Sharma [71] are: $C_\mu = 0.09, C_{\varepsilon 1} = 1.44, C_{\varepsilon 2} = 1.92, \sigma_{\mathrm{k}} = 1.0, and\ \sigma_\varepsilon = 1.3.$

The rate of turbulence production models the energy interchange between the mean flow and turbulence, Eqn. *4.17*.

$$P_k = 2v_t S_{ij}\frac{dU_i}{dx_j} \qquad 4.17$$

For an incompressible flow the rate of turbulence production reduces to:

$$P_k = v_t \boldsymbol{S}^2 \qquad 4.18$$

Where $\boldsymbol{S}$ is an invariant measure of the strain rate, Eqn. *4.21*, and the kinematic eddy-viscosity, Eqn. *4.20*, is representative of the large-scale turbulence.

$$\boldsymbol{S} = \sqrt{2S_{ij}S_{ij}} \qquad 4.19$$

$$v_t = C_\mu \frac{k^2}{\varepsilon} \tag{4.20}$$

The kinematic eddy-viscosity is determined for a single turbulence length scale, when in reality there are multitude of length scales that contribute to turbulent diffusion. The model equation for k is comparable to the exact k equation with only minor modifications, while the model equation for ε contrasts considerably from the exact ε equation due to several unknown correlations [44].

4.2.2.2. k − ω Turbulence Model

The standard k − ω model of Wilcox [72] is a modified version of the turbulent kinetic energy, Eqn. *4.21*, and the specific turbulence dissipation rate (or turbulent frequency), ω, in Eqn. *4.22*. It is a modified version in that a transformation of the dependent variables is accomplished using Eqn. *4.14*, and the cross-diffusion term is not modeled. The production rate for turbulence is calculated as in the k − ε model, Eqn. *4.14*, while the modeled kinematic eddy-viscosity is calculated using Eqn. *4.23*. As in [72], the closure coefficient values of the k − ω model are: $\beta' = 0.09, \alpha_1 = \frac{5}{9}, \beta_1 = 0.075, \sigma_{k1} = 2.0, and\ \sigma_{\omega 1} = 2.0$.

$$\begin{aligned} \frac{Dk}{Dt} &= \frac{d(k)}{dt} + \frac{d}{dx_j}\left(U_j k\right) \\ &= \frac{d}{dx_j}\left[\left(v + \frac{v_t}{\sigma_{k1}}\right)\frac{dk}{dx_j}\right] + \widetilde{P_k} - \beta' k\omega \end{aligned} \tag{4.21}$$

$$\begin{aligned} \frac{D\omega}{Dt} &= \frac{d(\omega)}{dt} + \frac{d}{dx_j}\left(U_j \omega\right) \\ &= \frac{d}{dx_j}\left[\left(v + \frac{v_t}{\sigma_{\omega 1}}\right)\frac{d\omega}{dx_j}\right] + \alpha_1 \frac{\omega}{k}\widetilde{P_k} - \beta_1 \omega^2 \end{aligned} \tag{4.22}$$

$$v_t = \frac{k}{\omega} \tag{4.23}$$

4.2.2.3. SST Turbulence Model

The Shear Stress Transport (SST) model of Menter [73] is identical to his baseline (BSL) $k-\omega$ model in that a blending between the $k-\omega$ model for the inner region and the $k-\varepsilon$ in the outer region of the boundary layer is achieved, combining the best elements of existing EVM's. This is to improve the predictive capability of flows with strong adverse pressure gradients and separation, which is the main deficiency in two-equation models [74]. This is accomplished by transforming the $k-\epsilon$ model into a $k-\omega$ formulation, where the transformed coefficients become $\beta' = 0.09, \alpha_2 = 0.44, \beta_2 = 0.0828, \sigma_{k2} = 1.0, and\ \sigma_{\omega 2} = 1/0.856$ [67]. The SST turbulence model equations are:

$$\frac{Dk}{Dt} = \frac{d(k)}{dt} + \frac{d}{dx_j}\left(U_j k\right) = \frac{d}{dx_j}\left[(v + \frac{v_t}{\sigma_{k3}})\frac{dk}{dx_j}\right] + \widetilde{P_k} - \beta' k\omega \tag{4.24}$$

$$\frac{D\omega}{Dt} = \frac{d(\omega)}{dt} + \frac{d}{dx_j}\left(U_j \omega\right) = \frac{d}{dx_j}\left[(v + \frac{v_t}{\sigma_{\omega 3}})\frac{d\omega}{dx_j}\right] + 2(1-F_1)\frac{1}{\sigma_{\omega 3}\omega}\frac{dk}{dx_j}\frac{d\omega}{dx_j} + \alpha_3\frac{\omega}{k}\widetilde{P_k} - \beta_3\omega^2 \tag{4.25}$$

The blending function takes place in the wake region of the boundary layer where it is one near the wall region, activating the $\kappa-\omega$ model and zero away from the surface, activating the $\kappa-\varepsilon$ model [73]. The closure coefficient values of the SST model are a

linear combination of the original $\kappa - \omega$ model coefficients and the transformed $\kappa - \epsilon$ model coefficients that incorporates the blending function, Eqn. 4.26.

$$\phi_3 = F_1\phi_1 + (1 - F_1)\phi_2 \tag{4.26}$$

Unlike the BSL model, the SST model also modifies the definition of the eddy-viscosity to account for the transport of the principal turbulent shear stress, Eqn. 4.27.

$$v_t = \frac{a_1 k}{max(a_1\omega; \boldsymbol{S}F_2)} \tag{4.27}$$

Where F_2 is a blending function for the eddy-viscosity. This enforces Bradshaw's hypothesis that the principal shear stress is proportional to the turbulent kinetic energy. The formulation of the blending functions is based on the flow variables and distance to the nearest wall,y, in the following way:

$$F_1 = tanh\left(\left[min\left(max\left[\frac{\sqrt{k}}{\beta'\omega y}, \frac{500v}{y^2\omega}\right], \frac{4\rho\sigma_{\omega 2}k}{CD_{k\omega}y^2}\right)\right]^4\right) \tag{4.28}$$

$$CD_{k\omega} = max\left(2\rho\frac{1}{\sigma_{\omega 2}\omega}\frac{dk}{dx_j}\frac{d\omega}{dx_j}, 1.0 * 10^{-10}\right) \tag{4.29}$$

$$F_2 = tanh\left(max\left[\frac{2\sqrt{k}}{\beta'\omega y}, \frac{500v}{y^2\omega}\right]^2\right) \tag{4.30}$$

Although the SST model improves the prediction of separation, the flow recovery prediction is too slow when compared to experiments as shown by Menter and Langtry [74].

4.2.3. Production Limiters

The two-equation models have been shown to have excessive build-up of turbulent kinetic energy in stagnation regions. A production limiter formulation is then needed to prevent this build-up of turbulence without affecting the performance of the model. The

production limiter, Eqn. *4.31*, has a clip factor, C_{lim}, of 10 for ω based turbulence models, which is enabled by default for the original SST turbulence model [74].

$$\widetilde{P_k} = min(P_k, C_{lim}\beta'\rho k\omega) \tag{4.31}$$

4.2.4. Curvature Correction for Two-Equation Models

Streamline curvature and system rotation add to the complexity of determining the flow structure and turbulence quantities found in curved blades of axial-flow turbines. Eddy-viscosity models have to be refined to include such features. An empirical function suggested by Spalart and Shur [75], first applied to the one equation Spalart-Allmaras (S-A) turbulence model, allows a modification of the production term by a multiplier. The multiplier, Eqn. *4.32*, allows sensitization to streamline curvature and system rotation.

$$f_{rotation} = (1 + c_{r1})\frac{r^*}{1 + r^*}[1 - tan^{-1}(c_{r2}\tilde{r})] - c_{r1} \tag{4.32}$$

The multiplier is first limited, Eqn. *4.33*, to account for the changes that arise due to curvature by either increasing or decreasing the production around concave and convex curvatures, respectively.

$$f_{r1} = max\{min(f_{rotation}, 1.25),0.0\} \tag{4.33}$$

In this manner the magnitude of f_{r1} is limited from 0 corresponding to a strong convex curvature up to 1.25 corresponding to a strong concave curvature. The value of 1.25 restricts the over generation of eddy-viscosity, providing the best results when applied to a study of flow through a U-turn, centrifugal compressor, and NACA wing tip vortex [76]. In the same way the constants c_{r1}, c_{r2} and c_{r3} where found to be 1.0, 2.0 and 1.0, respectively. Equation *4.34* shows how the curvature correction modifies the production term.

$$\widetilde{P_k} = f_{r1} P_k \tag{4.34}$$

The other variables are defined assuming that they are with respect to the reference frame rotating at a rate of Ω^{rot}, as follows:

$$r^* = \frac{\boldsymbol{S}}{\boldsymbol{\Omega}} \tag{4.35}$$

$$\tilde{r} = 2\Omega_{ik} S_{jk} \left[\frac{DS_{ij}}{Dt} + \left(\varepsilon_{imn} S_{jn} + \varepsilon_{jmn} S_{in} \right) \Omega_m^{rot} \right] \frac{1}{\boldsymbol{\Omega} D^3} \tag{4.36}$$

$$D^2 = max(\boldsymbol{S}^2, 0.09\omega^2) \tag{4.37}$$

Where, $\boldsymbol{\Omega}$ is the magnitude of the vorticity rate, Eqn. *4.38*, and Ω_{ij} is the vorticity tensor, Eqn. *4.39*.

$$\boldsymbol{\Omega} = \sqrt{2\Omega_{ij}\Omega_{ij}} \tag{4.38}$$

$$\Omega_{ij} = \frac{1}{2}\left(\left(\frac{du_i}{dx_j} - \frac{du_j}{dx_i} \right) + 2\epsilon_{mji}\Omega_m^{rot} \right) \tag{4.39}$$

Smrnov and Menter [76] have effectively demonstrated the performance of the developed $SST - CC$ turbulence model. Test also conducted by Elliot et al. [77] showed that the $SST - CC$ turbulent kinetic profiles showed appropriate sensitivity to curvature, with increased turbulent kinetic energy on the concave side and decreased turbulent kinetic energy on the convex side. Curvature correction can be used on ε and ω based EVM's, such as the $k - \epsilon$, $k - \omega$, and SST turbulence models [67].

4.2.5. Transition Model

Laminar-turbulent transition in CFD predictions mainly use two modeling concepts to capture the different mechanisms causing flow instabilities leading to natural transition, bypass transition, separation induced transition, and relaminarization. The first is Low-Reynolds number turbulence models that trigger transition onset by the wall damping

functions without inclusion of an intermittency equation. Langtry and Menter [78] mention that these damping functions do not predict transition from laminar to turbulent flow instead replicating the viscous sublayer behavior, making their ability to predict transition coincidental.

The second is a full transition model that uses the strain rate Reynolds number, Re_v, and empirical transition models with two transport equations for the intermittency, γ, and transition momentum thickness Reynolds number, $\check{R}e_{\theta t}$, known as the Gamma-Theta Model. The full transition model and its implementation is described briefly; a detailed description can be found in Menter et al. [79]. This presentation includes the current model implemented in ANSYS CFX that includes improvement made by Menter and Langtry [80]. Langtry and Menter [78] suggest that these types of models appear "superior to conventional low-Reynolds models, as they implicitly contain information of the thickness of the boundary layer."

The intermittency gives a measure of periodic and chaotic dynamics, where a value of one is given for fully turbulent and a value of zero for having no turbulence, locally triggering transition. The transport equation for the intermittency is given in Eqn. *4.40*.

$$\frac{D\gamma}{Dt} = \frac{d(\gamma)}{dt} + \frac{d}{dx_j}\left(U_j\gamma\right) = P_\gamma - E_\gamma + \frac{d}{dx_j}\left[\left(v + \frac{v_t}{\sigma_\gamma}\right)\frac{d\gamma}{dx_j}\right] \qquad 4.40$$

Where the transition source, P_γ, and the destruction and relaminarization sources, E_γ, are given by Eqns. *4.41* and *4.42*, respectively.

$$P_\gamma = c_{a1}F_{length}\rho\boldsymbol{S}[\gamma F_{onset}]^{0.5}[1 - c_{\varepsilon 1}\gamma] \qquad 4.41$$

$$E_\gamma = c_{a2}\rho\boldsymbol{\Omega}\gamma e^{-\left(\frac{R_T}{4}\right)^4}[c_{\varepsilon 2}\gamma - 1] \qquad 4.42$$

The viscosity ratio, R_T, is given by Eqn. *4.43*.

$$R_T = \frac{\rho k}{\mu \omega} \tag{4.43}$$

The transition onset, F_{onset}, is controlled by a set of functions, Eqns. *4.44* to *4.47*.

$$F_{onset\,1} = \frac{Re_v}{2.193 Re_{\theta c}} \tag{4.44}$$

$$F_{onset\,2} = min(max(F_{onset\,1}, F^4_{onset\,1}), 2.0) \tag{4.45}$$

$$F_{onset\,3} = max(1 - \left(\frac{R_T}{2.5}\right)^3, 0) \tag{4.46}$$

$$F_{onset} = max(F_{onset\,2} - F_{onset\,3}, 0) \tag{4.47}$$

Where, Re_v is the strain rate Reynolds number, Eqn. *4.48*.

$$Re_v = \frac{\rho y^2 \boldsymbol{S}}{\mu} \tag{4.48}$$

Re_v increases as the shape factor does, where the growth of the boundary layer disturbances is characterized by y^2S and $\frac{\rho}{\mu}$ is responsible for damping the growth [78]. The critical Reynolds number, $Re_{\theta c}$, and the length of transition, F_{length}, are empirical correlations dependent on the transition momentum thickness Reynolds number, as follows:

$$F_{length} = f(\check{R}e_{\theta t}) \tag{4.49}$$

$$Re_{\theta c} = f(\check{R}e_{\theta t}) \tag{4.50}$$

The constants for the intermittency equation as given by Langtry and Menter [80] are: $c_{a1} = 2.0$, $c_{a2} = 0.06$,$c_{\varepsilon 1} = 1.0$, $c_{\varepsilon 2} = 50$, and $\sigma_\gamma = 1.0$.

A modification to account for separation-induced transition, γ_{sep}, has been implemented to better predict the turbulent reattachment due to the deficiency in the prediction of the turbulent kinetic energy. Intermittency due to separation is found using Eqn. *4.51*.

$$\gamma_{sep} = min\left(s_1\, max\left[0, \left(\frac{Re_v}{3.235 Re_{\theta c}}\right) - 1\right] e^{-\left(\frac{R_T}{20}\right)^4}, 2\right) F_{\theta t} \qquad 4.51$$

The size of the separation bubble has been adjusted to the constant $s_1 = 2.0$ as in [79]. The effective intermittency, γ_{eff}, is the highest intermittency when comparing the original intermittency to the intermittency due to separation as in Eqn. 4.52.

$$\gamma_{eff} = max(\gamma, \gamma_{sep}) \qquad 4.52$$

The transport equation for the transition momentum thickness Reynolds number $\check{R}e_{\theta t}$ is given in Eqn. 4.53.

$$\begin{aligned} \frac{D\check{R}e_{\theta t}}{Dt} &= \frac{d\left(\check{R}e_{\theta t}\right)}{dt} + \frac{d}{dx_j}\left(U_j \check{R}e_{\theta t}\right) \\ &= P_{\theta t} + \frac{d}{dx_j}\left[\sigma_{\theta t}\left((v + v_t)\frac{d\check{R}e_{\theta t}}{dx_j}\right)\right] \end{aligned} \qquad 4.53$$

Where the source term $P_{\theta t}$, Eqn. 4.54, includes a time scale t, Eqn. 4.55.

$$P_{\theta t} = c_{\theta t}\frac{\rho}{t}\left(Re_{\theta t} - \check{R}e_{\theta t}\right)(1.0 - F_{\theta t}) \qquad 4.54$$

$$t = \frac{500\mu}{\rho U^2} \qquad 4.55$$

The source term is designed so that inside the boundary layer the blending function $F_{\theta t}$, Eqn. 4.56, is equal to one, turning it off, and in the free stream it is equal to zero, enabling it.

$$\begin{aligned} F_{\theta t} = min\Bigg(max\Bigg(&F_{wake} e^{-(y/\delta)^4}, 1.0 \\ &- \left(\frac{\gamma - 1/C_{\varepsilon 2}}{1.0 - 1/C_{\varepsilon 2}}\right)^2\Bigg), 1.0\Bigg) \end{aligned} \qquad 4.56$$

Where, F_{wake} assures that the blending function is activated in the wake regions downstream of the airfoil, Eqn. 4.57 [80].

$$F_{wake} = e^{-\left(\frac{Re_\omega}{1x10^5}\right)^2} \quad 4.57$$

The additional correlations are given in Eqns. *4.58* to *4.61*.

$$\delta = \frac{50\Omega y}{U}\delta_{BL} \quad 4.58$$

$$\delta_{BL} = \frac{15}{2}\theta_{BL} \quad 4.59$$

$$\theta_{BL} = \frac{\check{R}e_{\theta t}\mu}{\rho U} \quad 4.60$$

$$Re_\omega = \frac{\rho\omega y^2}{\mu} \quad 4.61$$

The model constants for the transition momentum thickness Reynolds number are $c_{\theta t} = 0.03, \sigma_{\theta t} = 2.0$ as in [80]. The model includes three empirical correlations, the first two were given in Eqns. *4.49* and *4.50*, and the other is, $Re_{\theta t}$, the transition onset as observed in experiments, Eqn. *4.62*.

$$Re_{\theta t} = f(Tu, \lambda_\theta) \quad 4.62$$

The exact value of these correlations are given in [80].

Currently the transition model in ANSYS CFX can only be used with the *SST* turbulence model and not the $k-\epsilon$ and $k-\omega$ turbulence models. The transition model interacts with the *SST* turbulence model, through the production term of the turbulent kinetic energy, Eqn. *4.63*, and destruction term, Eqn. *4.64*.

$$\check{P}_k = \gamma_{eff} P_k \quad 4.63$$

$$D_k = \min\left(\max\left(\gamma_{eff}, 0.1\right), 1.0\right) D_{k\,orig} \quad 4.64$$

The intermittency interacts directly with the production term of the turbulent kinetic transport equation, whereas the production term of the dissipation rate equation is not

modified. The transition model implementation also effects the blending function, Eqn. *4.65*, which needs the correlations of Eqn. *4.66*. .

$$F_1 = \max(F_{1\,orig}, F_3) \tag{4.65}$$

$$F_3 = e^{-\left(\frac{\rho y\sqrt{k}}{\mu}\frac{1}{120}\right)^8} \tag{4.66}$$

The original blending function is modified to ensure that the $k-\omega$ model is active in the laminar boundary layer, $F_1 = 1.0$. The default production term for this model, when the transition model is used in ANSYS CFX is given in Eqn. *4.67*, this imposes the Kato-Launder modification to the production term [67].

$$P_k = v_t S\Omega \tag{4.67}$$

This replaces the production term to be a function of the magnitude of the strain rate and vorticity rate, as the vorticity rate is nearly irrotational near a stagnation point, allowing it to turns off the overproduction of turbulence outside of a boundary-layer and wake.

5. SIMPLE RADIAL EQUILIBRIUM ANALYSIS

Satisfying simple radial equilibrium through a free-vortex condition is a superficially attractive choice for axial-flow turbine designs as a velocity diagram approach can be taken to solve for the flow variables. The derivation of the free-vortex condition needed to satisfy radial equilibrium equation is demonstrated in [41] [81] [82] [83]. For simple radial equilibrium to hold, we assume constant streamlines, the pressure gradient must balance the centrifugal forces of the rotating fluid and the radial distribution of the enthalpy and entropy must be constant at the inlet and outlet planes of interest giving Eqn. *5.1*.

$$\frac{1}{\rho}\frac{\partial P}{\partial r} = \frac{V_\vartheta^2}{r} \tag{5.1}$$

Where, V_ϑ is the tangential or circumferential velocity, r is the radius, and the viscous forces are neglected. The axisymmetric solution is coupled with a constant axial velocity,V_Z, and constant angular momentum, Eqn. *5.2*, to give a free-vortex flow or a flow with no axial vorticity component.

$$rV_\vartheta = constant \tag{5.2}$$

In this design the work done per unit mass of gas is equal at all radii, while the radial velocity, V_r, along the span is negligible. The flow in the annular passage can be thought to be two-dimensional in the sense that there is no radial component of velocity, although the variation in blade speed, ϑ_r, which is inversely proportional to the radius, Eqn. *5.3*, is accounted for, hence why only a mean-line analysis is not applicable.

$$\vartheta_r = r\omega_a \quad (5.3)$$

Where, ω_a is the rotational speed of the rotor in rad/s.

Radial equilibrium obtained through a free vortex condition enables radial variation in flow angles, flow coefficients, degree of reaction, and blade loading coefficient in the design through vortex blading starting with a mean-line analysis. This method does not account for loss of stagnation pressure due to secondary flow loss, endwall boundary layer flows, tip clearance flows, and wake losses. To account for the losses empirical formulas have been derived from blade section performance characteristics, but such empiricism is usually only applicable to a very limited range of machines, usually only those for which they were derived for.

At the design point the flow at the nozzle inlet and rotor exit are completely axial, giving no swirl component ($\alpha_1 = \alpha_3 = 0$). This is just one of many possible conditions, but one that is desirable for a single-stage turbine. The current annular configuration has a casing diameter of 500-mm and hub diameter of 350-mm with a uniform inlet velocity, V_1, of 4.47 m/s at 20°C ($\rho = 1.205$ kg/m^3). The flow exits the nozzle midline exit plane at an absolute flow angle (α_2) of 67.4°, and the rotor angular velocity is 402 revolutions per minute (RPM). The nozzle analysis is conducted in the absolute frame of reference, whereas the rotor analysis is conducted in the relative frame of reference considered to be stationary relative to the rotor blades, allowing the flow to appear steady. Figure 14 shows the cross-sectional view and velocity triangles for the single stage axial turbine with the nomenclature employed.

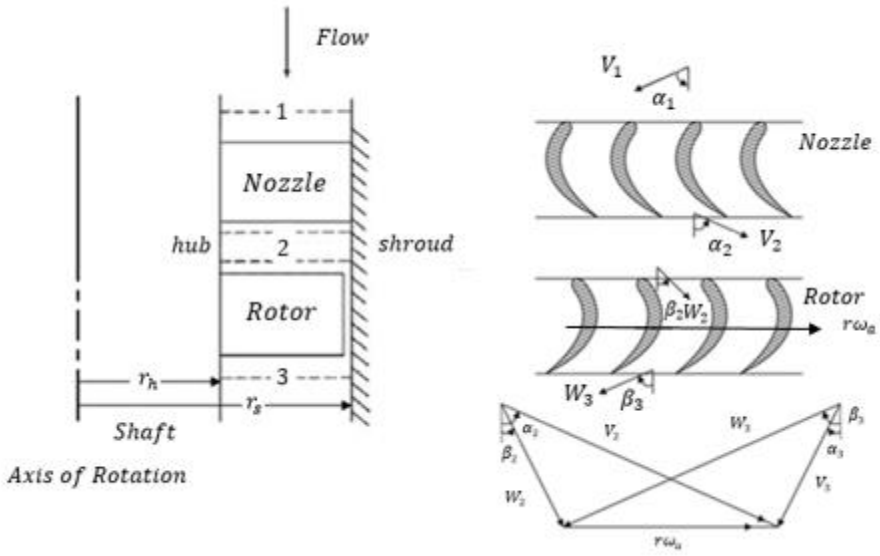

(a) *(b)*

Figure 14: Single stage Axial Turbine (a) Cross-sectional view and (b) Velocity Triangles

For the mean line tangential velocity to be determined the mean radius, r_m, is taken as the average of the tip radius, r_t, and the hub radius, r_h, Eqn. 5.4. The tip and hub radii are used to determine the nozzle and rotor blade heights, H, Eqn. 5.5.

$$r_{mid} = \frac{1}{2}(r_{tip} + r_{hub}) \tag{5.4}$$

$$H = r_{tip} - r_{hub} \tag{5.5}$$

With the mean radius determined the midline parameters for the flow coefficient, loading coefficient, reaction ratio, rotor relative inlet and outlet flow angle are found using Eqns. 5.6 through 5.10, respectively.

$$\phi_{mid} = \frac{V_Z}{U_{mid}} \tag{5.6}$$

$$\psi_{mid} = \phi_{mid} \tan \alpha_{2,mid} \tag{5.7}$$

$$Rr_{mid} = 1 - \frac{1}{2}\phi_{mid} \tan \alpha_{2,mid} \tag{5.8}$$

$$\beta_{2,mid} = \tan^{-1}(\tan \alpha_{2,mid} - \frac{U_{mid}}{V_Z}) \quad 5.9$$

$$\beta_{3,mid} = \tan^{-1}(\tan \alpha_{3,mid} - \frac{U_{mid}}{V_Z}) \quad 5.10$$

Now, the radial variations of the flow angles, velocity, reaction, loading and flow coefficient distributions can be determined. This analysis gives rise to the following equations for calculation of the radial distribution of the absolute flow angle at the nozzle exit, relative flow angles at the rotor inlet and outlet, flow coefficient, loading coefficient, and reaction ratio using Eqns. *5.11* to *5.16*.

$$\alpha_2 = \tan^{-1}(\frac{r_{mid}}{r}\tan \alpha_2) \quad 5.11$$

$$\beta_2 = \tan^{-1}\left(\tan \alpha_2 - \frac{\vartheta_r}{V_Z}\right) \quad 5.12$$

$$\beta_3 = -\tan^{-1}(\tan \alpha_3 - \frac{\vartheta_r}{V_Z}) \quad 5.13$$

$$\phi = \frac{V_Z}{\vartheta_r} \quad 5.14$$

$$\psi = \phi \tan \alpha_2 \quad 5.15$$

$$Rr = 1 - \frac{1}{2}\phi \, tan \, \alpha_2 \quad 5.16$$

Figure 15 and Figure 16 show the variation of flow coefficients and flow angles along the radial span of the blades based on the simplified fundamental equations for this particular turbine stage setup. These are nearly identical to those presented in *Table 2*.

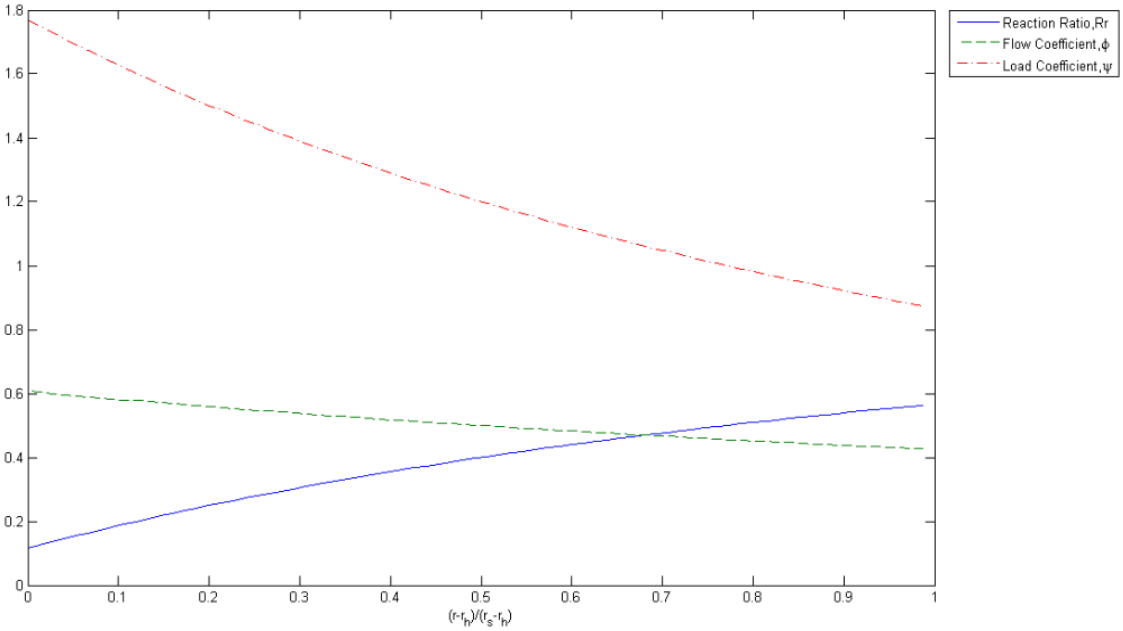

Figure 15: Variation of coefficients along blade span

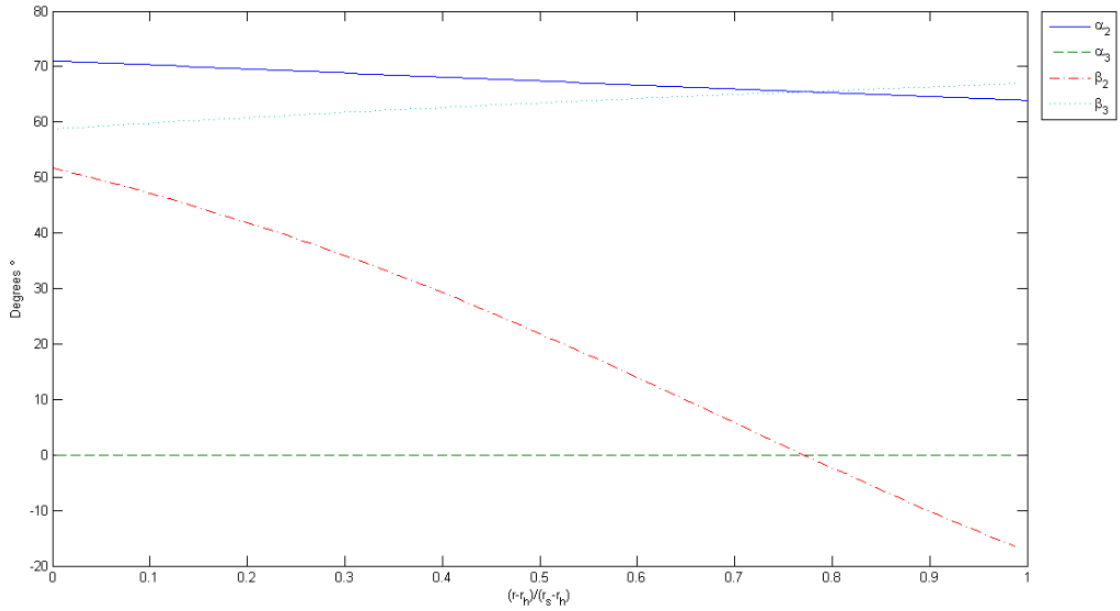

Figure 16: Variation of flow angles along blade span

With the axial velocity assumed constant over the annulus, the radial distributions of velocities at the rotor inlet and outlet can be determined with Eqns. *5.17* to *5.20*.

$$V_2 = \frac{V_Z}{\cos(\alpha_2)} \qquad 5.17$$

$$V_3 = \frac{V_Z}{\cos(\alpha_3)} \tag{5.18}$$

$$W_2 = \frac{V_Z}{\cos(\beta_2)} \tag{5.19}$$

$$W_3 = \frac{V_Z}{\cos(\beta_3)} \tag{5.20}$$

Where the average velocities are calculated from the flow variations from hub to tip. The average absolute nozzle exit velocity and average relative rotor exit velocity are calculated in Eqns. *5.21* and *5.22*, respectively.

$$V_{2,Avg} = \int_{\alpha_{2,r_h}}^{\alpha_{2,r_s}} \frac{V_Z}{\cos(\alpha_2)} d\alpha_2 \tag{5.21}$$

$$W_{3,Avg} = \int_{\beta_{2,r_h}}^{\beta_{2,r_s}} \frac{V_Z}{\cos(\beta_3)} d\beta_2 \tag{5.22}$$

The absolute and relative velocities at all the other stations can be calculated in a similar manner.

The validity of the results obtained with this method can be compared directly to those of the experiment and design values given by Matsunuma [24]. First, the mid-span absolute and relative velocities can be compared to the mid-span design velocities shown in *Table 4*. Next, *Table 5* compares the average absolute and relative velocities before and after the blade rows to the experimental values. The mid-span design values are nearly identical, while all the design values are within 10% of the experimental values.

Table 4: Design velocity at mid-span

Mid-span Velocity	Simple Radial Equilibrium through a Free Vortex Condition Design (m/s)	Design Velocity as given by Matsunuma [24] (m/s)
V_1	4.47	4.47
V_2	11.63	---
V_3	4.47	---
W_2	4.83	---
W_3	9.98	9.99

Table 5: Design velocity

Average Velocity	Simple Radial Equilibrium through a Free Vortex Condition Design (m/s)	Experimental Velocity as given by Matsunuma [24] (m/s)
V_1	4.47	---
V_2	11.75	10.7
V_3	4.47	---
W_2	5.22	---
W_3	9.99	9.27

The Euler equation for a turbomachine relates the power extracted in terms of the flow characteristics. Here the power is the rate at which work is done, Eqn. *5.23*.

$$\dot{w} = \dot{m}w \qquad 5.23$$

The simple radial equilibrium with a free vortex condition delivers constant work at all radii. The specific work output is the work done by the fluid on the rotor per unit mass, given from the classical Euler energy equation, Eqn. *5.24*, simplified to acknowledge the constant axial velocity.

$$w = \vartheta_r V_Z tan\alpha_2 \qquad 5.24$$

The specific work and power delivered by the turbine stage is shown in *Table 6*. This analysis of a free-vortex condition to satisfy radial equilibrium is essential in determining the design characteristics of the single-stage axial-flow turbine.

Table 6: Specific work and power delivered by turbine stage

	Specific Work ($\frac{J}{kg}$)	Power ($\frac{J}{s}$)
Mid-span	96.06	51.81
Average	96.06	51.81

6. NUMERICAL APPROACH

The numerical approach consists of three main phases: geometry creation, mesh generation and CFD modeling. The geometry creation phase involves creating the computational domain using the three-dimensional computer-aided design (CAD) software SolidWorks. The mesh generation uses the exported CAD file to create discrete points in the domain, done in ANSYS ICEM CFD. Lastly, the CFD modeling is accomplished with the commercial package ANSYS CFX.

6.1. Geometry Creation

The first step in any CFD analysis is geometry creation of the computational flow domain. The flow domain is the invisible volume in which the flow takes place, built around the turbine cascade specifications given in *Table 2*. The fluid domain for the single stage low Reynolds number turbine begins 30-mm upstream from the nozzle mid-spans leading edge and ends 117.98-mm downstream of the rotors trailing edge mid-span. The inlet is positioned at the same location where the inlet flow conditions were measured and the outlet distance is chosen to prevent back flow at the downstream outlet boundary.

The Whole Flow Domain is divided into three sections: Nozzle Flow Domain, Rotor Flow Domain, and Downstream Flow Domain. These flow domains are stationary, rotating, and stationary, respectively. To reduce the computational effort, only a section of the full geometry for each domain is modeled. It is assumed that all the nozzle and rotor airfoils are identical so that the computational domain only consists of one stator and one rotor blade channel. Since the flow is repeated, the flow field is solved for in a single

passage with periodic boundary conditions in the pitch-wise direction giving 12.857° and 11.613° degree sections for the stator and rotor/downstream flow domains, respectively. This results in a stator/rotor pitch ratio at the interface equal to 1.107. The downstream flow domain has a pitch ratio of 1.0 with the rotor flow domain.

The three-dimensional modeling is based on the actual tip and hub geometry used in the experiments to fully define the nozzle and rotor airfoils. The nozzle and rotor airfoil geometry are given from LDV measurements obtained from the experimental results by Matsunuma [24]. These LDV measurements supply the airfoil X, Y, and Z coordinates at the hub and shroud along the annulus. These coordinates are not sufficient to properly define the airfoil geometries, so more points had to be generated to increase the accuracy of the model, utilization of Microsoft Excel and MATLAB programs was essential to fully define the CAD model in SolidWorks. In order to reduce the geometry error author refers the readers to Matsunuma [84], which gives three-dimensional coordinates along the airfoils suction and pressure surface at different spanwise planes.

Microsoft Excel is used to read the coordinates of the airfoils supplied. This program is also an invaluable tool that can allow the data to be formatted as a Macro in order to interface with SolidWorks. It is also a very strong tool as it allows for topological parameterization. The X, Y and Z coordinates are inserted into a Microsoft Excel file that contains the Macro, Figure 17. After the coordinates are inserted and a new part document is opened in SolidWorks, the ‘Create 3D Points’ is selected to start the Macro, importing the points into SolidWorks. The imported points in SolidWorks are shown in Figure 18. These are the reduced coordinates for just one rotor and stator blade section. The nozzle airfoil only has hub and casing points, whereas the rotor airfoil only has hub and tip points.

As stated before, these are not sufficient to fully define the airfoil profiles. Thus a MATLAB M-file is used to create additional points at 25%, 50%, and 75% of the airfoil span. The additional points needed to fully define the profiles of the airfoils are shown in Figure 19, along with the original points. The axial chord and gap measurements in SolidWorks are within one-tenth of those given in *Table 2*.

	A	B	C	D	E	F	G	H	I	J	K	L	M	N	O
1	-174.473	179.0509	-47.9523												
2	-174.84	178.6925	-47.869												
3	-175.099	178.439	-47.6973												
4	-175.342	178.2003	-47.4322												
5	-175.569	177.9763	-47.0694												
6	-175.777	177.7707	-46.605				Copy and paste your x, y, z data into the first 3 columns of this								
7	-175.96	177.5892	-46.0359		Create 3D Points		spreadsheet								
8	-176.112	177.4388	-45.3598												
9	-176.224	177.328	-44.5755				NOTE: Have a part document open in SolidWorks before clicking								
10	-176.286	177.2659	-43.6831		Create 3D Lines		either of the 2 buttons								
11	-176.288	177.2644	-42.6289												
12	-176.155	177.396	-40.9606				The macro will create a new 3D sketch containing either points or								
13	-175.879	177.6697	-39.3016				lines.								
14	-175.476	178.0677	-37.6634		Create 2D Points										
15	-174.959	178.5762	-36.0532												
16	-174.336	179.1839	-34.4756				The 2D Options will ignore values in the C Column and create a sketch on the Front Plane								
17	-173.616	179.8815	-32.9324												
18	-172.805	180.661	-31.4239		Create 2D Lines										
19	-171.907	181.5154	-29.9492												
20	-170.927	182.4391	-28.5071												

Figure 17: Macro formatted in Excel sheet

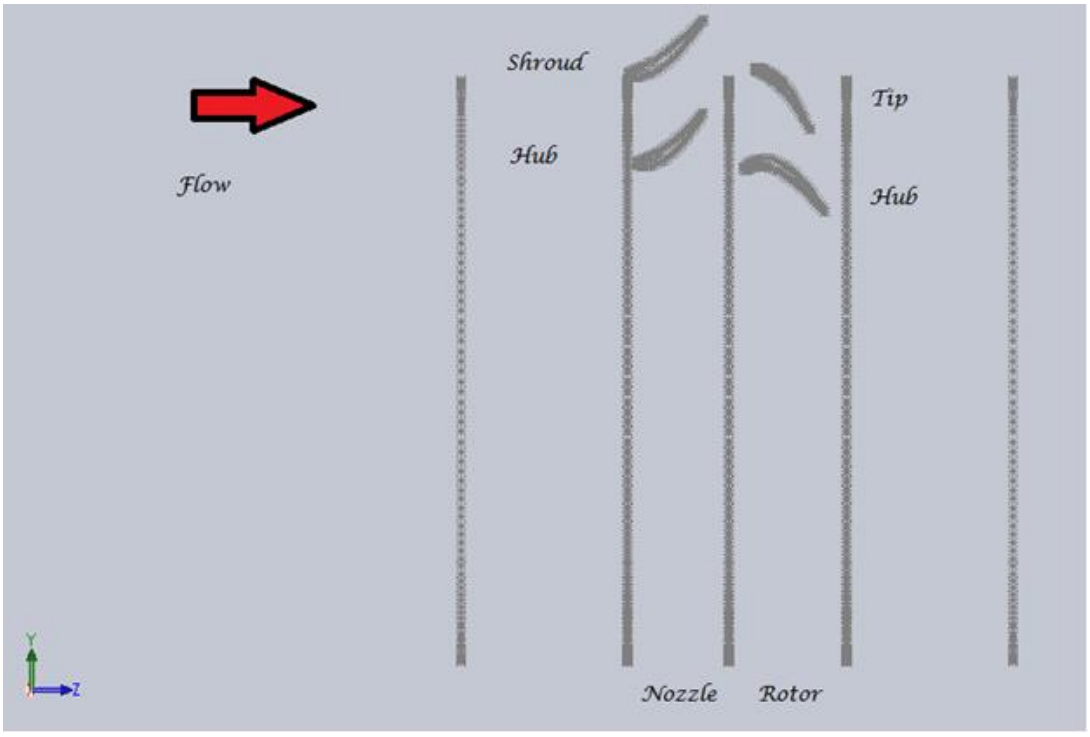

Figure 18: Original imported points

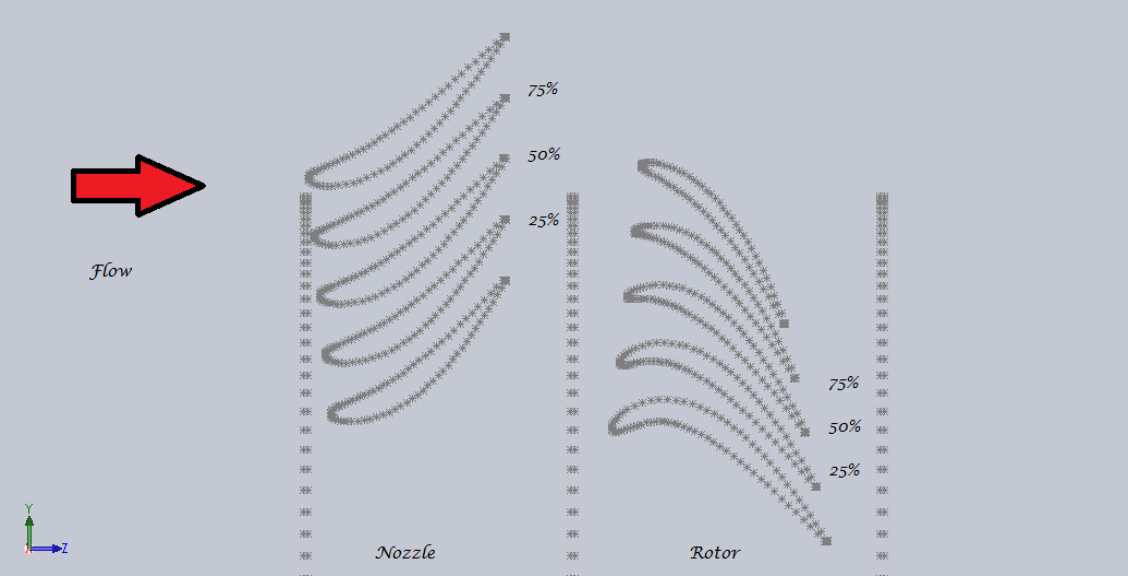

Figure 19: Nozzle and rotor airfoil span-distribution

Once the points are imported into a SolidWorks part file they are turned into curves at each span for both airfoils. The curves are interconnected at the leading and trailing edges with a 3D line. The 'Boundary Boss/Base' feature in SolidWorks is then used to create the high quality airfoils, Figure 20. The nozzle and rotor airfoil geometries allow for the internal fluid flow domain to be extracted for further analysis. This provides the computational domain in which the governing equations are solved. The flow domain is made using a pre-existing flow domain for a similar design made using ANSYS BladeModeler. A 'Boolean' command is used to subtract the airfoils area from the flow domain. The hub and shroud radii had to be adjusted due to the points of the fluid domain and airfoil being so close. They were adjusted to 175.005-mm at the hub and 249.995-mm at the shroud, they are within one-one hundredth of those given in *Table 2*. The complete computational domain is shown in Figure 21, with the axial dimensions provided. The SolidWorks files are saved in a '.x_t' file format, better known as a parasolid format, for importing into ANSYS ICEM CFD.

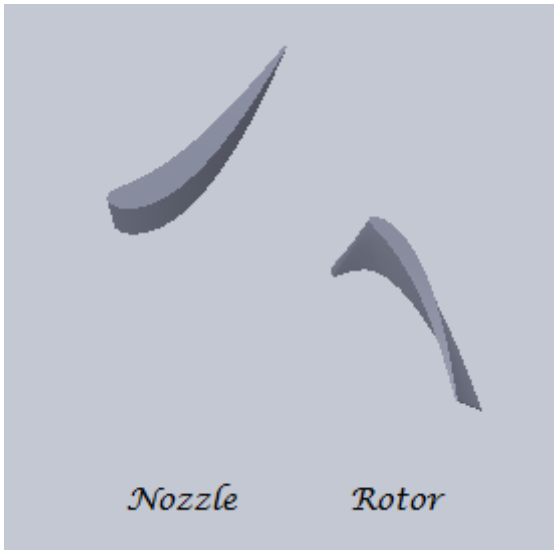

Figure 20: SolidWorks nozzle and rotor airfoils geometries

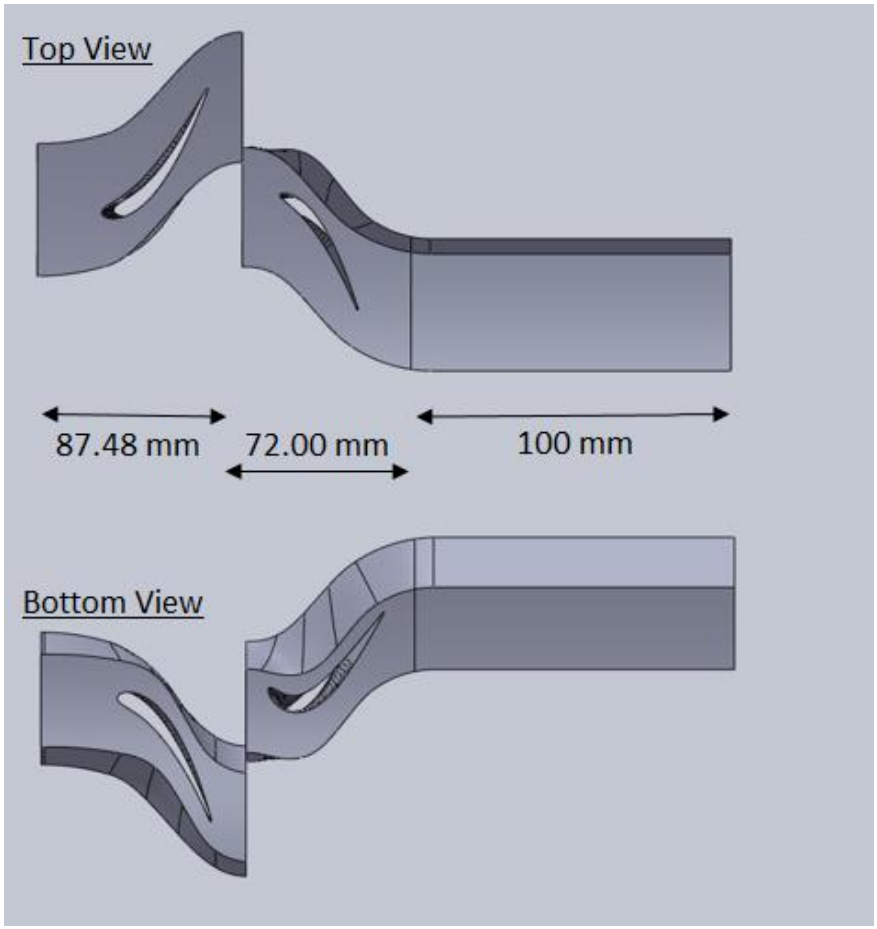

Figure 21: Complete computational domain

6.2. Mesh Generation

In this study the commercial mesh generation program ANSYS ICEM CFD (ver. 13) is used to generate the mesh. ANSYS CFX requires that the computational mesh be of high quality, where the acceptable range requires that the orthogonality angle be greater than 20°, maximum expansion factor be less than 20, and maximum aspect ratio be less than 1,000 for double precision [84]. For complicated geometries such as the present nozzle and rotor computational domains a great deal of planning and creativity is needed in order to not only produce a quality hexahedral mesh, but to also keep the total element count low while still ensuring that key locations in the domain are highly resolved. The ω based turbulence models are suitable for a low Reynolds near wall approach that resolves the viscous sublayer [84]. To satisfy the low Reynolds near wall approach the $Y^{+}\sim 1$ criterion should be satisfied for the endwalls, blade surfaces, and tip clearance, this approach refers to the turbulent Reynolds number not the flow Reynolds number. The radial stacking of the airfoil and tip clearance of the rotor provide a significant challenge in producing a production-quality mesh. A high mesh quality is important to resolve the complex flow phenomena.

The near wall fine mesh and the complex domain features make the standard ICEM-Tetra/Prism unstructured mesh impractical due to its high element count. The entire geometry is meshed using ICEM-HEXA to generate ordinary hexahedral grids, assembled following a structured multi-block strategy. The nozzle and rotor blocking was achieved through an H-grid with an O-grid wrapping around the airfoil, for boundary layer resolution. Figure 22 shows the block topology employed for the nozzle and rotor computational domains. The downstream domain uses a simple blocking scheme. The

structured multi-block meshes are converted into an unstructured hexa mesh for use within ANSYS CFX.

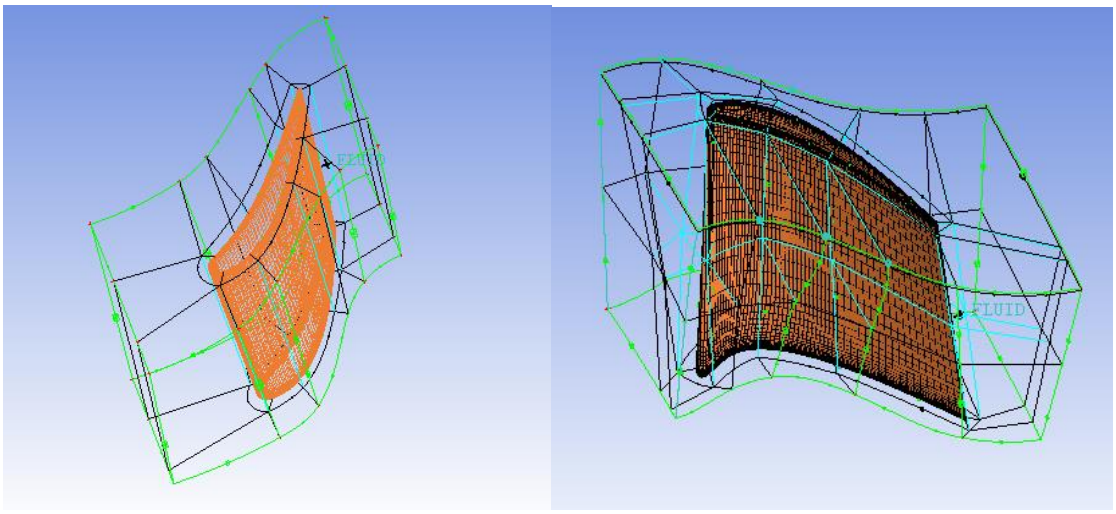

(a) Nozzle (b) Rotor

Figure 22: Block topology

A challenging step using structured spectral elements is to provide appropriate coarsening away from the boundary layer flow. The current strategy involves coarsening structures away from the boundary layer flow, while having conforming meshes near the blade surfaces, endwalls, and tip clearance. The near wall mesh refinement depends on the turbulence model used, where a minimum of 15 nodes inside the boundary layer are necessary for a low-Reynolds near wall formulation and 10 nodes for wall functions [84]. In CFX, the laminar model uses the law of the wall, $k-\varepsilon$ based turbulence models use scalable wall functions, and $k-\omega$ based turbulence models use the automatic near-wall treatment to model the boundary layer flow [84]. The automatic-near wall treatment has the advantage of switching from a wall function formulation to a low-Reynolds near wall formulation as the mesh is refined [84]. The dimensionless parameter Y^+, Eqn. 6.1, is used to check the location of the first node from the wall.

$$Y^+ = \frac{\Delta y}{\nu}\sqrt{\frac{\tau_w}{\rho}} \qquad 6.1$$

where, $\tau_w$is the wall shear stress.

A high-resolution mesh is necessary to capture the flow behavior present. In order to allow the mesh to naturally coarsen away from the endwalls and blade surfaces, the exponential distribution is used so that a portion of the finer mesh at the endwalls is self-contained. For the streamwise and pitch-wise distributions a geometric distribution is used. For the present study, a significant savings on the total element count was achieved compared to the unstructured mesh approach. Figure 23 shows the computational mesh at different views for the lowest mesh count; some of the boundaries are removed for clearness.

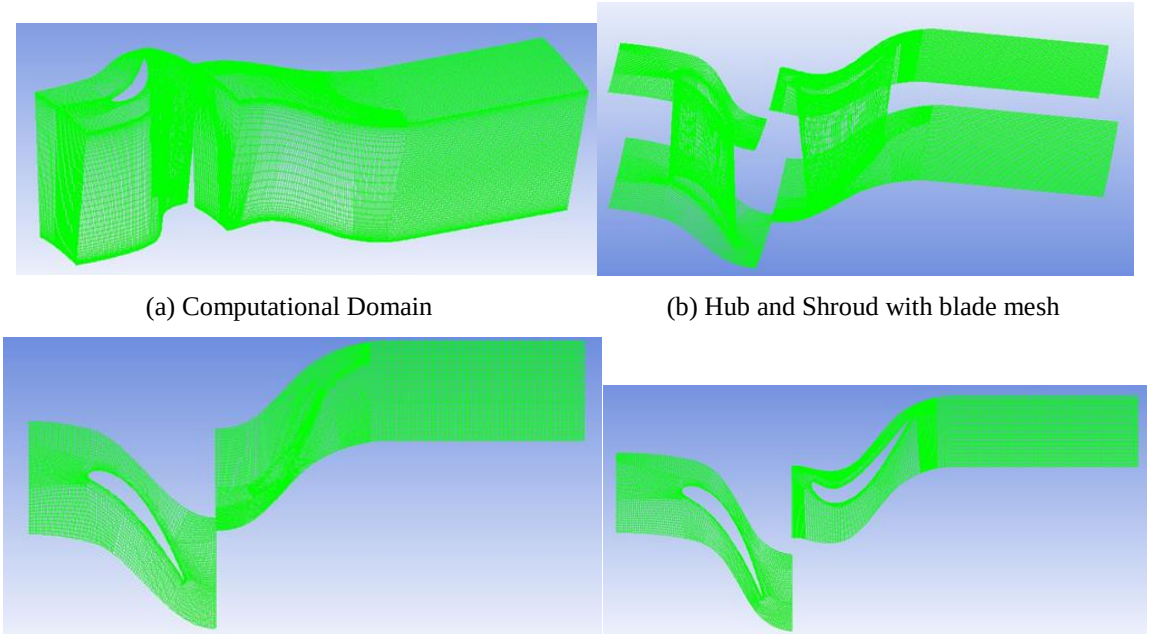

(a) Computational Domain (b) Hub and Shroud with blade mesh

(c) Casing (d) Hub

Figure 23: Multiple views of computational mesh

Five meshes, namely: M1, M2, M3, M4, and M5, were used to optimize the grid using a total element size ranging from 1.28 to 6.91 million. *Table 7* gives the element size

for the individual computational domains and the total element count. The different meshes were obtained using a systematic mesh refinement of the initial mesh, M1. Average Y^+ values on the hub, shroud, tip, and blade surface for the five meshes considered are given in *Table 8*, *Table* 9, and *Table 10*. It should be noted that only small changes in the values of Y^+ occurred as the total number of elements in the mesh increased. It was found that a number of cells in the range of 6.91 million gives satisfactory results when compared to the experimental findings. Therefore, the maximum total number of elements was limited to 6.91 million to compromise between the refinement level, mesh quality, and computer capability.

Table 7: Mesh element size variation

Mesh	Elements for Nozzle Computational Domain	Elements for Rotor Computational Domain	Elements for Downstream Computational Domain	Total number of Elements
M1	373,000	522,000	382,000	1,280,000
M2	848,000	1,060,000	766,000	2,670,000
M3	1,260,000	1,670,000	1,160,000	4,080,000
M4	1,720,000	2,310,000	1,530,000	5,560,000
M5	2,130,000	2,820,000	1,960,000	6,910,000

Table 8: Nozzle computational domain Y^+ parameters

Mesh	Average Y^+ on Blade	Average Y^+ on Hub	Average Y^+ on Shroud
M1	2.199 e-01	3.242 e-01	3.091 e-01
M2	3.440 e-01	3.329 e-01	3.162 e-01
M3	2.287 e-01	3.288 e-01	3.113 e-01
M4	3.186 e-01	3.346 e-01	3.180 e-01
M5	3.438 e-01	3.352 e-01	3.188 e-01

Table 9: Rotor computational domain Y^+ parameters

Mesh	Average Y^+ on Blade	Average Y^+ on Hub	Average Y^+ on Shroud	Average Y^+ on Blade Tip
M1	3.766 e-01	4.778 e-01	6.263 e-01	9.004 e-01
M2	3.236 e-01	3.757 e-01	4.957 e-01	8.802 e-01
M3	4.709 e-01	3.823 e-01	4.988 e-01	9.091 e-01
M4	3.495 e-01	3.184 e-01	5.021 e-01	6.176 e-01
M5	3.462 e-01	3.193 e-01	5.022 e-01	6.117 e-01

Table 10: Downstream computational domain Y^+ parameters

Mesh	Average Y^+ on Hub	Average Y^+ on Shroud
M1	2.459 e-01	2.681 e-01
M2	2.210 e-01	2.548 e-01
M3	2.240 e-01	2.571 e-01
M4	2.232 e-01	2.566 e-01
M5	2.241 e-01	2.558 e-01

The quality of the mesh is of great importance for the convergence and accuracy of the numerical solution. The average solver mesh statistics are shown in ***Table 11***, where

the mesh quality is divided into three levels: **OK** (good), **ok** (acceptable), and **!** (poor). The poor quality of the meshes was attributed to the complex meshing of the trailing edge, tip clearance, and blade radial stacking. For the most part the five computational domains have a good mesh quality.

Table 11: Average solver mesh statistics

Computational Domain Name	Minimum Orthogonal Angle (deg)			Maximum Expansion Factor			Maximum Aspect Ratio		
	% !	% ok	%OK	% !	% ok	%OK	% !	% ok	%OK
Downstream	0	0	100	0	<1	100	0	0	100
R1	<1	9	91	1	1	98	0	0	100
S1	0	1	99	<1	<1	100	0	0	100
Global	<1	4	96	<1	1	99	0	0	100

6.3. CFD Modeling

For the CFD modeling, the general-purpose code ANSYS CFX 15 is implemented. ANSYS CFX uses an element-based finite volume [67] technique for solving the three-dimensional Navier-Stokes equations on generally unstructured meshes with an implicit coupled solver. ANSYS CFX as a coupled solver [85] solves for the pressure and velocity simultaneously. Many different turbulence models that complete closure of the RANS equations are available through this software package. For turbulence closure, the computations were performed using the standard $k-\varepsilon$ model of Lauder and Sharma [71], the standard $k-\omega$ model of Wilcox [72], and the shear stress transport (SST) $k-\omega$ model of Menter [73]. These models are tuned to incorporate the empirical curvature correction function of Spalart and Shur [75], which attempts to correct the effect of

streamline curvature and system rotation by acting as a multiplier to the production term of the transport equations. In addition to these turbulence models, the multimode transition model is used, which is suitable for different types of boundary layer transitions such as bypass, wake induced, natural, and separation induce transitions [80]. The application of the two-equation Gamma Theta model with the empirical correlations of Menter and Langtry [80] was considered necessary to capture the separation on the nozzle suction side surface, although in ANSYS CFX it can currently only be coupled with the SST turbulence model. Transition modeling further increases the numerical cost by having to solve two additional transport equations. The laminar model was also considered as most of the nozzle flow is laminar [24], [53]. The five cases considered in this investigation are:

1. No Turbulence ($Laminar\ Flow$)
2. $k-\varepsilon$ Turbulence Model with Rotation/Curvature Correction ($k-\varepsilon-CC$)
3. $k-\omega$ Turbulence Model with Rotation/Curvature Correction ($k-\omega-CC$)
4. Shear Stress Transport (SST) $k-\omega$ Turbulence Model with Rotation/Curvature Correction ($SST-CC$)
5. Shear Stress Transport (SST) $k-\omega$ Turbulence Model with Transition Modeling and Rotation/Curvature Correction ($SST-Transition-CC$)

Different discretization schemes are available, but the ANSYS 'High Resolution' discretization Scheme used for the advection scheme is a bounded second-order upwind based discretization scheme recommended by Menter et al. [79] and Langtry et al. [87] for separated flows with transition modeling, but can be used for a multitude of flows. This scheme is second-order accurate in space but locally reduces to first-order accuracy, where required to avoid non-physical oscillations [84]. The advection scheme for the turbulence

equations also uses the second-order high-resolution advection scheme, and the second-order high-resolution transient scheme [87]. The temporal discretization uses a second-order backward Euler method.

For all the cases, the frozen rotor interfaces allow the steady state solution to be calculated, through a false time step until the convergence criteria is satisfied or the maximum number of iterations is reached. The frozen rotor approach keeps the relative orientation of the components but accounts for the change in reference frame and the equations are scaled based on the pitch change [84]. Transient effects at the frame change are not modeled with a frozen rotor interface; a transient rotor/stator interface is needed. In the transient simulation, the flow shows the transient effects as the flow advances in time by modeling the time-dependent relative position, where inner coefficient loops must also show sufficient convergence for each individual time step. The theory and methods of ANSYS CFX can be found in [67], [85], [87], [88], and [89], while code validation based on experimental results can be found in [90] and their tutorials in [91].

CFD packages are predictive tools for various designs, all with three main stages: pre-processing, solving, and post processing. ANSYS CFX provides a GUI (Graphical user interface) for each of these stages: CFX-Pre, CFX-solve, and CFD-post. The pre-processing stage involves importing the mesh, defining the physics of the model, setting up the B.C.'s and solver parameters. The solving stage is where the solution to the algorithm is obtained, after parallelization and partitioning are implemented. Post-processing allows for evaluation of the results of the solver.

6.3.1. Pre-Processing

For the pre-processing stage it is assumed the mesh has been generated and it only

needs to be imported. After the mesh is imported, the physics of the model are defined with proper B. C's and the solver parameters are set. An advantage that CFX-Pre has is its turbomachinery mode [87], customized for quick setup of turbomachinery simulations, such as compressors or turbines. For the basic setting, an axial turbine is selected for quick setup. The three computational domains are added, where the nozzle and downstream sections are given stationary while the rotor is given a rotating frame of reference. The passages and alignment section is edited as needed to match the turbine cascade specifications, *Table 2*. *Table 12* shows the region information linked for each computational domain, the other pitch-wise surfaces are prescribed with a periodic condition. In order to have one inlet and outlet there are two main interfaces: nozzle outlet to rotor inlet, and rotor outlet to downstream inlet. These are modeled using ANSYS CFX's general grid interface (GGI), allowing unmatched grids to interface together, and multiple frame of reference (MFR) that allows domains to rotate relative to one another [67]. The inlet, outlet, periodic, and interface boundaries are shown in Figure 24, not labeled are the blades, blade tip, hub and shroud boundaries.

Table 12: Region information for computational domains

Region Information	Computational Domain		
	Nozzle	Rotor	Downstream
Inlet	X	X	X
Outlet	X	X	X
Hub	X	X	X
Shroud	X	X	X
Blade	X	X	
Blade Tip[1]		X	

1. Tip clearance at shroud Only

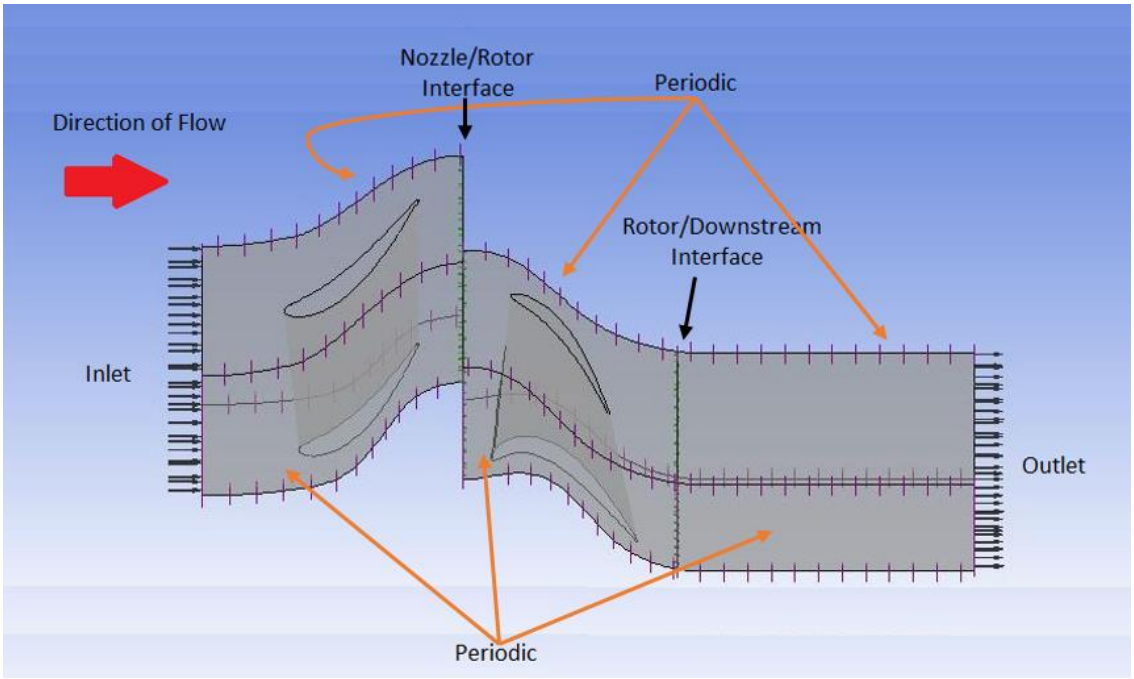

Figure 24: CFX-Pre layout

The flow was modeled as incompressible using air as the working fluid, here heat transfer is neglected, hence the energy equation is not included. The solid boundaries (hub, shroud, and blade) are modeled with adiabatic no-slip boundary conditions. The CFD simulations have been performed with the same inlet conditions as those of the experiments, where the inlet velocity distribution in Figure 9 is multiplied by 4.47 m/s to give the inlet velocity distribution as seen in Figure 25. The rotor is given an angular speed of 402 RPM, with the shroud set as stationary. At the exit, static pressure is specified as the outlet boundary condition. A steady-state simulation is the preferred choice for a stationary gas turbine operating at a constant load [89]. *Table 13* summarizes the general settings for the steady state solutions. The use of the different meshes is needed to determine the spatial discretization error associated with the numerical results.

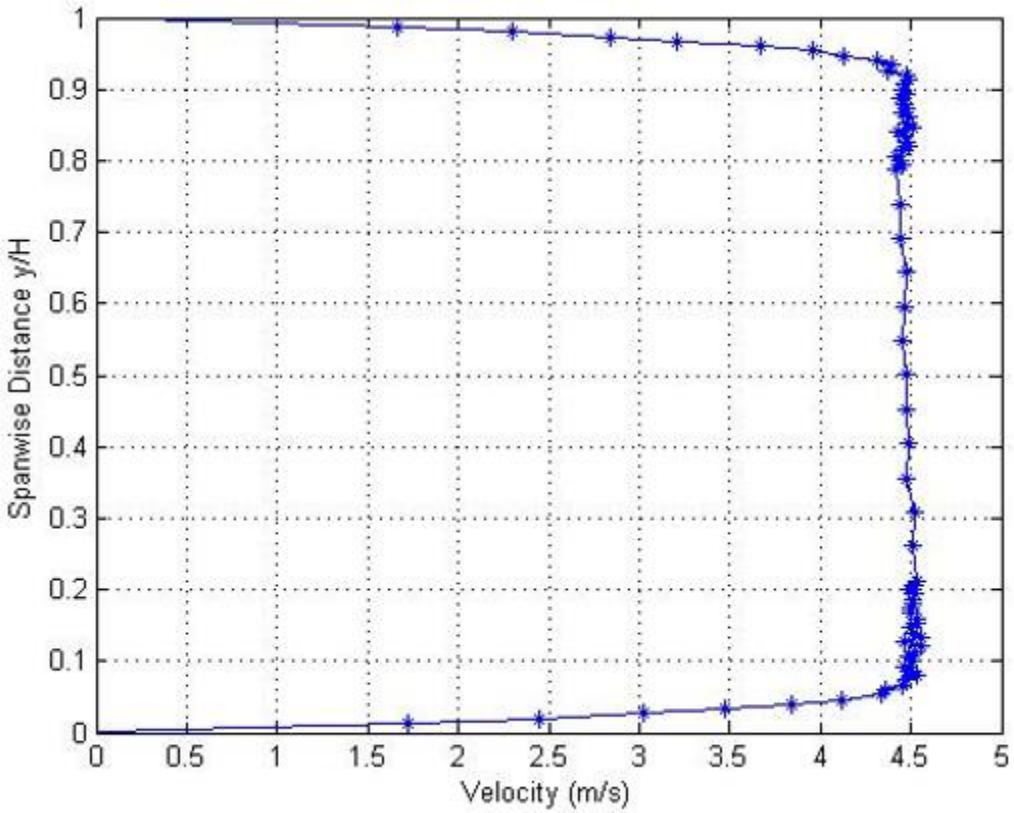

Figure 25: Inlet velocity distribution

Table 13: General settings used for steady state CFD models

Analysis type	Steady State
Turbulence Cases	$Laminar\ Flow$ $k-\varepsilon-CC$ $k-\omega-CC$ $SST-CC$ $SST-Transitional-CC$
Wall function	None for $Laminar\ Flow$ Scalable for ε based models Automatic for ω based models
Heat Transfer	None
Advection scheme	High Resolution
Turbulence Numerics	High Resolution
Timescale control	Auto-timescale
Convergence criteria: Residual type Residual target Iterations	 RMS Less than 1E-3 500
Interfaces	Frozen Rotor
Flow Specifications	Cylindrical components in axial direction
Fluid	Air at 20℃
Inlet: Velocity Turbulence intensity	 Inlet velocity distribution per Figure 25 Low (1%)
Rotor rotational speed	402 [RPM]
Outlet: Static Gauge Pressure	 0 [atm]
Wall boundaries: Mass and momentum Wall roughness Heat transfer	 No-slip wall Smooth wall Adiabatic

The transient simulation is begun from the converged steady-state simulation, where different time steps are needed to calculate the temporal discretization error. *Table 14* shows the additional settings needed for the transient solution, where the time duration accounts for ten rotor pitch revolutions. The transient solution is obtained for the steady state case that best exploits the three-dimensional nature of the flow field within the axial-turbine operating at a low Reynolds number, determined by how well it fits the experimental data. The transient results are time-averaged by collecting data at a fixed interval pertaining to ten time-steps.

Table 14: General settings used for transient CFD model

Analysis type	Transient
Transient scheme	Second-Order Backward Euler
Time Duration	4.8146e-2 [s]
Time steps	1.55311e-4 [s] 8.75389e-5 [s] 4.81464e-5 [s]
Inner Loop Convergence criteria: Residual type Residual target Coefficient Loops	 RMS Less than 1E-3 10
Interfaces	Transient Rotor/Stator

6.3.2. CFX-Solver

The parallel solver is used in 'double precision', i.e. double precision floating-point format, where the parallel solver uses a node-based partitioning [84]. The default MeTiS partitioning package is used with the additional details shown in *Table 15*. The partitioning

overlap should be ideally less than 10% and not exceed 20% [84]. *Table 16* shows that the partitioning implemented satisfies the overlap requirement.

Table 15: MeTiS partitioning detail

MeTiS Type	k-way
Multidomain Option	Coupled Partitioning
Multipass Partitioning: Steady-State Transient	 None Transient Rotor Stator

Table 16: Solver detail of mesh partitioning

Mesh	Partitioning Number	Vertices Overlap %			
		Minimum	Maximum	Average	Sum
M1	12	5.8	10.2	8.1	8.1
M2	16	5.0	8.5	7.1	7.1
M3	16	4.2	9.6	6.4	6.4
M4	24	4.6	10.4	7.8	7.8
M5	24	4.6	9.3	7.3	7.3

6.3.3. CFD-Post

CFD-Post's unique turbo plots mode allows for efficient post-processing of the numerical data. Turbo plots allows mass flow averaging of spanwise planes at constant-streamwise coordinates, mass flow averaging at uniform distances from hub to shroud, and circumferential sampling at a selected streamwise and spanwise location. These tools were essential for calculation of the discretization errors. CFD-Post also allows for graphical outputs, Figure 26 shows the nozzle and rotor exit spanwise outlet planes where direct

comparisons to the experimental data is conducted. The nozzle and rotor exit planes correspond to a normalized streamwise location of 0.9075 and 1.8320, respectively.

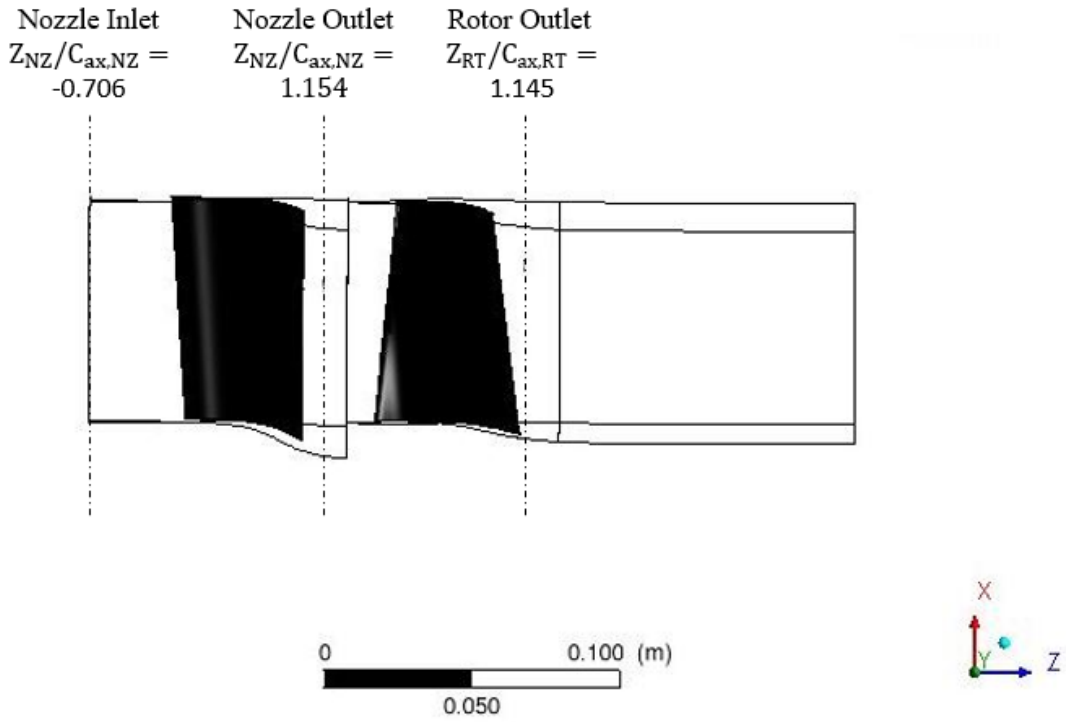

Figure 26: Data extraction planes for comparison with experimental data

Turbo Plots calculates velocity components in a multitude of ways that are ideal for turbomachinery flows. Figure 27 shows the velocity components with a nomenclature that is of the same type as the experimental data, essential in the calculation of the absolute and relative flow angles. The meridional plane velocities calculate the velocity magnitude as shown in Eqn. 6.2.

$$V = \sqrt{V_m^2 + V_\vartheta^2} = \sqrt{V_z^2 + V_r^2 + V_\vartheta^2} \qquad 6.2$$

The absolute and relative flow angles are calculated through Eqn. 6.3.

$$\cos(\alpha) = \frac{V_\vartheta}{\sqrt{V_z^2 + V_\vartheta^2}} \qquad 6.3$$

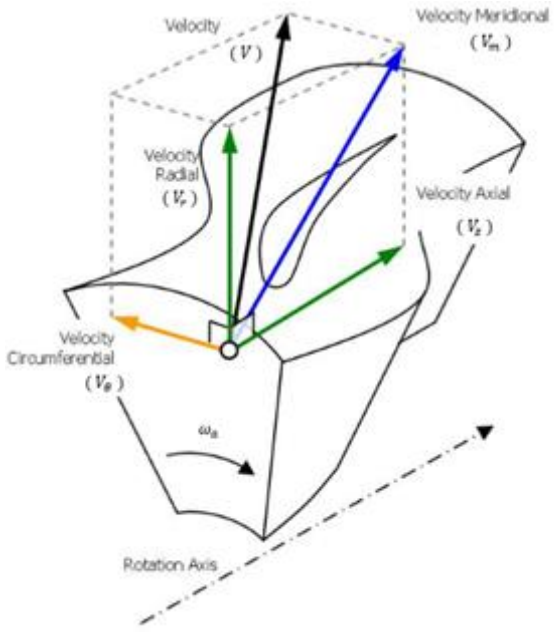

(a) Meridional Plane

Figure 27: Velocity components of interest in CFD-Post, (adapted from [92])

7. ANALYSIS OF NUMERICAL RESULTS & DISCUSSION

7.1. Spatial Verification & Validation

All the turbulence models achieved 500 iterations, as observation of the order of convergence and oscillatory behavior of the residual plots was a priority. The normalized root-mean-square (RMS) residuals of the equations and the mass flow rate surface monitor at the inlets and outlets of all the computational domains are tracked through the solver manager. Figure 28, Figure 29, Figure 30, and Figure 31 show the residuals of the equations for the $SST - Transition - CC$ turbulence model at the highest mesh, M5, while Figure 32 and Figure 33 shows the mass flow rate surface monitor at the inlet and outlet planes of the individual computational domains. Since the flow is incompressible; it has the same physical meaning as tracking the velocity at these planes. The mass flow rate change between the stator and rotor is due to the change in the modeled area, where the larger amount of rotor vanes gives it a smaller individual area.

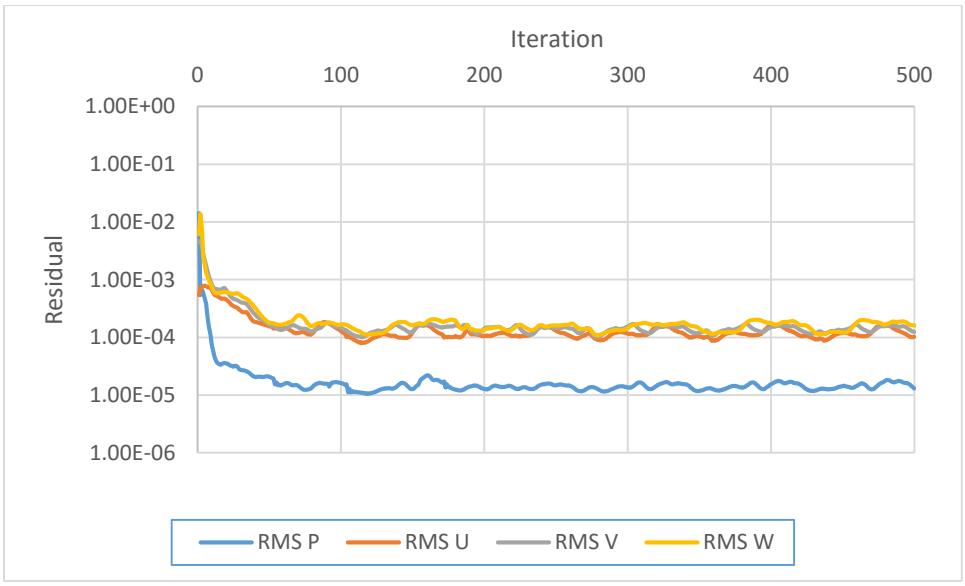

Figure 28: RMS residuals for mass continuity and momentum ($SST - Transition - CC$, M5)

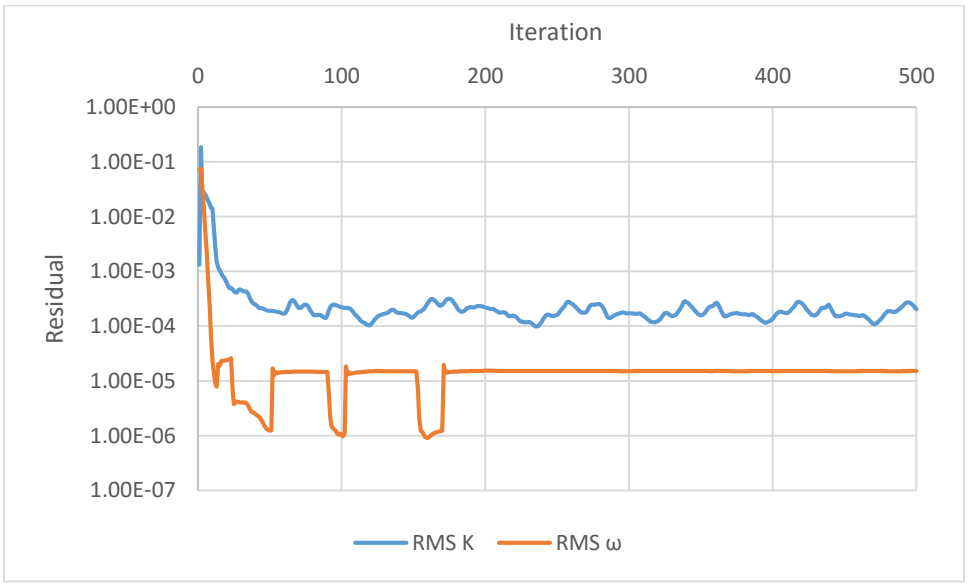

Figure 29: RMS residuals for the turbulent kinetic energy and specific dissipation ($SST - Transition - CC$, M5)

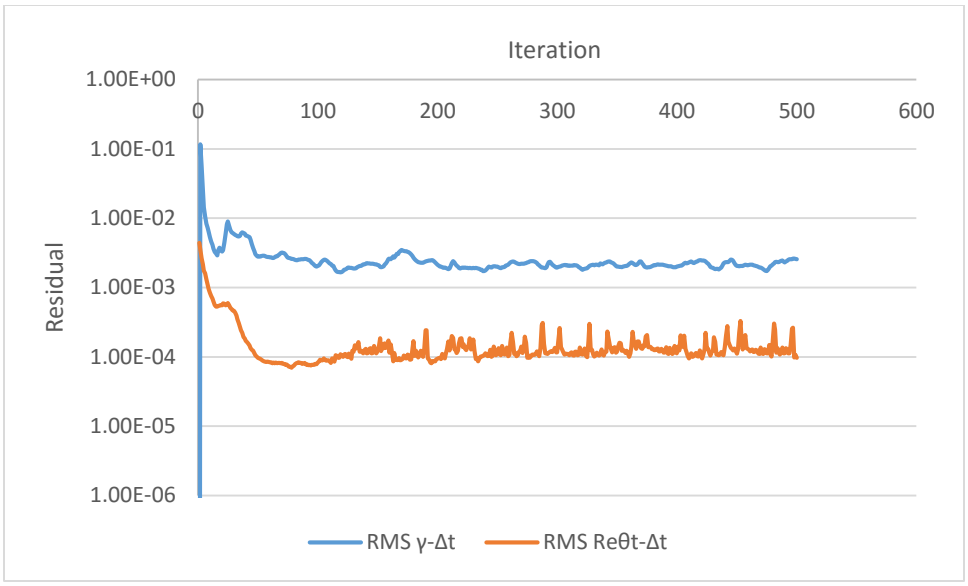

Figure 30: RMS residuals for intermittency and the transition momentum thickness Reynolds number ($SST - Transition - CC$, M5)

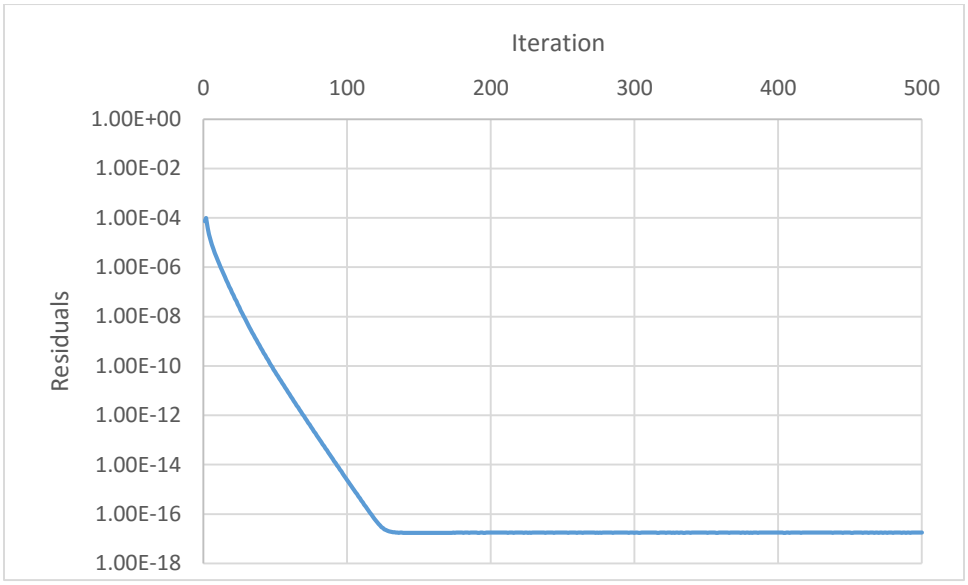

Figure 31: RMS residual for the wall scale ($SST - Transition - CC$, M5)

Figure 32: Mass flow rate surface monitor at stator planes ($SST - Transition - CC$, M5)

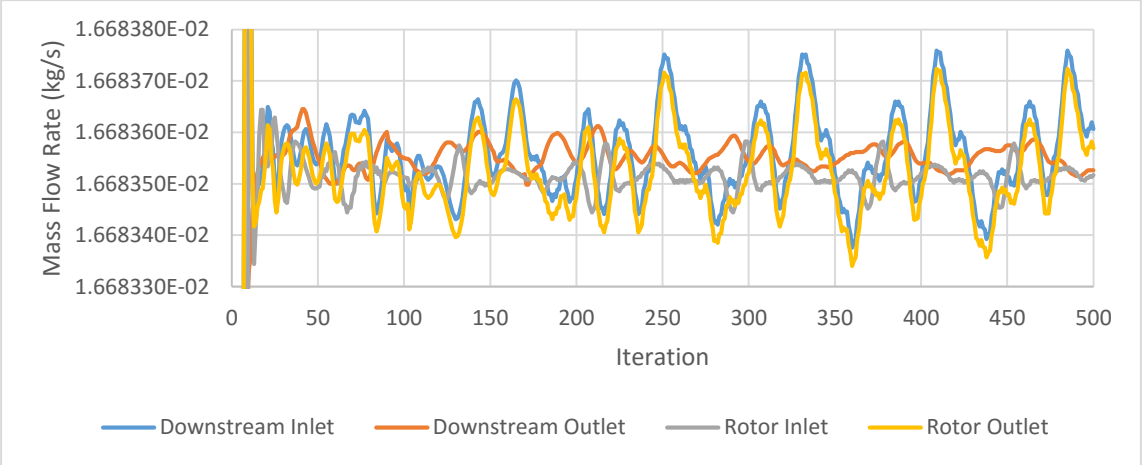

Figure 33: Mass flow rate surface monitor at rotor and downstream planes ($SST - Transition - CC$, M5)

Only the omega based models include the wall scale residual needed for the near wall treatment. The additional equation residuals for the $k - \omega - CC$ turbulence model kept converging in a monatomic fashion, while all the other turbulence model residuals either flat-lined or reached an oscillatory motion, the latter was the norm. The oscillatory behavior of the residual plots is either due to a transient or numerical effect. Decrease of the steady state time scale allows for observation of the oscillation period, where a constant period is likely a transient effect [84]. In this thesis, this is effect is considered in the

temporal verification of the steady state results through the reduction of the physical time scale.

The preliminary results indicate that the oscillation of the surface monitors are the same as those of the equation residuals, having a period of either 76 or 105 iterations, which indicates that a transient effect is plausible, although the amplitude only ranges from the hundred-thousandths to the ten-millionths place for the mass flow rate. This small amplitude signifies that there is small change in the mass flow rate surface monitor as the iteration period progresses in the steady state simulations. Figure 34 and Figure 35 best represents the oscillation and amplitude of the mass flow rate surface monitor at the stator and rotor domain outlet planes for all the models. The normalized RMS residuals for all the cases were below 1e-3, except for the intermittency transport equation for the transition model, which was below 1e-2. These values are sufficient to resolve major flow features and sufficient for a qualitative analysis [84]. The $SST - CC$ turbulence model achieved residual values below 1e-4 and the $k - \omega - CC$ model achieved values below 1e-5, showing relatively loose convergence and good convergence [84], respectively. The domain imbalance is verified to be below 1%; the advection time scale for the different models and meshes were verified to be greater than the auto-time scale, which is 2.37545E-3 seconds for all the models, which pertains to $0.1/\omega_a$.

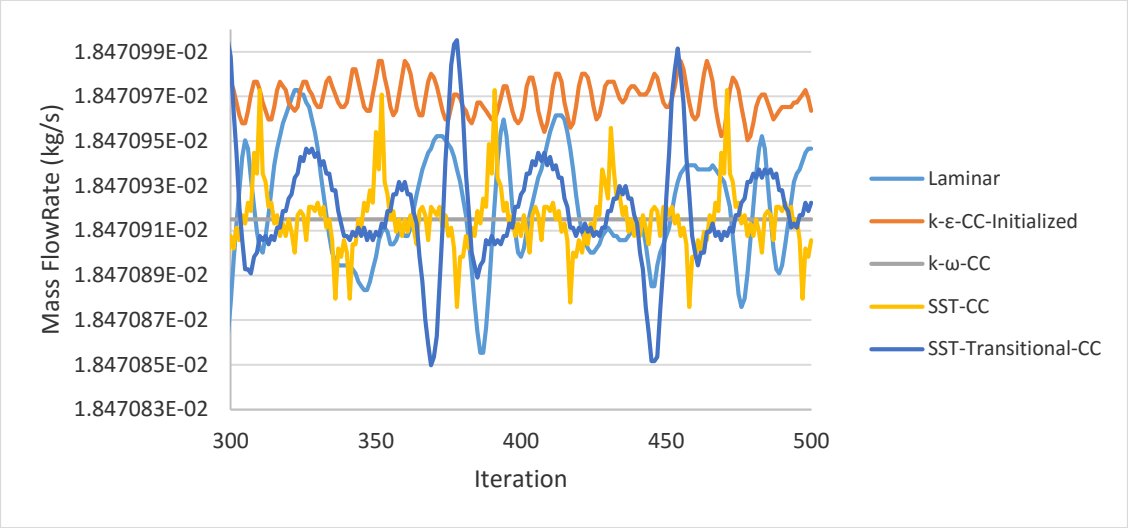

Figure 34: Mass flow rate surface monitor at stator domain exit for all the models

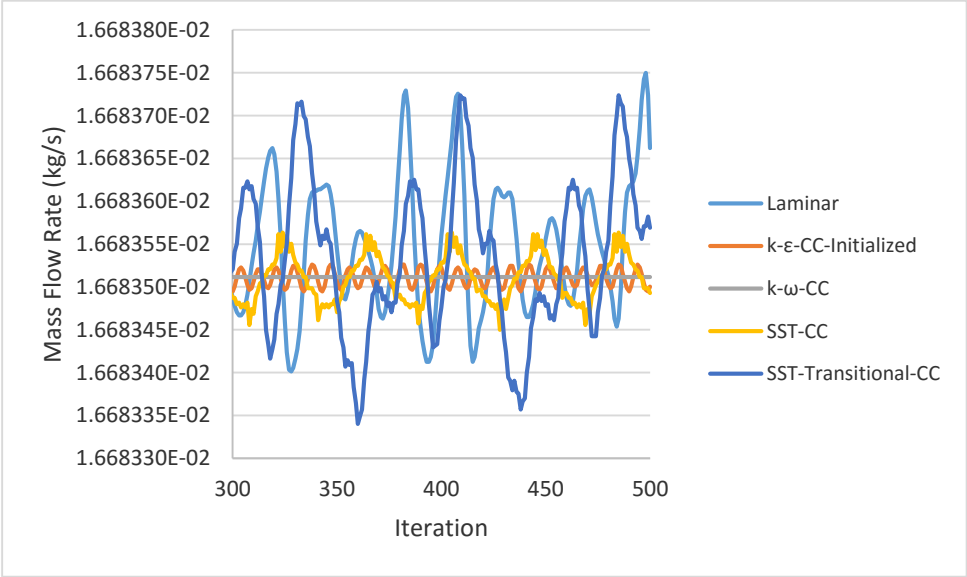

Figure 35: Mass flow rate surface monitor at rotor domain exit for all the models

Figure 36 shows CPU requirement versus the host memory allocation for the different models at the highest mesh size. The increased complexity of the turbulence models is associated with the observed increase in computational cost. This figure introduces two $k-\varepsilon$ models, one that starts from the initial conditions, and another that initializes from the *Laminar Flow* model results. This is essential as the solver had difficulties with one of the meshes starting from the initial conditions: there is reverse flow

at the outlet in the initial iterations that causes the solver to have a fatal error, while the others stabilized with no reverse flow at the outlet. The solver makes the outlet plane nodes a wall if it has reverse flow, and specifies that an opening boundary condition may be more suitable. The multiple simulations, essentially 5 meshes for each of the 5 cases, shows how routine it is to obtain numerical predictions, but the following studies, through verification and validation, show how making consistent and accurate predictions is not as routine.

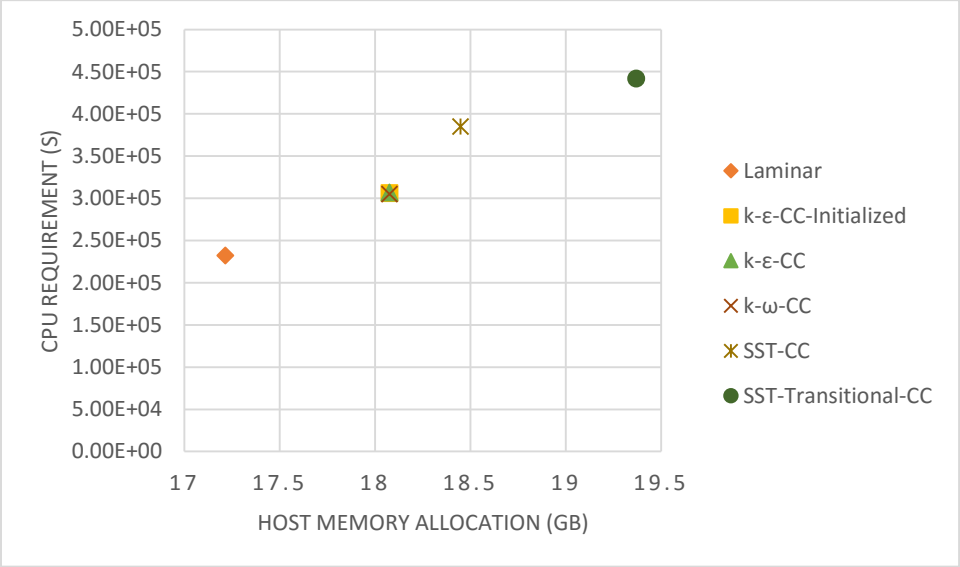

Figure 36: CPU requirement vs host memory allocation (steady state, M5)

7.1.1. Streamwise Spatial Verification

To verify that the equations are solved correctly, one has to show mesh independence by tracking the system response quantities (SRQ's). First, for the individual models the streamwise distribution of the SRQ's is plotted to show the effect mesh refinement has on their progression; do individual points behave monotonically or oscillate. Figure 37, Figure 38, Figure 39, and Figure 40 show the mesh dependency study for the $SST - Transition - CC$ turbulence model. Just as for this model, all the other

models visually seem to reach mesh independence for the absolute velocity, relative velocity, and pressure loss. The RMS of the turbulent velocity fluctuations increases as the mesh size does, as expected more of the mean velocity gradients are resolved allowing for the modeling of more of the turbulence effects through the prediction of the strain rate and vorticity rate. Therefore, increasing the mesh size directly effects the turbulence production term, which enhances the turbulent kinetic energy prediction.

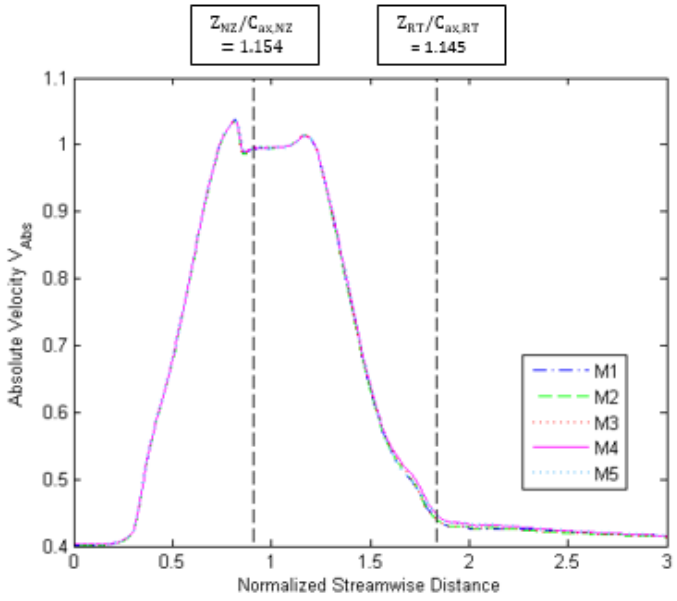

Figure 37: Streamwise mesh dependency study of the absolute velocity ($SST - Transition - CC$)

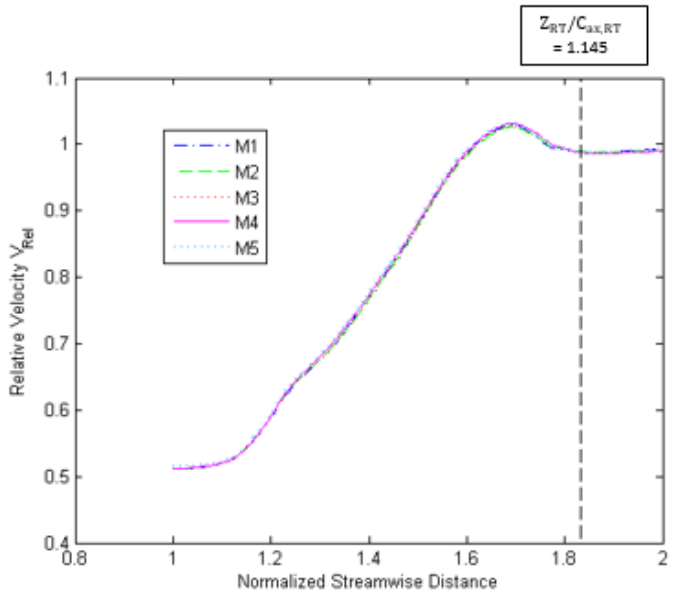

Figure 38: Streamwise mesh dependency study of the relative velocity ($SST - Transition - CC$)

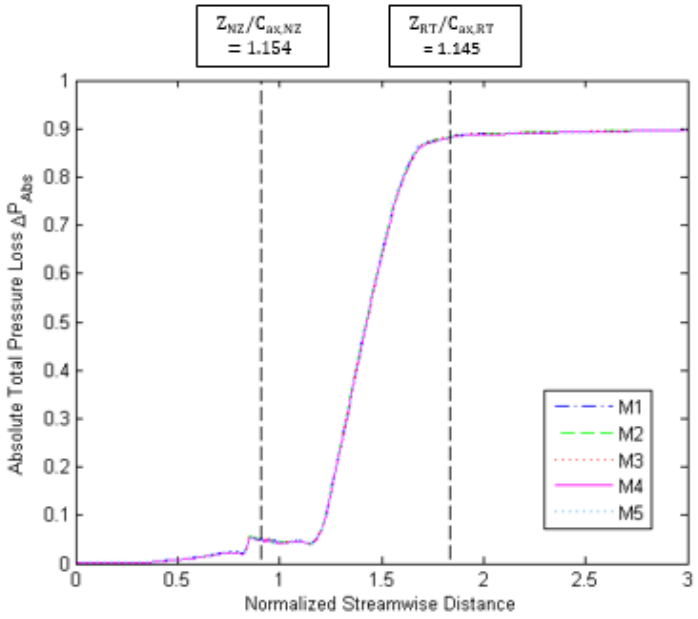

Figure 39: Streamwise mesh dependency study of the absolute total pressure loss ($SST - Transition - CC$)

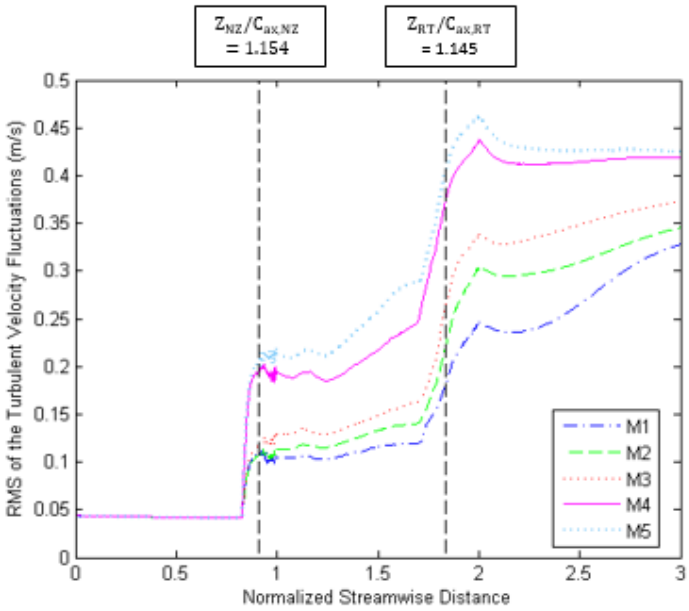

Figure 40: Streamwise mesh dependency study of the RMS of the turbulent velocity fluctuations ($SST - Transition - CC$)

For verification purposes, the fine grid global GCI is determined for uncertainty quantification. The GCI gives a better understanding of the global uncertainty associated with each SRQ in each model. The GCI was calculated for all the mesh combinations that had a refinement factor, rf, greater than 1.1. *Table 17* gives the refinement factor and associated meshes used to determine all the global GCI shown. *Table 18* gives the velocities at the nozzle and rotor exit plane that makes the most of the SRQ's dimensionless. *Table 19* gives the fine grid global GCI determined from the numerical results of the SRQ's of each turbulence models.

Table 17: Steady state refinement factor for each turbulence model

Turbulence Model	Grid N			Refinement Factor	
	Coarse	Mid	Fine	rf_{21}	rf_{32}
$Laminar\ Flow$ $k-\varepsilon-CC-Initialized$ $k-\omega-CC$ $SST-CC$ $SST-Transition-CC$	M1	M2	M5	1.37	1.28

Table 18:Exit plane velocities for the steady state models at mesh size M5

Turbulence Model	Exit Plane Velocities	
	V_2 (m/s)	W_3 (m/s)
$Laminar\ Flow$	10.94	9.61
$k-\varepsilon-CC-Initialized$	10.52	9.15
$k-\omega-CC$	10.94	9.47
$SST-CC$	10.95	9.45
$SST-Transition-CC$	10.93	9.44

Table 19: Streamwise global GCI for specified SRQ and turbulence model (spatial discretization)

SRQ	Turbulence Model	Richardson Nodes (%)	Observed Order p	Global GCI (%)
Absolute Velocity V_{Abs}	$Laminar\ Flow$	56.78	2.27	3.31
	$k-\varepsilon-CC-Initialized$	4.89	1.42	2.38
	$k-\omega-CC$	63.33	1.48	0.57
	$SST-CC$	49.33	1.91	0.39
	$SST-Transition-CC$	25.11	2.36	0.82
Relative Velocity V_{Rel}	$Laminar\ Flow$	26.67	1.90	1.75
	$k-\varepsilon-CC-Initialized$	41.00	4.45	0.03
	$k-\omega-CC$	79.33	3.20	0.12
	$SST-CC$	77.33	4.17	0.04
	$SST-Transition-CC$	42.33	2.26	1.11
Absolute Pressure Loss ΔP_{Abs}	$Laminar\ Flow$	89.44	2.56	12.31
	$k-\varepsilon-CC-Initialized$	23.56	2.40	3.50
	$k-\omega-CC$	83.67	2.02	5.85
	$SST-CC$	94.00	1.84	4.33
	$SST-Transition-CC$	50.44	2.38	3.36
RMS of the Turbulent Velocity Fluctuations u'	$k-\varepsilon-CC-Initialized$	99.89	1.40	13.64
	$k-\omega-CC$	94.11	1.46	15.13
	$SST-CC$	75.78	0.99	32.52
	$SST-Transition-CC$	75.56	1.78	47.83

The observed order of convergence, p, should be no higher than two to be within the formal order of convergence and to be considered in the asymptotic range. As the mesh size was increased the observed order of convergence begins to approach the formal order, but as noted from *Table 19* further mesh refinement is needed for the observed order of convergence to be within the formal order. It is seen that the greatest numerical uncertainty of the SRQ's of interest is in the prediction of the RMS of the turbulent velocity fluctuations, where the $SST - Transitional - CC$ turbulence model has a global GCI of 47.83%. This is mainly caused by the large local relative discretization errors. Figure 41 shows the local uncertainty associated with the prediction of the RMS of the turbulent velocity fluctuations for the finest mesh, based on the local fine mesh GCI.

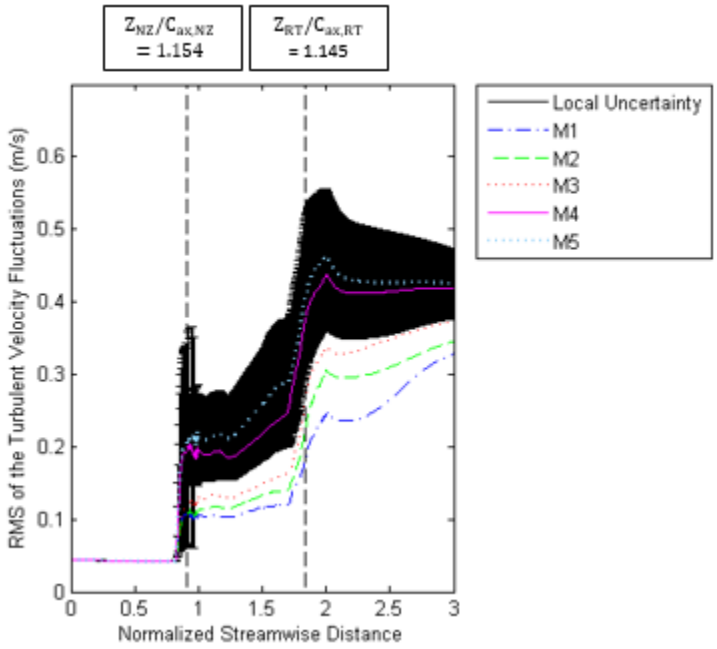

Figure 41: Local spatial uncertainty for RMS of the turbulent velocity fluctuations ($SST - Transition - CC$, M5)

As noted further mesh refinement is needed, but this is at a significant computational cost. The next mesh size would have to have a refinement factor of at least 1.3, but a value of 1.37 would be better suited to match the fine mesh refinement factor

used in *Table 17*. This would dictate an element size count of at least 17.77 million. Figure 42 shows the memory allocation needed for the different mesh sizes for the $SST - Transition - CC$ turbulence model and the $Laminar\ Flow$ model. These two models serve as the upper and lower bounds of the host memory allocation in Figure 36. Based on linear scaling a host memory allocation of 43.2 and 48.7 GB is needed to accommodate the mesh size increase.

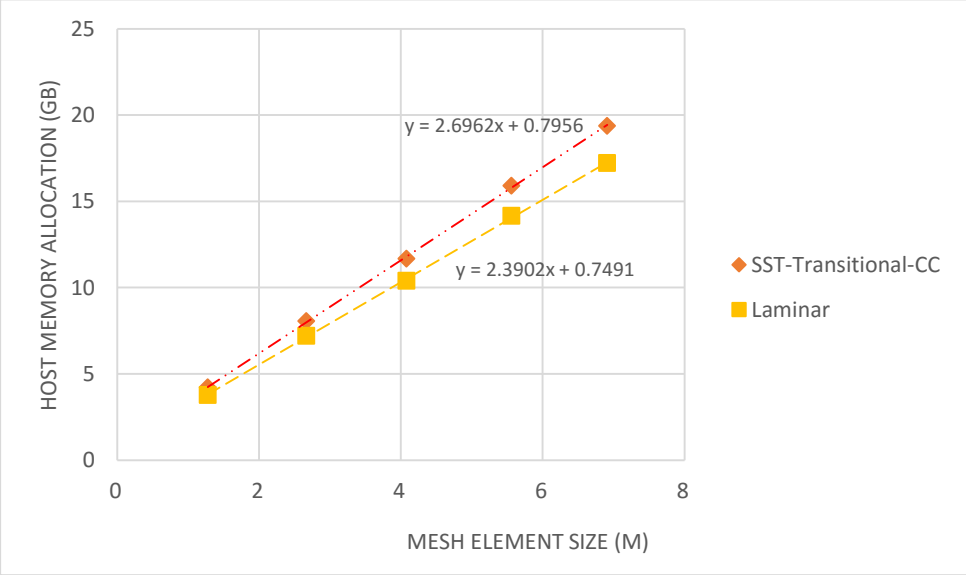

Figure 42: Memory allocation vs mesh element size

7.1.2. Streamwise Validation

To validate the results, the numerical solutions at the highest mesh, $M5$, are compared to the experimental results of Matsunuma [24]. Figure 43, Figure 44 and Figure 45 compare the SRQ's to the experimental LDV data by spanwise averaging at the different streamwise distances. Figure 44 includes the LDV measurement uncertainty given in *Table 3*, as given in Matsunuma [24]. Figure 46 shows the comparison of the absolute pressure loss at the highest mesh, M5, for all the turbulence models. It is evident that the streamwise mean velocities and pressure loss have a distribution that is nearly independent of the

turbulence models employed. There is a significant difference in the streamwise distribution of the RMS of the turbulent velocity fluctuations, for all the turbulence cases. The standard $k-\varepsilon$ turbulence model was found to have the same behavior that was within 1% of the $k-\varepsilon$ turbulence model initialized by the $Laminar\ Flow$ model results at mesh sizes M1, M3, M4, and M5, thus its uncertainty is not quantified due to the unobtainable results at mesh M2, its results at the highest mesh are shown for reference.

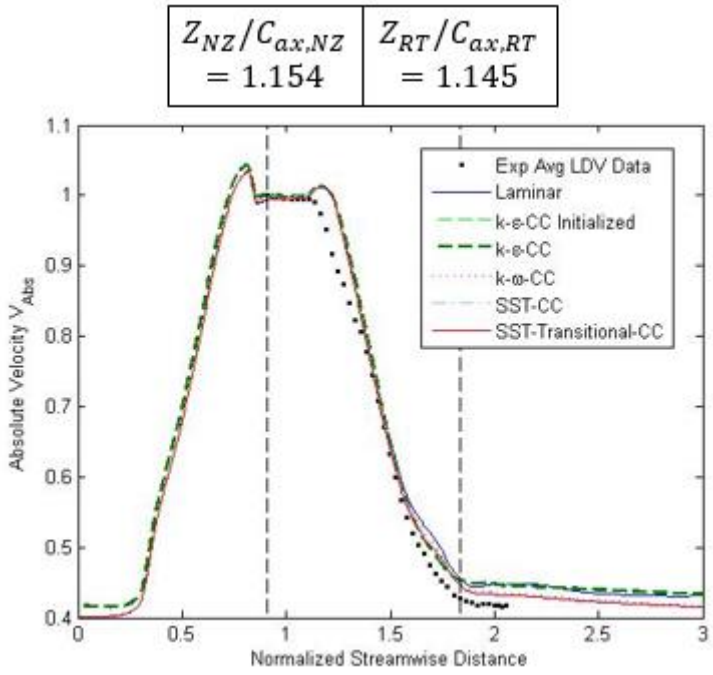

Figure 43: Streamwise distribution of the absolute velocity for all the models with comparison to experiment (M5, steady state)

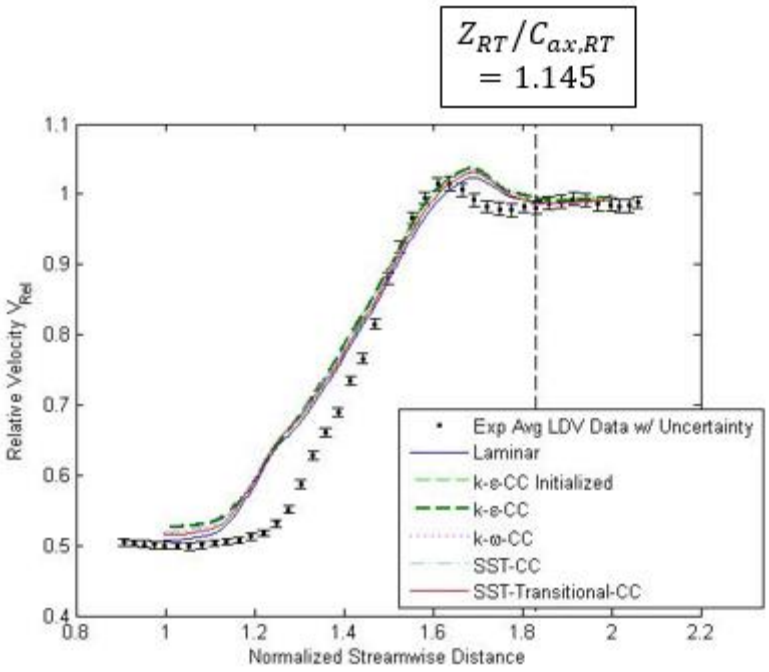

Figure 44: Streamwise distribution of the relative velocity for all the models with comparison to experiment (M5, steady state)

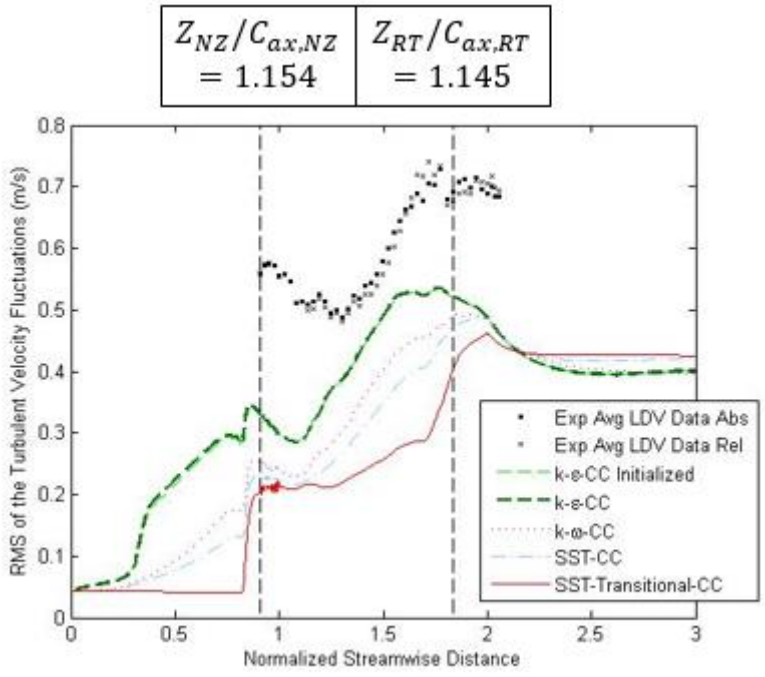

Figure 45: Streamwise distribution of the RMS of the turbulent velocity fluctuations for all the models with comparison to experiment (M5, steady state)

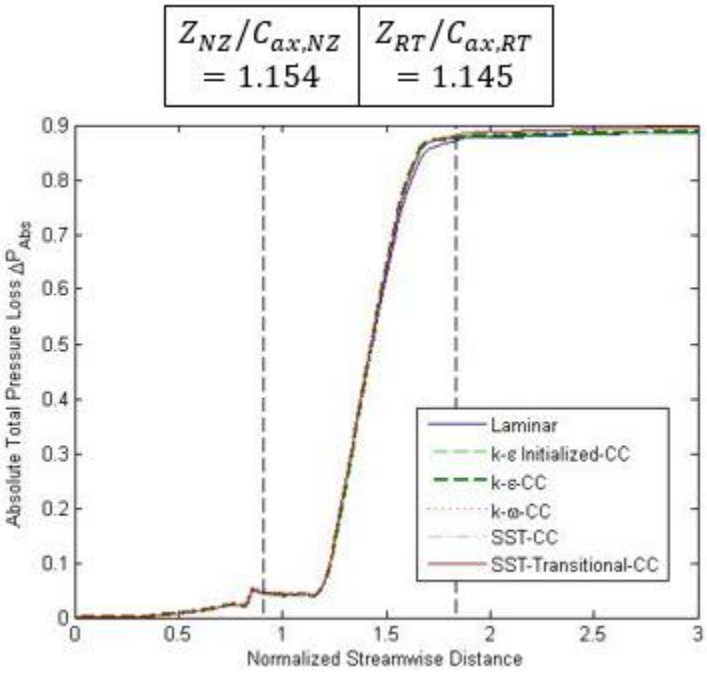

Figure 46: Streamwise distribution of the absolute pressure loss for all the models with comparison to experiment (M5, steady state)

The percent error is calculated between the experimental and numerical data by treating the experimental data as the exact value, as shown in Eqn. *7.1*.

$$\%\ Error = \frac{|Experimental - Numerical|}{|Experimental|}\ x100\% \qquad 7.1$$

This gives a measure of the absolute change between the experimental and numerical values normalized by the experimental value. *Table 20* and *Table 21* give the streamwise mean percent error of the velocities and RMS of the turbulent velocity fluctuations for all the applicable turbulence models. The mean percent error for the RMS of the turbulent velocity fluctuations is calculated with reference to the absolute and relative data given by Matsunuma [24].

Table 20: Mean error of the absolute and relative velocities in the streamwise direction for all the models (steady state, M5)

SRQ	Turbulence Model	Mean % Error
Absolute Velocity V_{Abs}	$SST - Transition - CC$	3.25
	$SST - CC$	3.62
	$k - \omega - CC$	3.89
	$k - \varepsilon - CC$	4.05
	$k - \varepsilon - CC - Initialized$	4.05
	$Laminar$	4.74
Relative Velocity V_{Rel}	$Laminar$	5.09
	$SST - Transition - CC$	5.62
	$k - \omega - CC$	6.00
	$SST - CC$	4.12
	$k - \varepsilon - CC$	6.15
	$k - \varepsilon - CC - Initialized$	6.16

Table 21: Mean error of the RMS of the turbulent velocity fluctuations in the streamwise direction for all the models (steady state, M5)

SRQ	Turbulence Model	Mean % Error	
		Experimental LDV Abs	Experimental LDV Rel
RMS of the Turbulent Velocity Fluctuations **u'**	$k - \varepsilon - CC$	15.12	25.81
	$k - \varepsilon - CC - Initialized$	15.14	25.84
	$k - \omega - CC$	27.79	36.92
	$SST - CC$	34.10	42.45
	$SST - Transition - CC$	45.60	52.49

The streamwise average of the absolute and relative velocities are within 4.8% and 6.2% for all the turbulence models, respectively. The prediction of the streamwise average of the RMS of the turbulent velocity fluctuations gives the largest mean percent error, which range from 15 to 53%. The RMS of the turbulent velocity fluctuations for the numerical calculations are a direct measure of the turbulent kinetic energy, k, as shown in Eqn. *3.4*. Although, the $k-\varepsilon$ models seem to have the smallest percent error for the RMS of the turbulent velocity fluctuations, it is known that this is in fact caused by the turbulence model being fully turbulent, allowing the kinetic energy prediction to be augmented at the nozzle outlet. The high global GCI of the RMS of the turbulent velocity fluctuations for the numerical simulations, as given in *Table 19*, indicates that the mean percent errors, shown in *Table 21*, can potentially be decreased, reiterating the importance of further mesh refinement.

7.1.3. Spanwise Verification

Although the streamwise results are statisfactory for the mean velocities, it is believed that the boundary layer flow in the hub and tip region will be harder to predict due to the wall functions and near-wall treatment employed by each respective model. Figure 47 and Figure 48 show the spanwise mesh dependency study of the absolute velocity and RMS of the turbulent velocity fluctuations at the nozzle outlet plane for the $SST-Transitional-CC$ turbulence model. *Table 22* gives the fine grid global GCI for the absolute velocity and RMS of the turbulent velocity fluctuations determined at the nozzle outlet plane for each of the numerical models.

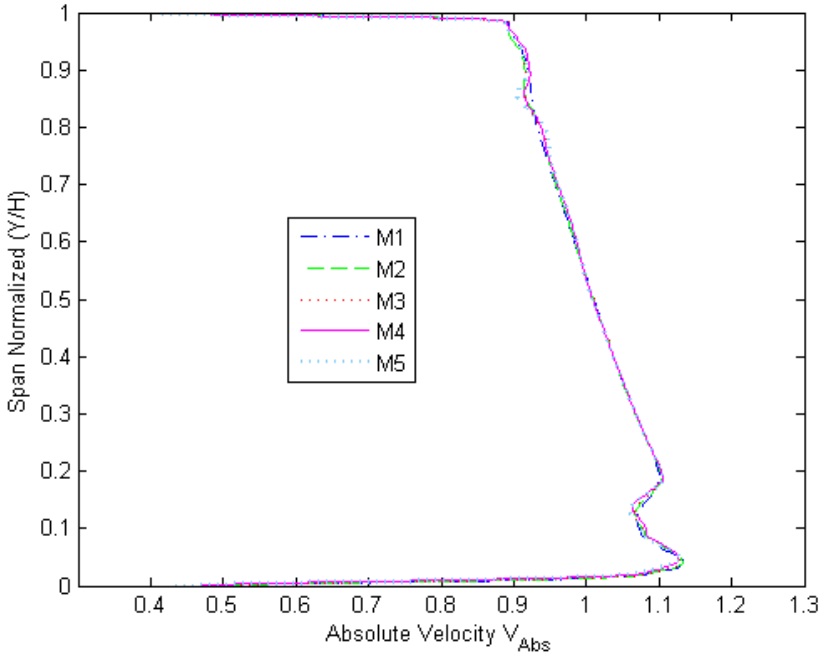

Figure 47: Spanwise mesh dependence of the absolute velocity at the nozzle exit plane ($Z_{NZ}/C_{ax,NZ} = 1.154$, $SST - Transition - CC$)

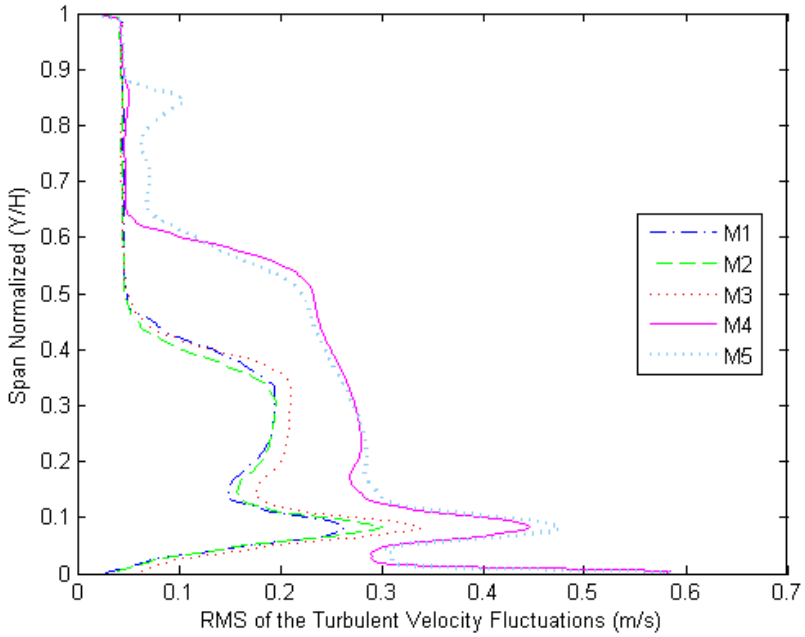

Figure 48: Spanwise mesh dependence of the RMS of the turbulent velocity fluctuations at the nozzle exit plane ($Z_{NZ}/C_{ax,NZ} = 1.154$, $SST - Transition - CC$)

Table 22: Spanwise global GCI for specified SRQ and turbulence model at the nozzle exit plane ($Z_{NZ}/C_{ax,NZ} = 1.154$, spatial discretization)

SRQ	Turbulence Model	Richardson Nodes (%)	Observed Order p	Global GCI (%)
Absolute Velocity V_{Abs}	$Laminar$	43.67	2.35	1.45
	$k-\varepsilon-CC-Initialized$	32.00	2.85	0.13
	$k-\omega-CC$	53.33	2.32	0.30
	$SST-CC$	36.00	2.26	0.51
	$SST-Transition-CC$	63.00	1.84	1.14
RMS of the Turbulent Velocity Fluctuations **u'**	$k-\varepsilon-CC-Initialized$	99.00	0.93	23.81
	$k-\omega-CC$	20.67	1.85	10.78
	$SST-CC$	20.67	1.83	31.34
	$SST-Transition-CC$	33.00	2.69	80.39

It is observed that the global GCI for the RMS of the turbulent velocity fluctuations of the $SST-Transiton-CC$ turbulence model needs further mesh refinement for the observed order of 2.69 to approach the formal order of the numerical scheme, and for the global GCI to be decreased; in agreement with the results found in the streamwise direction. Figure 48 shows why there are only 33% of Richardson nodes for calculation of the global observed order of convergence, as meshes $M1$ and $M2$ have areas of oscillatory motion. An alternative is to use meshes M1, M3, and M5 for calculation of the fine grid GCI. This would increase the amount of Richardson nodes to 52% when calculating the global observed order of convergence, which leads to an observed order of convergence of 19.13, which is nowhere near the asymptotic range, that leads to a notably smaller fine mesh GCI

of 3.25%. This is attributed to the augmented observed order of convergence, increased fine mesh refinement factor, and the large relative discretization errors, which collectively falsely represent the GCI. Essentially the mesh refinement needs to be able to produce low relative discretization errors and an observed order of convergence in the asymptotic range to properly capture the distribution of the RMS of the turbulent velocity fluctuations. Similar results are found when observing the rotor exit plane distributions. For the rotor exit plane, Figure 49, Figure 50 and Figure 51 show the spanwise distribution of the absolute velocity, relative velocity and RMS of the turbulent velocity fluctuations for the $SST - Transition - CC$ turbulence model. *Table 23* gives the fine grid global GCI associated with these variables at the rotor exit plan for all the applicable turbulence models.

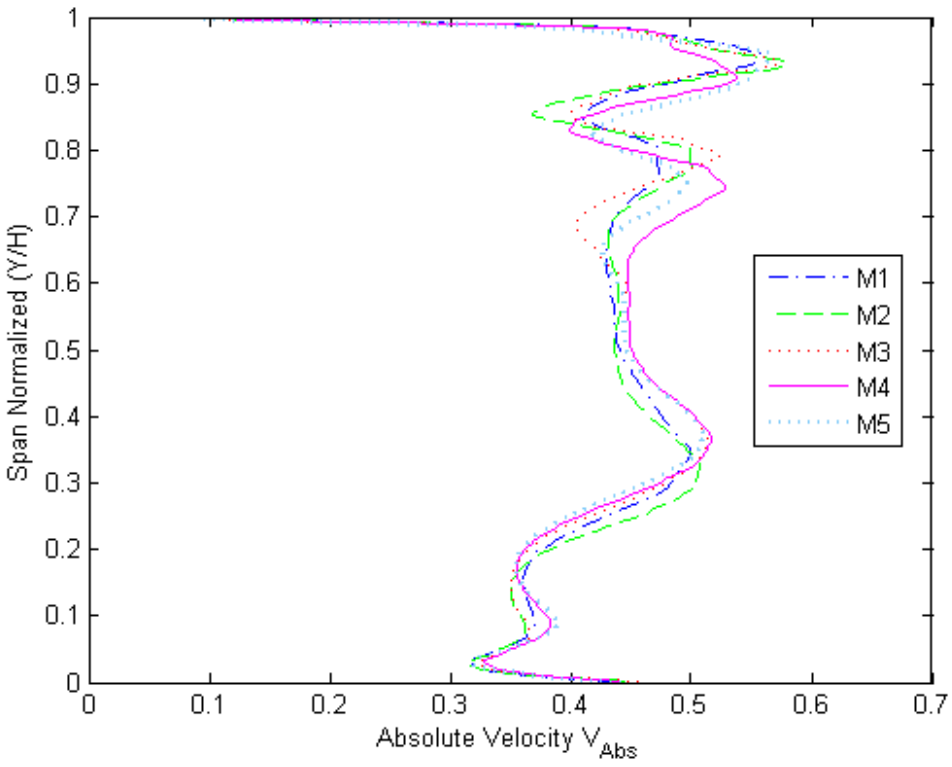

Figure 49: Spanwise mesh dependence of the absolute velocity at the rotor exit plane ($Z_{RT}/C_{ax,RT} = 1.145$, $SST - Transition - CC$)

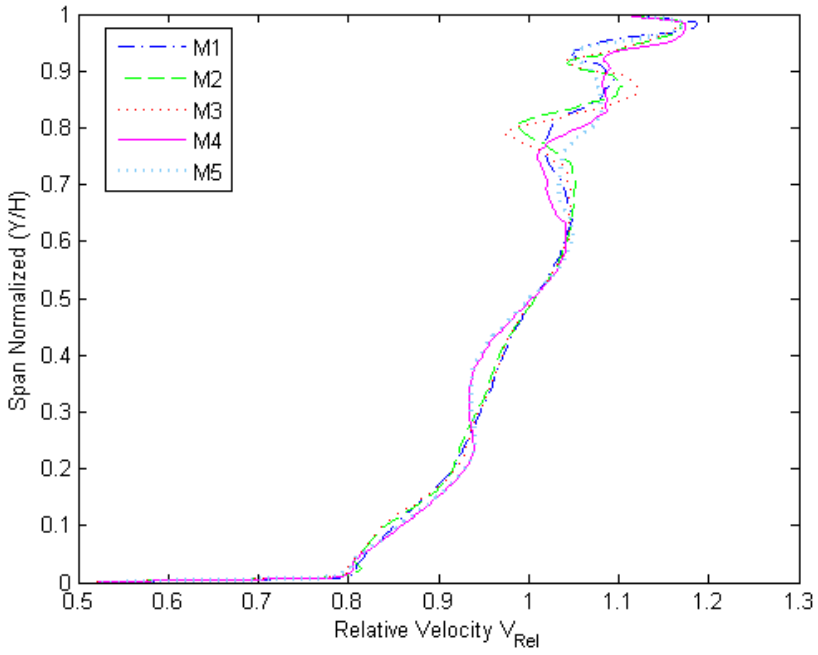

Figure 50: Spanwise mesh dependence of the relative velocity at the rotor exit plane ($Z_{RT}/C_{ax,RT} = 1.145$, $SST - Transition - CC$)

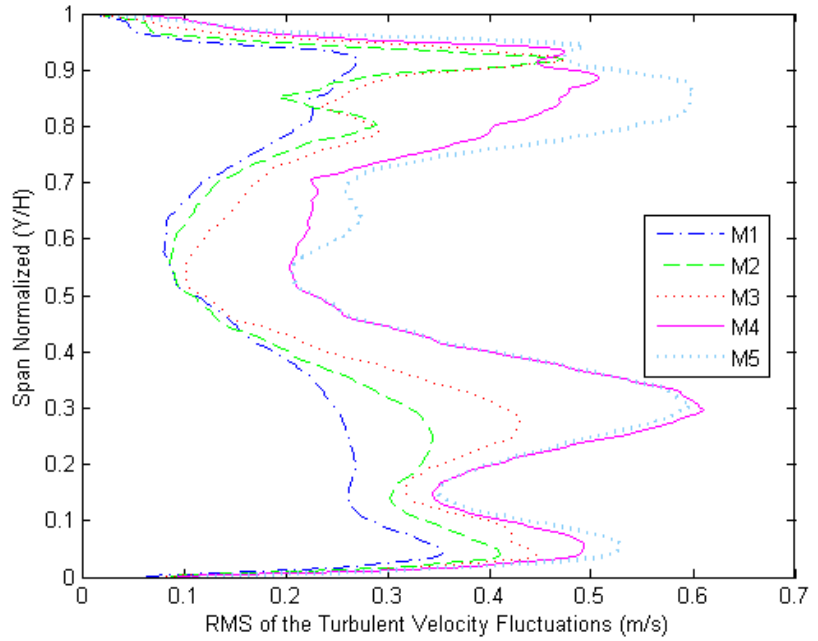

Figure 51: Spanwise mesh dependence of the RMS of the turbulent velocity fluctuations at the rotor exit plane ($Z_{RT}/C_{ax,RT} = 1.145$, $SST - Transition - CC$)

Table 23: Spanwise global GCI for specified SRQ and turbulence model at the rotor exit plane ($Z_{RT}/C_{ax,RT} = 1.145$, spatial discretization)

SRQ	Turbulence Model	Richardson Nodes (%)	Observed Order p	Global GCI (%)
Absolute Velocity V_{Abs}	$Laminar$	22.67	2.39	28.42
	$k-\varepsilon-CC-Initialized$	55.67	2.00	3.70
	$k-\omega-CC$	56.67	1.46	10.72
	$SST-CC$	58.00	1.73	6.96
	$SST-Transition-CC$	24.33	2.19	15.15
Relative Velocity V_{Rel}	$Laminar$	31.33	2.66	4.12
	$k-\varepsilon-CC-Initialized$	61.67	2.74	0.32
	$k-\omega-CC$	69.00	1.80	1.33
	$SST-CC$	60.67	1.71	1.37
	$SST-Transition-CC$	43.67	2.09	4.03
RMS turbulent velocity fluctuations **u'**	$k-\varepsilon-CC-Initialized$	97.33	2.16	10.74
	$k-\omega-CC$	88.00	1.25	29.09
	$SST-CC$	93.33	1.51	22.18
	$SST-Transition-CC$	88.33	1.90	79.50

7.1.4. Spanwise Validation

The experimental LDV data obtained by Matsunuma [24] is circumferentially averaged for validation of the spanwise numerical results obtained. Figure 52 shows the spanwise distribution of the absolute velocity for all the turbulence models compared to the experimental LDV and 5-hole pressure probe data at the nozzle exit plane. The

spanwise distribution of the RMS of the turbulent velocity fluctuations is shown in Figure 53. *Table 24* shows the mean percent error between the turbulence models and the experimental data at the nozzle outlet plane. The spanwise distribution of the absolute velocity at the nozzle exit plane is within 1.7% for all the models when compared to the circumferentially averaged LDV and 5-hole pressure probe data. At the nozzle exit plane the RMS of the turbulent velocity fluctuations is under predicted with a mean error as large as 68%, when compared to the value obtained from the relative LDV data, which correlates well with the large global uncertainty given in *Table* 22.

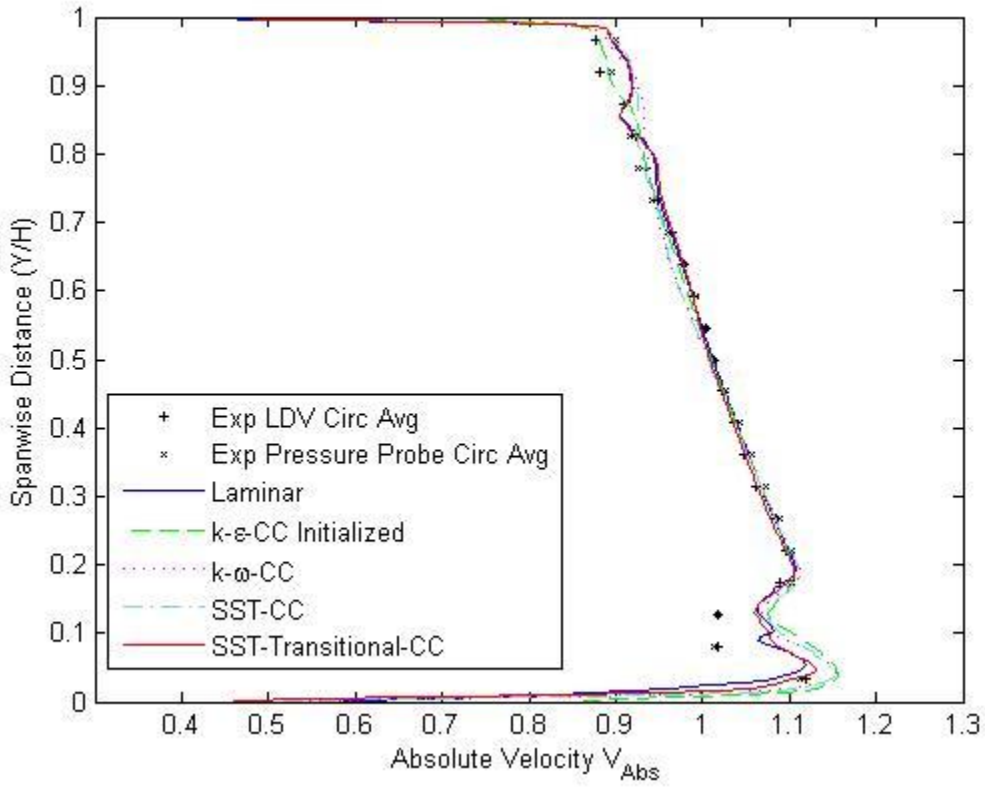

Figure 52: Spanwise distribution of the absolute velocity for all the models with comparison to experiment at the nozzle exit plane ($Z_{NZ}/C_{ax,NZ} = 1.154$, M5, steady state)

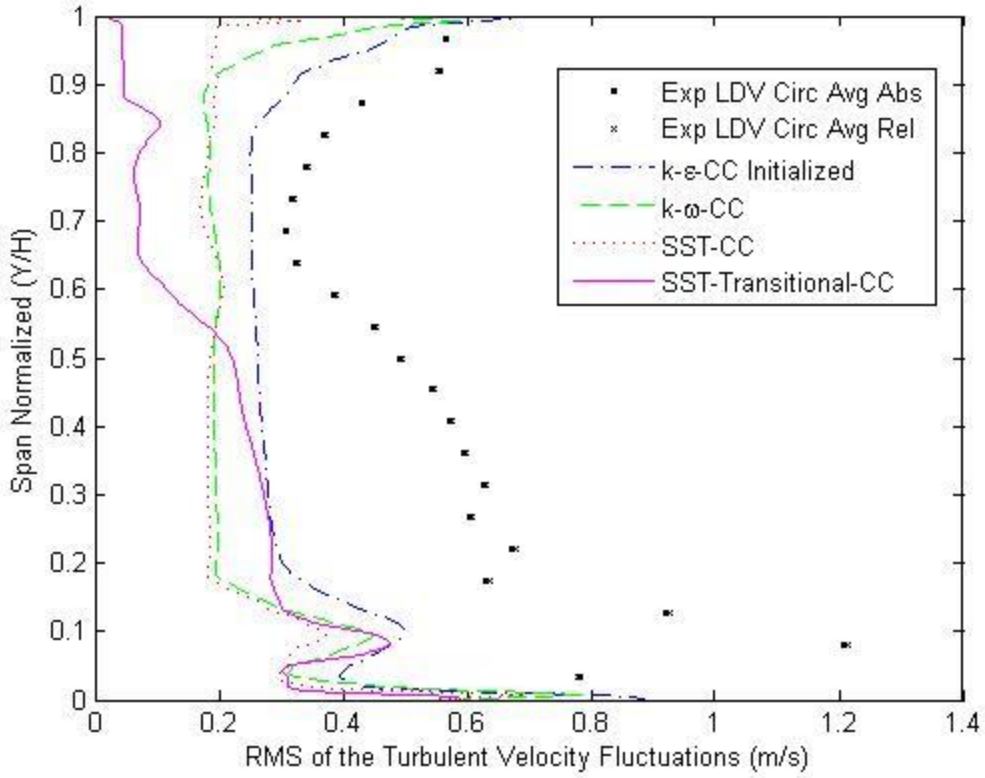

Figure 53: Spanwise distribution of the RMS of the turbulent velocity fluctuations for all the models with comparison to experiment at the nozzle exit plane ($Z_{NZ}/C_{ax,NZ} = 1.154$, M5, steady state)

Table 24: Mean error in the spanwise direction at the nozzle exit plane for all the models ($Z_{NZ}/C_{ax,NZ} = 1.15$, steady state)

SRQ	Turbulence Model	Mean % Error	
		Experimental LDV	Experimental Pressure Probe
Absolute Velocity V_{Abs}	$SST - Transition - CC$	1.13	1.23
	$Laminar$	1.22	1.27
	$k - \varepsilon - CC - Initialized$	1.34	1.46
	$k - \omega - CC$	1.71	1.58
	$SST - CC$	1.71	1.65
		Experimental LDV Abs	Experimental LDV Rel
RMS turbulent velocity fluctuations $\mathbf{u}'$	$k - \varepsilon - CC - Initialized$	40.76	41.05
	$k - \omega - CC$	57.13	57.34
	$SST - CC$	60.18	60.38
	$SST - Transition - CC$	67.76	67.95

At the rotor exit plane the absolute and relative velocity distributions are compared to the LDV data are shown in Figure 54 and Figure 55, while Figure 56 shows the spanwise distribution of the RMS of the turbulent velocity fluctuations for the applicable models. *Table 25* shows the mean percent error calculated between the LDV data and the turbulence models at the rotor outlet plane. The mean percent error is within 13.1% and 2.7% for the absolute and relative velocities at the rotor exit plane, respectively. At the rotor exit plane it is seen that the mean percent error for the RMS of the turbulent velocity fluctuations has decreased to within 43.5%, attributed to the increase in the average turbulence kinetic energy in the rotor.

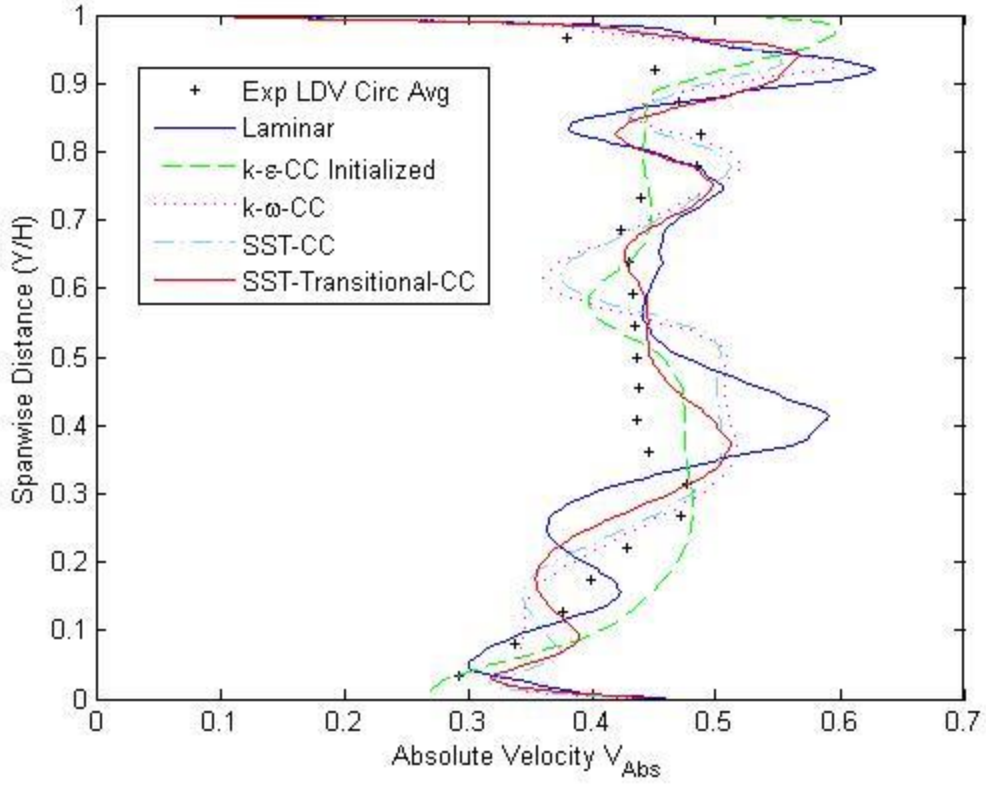

Figure 54: Spanwise distribution of the absolute velocity for all the models with comparison to experiment at the rotor exit plane ($Z_{RT}/C_{ax,RT} = 1.145$, M5, steady state)

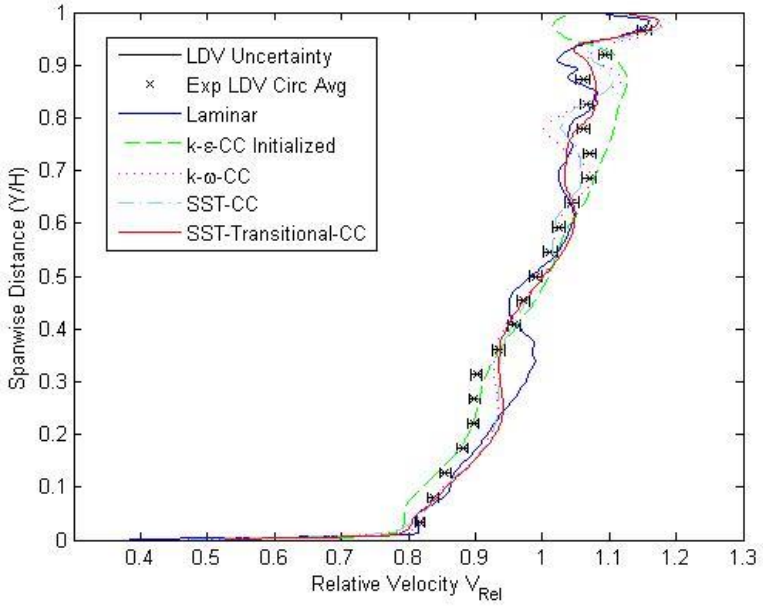

Figure 55: Spanwise distribution of the relative velocity for all the models with comparison to experiment at the rotor exit plane ($Z_{RT}/C_{ax,RT} = 1.145$, M5, steady state)

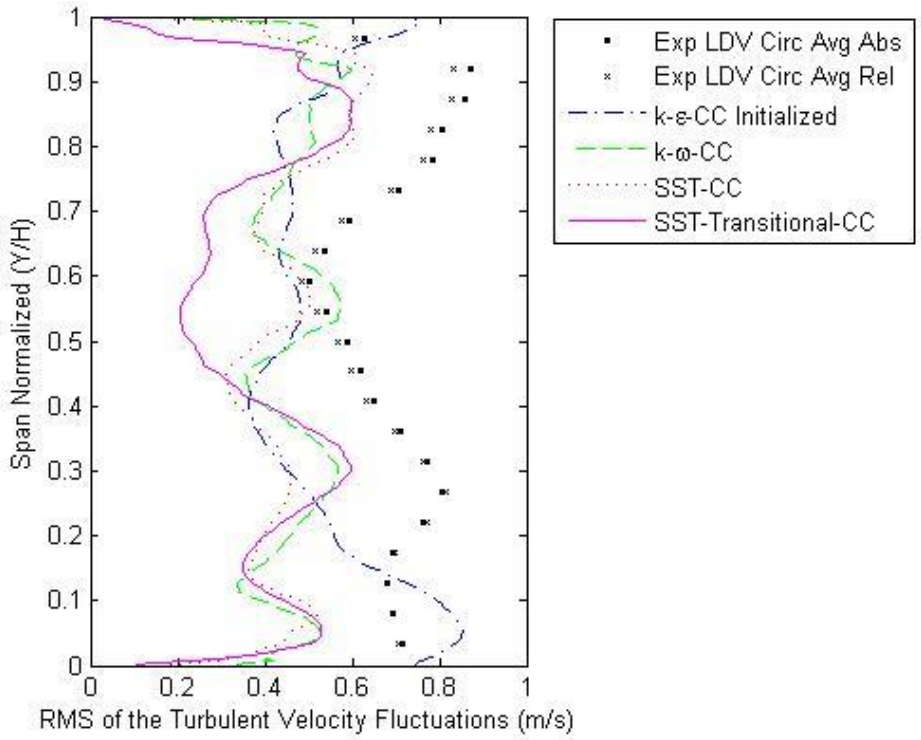

Figure 56: Spanwise distribution of the RMS of the turbulent velocity fluctuations for all the models with comparison to experiment at the rotor exit plane ($Z_{RT}/C_{ax,RT} = 1.145$, M5, steady state)

Table 25: Mean error in the spanwise direction at the rotor exit plane for all the models ($Z_{RT}/C_{ax,RT} = 1.145$, M5, steady state)

SRQ	Turbulence Model	Mean % Error	
Absolute Velocity V_{Abs}	$SST - Transition - CC$	8.95	
	$k - \varepsilon - CC - Initialized$	9.29	
	$k - \omega - CC$	10.44	
	$SST - CC$	10.55	
	$Laminar$	13.14	
Relative Velocity V_{Rel}	$SST - CC$	1.80	
	$k - \omega - CC$	1.87	
	$SST - Transition - CC$	2.05	
	$k - \varepsilon - CC - Initialized$	2.41	
	$Laminar$	2.65	
		Experimental LDV Abs	Experimental LDV Rel
RMS turbulent velocity fluctuations **u**'	$k - \varepsilon - CC - Initialized$	28.02	26.89
	$k - \omega - CC$	31.546	30.73
	$SST - CC$	34.33	32.79
	$SST - Transition - CC$	43.53	42.38

7.1.5. Nozzle Surface Flow

The shape factor, H_{12}, in the experiment is perceived to be approximately 2.3 at the tip and hub endwalls at the nozzle inlet [24]. For a Blasius boundary layer, i.e. laminar flat-plate boundary layer with zero pressure gradient, the shape factor has been reported to be 2.6, and for a turbulent boundary layer with zero pressure gradient as 1.4 [93]. Therefore, for a flat plate the shape factor contracts when going from a laminar to turbulent flow regime [94]. It is evident then that the incoming boundary layer is laminar, and

undergoes transition to a turbulent boundary layer. Consequently, at these low Reynolds numbers the nozzle surface flow is susceptible to boundary layer separation.

For a similar configuration with only the nozzle, which had a tip clearance of 0.5-mm, Matsunuma et al. [12] in 1998 found that the separation onset line on the suction surface moves downstream as the inlet Reynolds number is increased from $4x10^4$ to $12x10^4$, which correspond to a nozzle outlet Reynolds number increase from $9.6x10^4$ to $30.3x10^4$. They had difficulty with the flow visualizations at an inlet Reynolds number of $2x10^4$ and outlet Reynolds number of $4.7x10^4$ due to the velocity being too low. For this particular design, Matsunuma [24] in 2006 was able to show an oil-film visualization shown in Figure 57. The surface textures A through D correspond to the laminar boundary layer development at the inlet, strong radial flow after the separation onset line, reverse flow, and interaction between the hub passage vortex and separated inward flow, respectively [24].

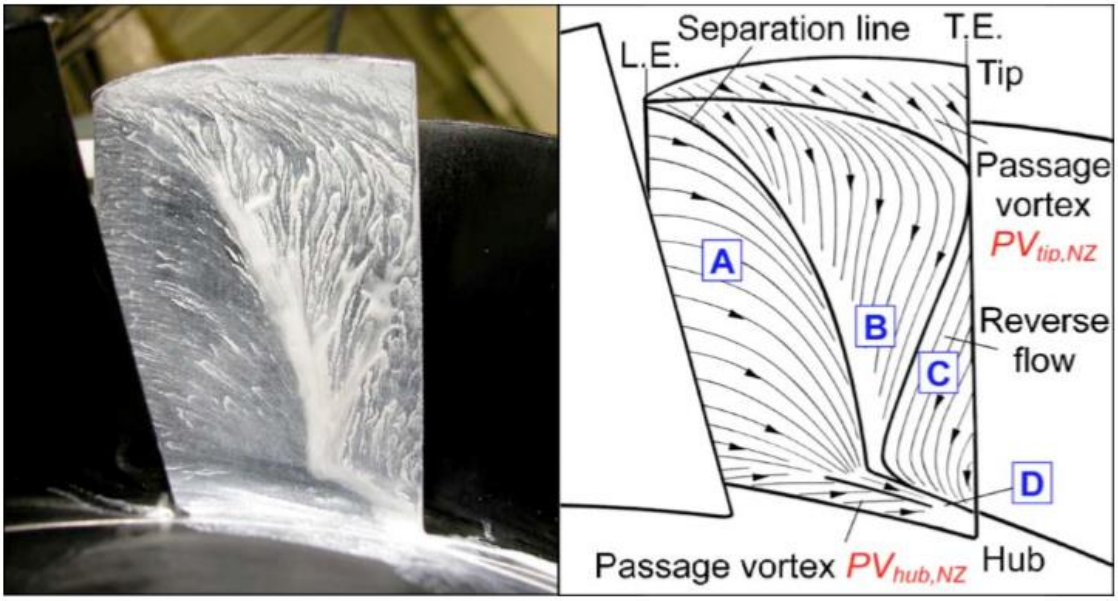

Figure 57: Oil-film visualization of nozzle suction surface [24]

The nozzle suction surface wall shear streamlines are shown for all the models at

the highest mesh, M5, in Figure 58. All the models predict some kind of flow turning at the hub and tip of the suction surface endwall due to the passage vortices. It is apparent that only the $Laminar\ Flow$ model and the $SST - Transtion - CC$ turbulence model are capable of predicting similar characteristics of the flow topology as found in the experiment, but the former is not capable of predicting transition to a turbulent flow. The $SST - CC$ turbulence model has been shown to do well with adverse pressure gradients, but in this particular investigation it is found to be incapable of predicting the suction surface flow topology, but its capability of incorporating a blending function between the $k - \varepsilon$ and $k - \omega$ is invaluable. It is worth noting that the suction surface flow for the $SST - CC$ turbulence model is ω based, which also happens to be activated in the laminar region of the $SST - Transition$ turbulence model, hence the $k - \omega - Transition$ turbulence model may be suited to model the suction surface flow topology, but this model is not currently accessible through ANSYS CFX.

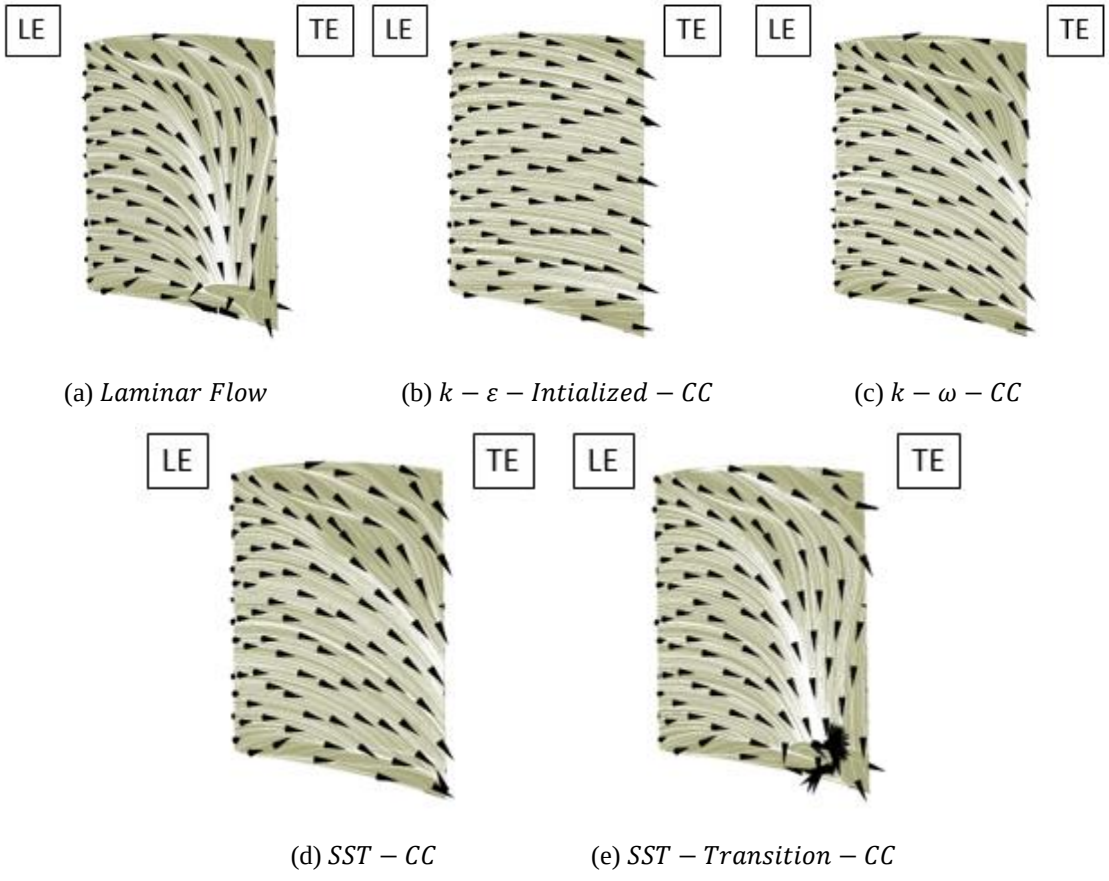

(a) $Laminar\ Flow$ (b) $k-\varepsilon-Intialized-CC$ (c) $k-\omega-CC$

(d) $SST-CC$ (e) $SST-Transition-CC$

Figure 58: Nozzle suction surface wall shear streamlines

7.1.6. Steady State Turbulence Model Discussion

The implementation of the various eddy-viscosity models (EVM's) is crucial in predicting the flow field within the axial-flow turbine at a low Reynolds number. The $Laminar\ Flow$ model does not include turbulence effects, while the $k-\varepsilon-CC$, $k-\omega-CC$, and the $SST-CC$ models are considered to be fully turbulent turbulence models. The $SST-Transition-CC$ turbulence model includes laminar, transitional, and turbulent effects. The EVM's predict the same streamwise characteristics for the velocities and absolute pressure loss as seen in Figure 43, Figure 44, and Figure 46. It is worth mentioning that the experimental streamwise points located from 1.1375 to 1.8042 in these figures may be misleading as there are fewer data points when taking the average, due to optical

blockage [24] caused by the shadow of the blade. This means that the individual streamwise points can have higher or lower average values.

In the streamwise direction, the RMS of the turbulent velocity fluctuations has the most discrepancy when comparing the different turbulence models and the experimental LDV data. As seen in Figure 45, the ε based models immediately predict a turbulent regime onset, while the ω based models have a delayed turbulent regime onset located before the leading edge of the nozzle, which is further delayed until just before the trailing edge of the nozzle for the transitional model. This indicates the $SST - Transition - CC$ turbulence model is predicting that slightly more than 80% of the nozzle computational domain is laminar after which it transitions rapidly to a turbulent state. The transition model has the highest mean percent error to the experimental LDV data when comparing the RMS of the turbulent velocity fluctuations, as seen in *Table 21*. Interestingly, all the models show a jump in the RMS of the turbulent velocity fluctuations before the nozzle outlet plane as seen in Figure 45. This streamwise location is at the exit of the nozzle suction surface, located at about 95% midspan. Figure 58 (e) shows the nozzle suction surface streamlines of the $SST - Transition - CC$ turbulence model. Comparing the flow topology of this numerical model and that of the experiment found in Figure 57, it is evident that the $SST - Transition - CC$ turbulence model is capable of predicting the laminar boundary layer separation, strong radial pressure gradient, reverse flow, and strong vortex interaction at the hub and shroud. This indicates that the increase in the RMS of the turbulent velocity fluctuations at this location is due to the nozzle wake and its interaction with intense trailing shear layer vortices.

The biggest discrepancy between the different models and the experimental data is

in the prediction of the RMS of the turbulent velocity fluctuations. At the nozzle exit plane, which is 6.6-mm from the midspan trailing edge, it can be inferred through Figure 53, that the experimental data has a peak of the RMS of the turbulent velocity fluctuations at the hub endwall that is more than twice of what any turbulence model predicts. This location is associated with the large absolute velocity deficit at the hub due to secondary flow losses, endwall boundary layer flows, and wake losses, which none of the model were able to properly predict. Also it is seen that the experimental RMS of the turbulent velocity fluctuations is lagged from the rest of the flow from 40.7% to 96.7% span with the lowest value found within these limits. All the turbulence models predict an increase in the RMS of the turbulent velocity fluctuations at the hub, but the $SST - Transtion - CC$ model does not predict the increase at the tip as most of the other models do, but it does predict a drop starting at about 52% span. It is evident that the transition model is predicting laminar flow at the tip of the nozzle exit plane, when in reality it should already be turbulent, as seen in the experimental LDV data. For the other turbulence models the RMS of the turbulent velocity fluctuations is nearly constant from 20% to 80% span, although the ε based model is notably offset from the ω based models.

It is apparent that only the $SST - Transitional - CC$ model employed is capable of predicting the separation induced transition that is encountered in the nozzle, although it is under predicting the turbulent kinetic energy production. The spanwise experimental data clearly shows that at the nozzle exit plane the flow distribution of the RMS of the turbulent velocity fluctuations from hub to tip is indicative of a turbulent flow. When looking at the model as a whole, only this model is capable of predicting the flow in the axial-flow turbine at a low Reynolds number, due to its transition modeling capability.

The experimental data shows that the flow field in just the rotor may be consider fully turbulent, similar to the numerical results for the turbulent models employed. At the rotor exit plane, none of the models are capable of properly predicting the absolute velocity distribution, which is thought to be due to the prediction of the relative flow angle. The transition model does a good job of capturing the absolute velocity distribution as seen in the experiments from 12.67% to 87.33% span, while there is good agreement between all the models in the distribution of the relative velocity. The experimental distribution of the RMS of the turbulent velocity fluctuations at the rotor exit plane show that it lags at the tip, 60% span and hub, as shown in Figure 56. Once more, the $SST - Transition - CC$ turbulence model predicts the same distribution, except close to the hub endwall. Therefore, the $SST - Transition - CC$ turbulence model should be the default choice when modeling the flow field through an axial-flow turbine at a low Reynolds number, due to its advanced capability in predicting separation-induced transition.

7.2. Steady State and Transient Temporal Verification and Validation

7.2.1. Steady State Temporal Verification

The steady state numerical simulation of the $SST - Transition - CC$ turbulence model at a mesh size of 6.91 million elements best replicates the actual flow field of the axial flow turbine at a low Reynolds in this investigation. To confirm the steady state numerical results for this mesh size the steady state timescale has to be refined to quantify its numerical effect. The auto-time scale transformation to a physical time scale allows for a numerical solution for the time scales in *Table 26*, where the largest time scale corresponds to the auto-timescale. If we consider the auto-time scale to be Δt, then the refined time scales correspond to $\Delta t/2$ and $\Delta t/4$, where $\Delta t/4$, the smallest time step,

satisfies the recommendation given in [88], when oscillatory residuals are apparent. The corresponding refinement factors are also shown in *Table 26*, where the temporal discretization refinement factor is modified as follows:

$$rf = \left[\frac{\Delta t_{Coarse}}{\Delta t_{Fine}}\right]^{1} \qquad 7.2$$

Table 26: Steady state physical time scale variation and associated refinement factor

Physical Time scale (Δt)			Refinement Factor	
Largest (Δt)	Medium ($\Delta t/2$)	Smallest ($\Delta t/4$)	rf_{21}	rf_{32}
2.37525e-3 [s]	1.18772e-3 [s]	5.9386e-4 [s]	2.00	2.00

Overall the residual values did not decrease as the time scale was reduced, signifying that the result have relatively loose convergence. Comparison of the residuals at the largest and smallest time scale show that the oscillations of the final 200 to 300 iterations experience the same periodic change, while comparison to the other time scale shows a reduction of about 25% in the oscillation period. The former could be indicative of a transient effect, while the latter is possibly a numerical effect. Going by the results of the largest and smallest time scales, the residual plots show that there is a transient effect in the numerical simulations; hence, a transient simulation is crucial. The reduction of the time scale also reduces the large amplitude of the RMS residuals for the transition momentum thickness Reynolds number as shown in Figure 59. This indicates that the auto-time scale may not be sufficient and a physical time scale smaller than $\frac{0.025}{\omega_a}$ is a more suitable time scale for the steady state simulations, for this particular numerical simulation. As the timescale was refined the amplitude of the mass flow rate surface monitors showed

no considerable pattern, although they appear to keep the same order.

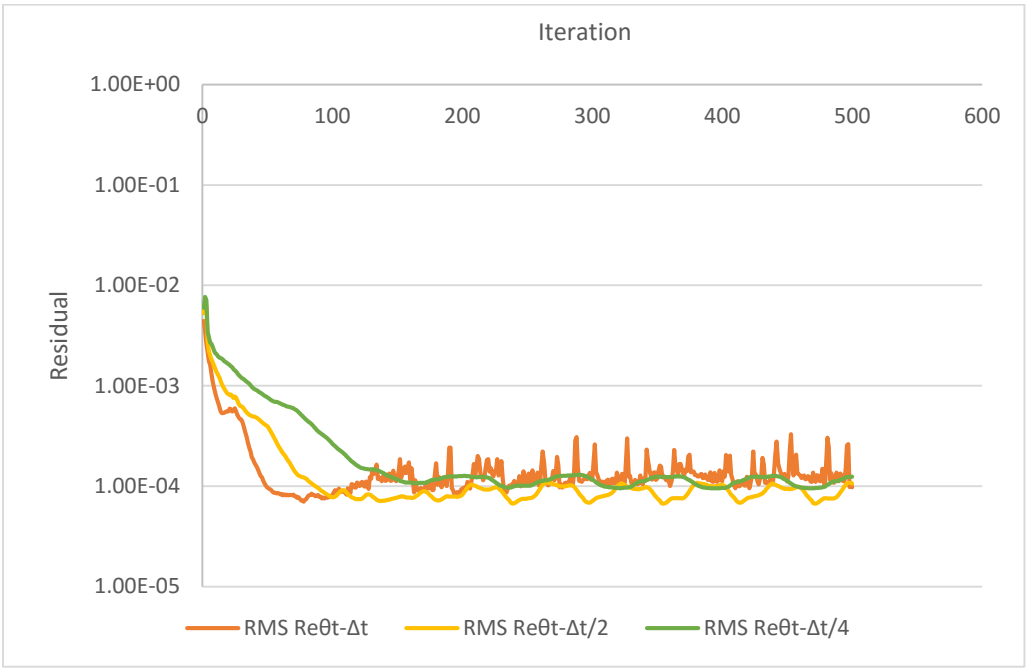

Figure 59: RMS residuals for transition momentum thickness Reynolds number at different time scales ($SST - Transition - CC$, M5)

To determine the numerical uncertainty of refining the steady state time scale the temporal discretization is crucial, although in this case it will be more conservative than the spatial discretization due to its greater refinement factor. *Table 27* shows the exit plane velocities at the different physical time scales. The global GCI shown in *Table 28* for the steady state temporal discretization indicates that there is less than 1% in numerical uncertainty with the reduction of the steady state time scale. The greatest numerical uncertainty is in the determination of the RMS of the turbulent velocity fluctuation, where Figure 60 shows the steady state time scale dependency. Figure 61 shows the local temporal uncertainty for the RMS of the turbulent velocity fluctuations, which indicates that there is marginal improvement as the time scale is reduced.

Table 27: Exit plane velocities at the specified physical time scale ($SST - Transition - CC$, M5)

Physical Time scale	Exit Plane Velocities	
	V_2 (m/s)	W_3 (m/s)
Largest (Δt)	10.93	9.44
Medium ($\Delta t/2$)	10.91	9.43
Smallest ($\Delta t/4$)	10.93	9.43

Table 28: Streamwise global GCI for specified SRQ ($SST - Transition - CC$, M5, steady state temporal discretization)

SRQ	Richardson Nodes (%)	Observed Order p	Global GCI (%)
Absolute Velocity V_{Abs}	34.11	2.63	0.06
Relative Velocity V_{Rel}	45.33	2.44	0.03
Absolute Pressure Loss ΔP_{Abs}	37.89	2.00	0.28
RMS of the Turbulent Velocity Fluctuations **u'**	34.67	1.94	0.94

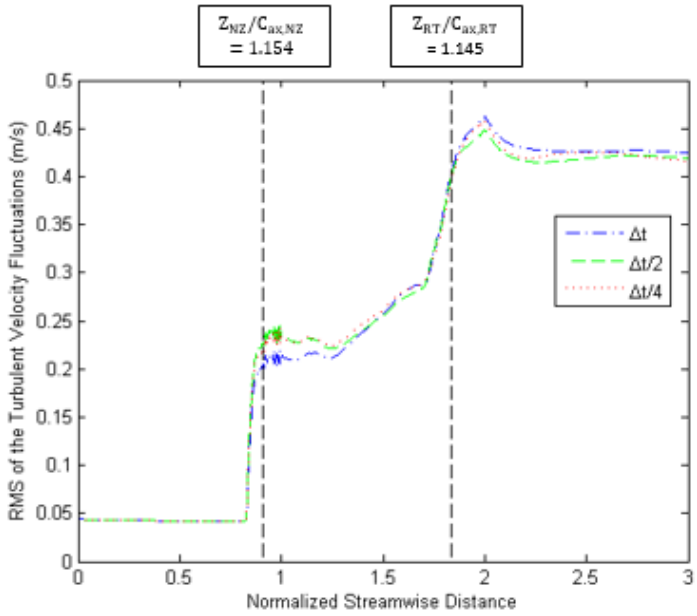

Figure 60: Streamwise steady state temporal dependency study of the RMS of the turbulent velocity fluctuations ($SST - Transition - CC$, M5)

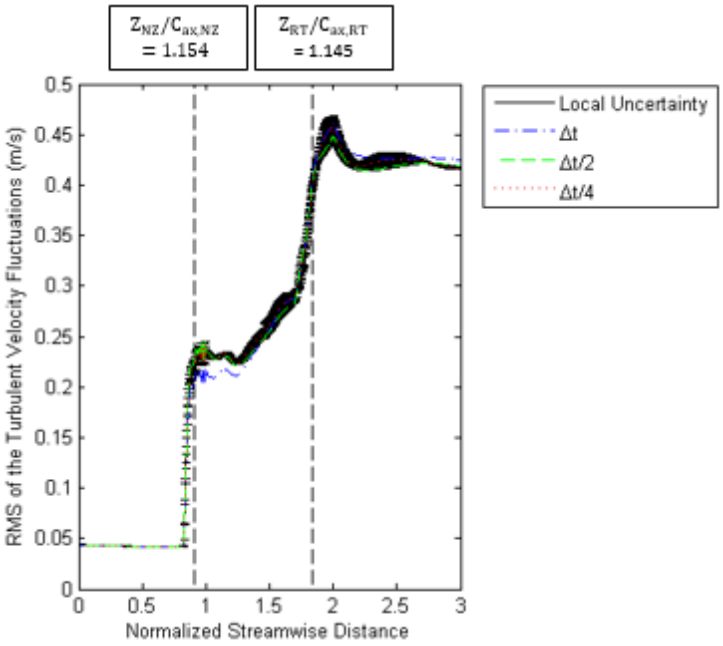

Figure 61: Local steady state temporal uncertainty for RMS of the turbulent velocity fluctuations ($SST - Transition - CC$ M5)

To further validate the steady state temporal results *Table 29* and *Table 30* present the global GCI for the SRQ's at the nozzle and rotor exit planes, respectively. The largest uncertainty is in the prediction of the RMS of the turbulent velocity fluctuations at both

exit planes. Figure 62 and Figure 63 show the RMS of the turbulent velocity fluctuations as a function of the time scale at the nozzle and rotor exit planes, respectively. At the nozzle exit plane the greatest change is found at 50% to 85% span, while at the rotor exit plane they are found from 75% to 95% span and concentrated around 30% span. The velocities at the exit planes only have marginal changes from 60% to 95% span. Therefore, reducing the time scale shows that most of the numerical uncertainty is concentrated in the upper half of the flow closest to the casing, when compared to that at the hub.

Table 29: Spanwise global GCI for specified SRQ at the nozzle exit plane ($Z_{NZ}/C_{ax,NZ} = 1.154$, $SST - Transition - CC$, M5, steady state temporal discretization)

SRQ	Richardson Nodes (%)	Observed Order p	Global GCI (%)
Absolute Velocity V_{Abs}	74.00	1.99	0.11
RMS of the Turbulent Velocity Fluctuations **u'**	23.33	1.70	6.09

Table 30: Spanwise global GCI for specified SRQ at the rotor exit plane ($Z_{RT}/C_{ax,RT} = 1.145$, $SST - Transition - CC$, M5, steady state temporal discretization)

SRQ	Richardson Nodes (%)	Observed Order p	Global GCI (%)
Absolute Velocity V_{Abs}	25.33	1.75	1.43
Relative Velocity V_{Rel}	43.67	1.54	0.98
RMS of the Turbulent Velocity Fluctuations **u'**	53.00	2.11	3.17

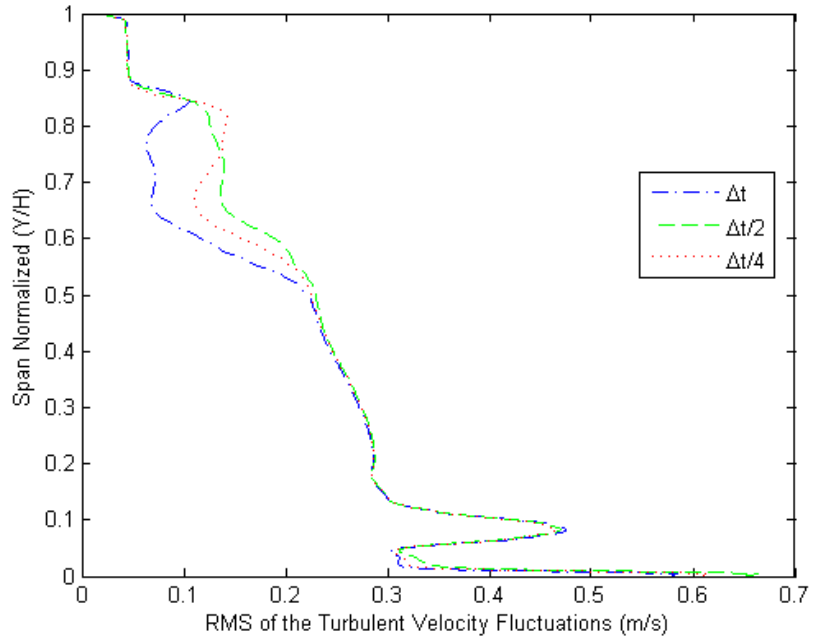

Figure 62: Spanwise steady state temporal dependency study of the RMS of the turbulent velocity fluctuations at the nozzle exit plane ($Z_{NZ}/C_{ax,NZ} = 1.154$, $SST - Transition - CC$, M5)

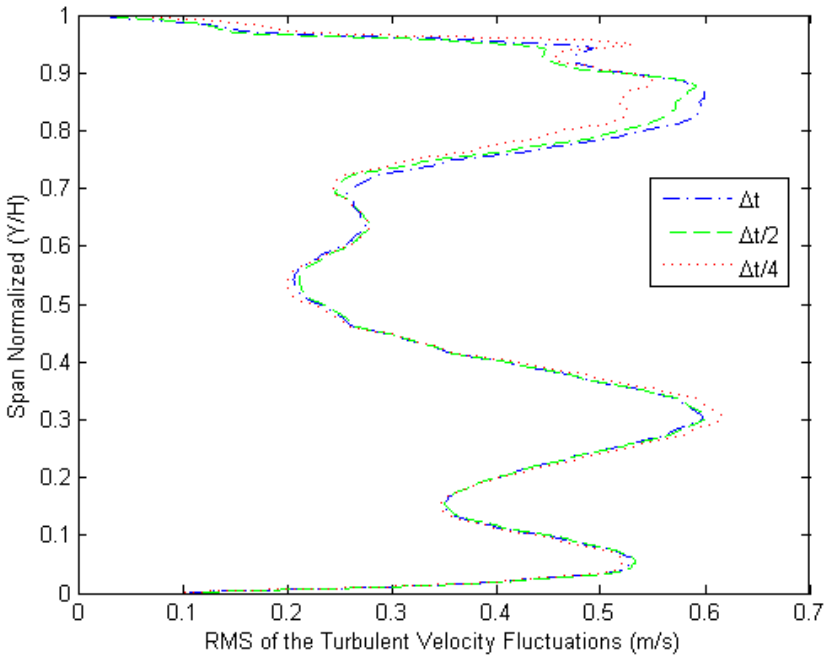

Figure 63: Spanwise steady state temporal dependency study of the RMS of the turbulent velocity fluctuations at the rotor exit plane ($Z_{RT}/C_{ax,RT} = 1.145$, $SST - Transition - CC$, M5)

7.2.2. Transient Temporal Verification

The quantification of the numerical uncertainty of the steady state temporal numerical results of the $SST - Transition - CC$ turbulence model with a mesh size of 6.91 million elements confirms that there is a transient effect present and a transient numerical simulation is crucial in order to replicate the actual flow field of the axial flow turbine at a low Reynolds. To confirm the transient results obtained, the time step has to be reduced to quantify its effect on the numerical predictions, where the steady state results associated with a time scale of $\Delta t/4$ serve as the initial condition to the transient numerical simulations. The time duration is set to 4.8146e-2 seconds to simulate ten rotor pitches, while numerical solutions are obtained for the three different time steps given in *Table 31*, where the largest time step corresponds to the indexing implemented in analyzing the experimental data.

Table 31: Transient time step variation and associated refinement factor

Transient Time step			Refinement Factor	
Largest $\left[\frac{20\pi}{31^2}\Delta t\right]$	Medium $\left[\left(\frac{20}{55}\right)\frac{\pi}{31}\Delta t\right]$	Smallest $\left[\left(\frac{1}{5}\right)\frac{\pi}{31}\Delta t\right]$	rf_{21}	rf_{32}
1.55311e-4 [s]	8.75389e-5 [s]	4.81464e-5 [s]	1.82	1.77

The rotor position is accounted for in the transient simulation at each time step, where each progression has ten inner coefficient loops. Figure 64 shows the residuals for the equations for the final five time steps, which helps to visualize its inner loop progression for the finest time step. It is evident that the inner loops converge successfully, this was confirmed for all the residuals. Figure 65, Figure 66 and Figure 67 show the residuals of the equations for only the outer loop residual at each individual time step for the smallest

time step. All the transient simulations achieved residual values below 1e-5, showing good convergence. *Table 32* shows the exit plane velocities for transient simulations at the different time steps; there was no change as the time step was reduced. Comparisons of the mass flow rate surface monitor at the different domain inlet and outlets show a period of 4.8146e-3 seconds, which corresponds to one rotor pitch, as shown in Figure 68, Figure 69, and Figure 70. The period amplitudes differ between the different time steps, but for the most part they increase as the time step is decreased, where the amplitudes are considerably less than those of the steady state mass flow rate surface monitors.

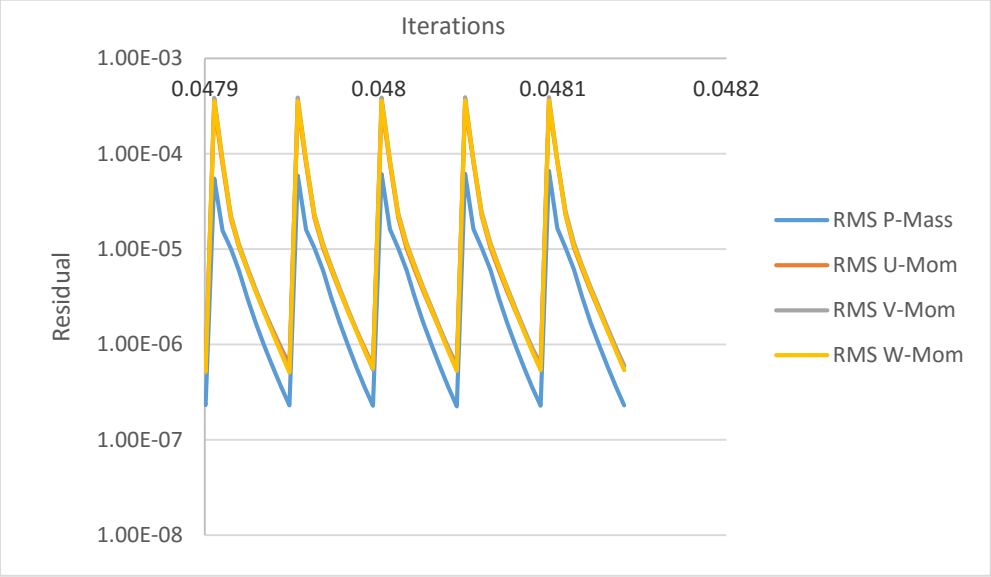

Figure 64: Inner coefficient loops of RMS Residuals for mass continuity and momentum ($SST - Transition - CC$, M5, transient, $\left(\frac{1}{5}\right)\frac{\pi}{31}\Delta t$)

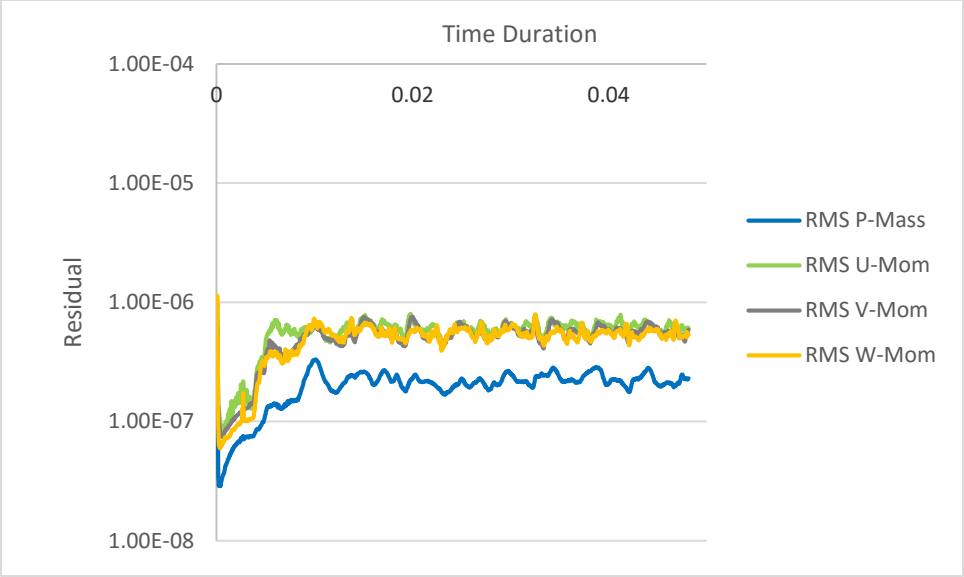

Figure 65: RMS Residuals for mass continuity and momentum ($SST - Transition - CC$, M5, transient, $\left(\frac{1}{5}\right)\frac{\pi}{31}\Delta t$)

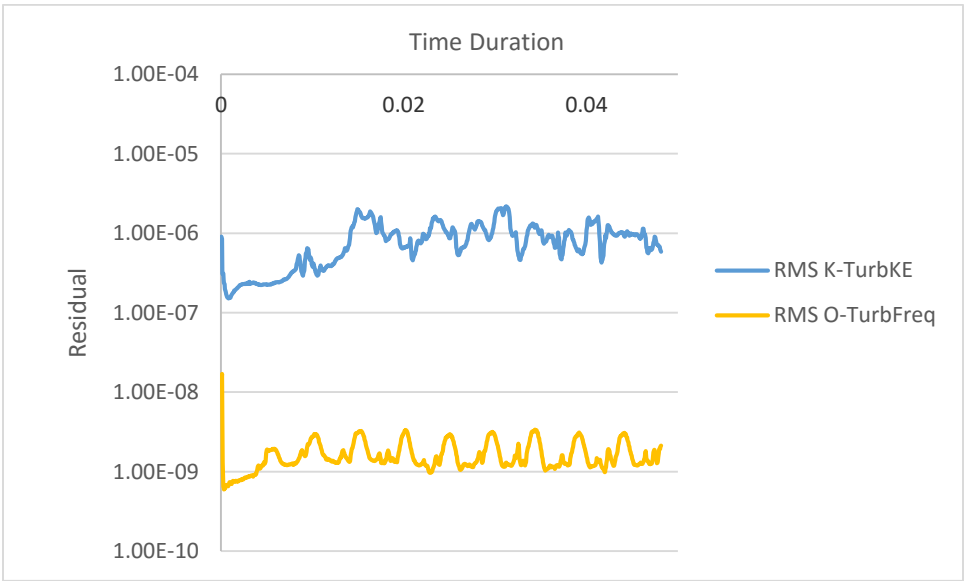

Figure 66: RMS residuals for the turbulent kinetic energy and specific dissipation ($SST - Transition - CC$, M5, transient, $\left(\frac{1}{5}\right)\frac{\pi}{31}\Delta t$)

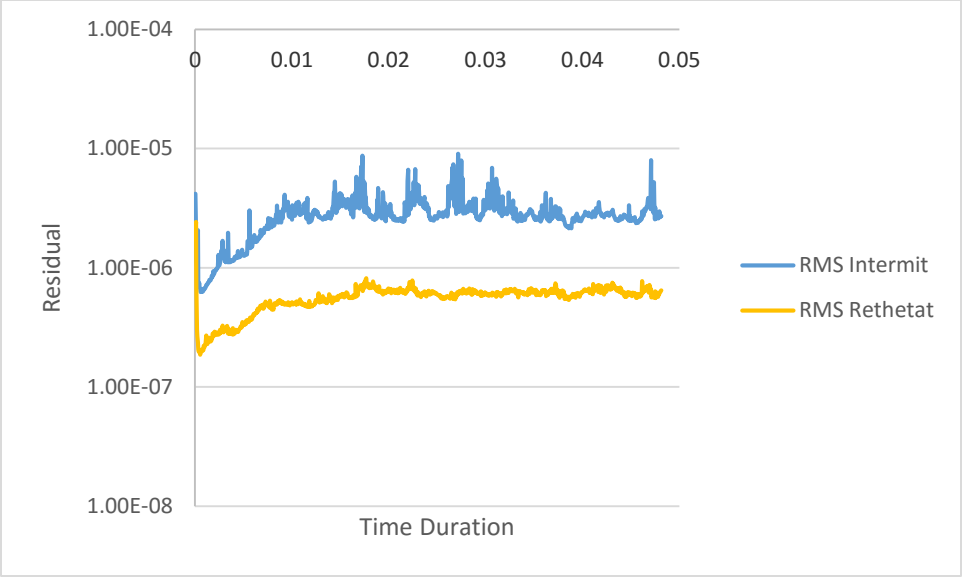

Figure 67: RMS residuals for intermittency and the transition momentum thickness Reynolds number ($SST - Transition - CC$, M5, transient, $\left(\frac{1}{5}\right)\frac{\pi}{31}\Delta t$)

Table 32: Exit Plane velocities at specified time step ($SST - Transition - CC$, M5)

Transient Time step	Exit Plane Velocities	
	V_2 (m/s)	W_3 (m/s)
Largest $\left[\frac{20\pi}{31^2}\Delta t\right]$	10.92	9.40
Medium $\left[\left(\frac{20}{55}\right)\frac{\pi}{31}\Delta t\right]$	10.92	9.40
Smallest $\left[\left(\frac{1}{5}\right)\frac{\pi}{31}\Delta t\right]$	10.92	9.40

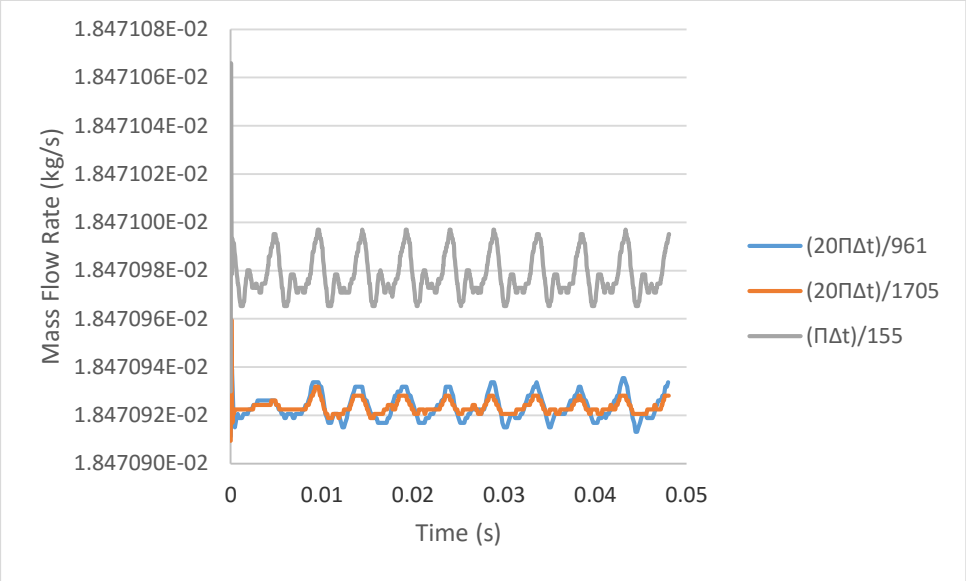

Figure 68: Mass flow rate surface monitor at nozzle exit plane for different time steps ($SST - Transition - CC$, M5)

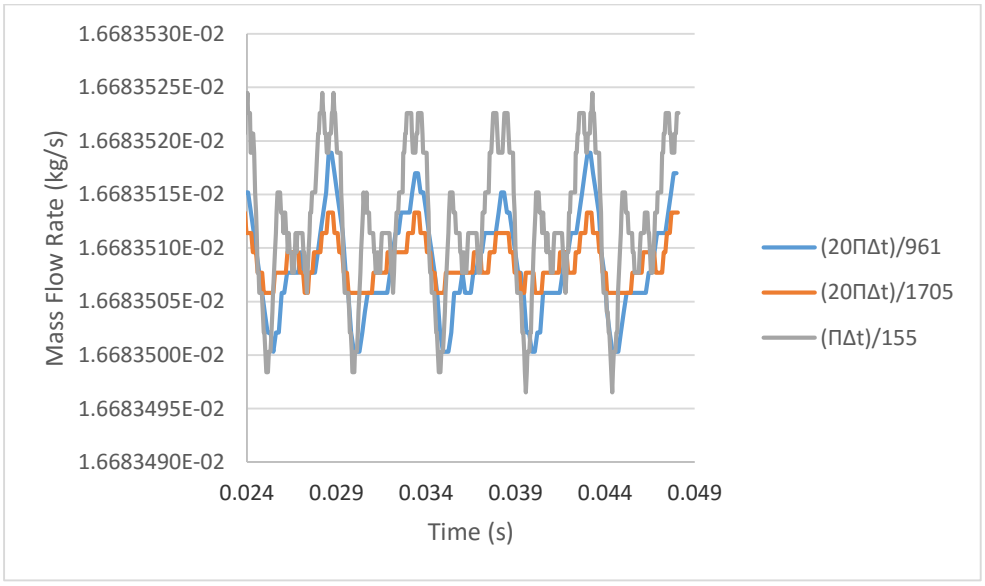

Figure 69: Mass flow rate surface monitor at rotor inlet plane for different time steps ($SST - Transition - CC$, M5)

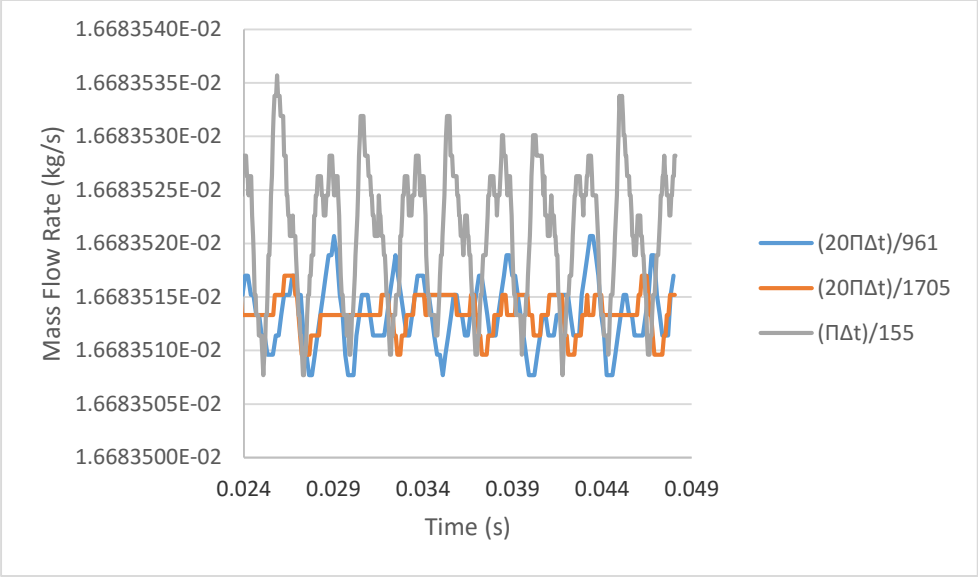

Figure 70: Mass flow rate surface monitor at rotor exit plane for different time steps ($SST - Transition - CC$, M5)

To quantify the transient numerical uncertainty, the time step is decreased, although in this case it will be more conservative than the spatial discretization but less conservative than the steady state temporal discretization, due to higher and lower refinement factor, respectively. The streamwise global GCI shown in *Table 33* for the transient temporal discretization shows that there is less than 0.25% in numerical uncertainty as the time step is reduced. Again the highest numerical uncertainty is found to be in the prediction of the RMS of the turbulent velocity fluctuations. Figure 71 shows the transient time step dependency. Overall the streamwise transient temporal discretization shows a marginal improvement in all the SRQ's as the time step is reduced. The preliminary transient results clearly show that the RMS of the velocity fluctuations is augmented at the mixing planes as more of the transient effects are modeled, this is also apparent for the other SRQ's.

Table 33: Streamwise global GCI for specified SRQ ($SST - Transition - CC$, M5, transient temporal discretization)

SRQ	Richardson Nodes (%)	Observed Order p	Global GCI (%)
Absolute Velocity V_{Abs}	85.44	1.69	0.03
Relative Velocity V_{Rel}	71.67	1.12	0.08
Absolute Pressure Loss ΔP_{Abs}	70.33	2.30	0.01
RMS of the Turbulent Velocity Fluctuations **u**'	86.68	1.50	0.24

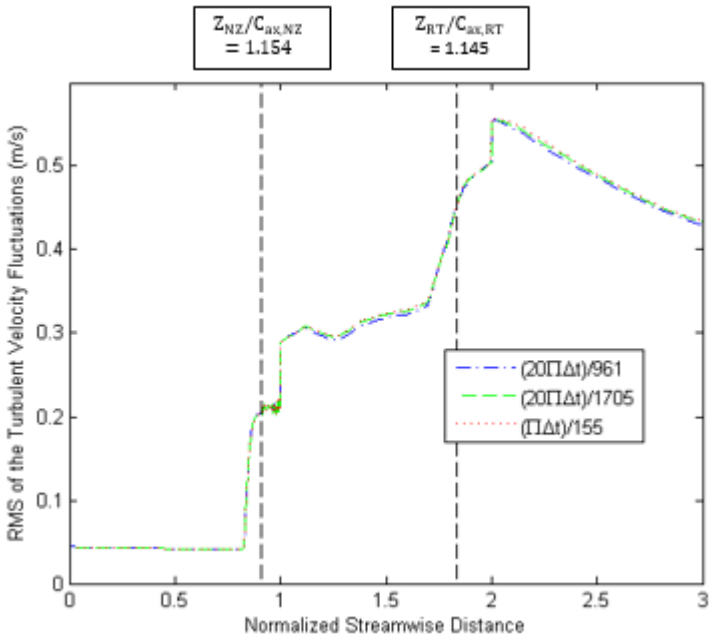

Figure 71: Streamwise transient temporal dependency study of the RMS of the turbulent velocity fluctuations (Transient, $SST - Transition - CC$, M5)

Table 34 and *Table 35* help to further validate the transient temporal results by showing the spanwise global GCI for the SRQ's at the nozzle and rotor exit planes,

respectively. It is evident that at the nozzle exit plane there is almost no variation of the absolute velocity and RMS of the turbulent velocity fluctuations in the spanwise direction as the time step is reduced. At the rotor exit plane the greatest uncertainty is in the prediction of the absolute velocity, while the RMS of the turbulent velocity fluctuations has the next highest uncertainty, although both have a low GCI of less than 1%. Figure 72, Figure 73, and Figure 74 show the spanwise time step dependency of the transient predictions for the specified SRQ's at the rotor exit plane. The time step dependency shows that the greatest variation is found between 75% and 99% span for the absolute velocity, and from 80% to 98% span for the relative velocity. The RMS of the turbulent velocity fluctuations show marginal variation along the span, but has its largest variation concentrated in the upper half of the flow closest to the casing, similar to the temporal steady state predictions.

Table 34: Spanwise global GCI for specified SRQ at the nozzle exit plane ($Z_{NZ}/C_{ax,NZ} = 1.154$, $SST - Transition - CC$, M5, transient temporal discretization)

SRQ	Richardson Nodes (%)	Observed Order p	Global GCI (%)
Absolute Velocity V_{Abs}	70.33	2.38	0.00
RMS of the Turbulent Velocity Fluctuations **u'**	87.67	2.50	0.01

Table 35: Spanwise global GCI for specified SRQ and turbulence model at the rotor exit plane ($Z_{RT}/C_{ax,RT} = 1.145$, $SST - Transition - CC$, M5, transient temporal discretization)

SRQ	Richardson Nodes (%)	Observed Order p	Global GCI (%)
Absolute Velocity V_{Abs}	59.00	1.66	0.87
Relative Velocity V_{Rel}	82.67	1.68	0.23
RMS of the Turbulent Velocity Fluctuations **u'**	63.33	2.56	0.78

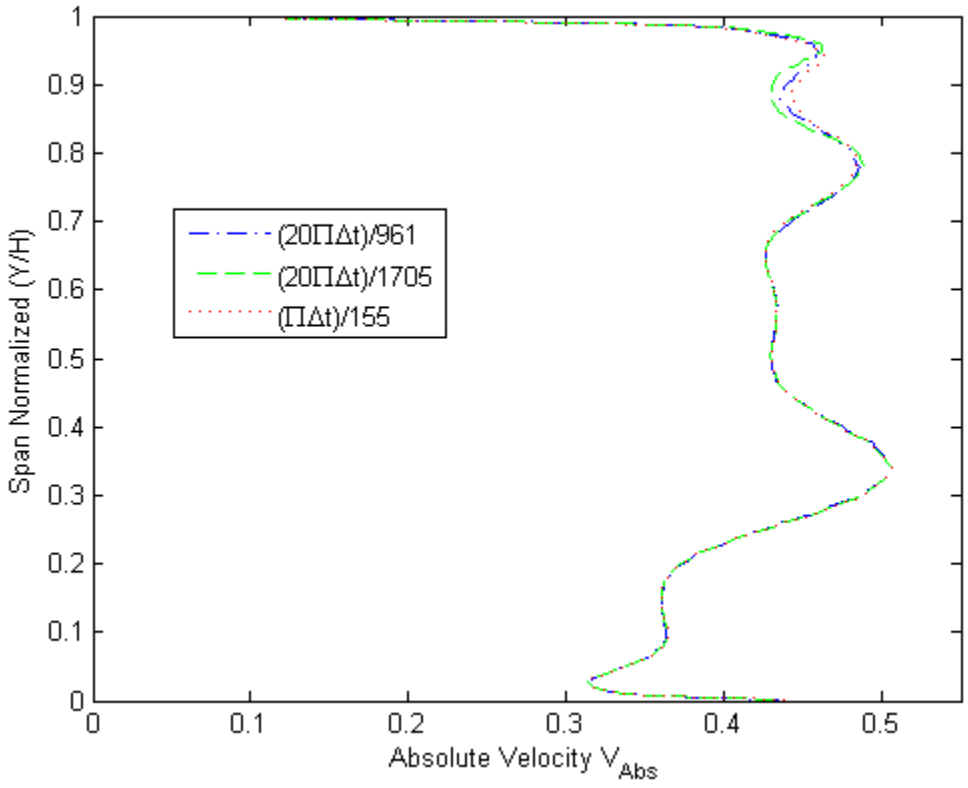

Figure 72: Spanwise transient temporal dependency study of the absolute velocity at the rotor exit plane ($Z_{RT}/C_{ax,RT} = 1.145$, $SST - Transition - CC$, M5)

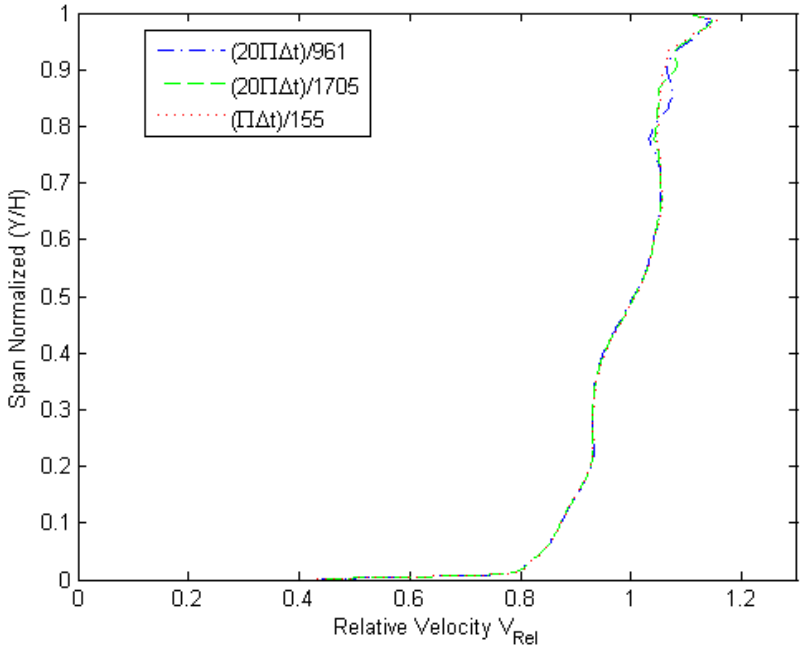

Figure 73: Spanwise transient temporal dependency study of the relative velocity at the rotor exit plane ($Z_{RT}/C_{ax,RT} = 1.145$, $SST - Transition - CC$, M5)

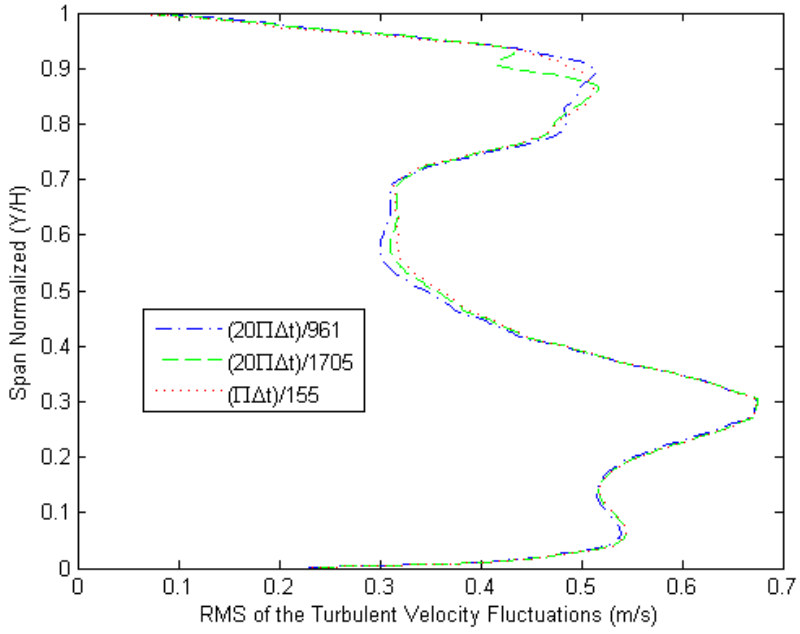

Figure 74: Spanwise transient temporal dependency study of the RMS of the turbulent velocity fluctuations at the rotor exit plane ($Z_{RT}/C_{ax,RT} = 1.145$, $SST - Transition - CC$, M5)

7.2.3. Transient and Steady State Temporal Validation

Validation of the transient and steady state solutions at the smallest time step and time scale, respectively, is accomplished by comparing these numerical results to the experimental results of Matsunuma [24]. Figure 75, Figure 76 and Figure 77 compare the selected SRQ's to the experimental data for the steady state results at a time scale of $\Delta t/4$ and the transient results at a time step of $\left(\frac{1}{5}\right)\frac{\pi}{31}\Delta t$. The biggest differences are found in the prediction of the streamwise distribution of the RMS of the turbulent velocity fluctuations between the two models, where the transient predictions are offset due to the transient effect that is accounted for at the mixing planes. Figure 78 compares the numerical results of the absolute pressure loss for the steady state predictions at a time scale of $\Delta t/4$ and the transient predictions at a time step of $\left(\frac{1}{5}\right)\frac{\pi}{31}\Delta t$.

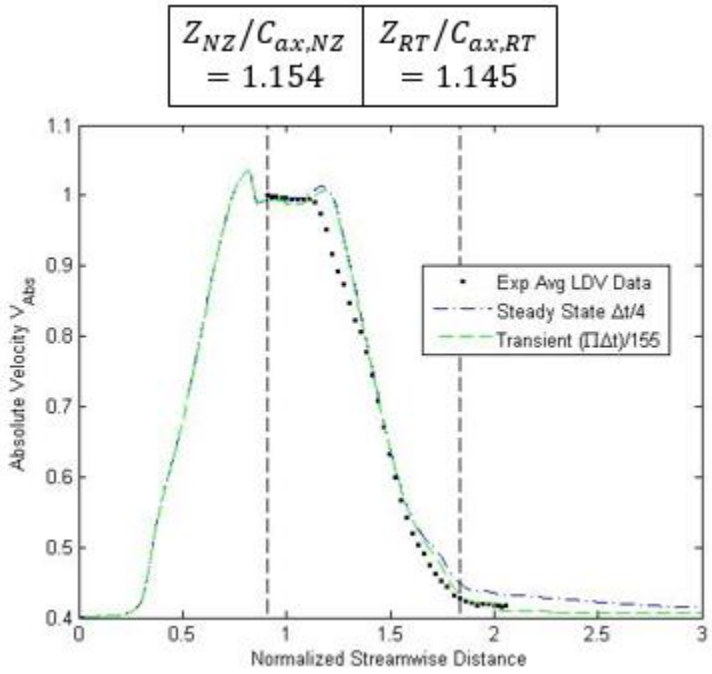

Figure 75: Streamwise distribution of the absolute velocity with comparison to experiment (steady state – $\Delta t/4$ and transient - $\left(\frac{1}{5}\right)\frac{\pi}{31}\Delta t$)

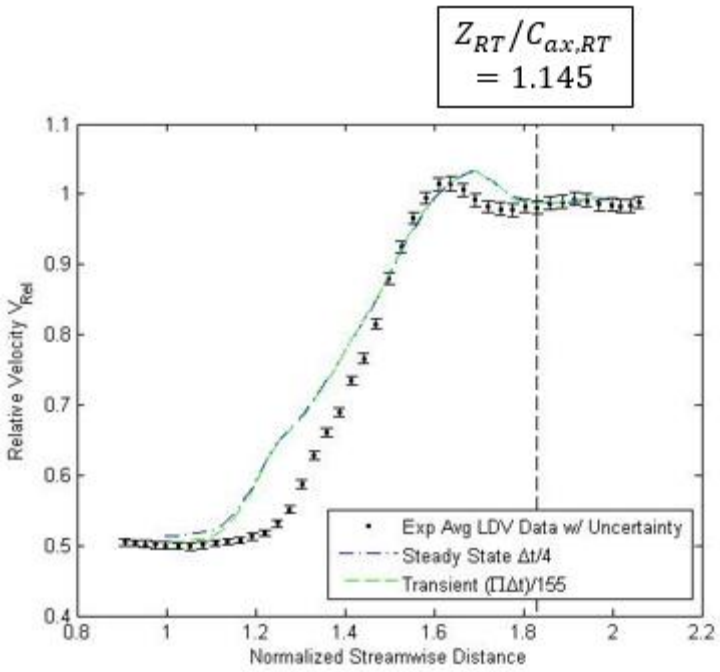

Figure 76: Streamwise distribution of the relative velocity with comparison to experiment (steady state – $\Delta t/4$ and transient - $\left(\frac{1}{5}\right)\frac{\pi}{31}\Delta t$)

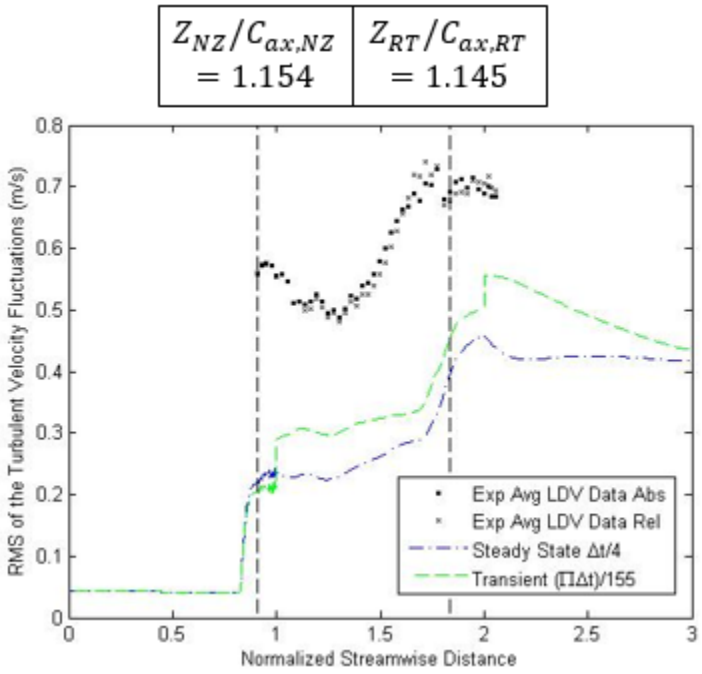

Figure 77: Streamwise distribution of the absolute pressure loss with comparison to experiment (steady state – $\Delta t/4$ and transient - $\left(\frac{1}{5}\right)\frac{\pi}{31}\Delta t$)

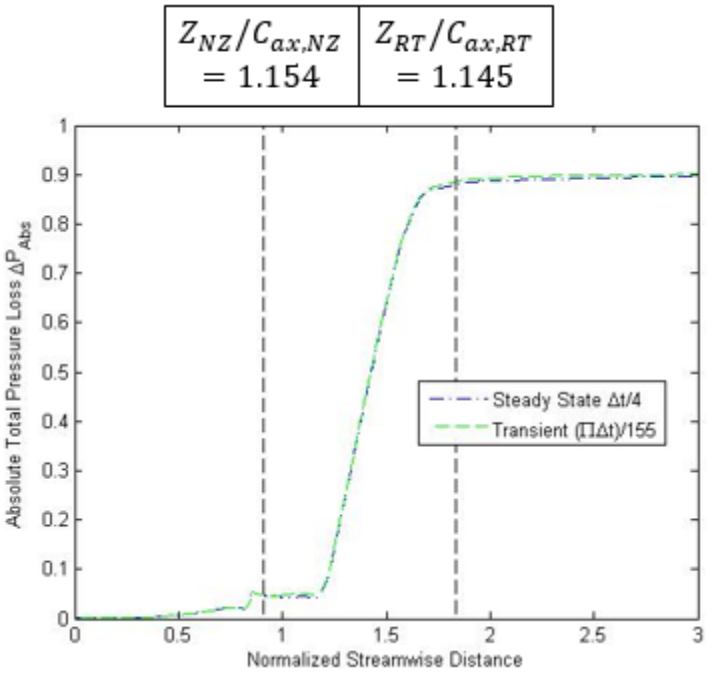

Figure 78: Streamwise distribution of the RMS of the turbulent velocity fluctuations with comparison to experiment (steady state – $\Delta t/4$ and transient - $\left(\frac{1}{5}\right)\frac{\pi}{31}\Delta t$)

Table 36 compares the mean error of the selected SRQ's to the experimental LDV data of both model solutions in the streamwise direction to help determine which one best predicts the actual flow field of the axial flow turbine at a low Reynolds number. For the most part, the reduction in time scale and time step of the numerical simulation further reduces the mean percent error of the predictions, when compared to the steady state results at a time scale of Δt in *Table 20*. Especially in the transient prediction of the streamwise averaged absolute velocity, relative velocity, and RMS of the turbulent velocity fluctuations. The transient predictions of the RMS of the turbulent velocity fluctuations reduce the mean percent error to a range of 32% to 41%, compared to 44% to 52% for the steady state results. The low global GCI's of the RMS of the turbulent velocity fluctuations as determined from the numerical simulations, as given in *Table 33*, *Table 34* and *Table 35*, indicate that the mean percent errors, shown in *Table 36*, do not decrease significantly

as the time scale and time step is reduced. The results show the importance of the spatial mesh refinement in comparison to the steady state time scale and transient time step reduction.

Table 36: Mean error for the specified SRQ's in the streamwise direction (steady state – $\Delta t/4$ and transient - $\left(\frac{1}{5}\right)\frac{\pi}{31}\Delta t$)

SRQ	Turbulence Model	Mean % Error	
Absolute Velocity V_{Abs}	$SST - Transition - CC - Transient$	2.44	
	$SST - Transition - CC - Steady\ State$	3.59	
Relative Velocity V_{Rel}	$SST - Transition - CC - Transient$	5.27	
	$SST - Transition - CC - Steady\ State$	5.61	
		Experimental LDV Abs	Experimental LDV Rel
RMS turbulent velocity fluctuations **u**'	$SST - Transition - CC - Transient$	32.13	40.69
	$SST - Transition - CC - Steady\ State$	44.42	51.45

To further validate the numerical predictions, the spanwise distributions are compared to the experimental LDV data. Figure 79 shows the spanwise distribution of the absolute velocity of the transient and steady state numerical results compared to the experimental LDV and 5-hole pressure probe data at the nozzle exit plane. Both models predict the same distribution, except between 67.4% and 87.4% span. Figure 80, shows the spanwise distribution of RMS of the turbulent velocity fluctuations for both models compared to the LDV data at the nozzle exit plane, where the difference in the spanwise distribution of both model is found from 50 to 87.4% span. *Table 37* shows the mean

percent error between both models and the experimental data at the nozzle exit plane. Both models show marginal improvement to the numerical predictions at the nozzle exit plane compared to the steady state predictions at a time scale of Δt, given in *Table 24*. The mean absolute velocity mean errors are slightly increased for both models, and the prediction of the RMS of the turbulent velocity fluctuations for the steady state results has the lower mean error at the nozzle exit plane. The transient results confirm that the flow within the nozzle domain is mostly steady. Both models under predict the velocity deficit and the RMS of the turbulent velocity fluctuations due to the secondary flow losses, endwall boundary layer flows, and wake losses.

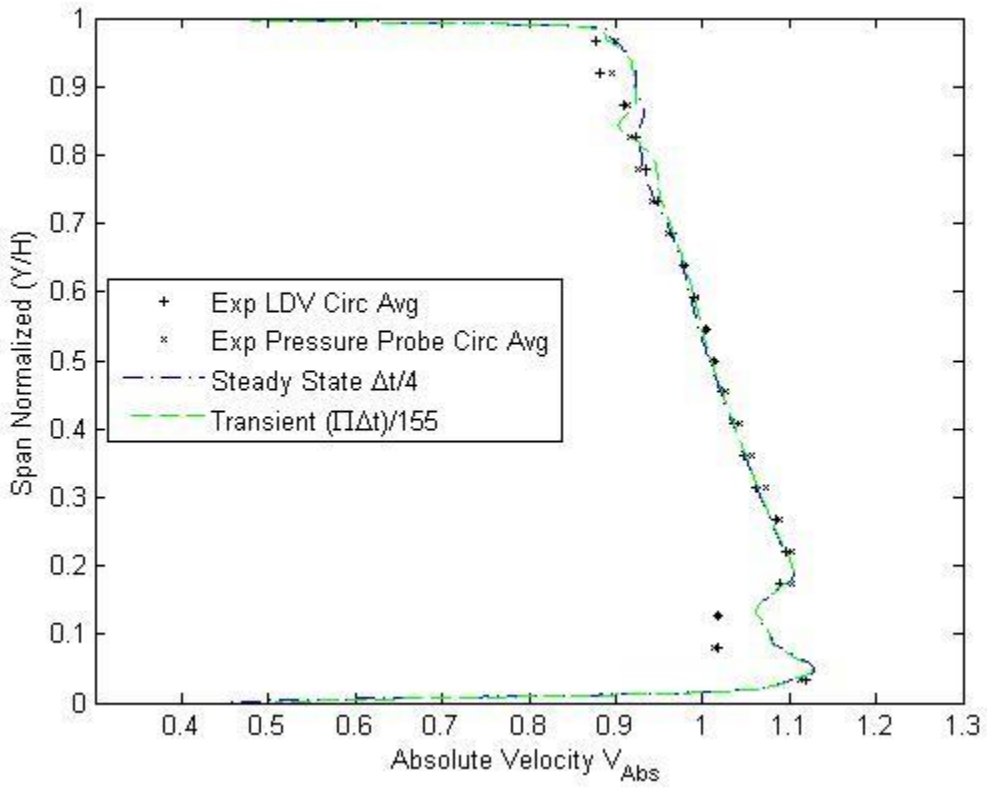

Figure 79: Spanwise distribution of the absolute velocity with comparison to experiment at the nozzle exit plane ($Z_{NZ}/C_{ax,NZ} = 1.154$, steady state – $\Delta t/4$ and transient - $\left(\frac{1}{5}\right)\frac{\pi}{31}\Delta t$)

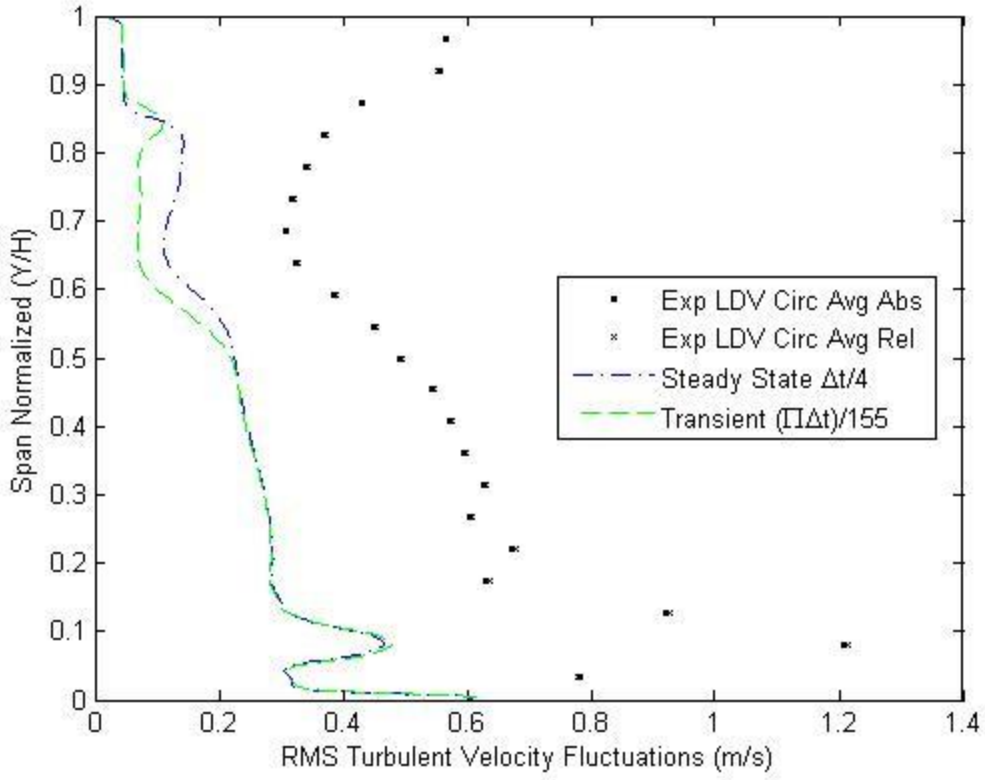

Figure 80: Spanwise distribution of the RMS of the turbulent velocity fluctuations with comparison to experiment at the nozzle exit plane ($Z_{NZ}/C_{ax,NZ} = 1.154$, steady state – $\Delta t/4$ and transient - $\left(\frac{1}{5}\right)\frac{\pi}{31}\Delta t$)

Table 37: Mean error in the spanwise direction at the nozzle exit plane ($Z_{NZ}/C_{ax,NZ} = 1.154$ for steady state – $\Delta t/4$ and transient - $\left(\frac{1}{5}\right)\frac{\pi}{31}\Delta t$)

SRQ	Turbulence Model	Mean % Error	
		Experimental LDV	Experimental Pressure Probe
Absolute Velocity V_{Abs}	$SST - Transition - CC - Transient$	1.19	1.29
	$SST - Transition - CC - Steady\ State$	1.26	1.31
		Experimental LDV Abs	Experimental LDV Rel
RMS turbulent velocity fluctuations **u'**	$SST - Transition - CC - Steady\ State$	63.17	63.39
	$SST - Transition - CC - Transient$	67.83	68.02

The rotor exit plane spanwise distributions of the absolute and relative velocities for both models compared to the experimental LDV data are shown in Figure 81 and Figure 82, respectively. The transient numerical predictions seem to best replicate the absolute velocity distribution close to the casing between 45.3% to 96.7% span, while the main difference between the relative velocity predictions of the models is concentrated around 92% span. Figure 83 shows the spanwise distribution of the RMS of the turbulent velocity fluctuations in comparison to the experimental LDV data for both models. The transient results mostly predict a higher velocity fluctuation with a smoother profile, when compared to the steady state results. *Table 38* shows the mean percent error calculated between the models and the experimental LDV data at the rotor outlet plane. Again, the transient numerical simulation produces a mean percent error that is less than the steady state results. Most significantly the mean percent error of the absolute velocity and RMS of the velocity fluctuations is reduced by almost 50% and 24%, respectively, when compared to the steady state results obtained at the smallest time scale. The results confirm that the flow field within the rotor domain must be unsteady or transient, thus justifying the transient simulation.

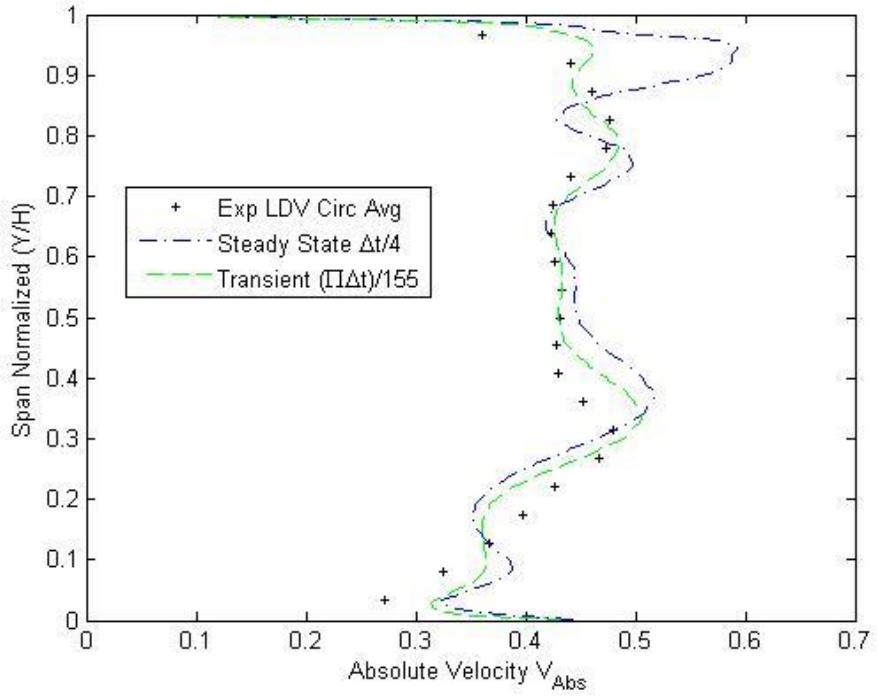

Figure 81: Spanwise distribution of the absolute velocity with comparison to experiment at the rotor exit plane ($Z_{RT}/C_{ax,RT} = 1.145$, steady state – $\Delta t/4$ and transient - $\left(\frac{1}{5}\right)\frac{\pi}{31}\Delta t$)

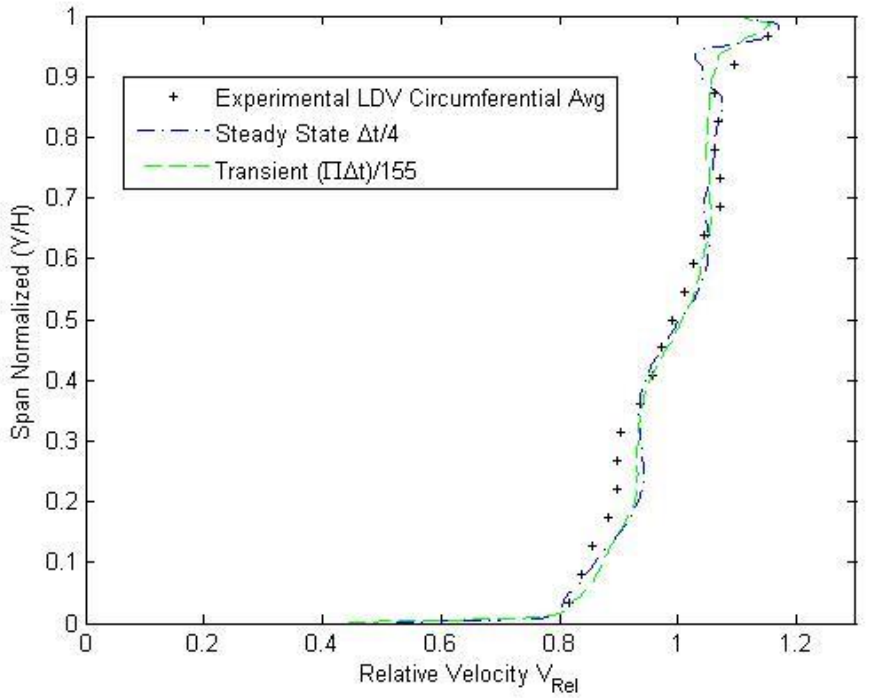

Figure 82: Spanwise distribution of the relative velocity with comparison to experiment at the rotor exit plane ($Z_{RT}/C_{ax,RT} = 1.145$, steady state – $\Delta t/4$ and transient - $\left(\frac{1}{5}\right)\frac{\pi}{31}\Delta t$)

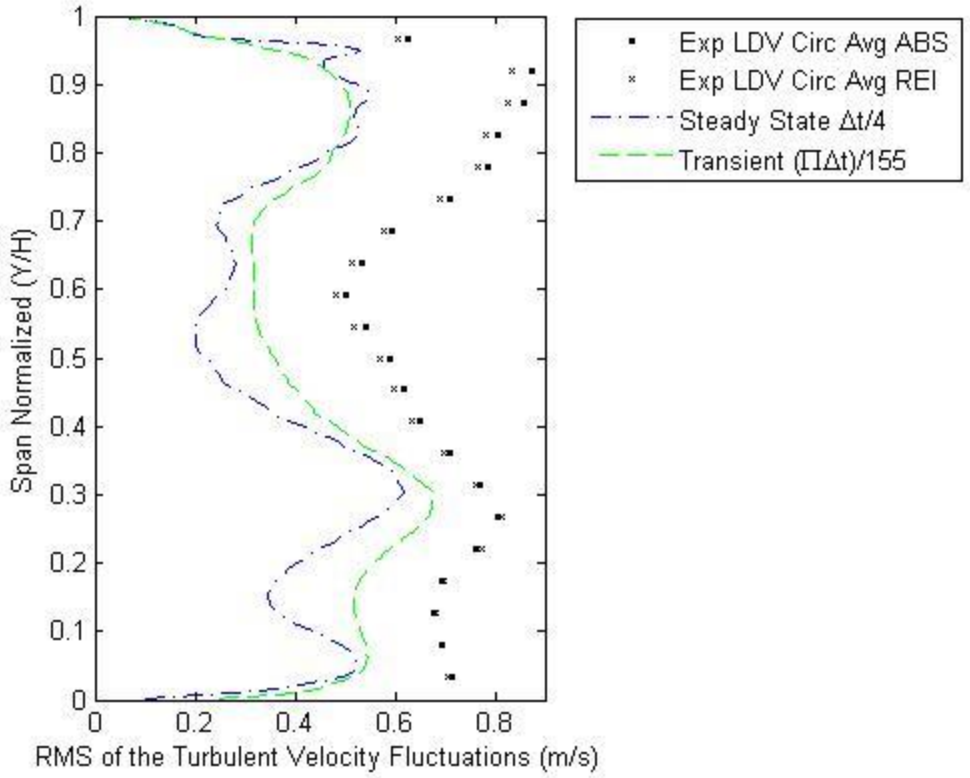

Figure 83: Spanwise distribution of the RMS of the turbulent velocity fluctuations with comparison to experiment at the rotor exit plane ($Z_{RT}/C_{ax,RT} = 1.145$, steady state – $\Delta t/4$ and transient - $\left(\frac{1}{5}\right)\frac{\pi}{31}\Delta t$)

Table 38: Mean error in the spanwise direction at the rotor exit plane ($Z_{RT}/C_{ax,RT} = 1.145$ for steady state – $\Delta t/4$ and transient - $\left(\frac{1}{5}\right)\frac{\pi}{31}\Delta t$)

SRQ	Turbulence Model	Mean % Error	
Absolute Velocity V_{Abs}	$SST - Transition - CC - Transient$	5.57	
	$SST - Transition - CC - Steady\ State$	10.82	
Relative Velocity V_{Rel}	$SST - Transition - CC - Transient$	1.95	
	$SST - Transition - CC - Steady\ State$	1.96	
		Experimental LDV Abs	Experimental LDV Rel
RMS turbulent velocity fluctuations **u'**	$SST - Transition - CC - Transient$	34.04	32.75
	$SST - Transition - CC - Steady\ State$	44.42	43.31

7.2.4. Steady State and Transient Model Discussion

The flow field of axial flow turbine at a low Reynolds number was determined to be best predicted by the $SST - Transition - CC$ turbulence model. This is accredited to its transition modeling capabilities, as it was confirmed that the flow field in the nozzle is initially laminar then transitions to a turbulent flow regime within the rotor. The five steady state numerical cases at a fixed time scale of Δt for the five different meshes shows that there is a large numerical uncertainty associated with the prediction of the RMS of the turbulent velocity fluctuations, but a considerably lower numerical certainty is associated with the prediction of the absolute velocity, relative velocity, and absolute pressure loss. In order to decrease the numerical uncertainty of the RMS of the turbulent velocity fluctuations the spatial mesh has to be refined further, surpassing a total mesh size of seven

million elements, which is approximately the finest mesh size used for the steady state predictions presented here. To further validate the steady state results at the highest mesh size the time scale was reduced, as shown in the steady state temporal verification analysis. Reducing the time scale increased the overall simulation time, hence the computational requirements increase, while using the same amount of computational resources, as shown in Figure 84. The low numerical uncertainty for these results confirmed that the predictions made are converging towards a common solution.

Figure 84: CPU requirement vs host memory allocation ($SST - Transition - CC$, M5, steady state time scale dependency)

Finally, with the steady state results at a time scale of $\Delta t/4$ confirmed to give results with a low numerical uncertainty for a spatial mesh of 6.91 million, M5, the transient numerical results may be obtained. The time step dependency of these results was also shown to give a low numerical uncertainty at the largest time step of $\left(\frac{1}{5}\right)\frac{\pi}{31}\Delta t$. These predictions came at a significant cost in computational time and increased computational resources, as shown in Figure 85. The transient numerical simulation at the largest time step of $\left(\frac{1}{5}\right)\frac{\pi}{31}\Delta t$ took roughly 195 hours of computational time to obtain, when compared

to 10 hours for the steady state simulation at a time scale of $\Delta t/4$. The results obtained clearly show that the spatial mesh discretization is significantly more important than the temporal discretization. If the spatial mesh can be properly discretized the results obtained will have a low numerical uncertainty, which helps verify the numerical predictions. It is essential that this is done first due to the significantly larger computational time and resources needed for transient simulations. A transient simulation is essentially crucial as the flow is unsteady in the rotor, and it was shown to give better results in predicting the actual flow field in the rotor, when compared to the steady state numerical predictions.

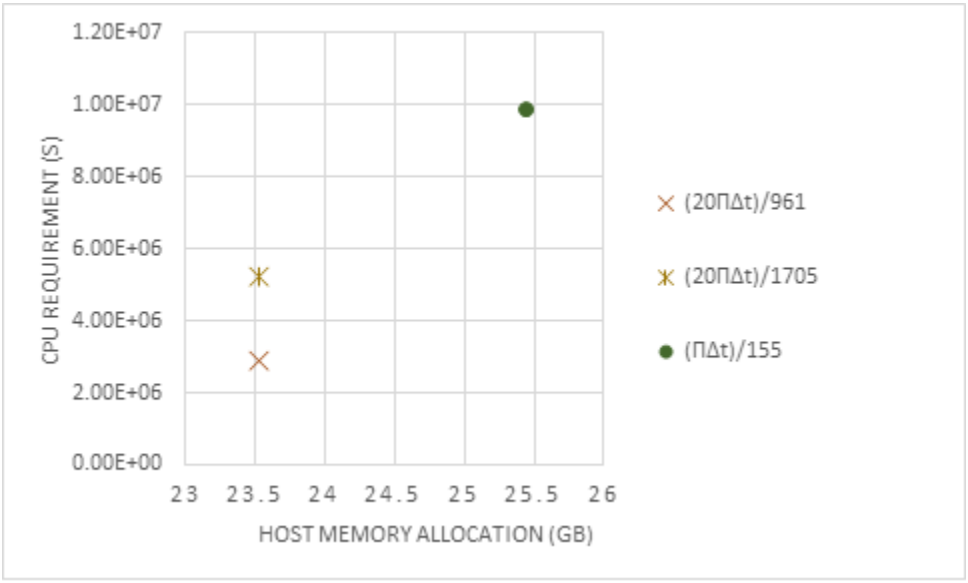

Figure 85: CPU requirement vs host memory allocation ($SST - Transition - CC$, M5, transient time step dependency)

8. FLOW FIELD ANALYSIS AND DISCUSSION

In this section, an attempt at depicting the flow field found in the region of interest is accomplished by examining the flow topology of the skin friction and vorticity fields, as well as the use of several contour plots achieved by post-processing the numerical data. At the nozzle exit plane, it was found that the transient and steady state $SST - Transition - CC$ turbulence models, for the most part, predict the same spanwise distribution of the absolute velocity and RMS of the turbulent velocity fluctuations as seen in Figure 79, Figure 80, and *Table 37*. The minor difference between the flow fields is found closer to the shroud or upper half of the flow, this is attributed to the transient modeling of the potential field of the downstream rotor. This helps to confirm that the flow in the nozzle is operating in a steady state fashion. To help describe the flow endwall topology in the nozzle passage the skin friction and vorticity field at the tip and hub walls of the nozzle are shown in Figure 86 and Figure 87, respectively. Three nozzle pitches are shown for reference to help visualize the flow.

The topologies at both respective ends show that as the flow enters the nozzle blade passage it is split into two distinct three-dimensional families around the nozzle airfoil, separated by the reattachment line R that is associated with the saddle point A. The separation line S is also associated with the saddle point A, which pertains to the boundary layer separation upstream of the primary horseshoe vortex. The reattachment line divides the suction side (S_S) and pressure side (S_P) flows found in the formation of the multi-horseshoe vortex system. The horseshoe vortex forms due to the inlet boundary layer

approaching the leading edge of the nozzle, here the flow undergoes three-dimensional separation. The wall shear and vorticity field show that there is a multi-horseshoe vortex formation in front of the leading edge, where the hub and tip flow topologies show a double and triple separations, respectively. These separation lines in front of the leading edge are indicative of the amount of saddle points found along the reattachment line; for every saddle point separation line there is one attachment line. The fact that the horseshoe vortex isn't a single structure correlates well with the data found by Wang et al. [26].

The low Reynolds number inlet flow condition is the main culprit that causes different flow structures to take place. The hub side flow in front of the leading edge is similar to that described by Sieverding [31], as it also shows two saddle points along the reattachment line R. The schematic in Figure 88 shows the flow topology in the plane of symmetry, where the second saddle point is after the first nodal point of attachment. The separation line associated with the second saddle point pertains to the lift off line of the primary horseshoe vortex system. The symmetry plane topology clearly shows that at the hub side there are three horseshoe vortices formed in front of the leading edge, identical to the horseshoe vortex structures found in other studies [95] and showing the same separation seen in front of obstacles [96]. The tip side flow shows that there are three saddle points, where the upstream separation line closest to the leading edge pertains to the primary horseshoe vortex system, identical to the hub side flow. The primary horseshoe vortex at the nozzle hub has a clockwise direction for the pressure side leg, opposite to the primary horseshoe vortex found at the nozzle tip. In both cases the adjacent suction side leg has an opposite sense of rotation to the pressure side leg. Contrary to Matsunuma [24], the potential influence of the nozzle may actually effect the inlet measurements, specifically

close to the hub endwall, as Figure 87 shows that at the nozzle inlet there is a separation and attachment line; just ahead of the multi-horseshoe vortex system formation. Therefore, to prevent any potential influence of the nozzle, the inlet measurement plane should be moved upstream further than its current position of 30-mm from the nozzle leading edge mid-span.

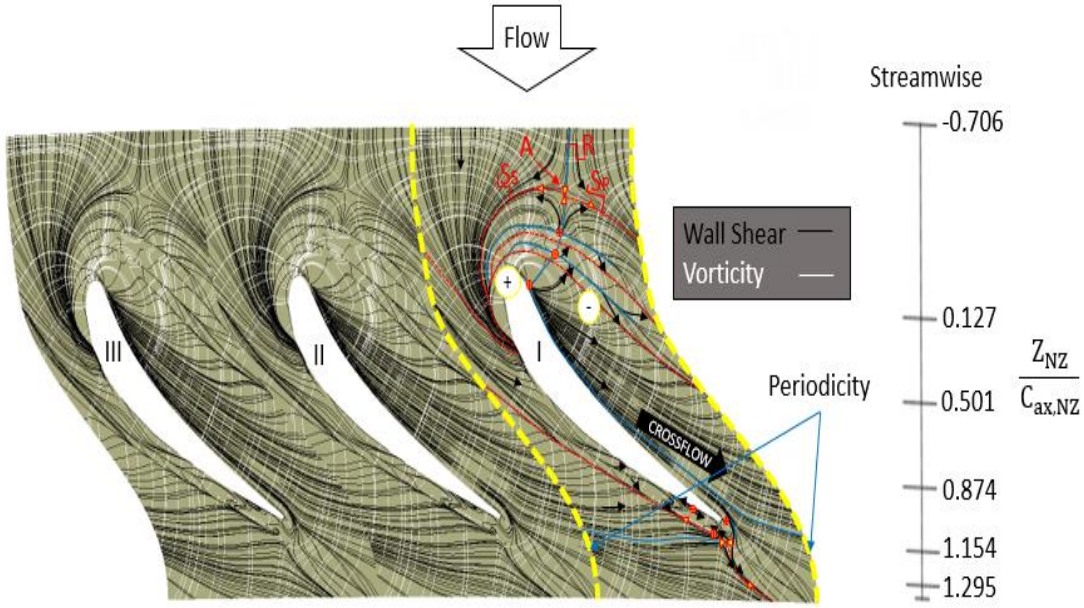

Figure 86: Nozzle tip topology (steady state – $\Delta t/4$)

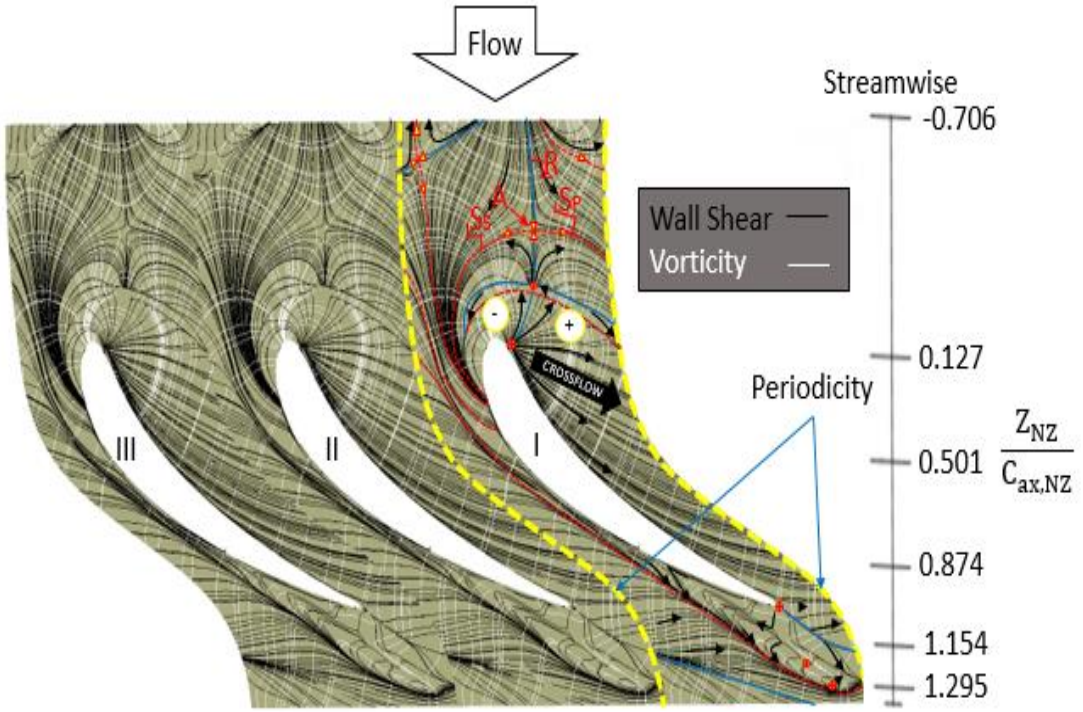

Figure 87: Nozzle hub topology (steady state – $\Delta t/4$)

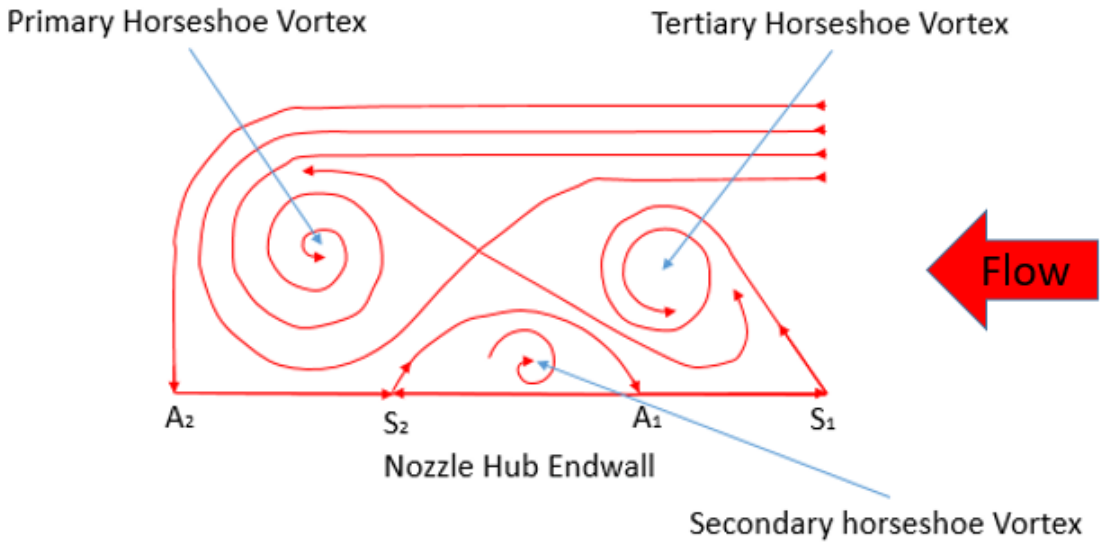

Figure 88: Nozzle hub endwall flow

The hub and tip side surface flows show distinct features of the horseshoe formation ahead of the leading edge, but immediately downstream of this formation they show very similar characteristics. Specifically, that the crossflow creates a strong

transverse pressure gradient from the pressure surface to the suction surface. This drives the pressure side leg towards the suction surface, where it is amplified due to the endwall boundary layer flow and the main flow to form the passage vortex that keeps the same sense of rotation. The passage vortex then travels along the suction surface to the passage exit. The suction side leg convects to the suction side, as seen by the large concentration of streamlines; it also travels along the suction surface, as well as interacting with the passage vortex; this is also where the separation lines meet.

To help describe the characteristics of the flow near the nozzle blade surface the suction and pressure surface wall shear and vorticity field streamlines are shown in Figure 89. The pressure surface flow shows that the there is a spanwise attachment line along the leading edge, with the nodal attachment node found to be close to the tip; at about 85% Span. The streamlines emanate from the leading edge attachment line; along the pressure surface they form mostly parallel geodesic lines. The suction surface flow topology shows that after the flow attaches on the leading edge it experiences a strong inward radial pressure gradient. Then, there is a strong interaction of the tip and hub passage vortices close to their respective endwalls. Next, the flow topology shows that the blade surface flow separates at the tip trailing edge at about 88% span and along the suction surface at the hub, close to the trailing edge at about 9% span. It appears that the suction surface downwash feeds the hub side trailing shear layer vortices. Figure 90 shows the wall shear and vorticity field at the mid-span plane of the nozzle passage. The flow field at the mid-span shows an ideal behavior as the flow is split at the leading edge stagnation point, here the streamlines split into the two passages that flow along the pressure and suction surface

to the exit of the passage. Compared to the endwall topology, the flow at the mid-span does not show strong three-dimensional characteristics.

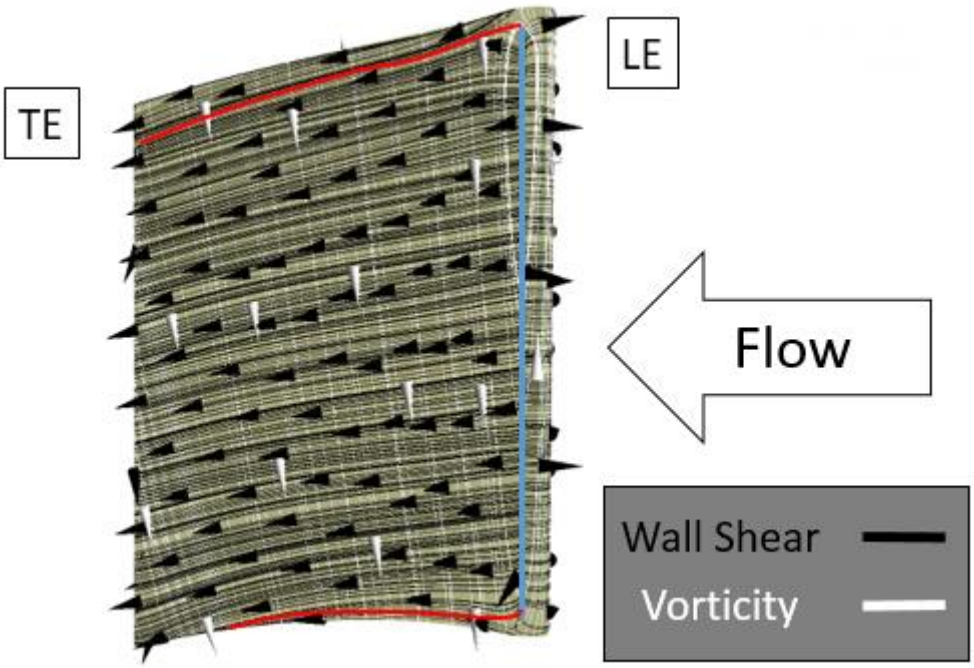

(a) Pressure Surface

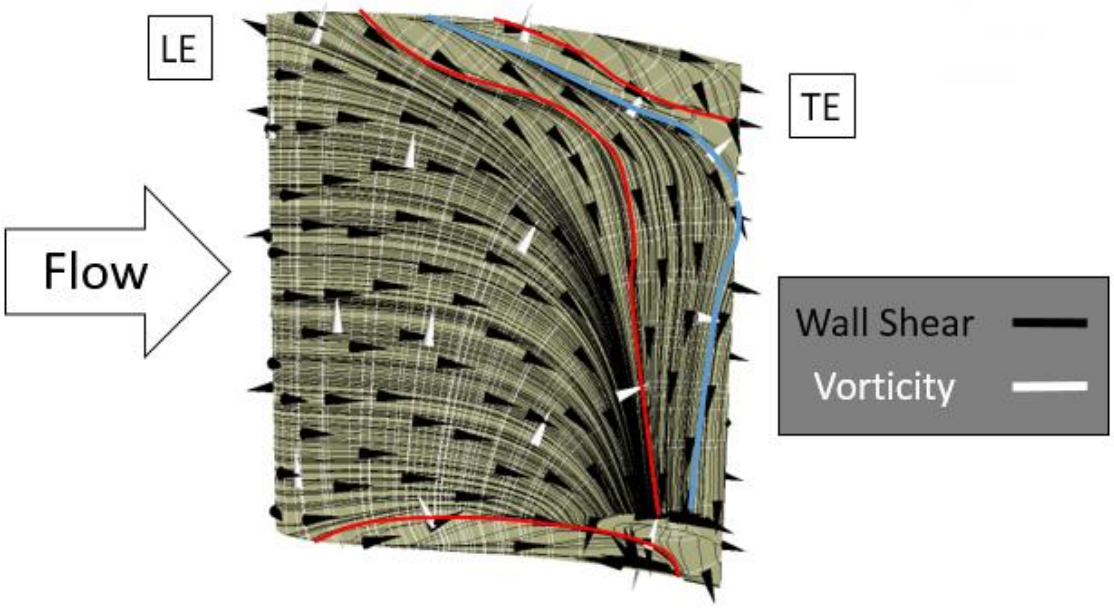

(b) Suction Surface

Figure 89: Nozzle blade topology (steady state – $\Delta t/4$)

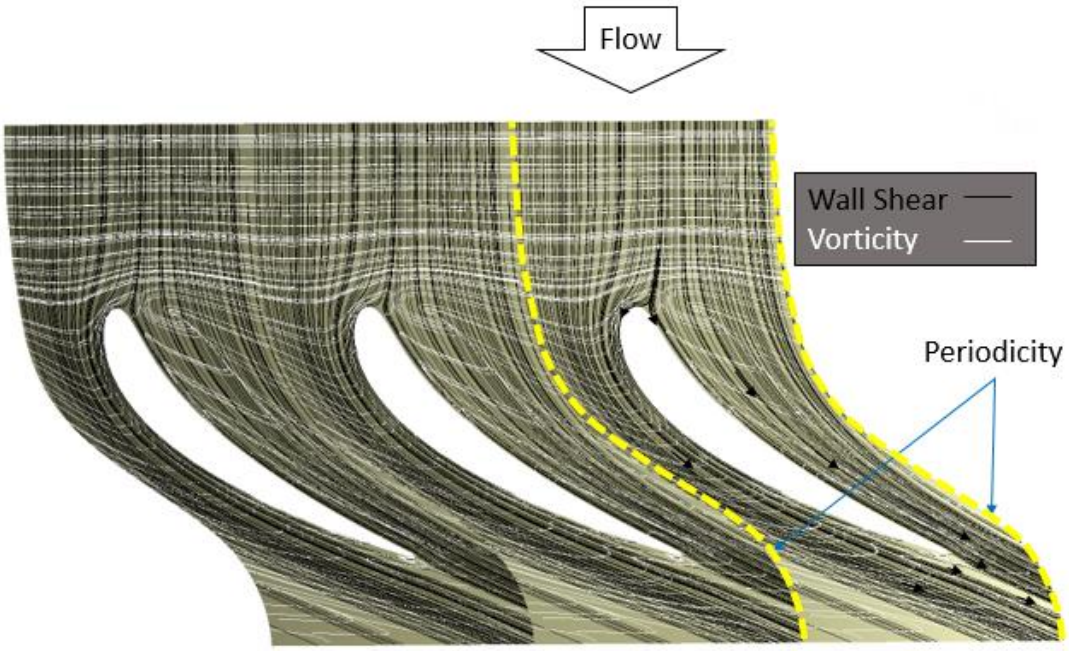

Figure 90: Nozzle mid-span topology (steady state – $\Delta t/4$)

Contour plots are needed to compare the flow fields by specifically looking at the velocities and turbulence intensities at both the nozzle and rotor outlet planes, while also using other contour plots made accessible through the numerical solutions. Figure 91 shows the steady state distribution of absolute velocity, total pressure loss, turbulence intensity, and static pressure loss at the nozzle exit plane, which helps to present the dominant flow features for direct comparisons with the time-averaged and time-resolved absolute velocity of the experimental data shown in Figure 10 and Figure 11. Figure 92 shows the time-averaged and time-resolved turbulence intensity of the LDV data to further help describe the flow field characteristics at the nozzle exit plane, as measured by Matsunuma [24].

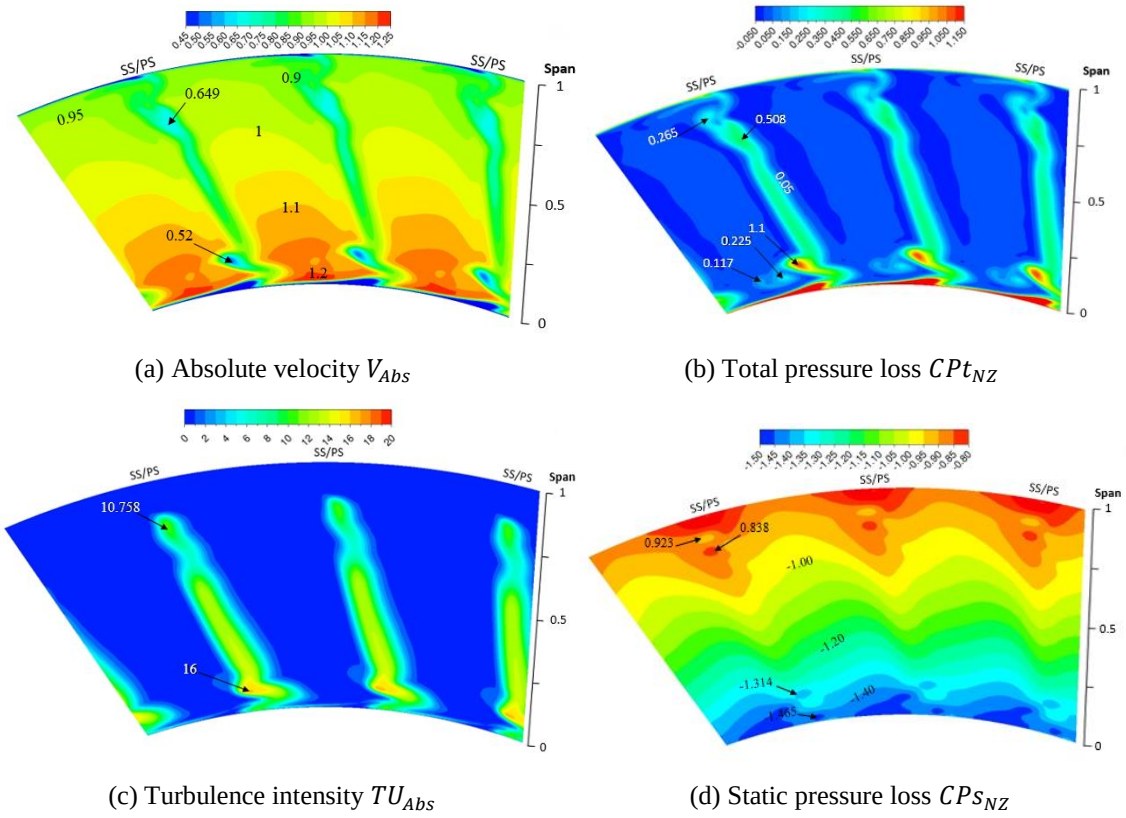

(a) Absolute velocity V_{Abs}

(b) Total pressure loss CPt_{NZ}

(c) Turbulence intensity TU_{Abs}

(d) Static pressure loss CPs_{NZ}

Figure 91:Distributions of absolute velocity, total pressure, turbulence intensity, and static pressure at the nozzle exit plane ($Z_{NZ}/C_{ax,NZ} = 1.154$,steady state ($\Delta t/4$))

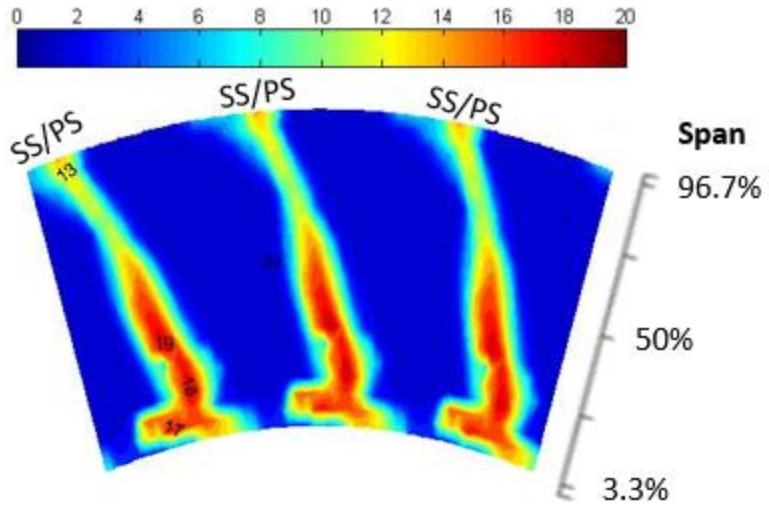

(a) Time-averaged turbulence intensity TU_{Abs} %

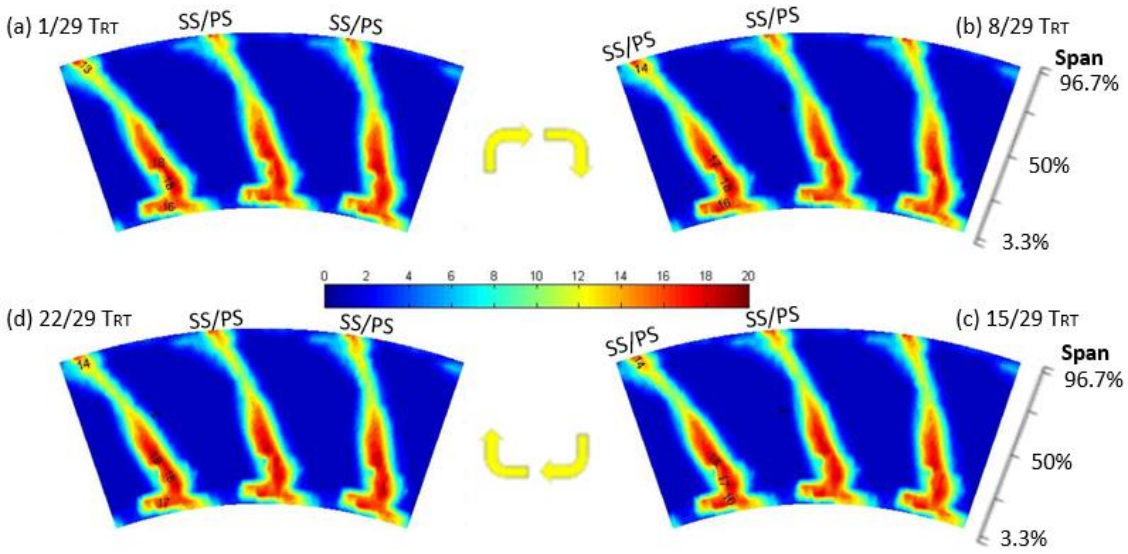

(b) Time-resolved turbulence intensity TU_{Abs} %

Figure 92: LDV Experimental data at the nozzle exit plane ($Z_{NZ}/C_{ax,NZ} = 1.154$)

The total and static pressure coefficients are essential in helping to describe the complex flow at the nozzle exit plane, as in various turbomachinery flows. Denton [49] describes how losses in turbomachinery flow can be improved by viewing the loss as entropy generation. He and Langston [30] have shown that in incompressible flows the total pressure loss can be considered to be a direct measure of the entropy generation. The vortices create areas of large pressure loss due to mixing and the velocity deficit associated

with the vortices. Furthermore, the static loss coefficient helps in identifying vortex structures as they create a center of low static pressure, because the vortex streamlines are spiraling around it. The vortex structures are further distinguished by looking at the vorticity magnitude, Ω, and the streamwise vorticity (SVO), where the streamwise vorticity is defined as follows:

$$SVO = (\omega_x \cdot V_u) + (\omega_y \cdot V_v) + (\omega_z \cdot V_w) \qquad 8.1$$

The steady state distribution of vorticity magnitude and SVO at the nozzle exit plane are shown in Figure 93. Figure 91 and Figure 93 show how the steady state numerical results can help decipher the effect of the various secondary flow structures downstream of the nozzle. The flow consists of two distinct regions, one characterized by the wake and secondary vortices, and the other by the potential flow. The nozzle wake separates the flow over the suction side from the flow on the pressure side. The trailing shear layer vortices (TSLV's) close to the suction surface have a clockwise rotation, while those close to the pressure surface have a counter-clockwise rotation. Due to the nature of the flow, the tip side passage vortex (indicated by "PV_{Tip}") has a clockwise direction and the hub side passage vortex (indicated by "PV_{Hub}") has a counter-clockwise direction, because the passage vortices transport endwall boundary layer material from the pressure side to the suction side.

The flow presents similar characteristics on the tip and hub side with counter-rotating vortices forming at the trailing edge tip and hub endwalls (indicated by TE-CV's), and the pressure side vortex filaments forming a trailing shear layer vortex with a counter-clockwise rotation (indicated by "PS-TSLV"). The suction side trailing shear layer vortex (indicated by "SS-TSLV") entraps the suction side vorticity and has a clockwise rotation.

At the tip side it was found that it separates at the tip trailing edge, which may have remanence of the suction side leading edge vortex, and at the hub it separates on the suction surface. The tip side nozzle wake causes two counter rotating wake induced vortices (indicated by "WIV" and "WICV") to form. The nozzle wake and secondary vortices at the nozzle exit plane form areas of high total pressure loss and low velocity. The transient solution shows the same flow characteristics for the wall shear and vorticity at the nozzle hub, mid-span, and tip; the time-averaged numerical data shows the same characteristics as the steady state results, while the time-resolved data show negligible changes in the streamlines. Figure 94 and Figure 95 show the same distributions for the time-averaged transient numerical simulation at the nozzle exit plane, for direct comparison with the numerical steady state and experimental data.

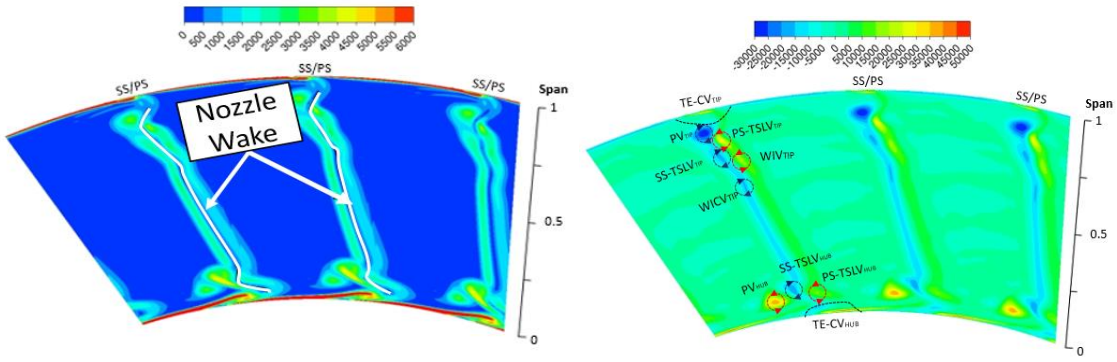

(a) Vorticity Ω $[1/s]$ (b) Streamwise vorticity SVO $[m/s^2]$

Figure 93: Distributions of vorticity and streamwise vorticity at the nozzle exit plane ($Z_{NZ}/C_{ax,NZ} = 1.154$,steady state ($\Delta t/4$))

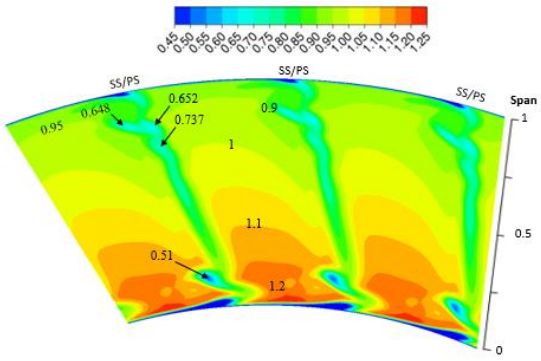

(a) Absolute velocity V_{Abs}

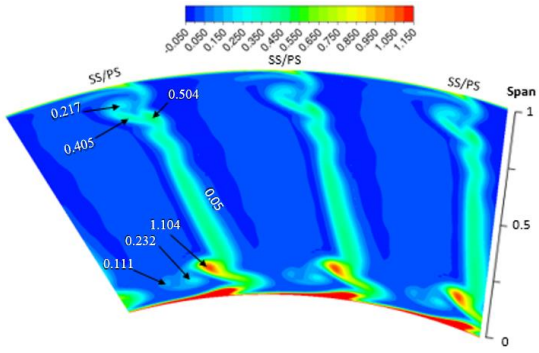

(b) Total pressure loss CPt_{NZ}

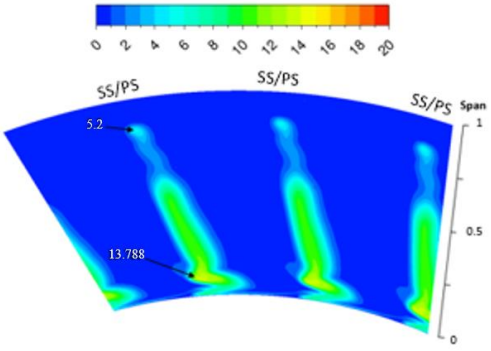

(c) Turbulence intensity TU_{Abs}

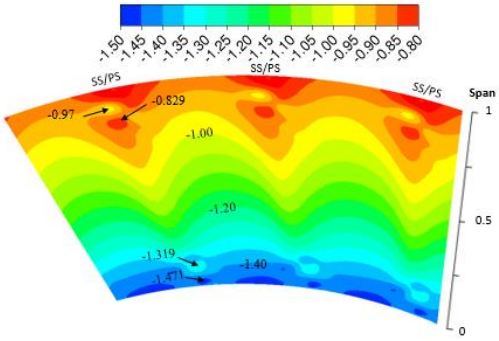

(d) Static pressure loss CPs_{NZ}

Figure 94: Time-averaged distributions of absolute velocity, total pressure, turbulence intensity, and static pressure at the nozzle exit plane ($Z_{NZ}/C_{ax,NZ} = 1.154$,Transient $\left(\left(\frac{1}{5}\right)\frac{\pi}{31}\Delta t\right)$)

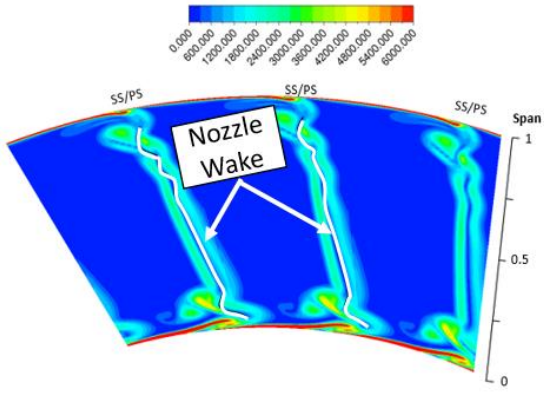

(a) Vorticity Ω $[1/s]$

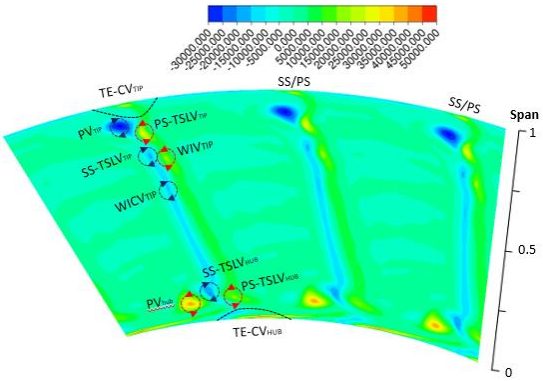

(b) Streamwise vorticity SVO $[m/s^2]$

Figure 95: Time-averaged distributions of vorticity and stream wise vorticity for the transient $\left(\left(\frac{1}{5}\right)\frac{\pi}{31}\Delta t\right)$numerical solution at the nozzle exit (axial position $Z_{NZ}/C_{ax,NZ} = 1.154$)

The steady-state and time-averaged transient numerical simulation contour plots clearly show similar characteristics. In both cases the hub and tip side peak values of the

total pressure, and turbulence intensity cores are associated with the TSLV found next to the passage vortex. The numerical results indicate that the velocity deficit associated with the hub endwall flow is acting over a smaller effective area when compared to the experimental findings. Although, both models predict the same secondary flow vortices at the nozzle exit plane they vary in strength and size. Most notably, the transient numerical simulations show that the tip side passage vortex has a larger velocity deficit, as it interacts with the PS-TSLV, which in turn causes a reduction in the predicted turbulence intensity. The RMS of the turbulent velocity fluctuations is best predicted by the steady state results, as it predicts higher peak values of the order of those measured. Both models failed to properly predict the turbulence intensity associated with the passage vortices, and tip side corner vortices. The measured data shows that areas of high intensity conform to areas of high loss, which is not the case in the numerical predictions. The transient results did identify and confirm that the potential flow of the downstream rotor has negligible effect on the nozzle exit plane flow field distribution, deeming the flow within the nozzle mostly steady.

Overall both the steady state and transient numerical results show that the transition model needs fine tuning as it failed to properly predict and track the turbulence kinetic energy associated with blade wake and endwall secondary flow vortices. This lead to no turbulence intensity being associated with the passage vortex downstream of the nozzle, hence the reason for the under prediction of the RMS of the turbulent velocity fluctuations, but the steady state model does a decent job of predicting the turbulence intensity of the wake and trailing shear layer vortices. The numerical model must also be able to predict the strong radial pressure gradient on the suction surface that induces separation. This was

shown to only be predicted by the $Laminar\ Flow$ model, and the laminar nature of the transition turbulence model. Therefore, to properly model the flow field of the axial flow turbine at a low Reynolds number the turbulence production and intermittency equations of the $SST - Transitional - CC$ turbulence model must first be adjusted to properly track the turbulent kinetic energy production.

The numerical models are capable of predicting the nozzle flow features as found in the experiments, even with the model deficiencies mentioned, which is valuable as they help to further understand the low Reynolds number flow field in the axial flow turbine. First, a high loss region is found close to the suction side hub corner, although the models fail to properly predict the turbulence intensity associated with the passage vortex. The experimental data shows that this high loss region is characterized by a high turbulence intensity region due to the strong interaction of the passage vortex and separated flow close to the suction surface. The experimental and numerical data also show that the tip side passage vortex is weaker than the hub side passage vortex as it has a smaller total pressure loss and lower velocity deficit. It is worth noting that the secondary flow vectors and static pressures as measured by the 5-hole pressure probe data, as presented in Figure 96, show the presence of the tip side passage vortex and a strong interaction close to the hub side, the latter is possibly due to the multiple vortices found acting next to each other as in the numerical results. Matsunuma and Tsutsui [18] and Matsunuma [16] confirm that at the nozzle hub there is a trailing edge vortex to the right of the passage vortex, synonymous to the hub SS-TSLV denoted in the numerical results.

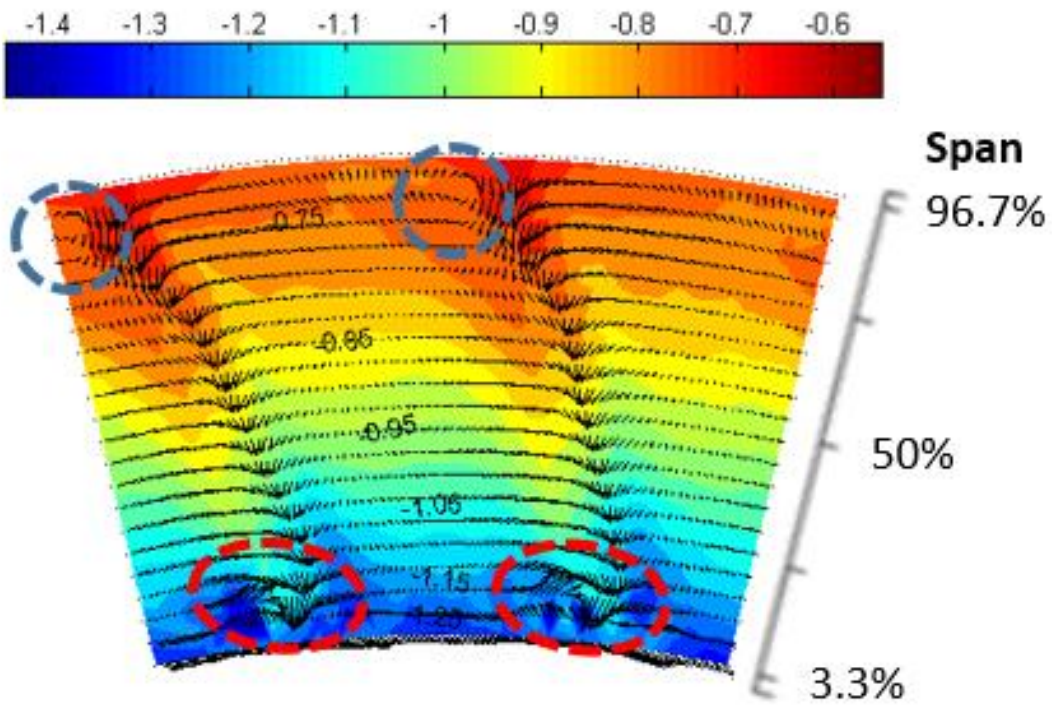

Figure 96: Static Pressure coefficient with secondary flow vectors overlaid (5-hole pressure probe)

The models must also predict the proper flow turning in the passage, as it directly effects how accurately the results can match the experimental data; if the nozzle exit flow angle is off it will further amplify the improper flow turning of the flow in the rotor passage. Matsunuma and Takayuki [16] mention that a reduction of one degree of the nozzle exit flow angle causes a decrease of 5 degrees in the rotor incidence angle. In order to see if the numerical models predict the flow as found in the experiments the spanwise distribution of the absolute flow angle at the nozzle exit plane is shown in Figure 97. The numerical and experimental data again show the same flow characteristics; it is the authors belief that the variation in Reynolds number up to at least $Re_{out,NZ} = 26.6x10^4$ should predict a similar flow angle distribution, similar to what was measured by Matsunuma and Takayuki [16]. The tip side under-turning located from 68.7% to 92.0% span is caused by the tip side secondary flow vortices, which encompass the tip side WIV to the PV. The hub side

under-turning from 7.97% to 17.3% span is caused by the PV, PS-TSLV and SS-TSLV. The TE-CV's also cause over-turning close to the tip and hub side endwalls. The numerical flow angle was found to be below the design flow angle, but with a mean error of less than 2% of the measured flow angle.

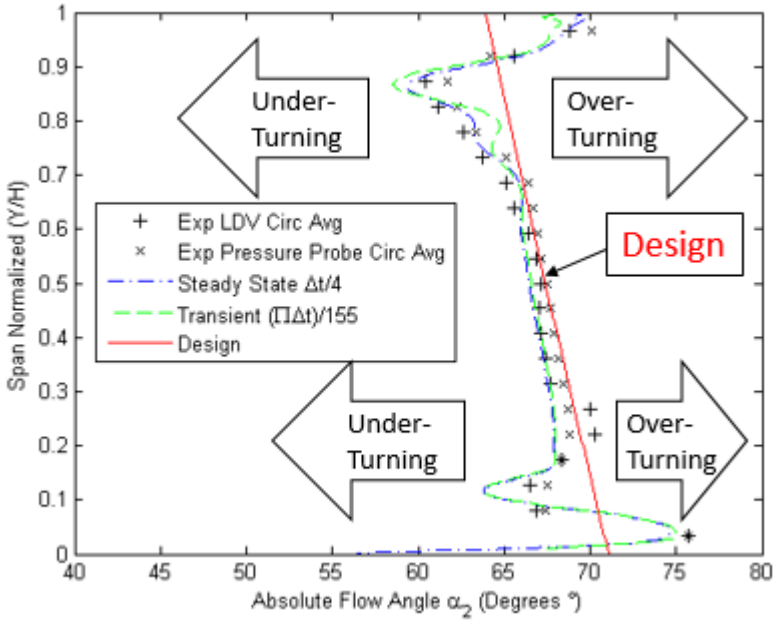

Figure 97: Spanwise distribution of the absolute flow angle at the nozzle exit plane ($Z_{NZ}/C_{ax,NZ} = 1.154$)

The other absolute velocity components also help to understand how well the flow is predicted by the numerical results at the nozzle exit plane. Figure 98 shows the spanwise distributions of the axial and tangential velocities at the nozzle exit compared to the experimental data. The design absolute velocity, $V_{2,Design}$, given in *Table 5* made the velocities dimensionless. The radial velocity distribution found in both numerical models is not shown as it is less than 4% of the nozzle exit plane velocity. The numerical distributions show that the under-turned flow has a higher axial velocity and lower tangential velocity, this is vice-versa to that of the over-turned flow, similar to the measured values. *Table 39* shows the mean errors associated with the spanwise flow angle, axial

velocity and tangential velocity compared to the experimental data. The steady state numerical results most accurately predicted the spanwise absolute exit flow angle and the transient numerical results bested predict the axial and tangential velocity distribution at the nozzle exit plane. The transient results therfore best predict the mean velocity flow field, as seen by the low mean percent error of the absolute velocity in *Table 37* and velocity components in *Table 39*.

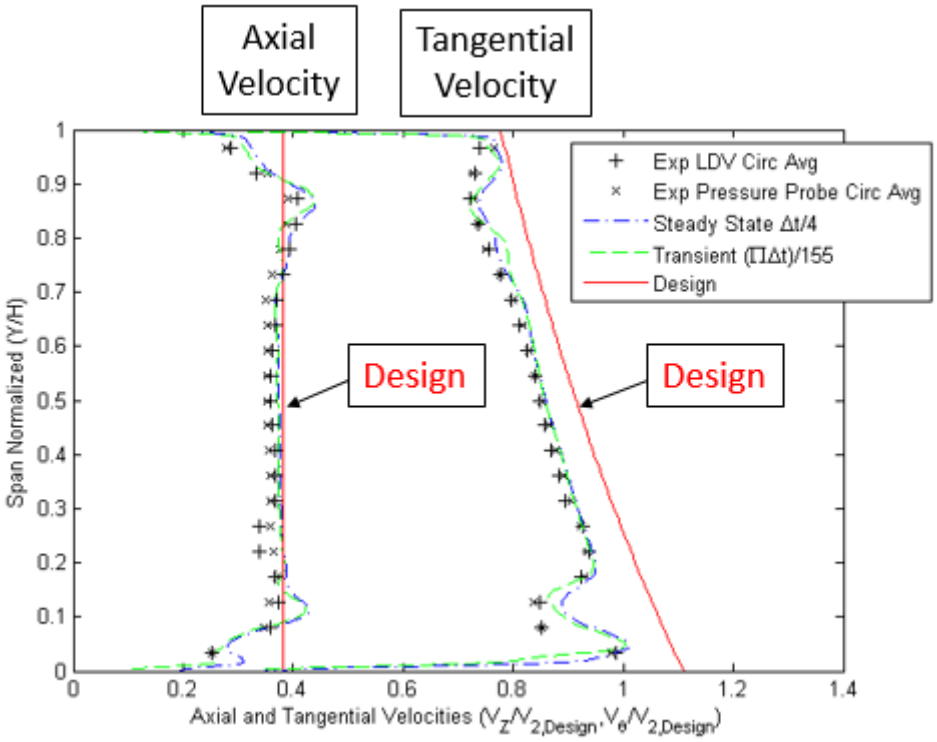

Figure 98: Distribution of axial and tangential velocities at the nozzle exit plane ($Z_{NZ}/C_{ax,NZ} = 1.154$)

Table 39: Spanwise mean error of the absolute flow angle, axial velocity and tangential velocity at the nozzle exit plane ($Z_{NZ}/C_{ax,NZ} = 1.154$)

SRQ	Turbulence Model	Mean % Error	
		Experimental LDV	Experimental Pressure Probe
Absolute Flow Angle α_2	$SST - Transition - CC - Steady\ State$	1.31	1.64
	$SST - Transition - CC - Transient$	1.51	1.72
Axial Velocity $\frac{V_Z}{V_{2,Design}}$	$SST - Transition - CC - Transient$	3.71	4.05
	$SST - Transition - CC - Steady\ State$	4.29	5.62
Tangential Velocity $\frac{V_\theta}{V_{2,Design}}$	$SST - Transition - CC - Transient$	1.97	1.72
	$SST - Transition - CC - Steady\ State$	2.15	1.82

To further gauge the numerical results obtained, the total pressure exit loss at the nozzle exit are shown in *Table 40* with comparison to the 5-hole pressure probe data measured by Matsunuma [24]. The numerical results under predict the mean total pressure exit loss at the nozzle exit, while mid-span total pressure exit loss shows a match between the 5-hole pressure probe data and the numerical data. Comparison to the pressure probe data specifically shows that the numerical models slightly over predict the profile loss at the mid-span, and vastly under predicts the secondary losses. However, Matsunuma et al. [15] measured a mean exit total pressure loss coefficient of 0.0823 at the nozzle exit plane, which shows that the secondary losses are almost within one-hundredth of that measured.

Table 40: Total Pressure Losses at the nozzle exit plane ($Z_{NZ}/C_{ax,NZ} = 1.154$)

	Mid-Span Exit Loss		Mean Exit Loss	
	$Re_{out,NZL}$	CPt_{NZ}	$Re_{out,NZL}$	CPt_{NZ}
$Steady\ State$	48,800	0.0575	48,600	0.0713
$Transient$	49,000	0.0590	48,700	0.0718
5-Hole Pressure Probe data	48,500	0.0541	48,100	0.0994

The numerical models achieved satisfactory results of the nozzle mean velocity distribution having achieved a mean error within $\pm 6\%$ to the measured data obtained by Matsunuma [24]. This allows for proper identification of locations of reverse flow on the nozzle blade surface as it is the main culprit in the high loss regions found in the nozzle blade passage. Figure 99 shows the time-averaged absolute flow angle in the direct vicinity of the nozzle blade surfaces for the transient numerical results. The negative flow angles identify key areas of reverse flow found along the blade surface. The pressure surface flow angle distribution shows that there is strong reverse flow at the leading edge, where the flow attaches. The suction surface flow angle distribution has multiple locations identified by strong reverse flow, which causes the flow close to the blade to stall. These areas are found along the nozzle blade trailing edge, two distinct areas on the tip and hub side away from the endwall, and along the shroud and tip endwalls. Future designs should focus towards ensuring that flow separation is delayed until the trailing edge in order to prevent retardation of the main flow.

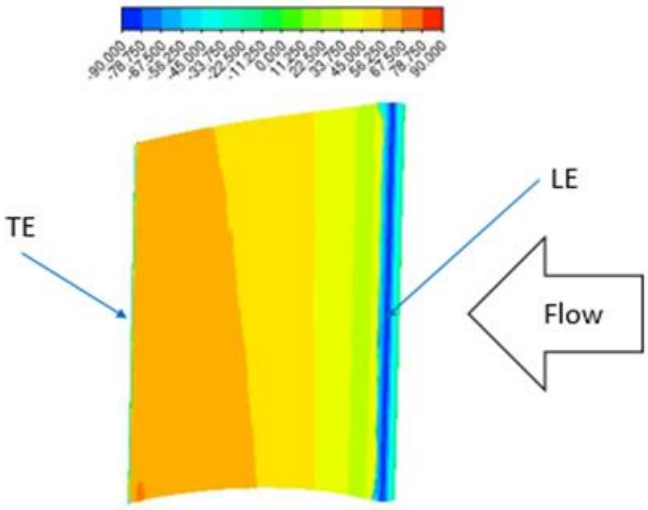

(a) Pressure Surface

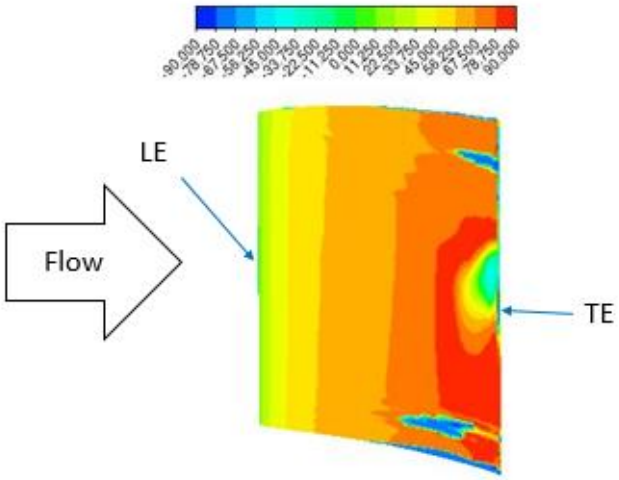

(b) Suction Surface

Figure 99: Time-averaged absolute flow angle on nozzle blade surface (transient $\left(\frac{1}{5}\right)\frac{\pi}{31}\Delta t$)

Unlike the results found in the nozzle, the absolute velocity and RMS of the turbulent velocity fluctuations in the rotor domain are best predicted by the transient simulation as seen in *Table 38*, which also shows that both models were relatively close in the prediction of the relative velocity distribution. Figure 12, Figure 100 and Figure 101 show the time-averaged and time-resolved relative velocity and turbulence intensity distributions at the rotor exit plane as measured in the experiments by Matsunuma [24].

For comparison the steady state and time-averaged transient numerical distributions of relative velocity, total pressure loss, turbulence intensity, and static pressure loss at the rotor exit plane are shown in Figure 102 and Figure 103. The steady state simulations predict larger velocity deficits closer to the tip endwall, where these higher velocity deficits lead to a higher total pressure loss that is associated with a lower static pressure loss.

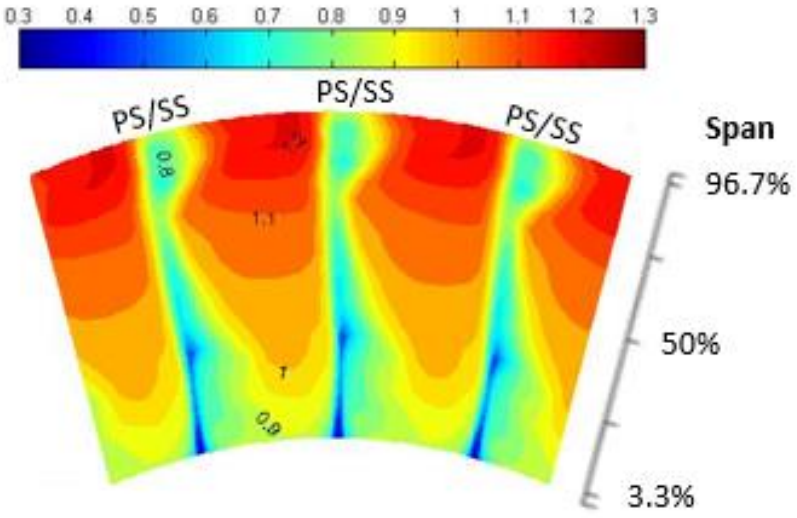

(a) Time-averaged relative velocity V_{Rel}

Figure 100: LDV Experimental data of velocity at the rotor exit plane ($Z_{RT}/C_{ax,RT} = 1.145$)

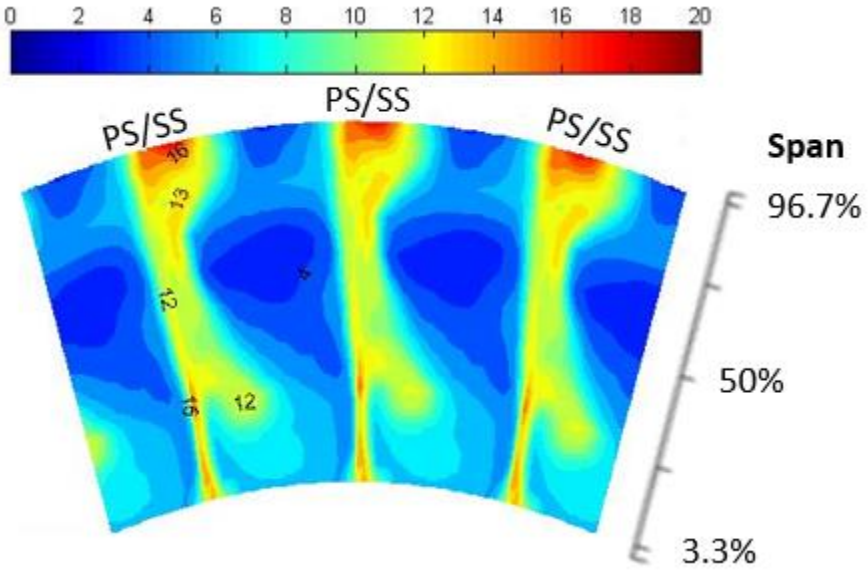

(a) Time-averaged turbulence intensity TU_{Rel} %

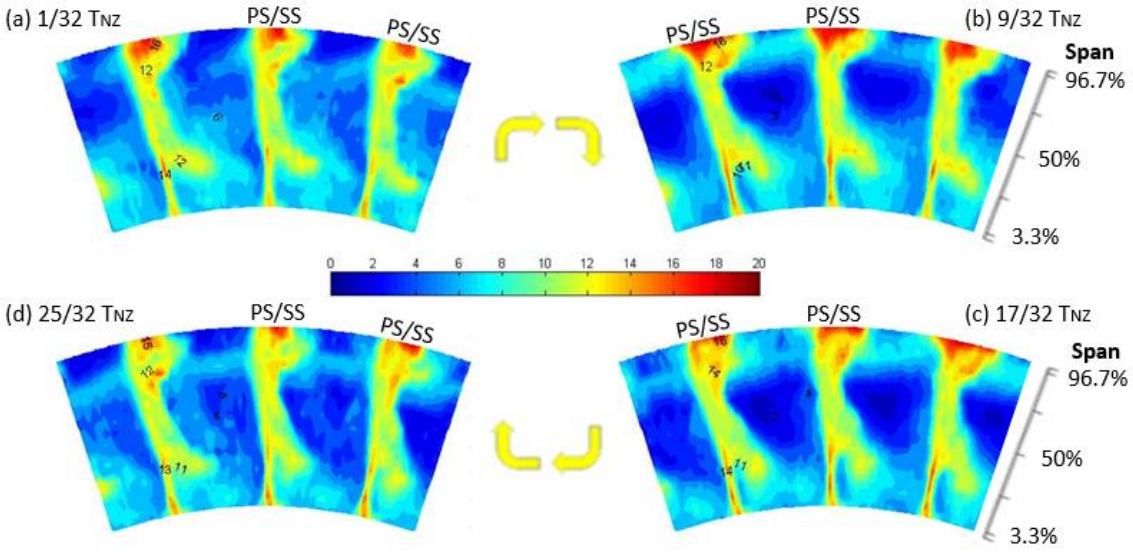

(b) Time-resolved turbulence intensity TU_{Rel} %

Figure 101: LDV Experimental data of turbulence intensity at the rotor exit plane ($Z_{RT}/C_{ax,RT} = 1.145$)

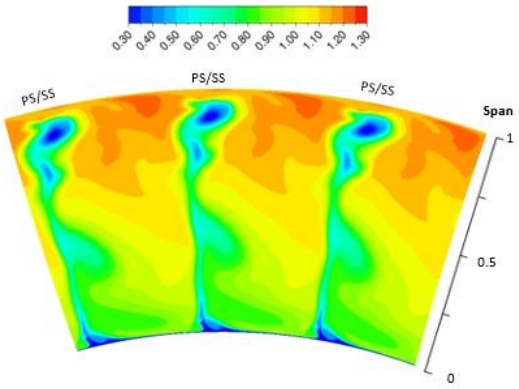

(a) Relative velocity V_{Rel}

(b) Total pressure loss CPt_{RT}

(c) Turbulence intensity TU_{Rel} %

(d) Static pressure loss CPs_{RT}

Figure 102: Distributions of absolute velocity, total pressure, turbulence intensity, and static pressure at the rotor exit plane ($Z_{RT}/C_{ax,RT} = 1.145$, steady state ($\Delta t/4$)

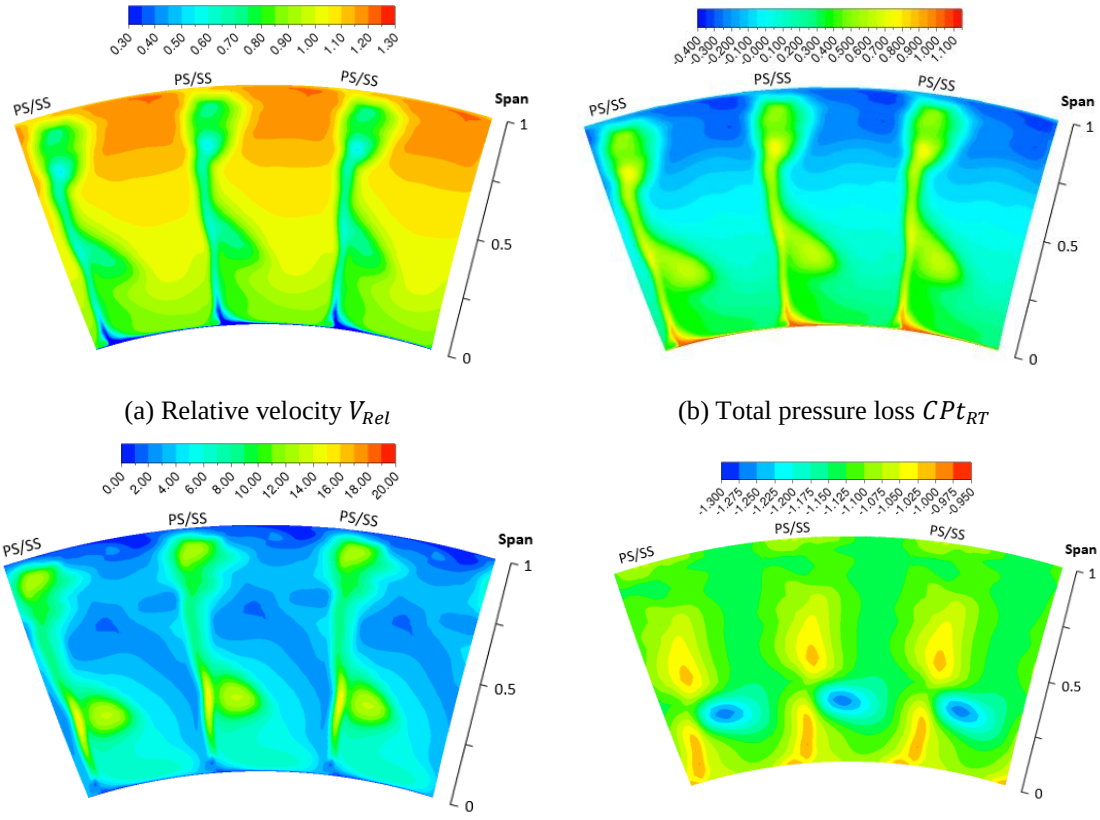

(a) Relative velocity V_{Rel}

(b) Total pressure loss CPt_{RT}

(c) Turbulence intensity TU_{Rel} %

(d) Static pressure loss CPs_{RT}

Figure 103: Time-averaged distributions of relative velocity, total pressure, turbulence intensity, and static pressure at the rotor exit plane ($Z_{RT}/C_{ax,RT} = 1.145$, transient ($\left(\frac{1}{5}\right)\frac{\pi}{31}\Delta t$)

The steady state distribution of the relative turbulence intensity at the rotor exit plane are more like those found at the nozzle wake, where the wake and secondary vortices manifest close to the trailing edge. This causes the steady state results at the rotor exit plane to not properly account for any wake and secondary vortex chopping, which in turn causes the results to have large areas with almost no turbulence intensity, which is found to be associated with a low total pressure loss. Fortunately, the incorporation of the transient simulation shows that the time-averaged numerical data is able to account for the wake and secondary vortex chopping and break down within the rotor, as there is more pitch-wise smearing of the turbulence intensity when obtaining the time-averaged data. This in turn causes the steady state results to have higher turbulence intensity peak values,

as the turbulence intensity presented by the time-averaged transient data is more spread out. Ultimately, the numerical data shows good comparison with the experimental data at the rotor exit plane.

It was shown in *Table 38* that the prediction of the absolute velocity distribution at the rotor exit plane had the highest mean error to that measured in the experiments. More specifically the steady state predictions have twice as much error than that associated with the transient prediction, where Figure 81shows that most of the error is concentrated close to the tip between 87.4% and 96.7% span. Figure 104 shows the distributions of the absolute velocity at the rotor exit plane as measured in the numerical models and experiment. Analysis of the flow close to the tip endwall shows that one of the reasons the steady state results differ from the measured data is in its prediction of the effect that the tip leakage vortex has on the flow. Unlike the flow found at the nozzle exit plane the flow at the rotor exit plane is unsteady, characterized by strong vortical structures. It is seen that the turbulence intensity of the potential flow has the same magnitude as that found at the nozzle exit, which indicates that the upstream vortices have merged with the viscous flow of the rotor similar to the results found by Sharma and Butler [17].

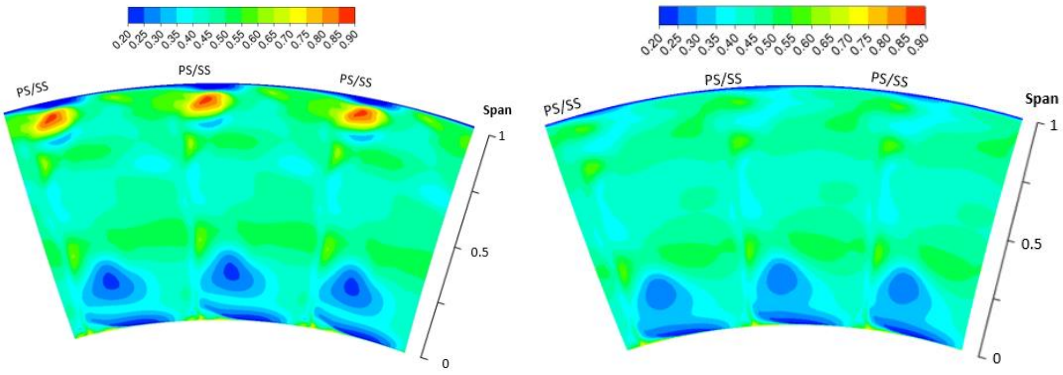

(a) Steady State ($\Delta t/4$)

(b) Time-averaged Transient ($\left(\frac{1}{5}\right)\frac{\pi}{31}\Delta t$)

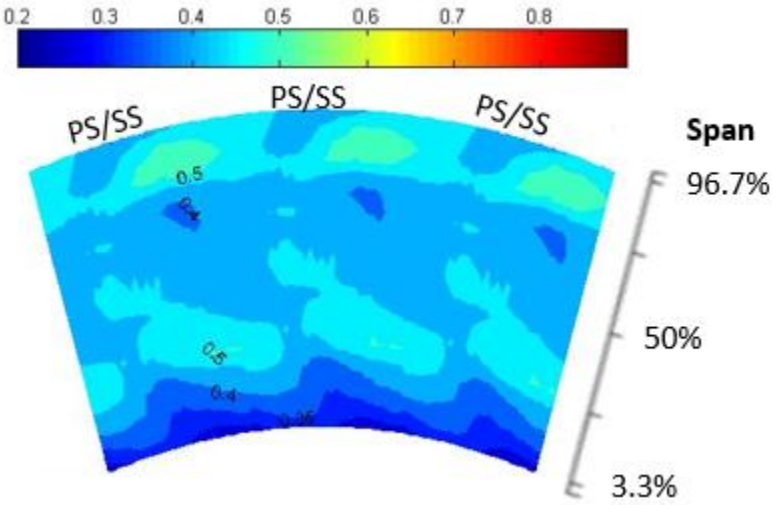

(c) Time-averaged LDV experimental data

Figure 104: Distributions of absolute velocity at the rotor exit ($Z_{RT}/C_{ax,RT} = 1.145$)

The distributions of the vorticity magnitude and SVO at the rotor exit plane are shown in Figure 105 and Figure 106 to help distinguish the secondary flow structures predicted by both numerical models. Due to the nature of the flow, the hub side passage vortex and tip side leakage vortex have a counter-clockwise direction, because the passage vortex transports the endwall boundary layer material from the pressure side to the suction side and the tip leakage vortex enters the rotor tip clearance from the pressure side then separates from the blade tip where it contracts into a jet on the suction side. The flow vortices predicted by the steady state simulations are easier to track, hence why it will be

analyzed first. The steady state flow presents similar characteristics on the tip and hub side with the formation of CV's on the endwalls. The CV's at the tip side entrap the LE-CV's formed at the rotor leading edge and interacts intensely with the tip leakage vortex (indicated by "LV"). The tip side nozzle passage vortex and TSLV's are convected through the rotor staying intact as they reach the rotor exit plane. Above the mid-span two counter-rotating vortices form at each side of the trailing edge (indicated by "PS-TSLV" and "SS-TSLV"). This is where the flow separates from the trailing edge close to the tip side. Additionally, only in the steady state numerical model does the PS-TSLV entraps the leading edge shear layer vortex, where the flow separates on the pressure side. The CV's at the hub side include the counter rotating TSLV's and remanence of the suction side leg of the horseshoe vortex. It is evident that the hub passage vortex climbs up the suction side wall, located between 17% to 41% span. The strong interaction of the PV with the rotor wake causes a counter-rotating WIV to form. It is worth noting that the steady state results do not predict a noticeable passage vortex at the tip side.

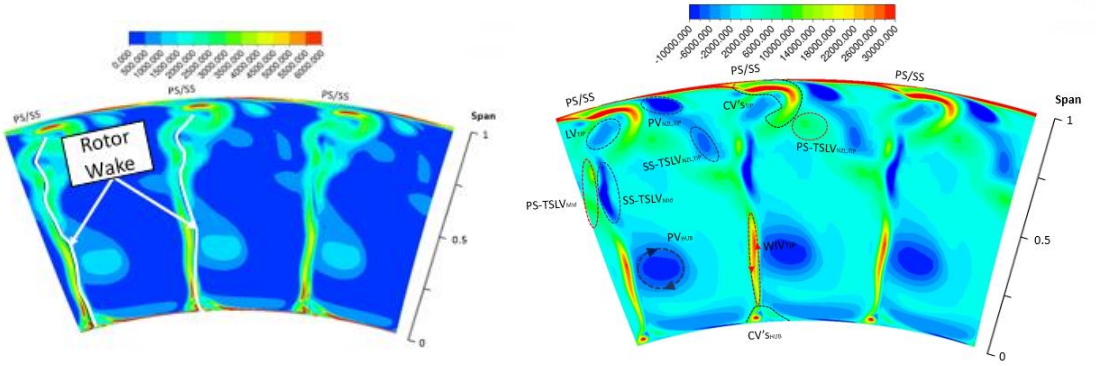

(a) Vorticity Ω $[1/s]$ (b) Streamwise vorticity SVO $[m/s^2]$

Figure 105: Distributions of vorticity and stream wise vorticity at the rotor exit plane ($Z_{RT}/C_{ax,RT} = 1.145$, steady state ($\Delta t/4$)

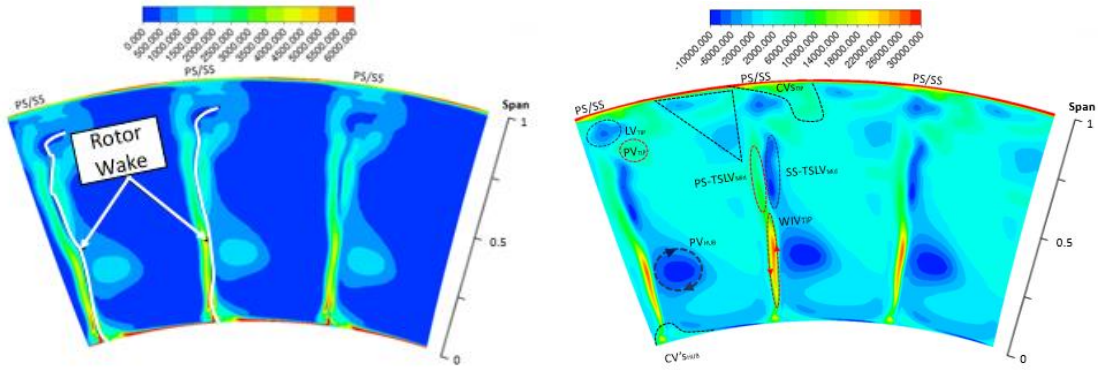

(a) Vorticity Ω $[1/s]$ (b) Streamwise vorticity SVO $[m/s^2]$

Figure 106: Time-averaged distributions of vorticity and stream wise vorticity at the rotor exit plane ($Z_{RT}/C_{ax,RT} = 1.145$, transient $\left(\left(\frac{1}{5}\right)\frac{\pi}{31}\Delta t\right)$)

The steady state results help to interpret the vortical structures found in the time-averaged transient numerical predictions, as they show similar distributions. The main differences are that the time-averaged data do not include any strong vortical structures due to separation at the leading edge, and the nozzle tip side secondary vortices that travel through the rotor passage are not as well defined but their effects are still visible by the strong vortical structures found at the tip side. The time-resolved data do show that there is a strong crossflow that interacts with the leakage vortex formation at the rotor shroud, therefore there is a passage vortex formation but it seems to dissipate as it interacts directly with the CV's at the tip side. For clarity it is shown where the passage vortex remanence

should be located at the rotor exit plane and a black triangle denotes where the nozzle wake and secondary vortices are located on the tip side.

For the most part, both numerical models predict the spanwise distribution of absolute flow angle at the nozzle exit plane as measured in the experiment. This is essential as it effects the prediction of the relative flow angle distribution in the rotor. The spanwise distributions of the relative flow angle at the rotor exit plane as measured in the numerical models and experiment are shown in Figure 107. The time-averaged transient and steady state numerical results show slight prediction differences to that measured by the LDV system, especially close to the tip side endwall. Both models do a good job of predicting the relative flow angle from 31.3% to 78.0% span, which is away from the strong secondary flow structures located at both respective endwalls. The strong three-dimensional flow located at the endwalls is characterized by large over-turning and under-turning of the relative flow angle. At the tip side from 78% to 96.7% span the LV, tip side CV's, and nozzle wakes and secondary vortices are best predicted by the time-averaged transient numerical model. The over prediction in their strength, which have higher velocity deficits, causes the steady state numerical model to have significant over and under-turning of the relative flow angle at the rotor exit. The effect that the hub side CV's and PV have on the relative flow angle is not accurately predicted by both numerical models. Overall the mean errors associated with the relative flow angles for the numerical models to the measured data were found to be within 3% and 6% for the transient and steady state models, respectively.

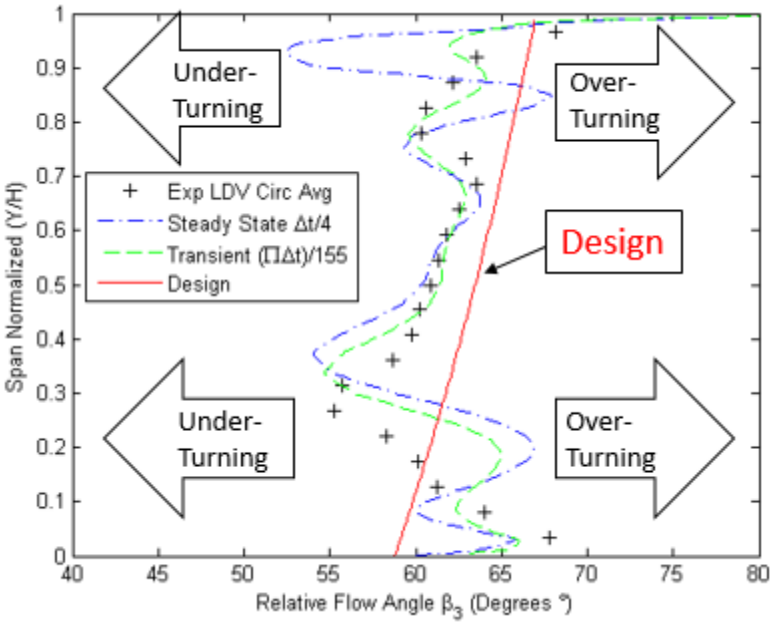

Figure 107: Spanwise distribution of the relative flow angle at the rotor exit plane ($Z_{RT}/C_{ax,RT} = 1.145$)

The relative velocity field can be broken down into its axial and circumferential components to determine how well the individual components are predicted by the numerical models at the rotor exit plane. Figure 108 shows the spanwise distributions of the axial and tangential velocities at the rotor exit plane compared to the experimental data, where the design relative velocity, $W_{3,Design}$, is given in *Table 5* which makes the velocities dimensionless. Again, the radial velocity distribution is not shown as in both numerical models it was shown to be less than 5% of the rotor exit plane velocity. *Table 41* shows the mean error associated with the spanwise distributions of the relative flow angle, axial velocity, and tangential velocity compared to the measured values. The results overwhelmingly show that the time-averaged transient numerical results best replicate the flow field in the rotor. Both models do show that the axial velocity is the hardest to predict, as indicated by its higher mean error.

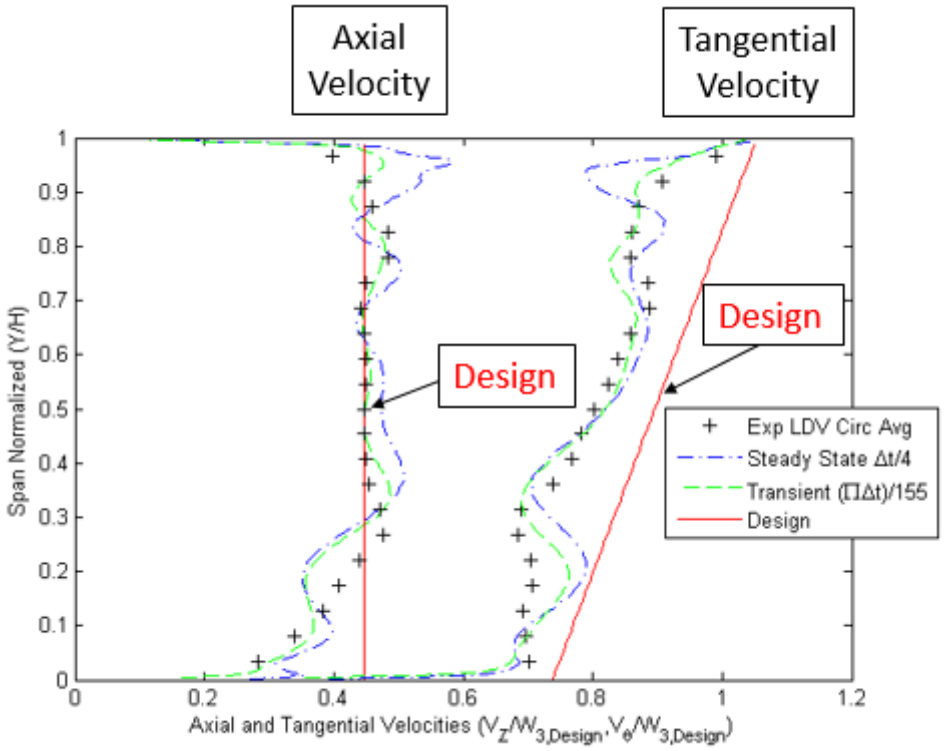

Figure 108: Distribution of axial and tangential velocities at the rotor exit plane ($Z_{RT}/C_{ax,RT} = 1.145$)

Table 41: Spanwise mean error of the relative flow angle, axial velocity and tangential velocity at the rotor exit plane ($Z_{RT}/C_{ax,RT} = 1.154$)

SRQ	Turbulence Model	Mean % Error
Relative Flow Angle β_3	$SST - Transition - CC - Transient$	3.09
	$SST - Transition - CC - Steady\ State$	5.70
Axial Velocity $V_Z/W_{3,Design}$	$SST - Transition - CC - Transient$	4.64
	$SST - Transition - CC - Steady\ State$	8.80
Tangential Velocity $V_\theta/W_{3,Design}$	$SST - Transition - CC - Transient$	3.03
	$SST - Transition - CC - Steady\ State$	4.35

Further, the total pressure loss at the rotor exit as calculated from the numerical models is shown in *Table 42*. The mid-span total pressure loss as predicted in the numerical results are significantly augmented to the extent that they over predict the total pressure loss compared to those presented by Matsunuma [24], see Figure 7. This is indication that the numerical results over-predict the losses found at the rotor exit plane, specifically in the time-averaged transient results. The differences in the losses may also be attributed to the Reynolds number, in which simulating a transient simulations cause the Reynolds number to increase by 18%, but generally the total pressure loss decreases as the Reynolds number is increased. This confirms that the transient simulation has a significant effect on the flow field predictions.

Table 42: Total Pressure Losses at the rotor exit plane ($Z_{RT}/C_{ax,RT} = 1.145$)

	Mid-Span Exit Loss		Mean Exit Loss	
	$Re_{out,RTR}$	CPt_{RTR}	$Re_{out,RTR}$	CPt_{RTR}
$Steady\ State$	35,700	0.0647	35,700	0.0662
$Transient$	42,200	0.0814	42,200	0.0831

Essentially, it is shown that the time-averaged transient results best match the results measured by the LDV system, although they do show a significantly higher total pressure loss than found in the literature. Further analysis of the time-averaged relative flow angle on the rotor blade as predicted by the transient results will identify areas along the blade that have reverse flow, and hence the areas of high losses. Figure 109 shows the time-averaged relative flow angle in the vicinity of the rotor blade for the transient numerical results. The negative flow angles found on the suction and pressure surface identify key locations where there is strong reverse flow; which lead to increased losses

within the rotor. There is a strong reverse flow at the leading edge of the pressure surface due to a saddle point found close to the leading edge hub side endwall, and strong separation close to the tip side trailing edge on the suction surface, most likely caused by the strong interaction of the leakage vortex. Future designs should focus on decreasing the reverse flow found at the leading edge of the pressure side, ensuring that flow separation occurs as close to the trailing edge as possible to decrease the tip leakage vortex. Figure 110 shows the wall shear and vorticity field in the direct vicinity of the rotor suction surface as predicted in the steady state simulation. The separation line at the hub that travels from the leading edge to the trailing edge pertains to the rotor hub passage vortex. This main separation line is found at about 36% span, which is in accordance with Matsunuma [25] who found that the rotor passage vortex created a high turbulence intensity region that reached the same spanwise location at the trailing edge.

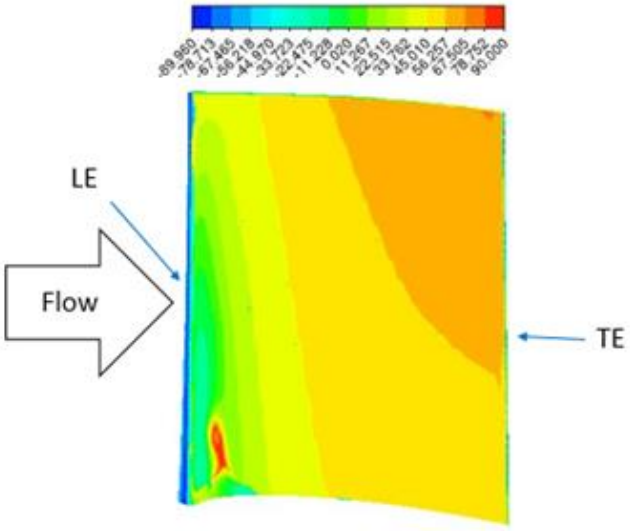

(a) Pressure Surface

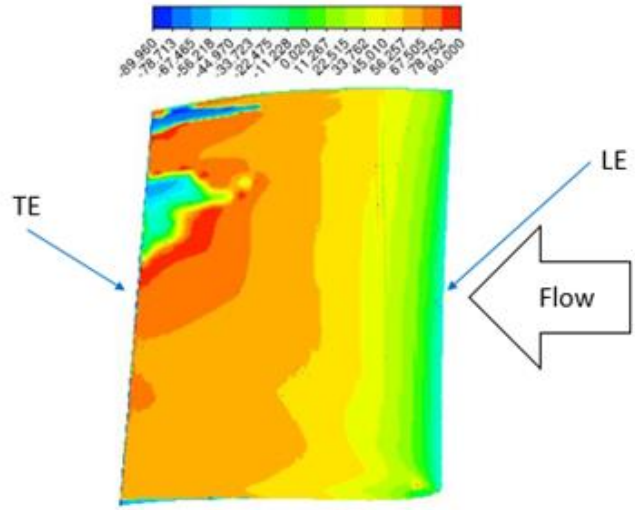

(b) Suction Surface

Figure 109: Relative flow angle on rotor blade surface (transient $\left(\frac{1}{5}\right)\frac{\pi}{31}\Delta t$)

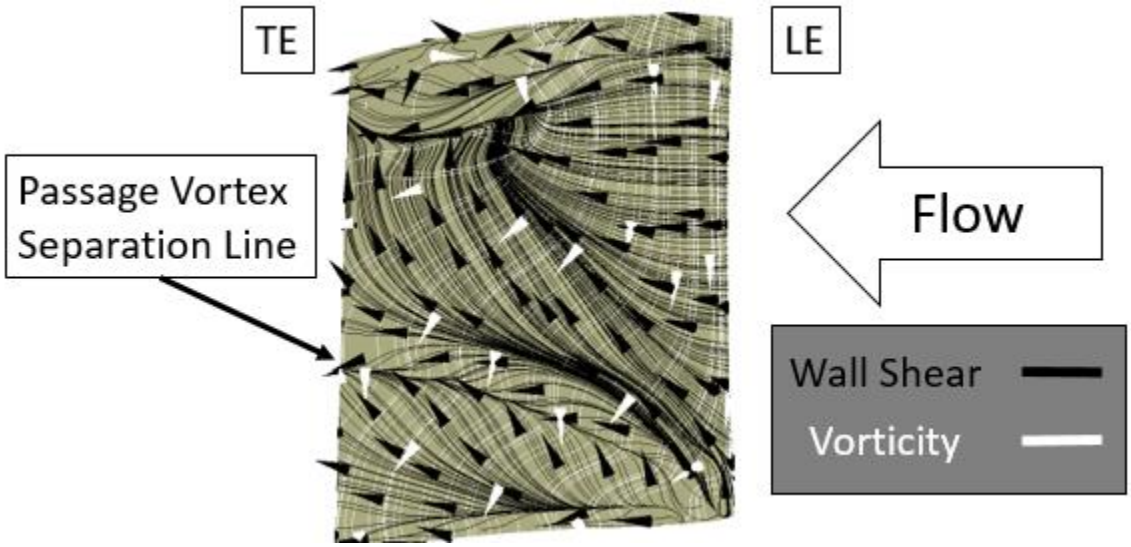

Figure 110: Rotor suction surface topology (steady state – $\Delta t/4$)

For the sake of completeness, the time-resolved relative velocity and relative turbulence intensity distributions at the rotor exit plane are shown in Figure 111 and Figure 112 for the last rotor revolution. These figures show the capability that the transient numerical simulations provide towards making time-accurate predictions in transient flows. The flow field should be analyzed at different streamwise locations to get a better grasp of how the nozzle vortical structures mix out in the rotor and their interaction with the rotor secondary flow structures.

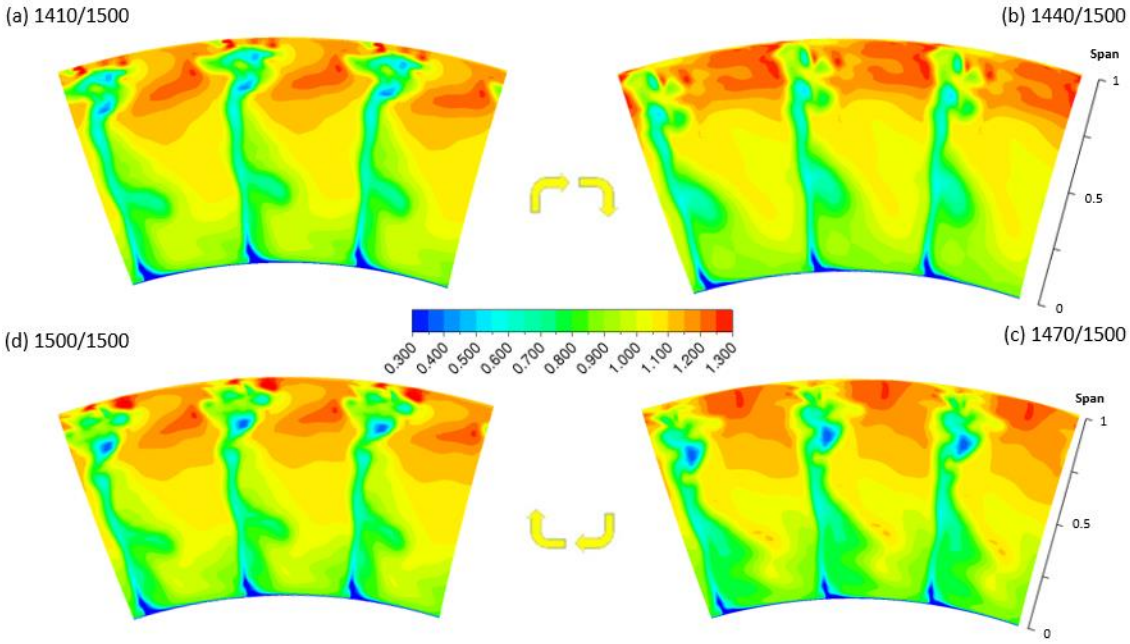

Figure 111: Time-resolved relative velocity at the rotor exit plane ($Z_{RT}/C_{ax,RT} = 1.145$, transient $\left(\left(\frac{1}{5}\right)\frac{\pi}{31}\Delta t\right)$)

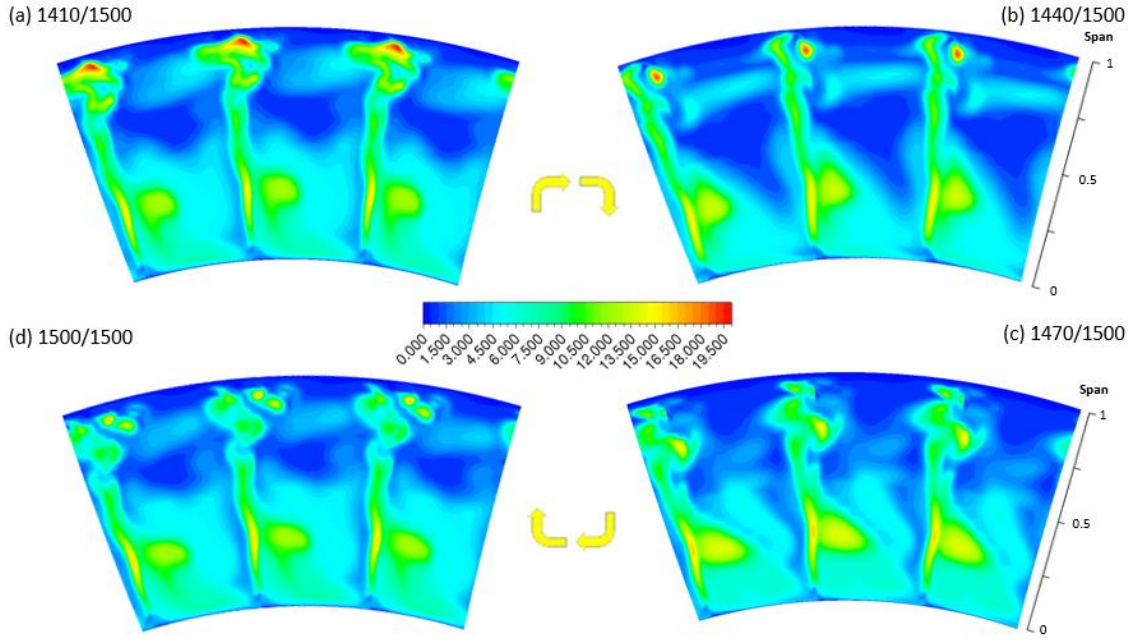

Figure 112: Time-resolved relative turbulence intensity at the rotor exit plane ($Z_{RT}/C_{ax,RT} = 1.145$, transient $\left(\left(\frac{1}{5}\right)\frac{\pi}{31}\Delta t\right)$)

9. CONCLUSION

The present work has been devoted towards making a detailed systematic numerical analysis of the steady and unsteady flow field of an axial turbine at a low Reynolds number with different parametrically tuned eddy-viscosity turbulence models. RANS simulations were employed to investigate the influences the EVM's have on the nozzle and rotor flow fields. All the simulated results obtained in the present thesis have been verified using a GCI for numerical uncertainty quantification and validated with experimental data acquired at AIST by Matsunuma [18]. The numerical simulations revealed that all the turbulence models employed were able to predicted the mean velocity flow field as measured in the experiments to some extent, but failed in accurately predicting the velocity fluctuations. The steady state simulation results showed that, although all the models gave satisfactory results of the mean velocity distribution, the $SST - Transition - CC$ turbulence models' capability in predicting the nozzle blade surface topology made it the default choice in predicting the flow field in an axial-flow turbine operating at a low Reynold number.

Review of the existing literature about this subject reveals that apart from the flow field being complex, it is highly unsteady. This made obtaining a solution to the URANS formulation crucial in presenting time-accurate and time-averaged numerical data. Therefore, a transient simulation of the $SST - Transition - CC$ turbulence model was analyzed and compared to the steady state numerical simulation and experimental data. The transient numerical simulation results proved to be superior to those of the steady state

simulation, as it better predicted the mean velocity flow field found at the nozzle and rotor exit planes, but failed in significantly improving the prediction of the velocity fluctuations. Ultimately, the transient results confirmed that the flow in the nozzle passage is mainly steady, and that the rotor has strong transient effects that must be modeled properly. The results of this investigation have shown the capability of CFD in predicting the flow field in an axial flow turbine at a low Reynolds number, but this comes at the expense of computational time and effort. Furthermore, further fine-tuning of the turbulence models is still needed to improve the prediction of the secondary flow structures and the prediction of the RMS of the turbulent velocity fluctuations.

APPENDIX

The Appendix presents a MATLAB code written to facilitate data processing of the experimental data and numerical results. MATLAB programs are used throughout the thesis for analysis and plotting of results. Source code 'LDV_NOZZLE_AVE.m' is attached here for post-processing the time-averaged experimental data distributions as measured by the LDV system. The built in programs 'meshgrid' and 'griddata' facilitate this process.

```
%LDV_NOZZLE_AVE.m
%Import and plot Nozzle Time-averaged LDV Data
%%%%%%%%%%%%%%%%%%%%%%%%%%%%%%%%%%%%%%%%%%%%%%%%%%%%%%%%%%%%%%%%
clear;clc
%Import Steady LDV AVG DATA%
fid_LDV_AVG = csvread('ABSAVE.csv',2,1);
ABS_VEL_AVG_LDV=fid_LDV_AVG(:,:);
loc=3;%Axial Position(1 to 44)(location 4 Nozzle Exit 1.154)
ABS_VEL_AVG_LDV_NOZZLE=ABS_VEL_AVG_LDV(1+2037*loc:2037+2037*loc,
:);%The variable arrays are traced separately by its spatial
%coordinates (x,y,z) and absolute velocity (V_Abs)
x=ABS_VEL_AVG_LDV_NOZZLE(:,4);y=ABS_VEL_AVG_LDV_NOZZLE(:,5);
z=ABS_VEL_AVG_LDV_NOZZLE(:,6);V=ABS_VEL_AVG_LDV_NOZZLE(:,7);
%%%%%%%%%%%%%%%%%%%%%%%%%%%%%%%%%%%%%%%%%%%%%%%%%%%%%%%%%%%%%%%%
n=100; %number of subdivisions for plotting purposes
%The points are converted to a Cylindrical Coordinate System
r=sqrt(x.^2+y.^2);%Radial coordinates
theta=atand(x./y);%Azimuthal coordinates
%%%%%%%%%%%%%%%%%%%%%%%%%%%%%%%%%%%%%%%%%%%%%%%%%%%%%%%%%%%%%%%%
nr=21;%The number of spanwise locations
ntheta=97;%The number of Pitchwise Locations
[ri,thetai]=meshgrid(linspace(min(r),max(r),nr),...
    linspace(min(theta),max(theta),ntheta));%Cylindrical Grid
%replicates the grid vectors r, theta to produce the coordinates
%of a cylindrical grid (ri,thetai)
%The points are converted to a Cartesian Coordinate System
yi=ri.*cosd(thetai);xi=ri.*sind(thetai);
%Griddata is used to interpolates the scattered data to produce
%gridded data
Vi=griddata(x,y,V,xi,yi);%decent         Methods:         Linear
(default),natural,cubic,v4
figure(1);set(gca,'XDir','Reverse')
[c,h]=contourf(xi,yi,Vi,14);colorbar;caxis([0.5,1.2]);
set(h,'EdgeColor','none')
```

REFERENCES

[1] M. V. Roode, "Ceramic Gas Turbine Development: Need for a 10 Year Plan," *ASME. J. of Eng. for Gas Turbines and Power,* vol. 132, no. 1, p. 8, 29 Sep 2009.

[2] Forecast International, "The Market for Microturbine Electrical Power Generation," Forecast International Inc., Newtown, CT, 2009.

[3] U.S. Environmental Protection Agency Combined Heat and Power Partenership, Catalog of CHP Technologies, United States Environmental Protection Agency, 2015.

[4] Capstone Turbine Corporation, "Product Specification: Models C600, C800, and C1000," Capstone Turbine Corporation, Chatsworth, 2009.

[5] FlexEnergy, "Flex Turbine GT250S," FlexEnergy, Portsmouth, 2015.

[6] FlexEnergy, "Flex Turbine GT333S," Portsmouth, 2015.

[7] Office of Energy Efficiency & Renewable Energy, "Improving the Operating Efficiency of Microturbine-Based Distributed Generation at an Affordable Price," DOE, 2014.

[8] I. Takehara, T. Tatsumi and Y. Ichikawa, "Summary of CGT302 Ceramic Gas Turbine Research and Development Program," *ASME J. Eng. Gas Turbines Power,* vol. 124, 2002.

[9] R. Shibata, Y. Nakayama, S. Machiya and K. Kobayashi, "The Development of 300kW class High Efficiency Micro Gas Turbine "RGT3R"," *International Gas Turbine Congress 2003 Tokyo,* 2003.

[10] U.S. Department of Energy, "Improving the Operating Efficiency of Microturbine-Based Distributed Generation at an Affordable Price," *U.S. Department of Energy,* 2014.

[11] GE Aviation, "GE Successfully Tests World's First Rotating Ceramic Matrix Composite Material for Next-Gen Combat Engine," GE Aviation, 2015.

[12] T. Matsunuma, H. Abe and Y. Tsutsui, "Characteristics of an Annular Turbine Cascade at Low Reynolds Numbers," in *ASME 1998 International Gas Turbine and Aeroengine Congress and Exhibition*, Stockholm, Sweden, 1998.

[13] L. Langston, M. Nice and R. Hooper, "Three-Dimensional Flow Within a Turbine cascade Passage," *ASME. J. of Eng. for Power,* vol. 99, no. 1, pp. 21-28, April 1977.

[14] L. Langston, "Crossflows in a Turbine Cascade Passage," *ASME. J. of Eng. for Power,* vol. 102, no. 4, pp. 866-874, October 1980.

[15] T. Matsunuma, H. Abe and Y. Tsutsui, "Influence of Turbulence Intensity on Annular Turbine Stator Aerodynamics at Low Reynolds Numbers," in *ASME International Gas Turbine and Aeroengine Congress and Exhibition*, Indianapolis, Indiana, 1999.

[16] T. Matsunuma, "Effects of Reynolds Number and Free-stream Turbulence on Turbine Tip Clearance Flow," *ASME J. of Turbomachin*, vol. 128, no. 1, pp. 166-177, 2005.

[17] O. Sharma and T. Butler, "Three-Dimensional Unsteady Flow in an Axial Flow Turbine," *J. of Propulsion and Power*, vol. 1, no. 1, pp. 29-38, 1985.

[18] T. Matsunuma and Y. Tsutsui, "Effects of Low Reynolds Number on Wake-Generated Unsteady FLow of an Axial-Flow Turbine Rotor," *International Journal of Rotating Machinery*, vol. 2005, no. 1, pp. 1-15, 2005.

[19] G. Persico, A. Mora, P. Gaetani and M. Savini, "Unsteady Aerodynamics of a Low Aspect Ratio Turbine Stage: Modeling Issues and Flow Physics," *ASME. J. of Turbomach*, vol. 134, no. 6, pp. 1-10, 2012.

[20] M. Restemeier, P. Jeschke, Y. Guendogdu and J. Gier, "Numerical and Experimental Analysis of the Effect of Variable Blade Row Spacing in a Subsonic Axial Turbine," *ASME. J. of Turbomach*, vol. 135, no. 2, pp. 1-9, 2013.

[21] C. Schneider, D. Schrack, M. Kuerner, M. Rose, S. Staudacher, Y. Guendogdu and U. Freygang, "On the Unsteady Formation of Secondary Flow Inside a Rotating Turbine Blade Passage," *ASME. J. of Turbomachin*, vol. 136, no. 6, pp. 1-10, 2014.

[22] T. Matsunuma and Y. Tsutsui, "LDV Measurements of Wake-Induced Flow within a Turbine Rotor Cascade," in *Proceedings of 10th International*

Symposium on Applications of Laser Techniques to Fluid Mechanics, Lisboa, 2000.

[23] T. Matsunuma and Y. Tsutsui, "LDV Measurements of Unsteady Midspan Flow in a Turbine Rotor at Low Reynolds Number," in *ASME Turbo Expo 2003, collocated with the 2003 International Joint Power Generation Conference*, Atlanta,Georgia, 2003.

[24] T. Matsunuma, "Unsteady Flow Field of an Axial-Flow Turbine Rotor at a Low Reynolds Number," *ASME Turbo Expo 2006: power for Land, Sea, and Air*, vol. 129, no. 2, pp. 360-371, 8-11 May 2006.

[25] T. Matsunuma, "Effects of Nozzle Secondary Vortices on Unsteady Hub-Endwall Flow of a Turbine Rotor," in *International Conference on Power Engineering-2007*, Hangzhou, China, 2007.

[26] H. Wang, S. Olson, R. Goldstein and E. Eckert, "Flow Visualization in a Linear Turbine Cascade of High Performance Turbine Blade," *ASME. J. of Turbomachin*, vol. 119, no. 1, pp. 1-8, 1997.

[27] T. Matsunuma, "Research Activities on Gas Turbine in National Institue of Advanced Industrial Science and Technology (AIST)," *Gas Turbine Society of Japan*, pp. 1-2, 2005.

[28] J. Denton, "Loss Mechanisms in Turbomachines," *ASME. J. Turbomachin*, vol. 115, no. 4, pp. 621-656, 1993.

[29] N. Wei, "Significance of Loss Models in Aerothermodynamic Simulation for Axial Turbines," [Doctoral Thesis] Department of Energy

Technology Division of Heat and Power Technology,Royal Institute of Technology, 2000.

[30] L. Langston, "Secondary Flows in Axial Turbines - A Review," *Annals of the New York Academy of Sciences,* vol. 934, pp. 11-26, 2001.

[31] C. Sieverding, "Recent Progress in the Understanding of Basic Aspects of Secondary Flows in Turbine Blade Passages," *ASME. J. of Engineering for Power,* vol. 107, no. 2, pp. 248-257, 1985.

[32] W. Hawthorne, "Secondary Circulation in Fluid Flow," *Proc. Roy. Soc. London, A.,* vol. 206, no. 1086, pp. 374-387, 1951.

[33] W. Hawthorne, "Rotational Flow Through Cascades Part I. The Components of Vorticity," *Q J Mechanics Appl Math,* vol. 8, no. 3, pp. 266-279, 1955.

[34] W. Hawthorne and W. Armstrong, "Rotational Flow Through Cascades Part II. The Circulation About The Cascade," *Q J Mechanics Appl Math,* vol. 8, no. 3, pp. 280-292, 1955.

[35] P. Lampart, "Investigation of Endwall Flows and Losses in Axial Turbines. Part I. Formation of Endwall Flows and Losses," *J. of Theoretical and Applied Mechanics,* vol. 42, pp. 321-342, 2009.

[36] O. Sharma and T. Butler, "Predictions of Endwall Losses and Secondary Flows in Axial Flow Turbine Cascades," *ASME. J. of Turbomach,* vol. 109, no. 2, pp. 229-236, 1987.

[37] R. Goldstein and R. Spores, "Turbulent Transport on the Endwall in the Region Between Adjacent Turbine Blades," *ASME. J. of Heat Transfer*, vol. 110, no. 4a, pp. 862-869, 1988.

[38] V. Chaluvadi, "Blade - Vortex Interactions in High Pressure Steam Turbines," [Doctoral Thesis] Department of Engineering,University of Cambridge, 2000.

[39] H. Hodson and W. Dawes, "On the Interpretation of Measured Profile Losses in Unsteady Wake - Turbine Blade Interaction Studies," *ASME. J. of Turbomach*, vol. 120, no. 2, pp. 276-284, 1998.

[40] D. Sanders, "CFD Modeling of Separation and Transitional Flow in Low Pressure Turbine Blades at Low Reynolds Numbers," [Doctoral Thesis] Mechanical Engineering, Virginia Polythechnic Institute and State University, Blackburg, VA, 2009.

[41] S. Dixon and C. Hall, Fluid Mechanics and Thermodynamics of Turbomachinery, Elsevier Inc., 2014, pp. 215-262.

[42] L. Fielding, Turbine Design: The Effect on Axial Flow Turbine Performance of Parameter Variation, ASME Press, 2000.

[43] B. Muth, M. Schwarze, R. Niehuis and M. Franke, "Investigation of CFD Prediction Capabilities for Low Reynolds Turbine Aerodynamics," in *ASME Turbo Expo 2009: Power for Land, Sea and Air*, Orlando, Florida, 2009.

[44] M. Schobeiri and S. Abdelfattah, "On the reliability of RANS and URANS Numerical Results for High-Pressure Turbine Simulations: A Benchmark Experimental and Numerical Study on Performance and Interstrage Flow Behavior of High-Pressure Turbines at design and Off-Design Conditons Using Two," *ASME. J. of Turbomach,* vol. 135, no. 6, pp. 1-12, 2013.

[45] N. Gourdain, G. Wang, F. Duchaine and L. Gicquel, "Application of Large-Eddy Simulation to Rotor/Stator Configurations," *Congres Francais de Mecanique,* 2013.

[46] T. Leanard, L. Y. Gicquel, N. Gourdain and F. Duchaine, "Steady/Unsteady Reynolds-Averaged Navier-Stokes and Large Eddy Simulations of a Turbine Blade at High Subsonic Outlet Mach Number," *ASME. J. of Turbomach,* vol. 137, no. 4, pp. 1-10, 2015.

[47] M. Kuerner, G. A. R. Reichstein, D. Schrack, M. G. Rose, S. staudacher, J. Gier and K. Engel, "Low Pressure Turbine Secondary Vortices: Reynolds Lapse," *ASME. J. of Turbomachin,* vol. 134, 2012.

[48] P. Straka, "Simulation of a 3D Unsteady Flow in an Axial Turbine Stage," *EPJ Web of Conferences,* vol. 25, pp. 1-9, 2012.

[49] J. Denton and W. Dawes, "Computational Fluid Dynamics for Turbomachinery Design," *Proc Instn Mech Engrs,* vol. 213, no. Part C, pp. 1-19, 1999.

[50] J. Horlock and J. Denton, "A Review of Some Early Design Practice Using Computational Fluid Dynamics and a Current Perspective," *ASME. J. of Turbomachin,* vol. 127, 2005.

[51] D. G. Holmes, B. J. Moore and S. D. Connell, "Unsteady vs Steady Turbomachinery Flow Analysis: Exploiting Large-Scale Computations to Deepen our Understanding of Turbmachinery flow," in *SciDAC Conference*, Denver, CO, 2011.

[52] T. Poehler, J. Niewoehner, P. Jeschke and Y. Guendogdu, "Investigation of Nonaxisymmetric Endwall Contouring and Three-Dimensional Airfoil Design in a 1.5-Stage Axial Turbine-Part I: Design and Novel Numerical Analysis Method," *ASME J. of Turbomach,* vol. 137, no. 8, pp. 1-11, 2015.

[53] X. Wang, "CFD Simulations of Complex Flows in Turbomachinery and Robust Optimization of Blade Design," [Doctoral Thesis] Department of Mechanical Engineering, Vrije Universiteit Brussel, 2010.

[54] "AIAA. Guide for the Verification and Validation of Computational Fluid Dynamics," American Institute of Aeronautics and Astronautics, Reston, VA, 1998.

[55] C. J. Freitas, "Journal of Fluids Engineering Editorial Policy Statement on the Control of Numerical Accuracy Editorial," *J. of Fluids Engineering*, vol. 115, pp. 339-340, 1993.

[56] W. L. Oberkampf and C. J. Roy, Verification and Validation in Scientific Computing, Cambridge University Press, 2010.

[57] P. Roache, "Perspective: A Method for Uniform Reporting of grid Refinement Studies," *J. of Fluids Engineering,* vol. 116, pp. 405-413, September 1994.

[58] "Procedure for Estimation and Reporting of Discretization Error in CFD Applications," *ASME. J. Fluids Eng.*, vol. 130, no. 7, pp. 1-4, 2008.

[59] J. Cadafalch, C. Perez-Segarra, M. Marcolino and R. Consul, "A Post Processing Procedure for Assessing the Credibility of Finite Volume Numerical Simulations on Steady State Fluid Flow and Heat Transfer," in *European Congress on Computational Methods in Applied Sciences and Engineering*, Barcelona, 2000.

[60] F. M. White, Fluid Mechanics, Seventh Edition ed., New York, NY: McGraw-Hill, 2011, pp. 609-620.

[61] C. Borgnakke and R. Sonntag, Fundamentals of Thermodynamics, Seventh Edition ed., Hoboken, NJ: John Wiley & Sons, Inc., 2009, p. 147.

[62] J. Katz and A. Plotkin, Low-Speed Aerodynamics, Second Edition ed., New York, NY: Cambridge University Press, 2001, pp. 1-43,69,508-516.

[63] Saffman, Vortex Dynamics, New York, NY: Cambridge University Press 1992, 1992, pp. 1-18,107-115,.

[64] E. Borenstein, Interviewee, *KOKO HPC Specifications.* [Interview]. 9 November 2015.

[65] J. D. Anderson Jr., Computational Fluid Dynamics: The Basics with Applications, New York, NY: McGraw-Hill, Inc., 1995, pp. 37-93.

[66] S. Chakraborty, *Mod-01 Lec-41 Introduction of Turbulence Modeling,* National Programme on Technology Enhanced Learning, 2012.

[67] ANSYS CFX-Solver Theory Guide, Canonsburg,PA: ANSYS,Inc., 2013.

[68] S. Chakraborty, *Mod-01 Lec-42 Introduction to Turbulence Modeling,* National Programme on Technology Enhanced Learning, 2012.

[69] S.-H. Peng, L. Davidson and S. Holmberg, "The Two-Equation Turbulence k-w Model Applied to Recirculating Ventilation Flows," in *Dept. of Thermo and Fluid Dynamics, Chalmers Univ. of Tech.*, Gothenburg, 1998.

[70] B. Lauder and B. Sharma, "The Prediciton of Laminarization with a Two-Equation Model of Turbulence," *J. of Heat and Mass Transfer,* vol. 15, pp. 301-314, 1972.

[71] B. Lauder and B. Sharma, "Application of the Energy Dissipation Model of Turbulence to the Calculation of Flow Near a Spinning Disc," *Letters in Heat and Mass Transfer,* vol. 1, no. 2, pp. 131-138, 1974.

[72] D. C. Wilcox, "Re-assessment of the Scale-Determining Equation fo Advanced Turbulence Models," *AIAA Journal,* vol. 26, no. 11, pp. 1299-1310, 1988.

[73] F. Menter, "Two-Equation Eddy-Viscosity Turbulence Models for Engineering Applications," *AIAA Journal*, vol. 32, no. 8, pp. 1598-1605, August 1994.

[74] F. Menter, M. Kuntz and R. Langtry, "Ten Years of Industrial Experience with the SST Turbulence Model," in *Turbulence, Heat and Mass Transfer 4*, Begell House, Inc, 2003, pp. 625 - 632.

[75] P. Spalart and M. Shur, "On the Sensitization of Turbulence Models to Rotation and Curvature," *Aerosp. Sci. Technol.*, vol. 1, no. 5, pp. 297-302, 1997.

[76] P. E. Smirnov and F. R. Menter, "Sensitization of the SST Turbulence Model to Rotation and Curvature by Applying the Spalart-Shur Correction Term," in *ASME Turbo Expo 2008: Power for Land, Sea, and Air*, Berlin, Germany, 2009.

[77] K. Elliott, E. Savory, C. Zhang, R. Martinuzzi and W. Lin, "Analysis of a Curvature Corrected Turbulence Model using a 90 Degree Curved Geometry Modelled after a Centrifugal Compressor Impeller," in *20th Annual Conference of the CFD Society of Canada*, Alberta, Canada, 2012.

[78] R. Langtry and F. Menter, "Transition Modeling for General CFD Applications in Aeronautics," in *43rd AIAA Aerospace Sciences Meeting and Exhibit*, Reno,Nevada, 2005.

[79] F. Menter, R. Langtry, Y. Suzen, P. Huang and S. Volker, "A Correlation-Based Transition Model Using Local Variables Part I: Model Formulation," *ASME. J. of Turbomach*, vol. 128, no. 3, pp. 413-422, 2006.

[80] F. Menter and R. Langtry, "Transition Modelling for Turbomachinery Flows," in *Low Reynolds Number Aerodynamics and Transition*, InTech, 2012, pp. 31-58.

[81] S. A. Korpela, Principles of Turbomachinery, Hoboken, New Jersey: John Wiley & Sons, Inc., 2011, pp. 165-217.

[82] R. H. Aungier, Turbine Aerodynamics: Axial-Flow and Radial-Inflow Turbine Design and Analysis, New York, New York: ASME Press, 2003, pp. 133-166.

[83] H. Cohen, G. Rogers and H. Saravanamutto, Gas Turbine Theory, 4th ed., Harlow, Essex CM20 2JE: Addison Wesley Longman Limited , 1996.

[84] T. Matsunuma, "Annular turbine blade column properties in the low Reynolds number range," [Japanese: Doctoral Thesis] Department of Mechanical Engineering, University of Tokyo, Tokyo, Japan, 2003.

[85] ANSYS CFX-Solver Modeling Guide, Canonsburg,PA: Ansys,Inc., 2013.

[86] ANSYS-CFX Introduction, 12.1 ed., Canonsburg,PA, PA: Ansys, Inc., 2013.

[87] R. Langtry, F. Menter, S. Likki, Y. Suzen, P. Huang and S. Volker, "A Correlation-Based Transition Model Using Local Variables Part II: Test

Cases and Industrial Applications," *ASME. J. Turbomach,* vol. 128, no. 3, pp. 423-434, 2004.

[88] ANSYS CFX-Pre User's Guide, Canonsburg,PA: Ansys,Inc., 2013.

[89] ANSYS CFX-Solver Manager User's Guide, Canonsburg,PA: ANSYS, Inc., 2013.

[90] ANSYS CFX Reference Guide, Canonsburg,PA: ANSYS,Inc., 2013.

[91] ANSYS Fluid Dynamics Verification Manual, Canonsburg,PA: ANSYS,Inc, 2013.

[92] ANSYS CFX Tutorials, Canonsburg,PA: ANSYS, Inc., 2013.

[93] ANSYS CFD-Post User's Guide, Canonsburg,PA: ANSYS,Inc., 2013.

[94] D. Schlichting, Boundary-Layer Theory, Sixth ed., McGraw-Hill Inc., 1968, p. 639.

[95] D. Schlichting, Boundary-Layer Theory, Seventh ed., McGraw-Hill Inc., 1979, p. 455.

[96] S. C. Praisner TJ, "The Dynamics of the Horseshoe Vortex and Associated Endwall Heat Transfer—Part I: Temporal Behavior," *ASME. J. Turbomach,* vol. 128, pp. (4):747-754, 2005.

[97] J. Delery, Three-dimensional Separated Flow Topology: Critical Points, Separation Lines, and Vortical Structures, Hoboken, New Jersey: John Wiley & Sons, Inc., 2013.